Small signal impedance modelling and stability assessment of HVDC systems

Yin Chen

A thesis presented in fulfilment of the requirements for the degree of Doctor of Philosophy

Department of Electronic and Electrical Engineering

University of Strathclyde, Glasgow, UK

August 2020

This thesis is the result of the author's original research. It has been composed by the author and has not been previously submitted for examination which has led to the award of a degree.

Signed: Date:

Acknowledgements

I would like to express my gratitude to all those who helped me during my life in UK. The PhD program is an unforgettable experience for me.

With my most sincere respect, I would like to thank my supervisor, Professor Lie Xu, who encouraged and inspired me during the most difficult time in my PhD life. His profound knowledge, rigorous research attitude and research enthusiasm will benefit me for life. I would like to express my heartfelt thanks to him again and hope our cooperation will go well in the future research.

My special gratitude goes to Dr. Agusti Egea Alvarez, Dr. Rui Li, Dr. Gabriele Amico and Dr. Dong Chen who gave me valuable comments and suggestions for my research. I would like to thank Dr. Derrick Holliday, Dr. Grain P Adam, Dr. Md Habibur Rahman and other colleagues in PEDEC research group for all the help and advices.

Grateful acknowledgement is made to my friends, Yujie Lu, Ding zhou, Xiaozuo Huang, Lei Shi, Wang Xiang and Deyang Guo, for all concerns and companies in the past few years.

Finally, I would like to express my most gratitude to my family, for their support during my PhD journey.

Abstract

With high penetration of converter interfaced renewable energy and distributed generation, and increased use of HVDC interconnections, the characteristics of power systems is undergoing significantly changes. Interaction between grid-connected converters and networks is likely to increase, which may lead to stability and resonance problems, and in particular, when the grid is “weak” as the relatively high system impedance. Therefore, that is important adequate method is developed for assessing system stability.

This thesis presents the small signal impedance modelling of grid-connected 2-level voltage source converters (VSC) and modular multilevel converter (MMC) for system stability assessment. In the case of 2-level VSC connected to weak grid system, the VSC impedance is mapped into the positive-negative (pn) sequence-frame for ease of analysis, and the stability problem associated with the coupling admittance is studied. It is found that traditional outer-loop controllers (e.g., active/reactive power and AC voltage controllers) create high coupling admittance that has negative impact on system stability. Improved outer-loop controllers are proposed and to improve the system stability which add compensation terms into the d and q-axis at the potential resonance frequency range. Small signal analysis and time domain simulation confirm the effectiveness of the proposed method.

Large number of MMC based HVDC systems for interconnection or offshore wind farm integration are already in operation and many more will be installed in the coming years. MMC has multiple internal harmonics, which causes complex internal dynamics and multifrequency response. To accurately model the multiple frequency response and include all internal harmonics dynamics with MMC, the harmonic state-space (HSS) modeling approach is adopted. A detailed procedure for deriving the small-signal

model of single-phase MMC system using HSS modelling approach is presented first. To address the issues related to single-phase MMC modelling including the existence of zero-sequence current and the use of controllers in abc frame, which are not in accordance with practical 3-phase system, impedance modelling and validation of the three-phase MMC based on HSS are conducted. In order to simplify the analysis on the coupling characteristics between different frequencies in MMCs, the proposed model is developed in pn frame, where the zero-sequence current in three-phase three-wire system is modelled in a simple way. A simplified 2 by 2 admittance matrix in pn frame is extracted from the MMC small-signal model for ease of system stability analysis. Different outer-loop controllers, operating points and working mode are adopted and compared in the analysis to illustrate the effects system stability. It is found that for AC grid with single MMC, high PLL bandwidth leads to a less stable system. Compared with inverter mode, MMC in rectifier mode is more likely to induce system instability.

Using the developed impedance model, the multi-infeed interaction factor (MIIF) measure is adopted to analyze the interactions for multi-infeed converter systems. Detailed studied are carried out for an AC network with two MMCs considering different MIIIF. Analytical studies and time-domain simulation results show that system with high MIIF where strong couplings between the two MMCs exist may lead to instability.

Contents

List of Figures

List of Tables

Chapter 1 Introduction

1.1 HVDC power transmission technologies

Renewable energy sources have experienced fast growth in recent years. In European Union (EU), the renewable energy share has reached around 20% in 2020 and is likely to increase to 32% in 2030 [1]. Generally, renewable power generation is located far away from the main load centers and thus transmission technology plays an important role under such scenario. High voltage direct current (HVDC) is now considered as the most attractive solution for power transmission over long distance [2][3].

Figure 1.1 shows the basic scheme of a HVDC link for power exchange between two AC systems, where power transmission from AC system 1 to AC system 2 is taking as an example. The AC system 1 is connected to the HVDC rectifier through a transformer and the AC power is converted to DC power. Through the HVDC cables or overhead lines, the DC power is then transmitted to the inverter, where is the DC power is converted back to AC power.

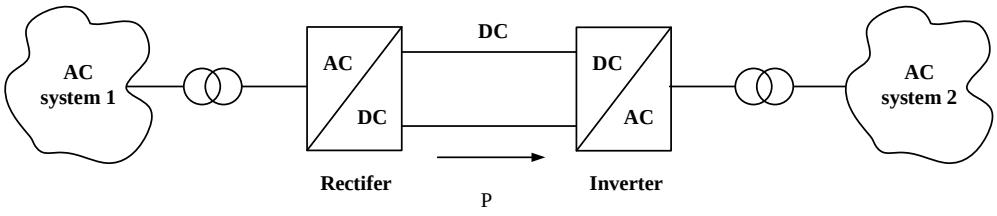

Figure 1.1 Basic scheme of an HVDC link

Depending on the converter technology used, HVDC system can be clarified as Line-commutated converter (LCC) based and voltage source converter (VSC) based

HVDC systems.

1.1.1 LCC based HVDC system

LCC is based on thyristors, which can only be controlled to switch on, whilst its switch off has to rely on the line voltage of the AC system to which the converter is connected in order to effect the commutation from one switching device to its neighbor [4]. Therefore, it is called line-commutated converter. LCC based HVDC systems have been used for power transmission for many decades due to its low operational losses, high power transmission capability, reliability and robustness [4][5]. Figure 1.2 shows the structure of a 12-pulse LCC bridge, where two 6-pulse converter bridges are connected in series at the DC side while the AC sides are connected through a star-star-delta transformer. With this structure, the 5^{th} and 7^{th} harmonic currents at the input AC side can be effectively eliminated. The main drawbacks of the LCC-HVDC system include the need of external voltage source for commutation, requiring large passive filters and the complexity during power reversal.

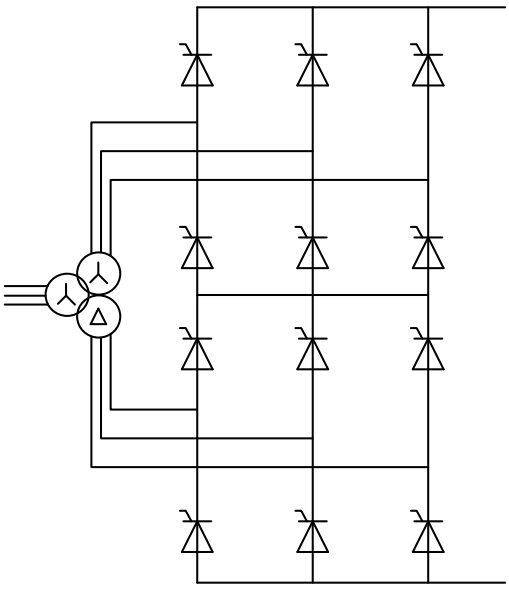

Figure 1.2 12-pulse bridge LCC

1.1.2 VSC based HVDC system

With the switching device insulated-gate bipolar transistor (IGBT), both turn-on and turn-off timing can be controlled, giving a second degree of freedom. As a result, IGBTs can be used to make self-commutated converters which are closer to a large inverter in operation. In such converters, the polarity of DC voltage is usually fixed and the DC voltage, being smoothed by a large capacitance, can be considered constant. For this reason, an HVDC converter using IGBTs is usually referred to as a voltage-source converter. VSC based HVDC system now attracts lots of attention due to its higher controllability. Comparing with LCC-HVDC, VSC-HVDC provides many advantages, such as no need of external voltage source, flexible power flow reversal and AC voltage support capability [7-10]. Early VSC-HVDC uses two-level converter, as shown in Figure 1.3. Fully controlled semiconductors, such as Insulated Gate Bipolar Transistors (IGBT) [6], are connected in parallel with freewheeling diodes at each arm [2]. The main drawbacks of two-level VSC include: (1) high switching losses caused by high switching frequency; (2) substantial filters for harmonic limitation ; and (3) unwanted electromagnetic interference caused by high dv/dt during switching [11].

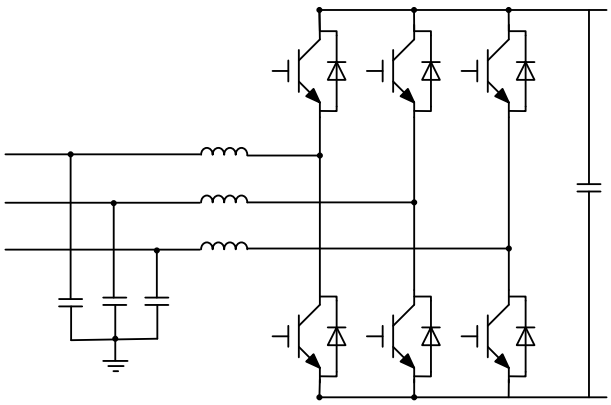

Figure 1.3 Two-level VSC

To address the issues with the two-level converter, modular multilevel converter (MMC) has been developed and is now regarded as a promising and competitive structure for VSC-HVDC. As shown in Figure 1.4 (a), it consists of 6 arms, each contains a large number of series-connected submodules. The submodule configuration used for MMCs i.e., the half-bridge submodule (HBSM) is shown in Figure 1.4 (b).

Compared with two-level VSCs, MMC has many attractive advantages, such as low power losses, modular design, and low harmonic distortion in the output AC voltage [12]-[15]. This technology is increasingly applied for large-scale offshore wind farms connection [16].

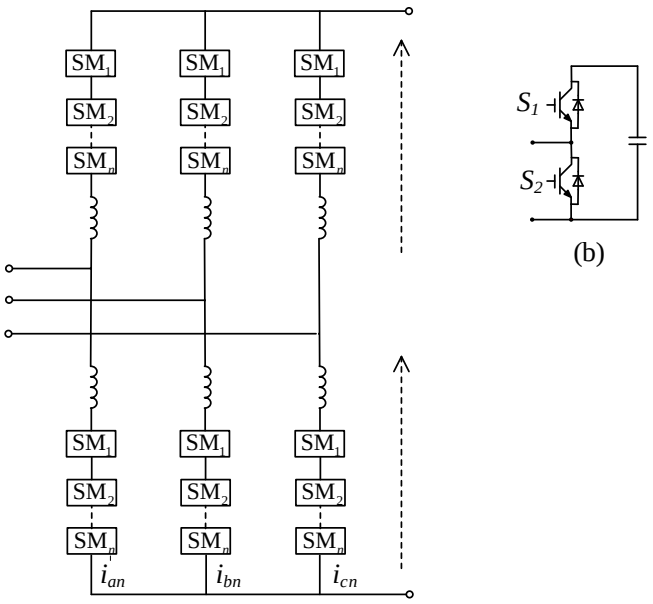

Figure 1.4 MMC and two sub-module topologies.

1.2 Stability issues of HVDC power transmission system

Increased penetration of renewable energy resources and the use of HVDC connections have significant impacts on power system behaviour. These power

generation units and transmission links are generally connected to the main grid through power electronics based converters. Although such converters offer fast control capability, the system inertial and damping are unavoidably decreased, which pose challenges on power system stable operation [17]. Recently, such stability issues caused by the interaction between the VSC-based HVDC and the power grid have drawn lots of attention [18]-[20]. Stability problems and studies have been reported in several LCC-HVDC transmission systems [21]. A 451Hz resonance led to shut down of several North Sea offshore wind farms when connected with MMC-based HVDC [22], and 1270Hz resonance was reported in Luxi back-to-back-HVDC project in China [23]. These resonance phenomena raise concern about the integration of renewable energy resources [24]. Efficient methods to identify the key causes of harmonic resonances and to mitigate such instability are crucial for future renewable energy development.

1.3 Small signal stability analysis

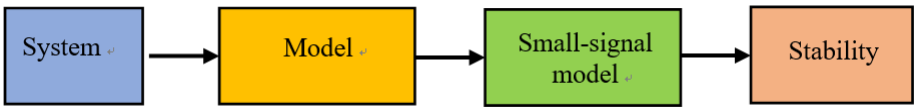

Figure 1.5 Procedure for system stability analysis

Figure 1.5 shows a typical procedure for system stability analysis. Based on the real system, an analytical system model is developed first. The model is then linearized to obtain the small-signal model and stability analysis is carried out to find the key courses of instability.

Modelling techniques are necessary prerequisite for analyzing the stability problem [25]. Power electronic circuits are time-variant and exhibit nonlinearity, and the time-variance is associated with the switching operation while the nonlinearity results from the dependence of power electronic switching instants on system

conditions [26]. The modelling techniques for power electronic converters can be broadly classified as time-domain and frequency-domain techniques [27]. The terms of time-domain and frequency-domain are referred to the signals being represented as a function of time and frequency, respectively [28].

The overview of existing techniques for modelling power electronic circuits, and identifying merits and disadvantages are presented in [25][29]. In general, time-domain modelling naturally accommodates nonlinear circuit behaviours, and relies on various mathematical methods to solve differential equations in time-domain [30]. So it may suffer from numerical oscillation and long time to reach the steady state. Although time-domain modelling methods are well established, they do not provide explicit information about the harmonic and inter-harmonic interactions around power electronic circuits [31].

On the other hand, frequency-domain modelling provides fast steady-state solutions, and explicitly represents the frequency coupling nature of power electronic circuits [32]. However, it cannot be used to capture the dynamics of a system. To capture the coupling frequency characteristics, models developed in the frequency-domain or its subset, the harmonic domain, are either iterative or linearized around an operating point [33]. The HSS i.e., Harmonic State-Space is an extension to the conventional frequency-domain in the sense that it preserves the explicit description of the frequency coupling nature of power electronic circuits, but more importantly, it extends the description of different frequencies coupling to the transient state [34][35].

1.4 Stability analysis method

For grid-converter interconnected system, eigenvalue-based analysis and impedance-based analysis are considered as the two main methods for stability analysis. They both have the advantages of less computation requirement and the ability to analyze the impact of controller dynamic and grid configuration on the

interconnected system stability [36].

1.4.1 Eigenvalue-based analysis

Eigenvalue-based analysis method was widely used to analyze the stability of grid connected wind farms [37] and HVDC transmission systems [38][39]. This method is generally based on one specific operating point and judges the system's global stability according to the damping of eigenvalues. However, when it is used to analyze the stability issues caused by the interaction between converters or between converter and grid, there are two main disadvantages:

- It requires a detailed analytical state-space model of the entire system, thereby highly depending on accurate parameters of the system. In many cases, it is very difficult to obtain the configuration and parameters of the grid network, and thus, eigenvalue-based analysis can lead to significant errors in this condition.

- To identify sustained harmonic oscillations in VSC systems, eigenvalue-based analysis requires discretizing the systems, leading to high computational requirement[36].

1.4.2 Impedance-based analysis

Impedance-based stability analysis method was introduced to evaluate interaction between a DC-DC converter based power supply and its source with an EMI filter in [40]. For the impedance-base method, the system can be partitioned into the source and the load subsystem and the small-signal stability of the system can be evaluated by applying Nyquist criteria to the source-load impedance ratio [41]. Recently, the impedance-based analysis method has been widely applied in stability analysis of grid-connected inverter at the interfacing point connecting to the grid [42][43]. The objective of the frequency-domain modeling is to linearize the converter dynamic model and find a Laplace transfer function type relationship between the selected input

and output variables and further derive the source-load impedance.

Figure 1.6 (a) and (b) show the small-signal representations using equivalent voltage and current source systems, respectively. For the voltage source system representation shown in Figure 1.6 (a), the source subsystem is modelled by its Thevenin equivalent circuit consisting of an ideal voltage source V_c in series with an output impedance Z_c, while the load subsystem is modelled by a current source I_g in parallel with an impedance Z_g. A shown, the current between the source subsystem and load subsystem is obtained as:

$$I(s) = \frac{V_c(s) + Z_g(s) I_g(s)}{Z_c(s) + Z_g(s)} \tag{1.1}$$

Equation (1.1) can be rewritten as:

$$I(s) = \left[\frac{V_c(s)}{Z_g(s)} + I_g(s) \right] \frac{1}{1 + Z_c(s)/Z_g(s)} \tag{1.2}$$

For system stability analysis, it can be assumed that the source voltage is stable when unloaded and the load current is stable without the voltage source. In this case, $V_c(s)$, $I_g(s)$ and $1/Z_g(s)$ are stable, such that stability of the current $I(s)$ depends on the stability of the second term on the right-hand side of (1.2), i.e.:

$$H(s) = \frac{1}{1 + Z_c(s)/Z_g(s)} \tag{1.3}$$

Obviously, (1.3) resembles the close-loop transfer function of a negative feedback control system where the forward gain is unity and the feedback gain is $Z_c(s)/Z_g(s)$. Thus, the system open loop gain is $Z_c(s)/Z_g(s)$ and the system is stable if and only if $Z_c(s)/Z_g(s)$ satisfies the Nyquist stability criterion i.e., the Nyquist curve

does not encircle the point (-1,0).

For the current-source system representation shown in Figure 1.6 (b), a Norton equivalent circuit in the form of a current source I_c in parallel with an output impedance Z_c, is adopted to represent the source. The load is represented by a voltage source V_g in series with an impedance Z_g. The current between the source subsystem and load subsystem is derived as:

$$I(s)=\left[I_c(s)-\frac{V_g(s)}{Z_c(s)}\right]\frac{1}{1+Z_c(s)/Z_g(s)} \tag{1.4}$$

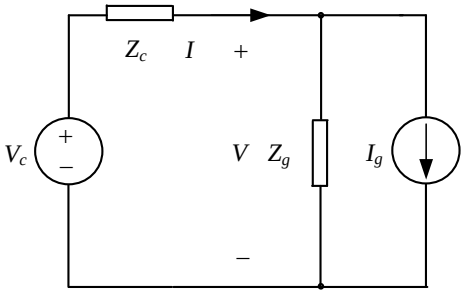

Thevenin equivalent circuit representation

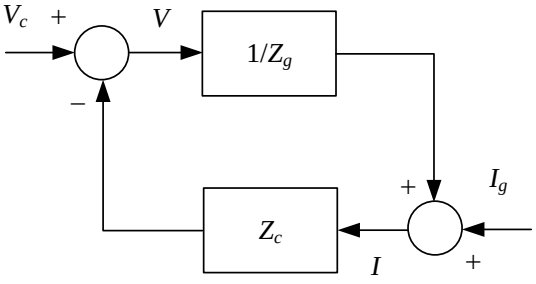

Block diagram representation

(a) Equivalent voltage source system

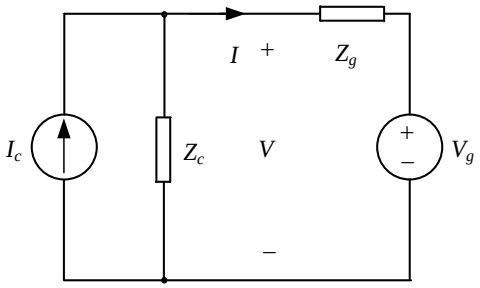

Norton equivalent circuit representation

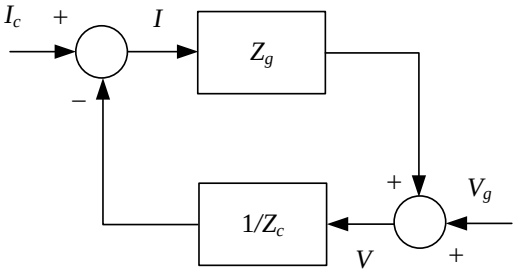

Block-Diagram Representation

(b) Equivalent current source system

Figure 1.6 Small-signal representation of the system

Following similar assumptions, the open loop gain is $Z_g(s)/Z_c(s)$ which can be used for assessing the system stability.

Note that the open loop gain of the voltage source system is different from the one of the current source system [41]. Since grid-connected converters are typically controlled using current loop, the system is better to be represented by the current source system as shown in Figure 1.6 (b), when impedance-based method is adopted.

Compared with eigenvalue-based analysis method, the grid side network can be deemed as a black box, i.e., detailed knowledge of the parameters and properties of the system is not required as long as measurements can be obtained at its terminals when impedance-based analysis is carried out. However, a weakness of the impedance method is the limited observability of certain states given its dependence on the definition of local source-load subsystems, which makes it necessary to investigate the stability at different interfacing points[44]-[47]. Moreover, when the source impedance and load impedance have Right Half-Plane Zeros, impedance-based analysis is invalid.

1.5 Definition of reference frame and frame transformation

Depending on the studies required, different reference frames can be used. Usually, the rotating synchronous dq frame or stationary αβ frame are the preferred frames for control designs, whereas the three-phase abc frame is the natural three-phase frame. Figure 1.7 shows the spatial relationships among the abc frame, αβ frame, and the dq frame. In addition, the pn frame (i.e. positive and negative sequence-frame) and fb frame (i.e. called modified sequence frame in [48]) may also be considered, and the relationships between the multiple reference frames are summarized in Figure 1.8 [49][50]. Based on the transformations between different frames, the impedance of converters can be calculated in a specific frame to reduce the complexity of impedance modelling. Moreover, the calculated impedance can be transformed into another frame for specific analysis requirements. In the following section, the transformations of a

variable from abc frame to dq frame, abc frame to pn frame, and dq frame to pn frame are presented.

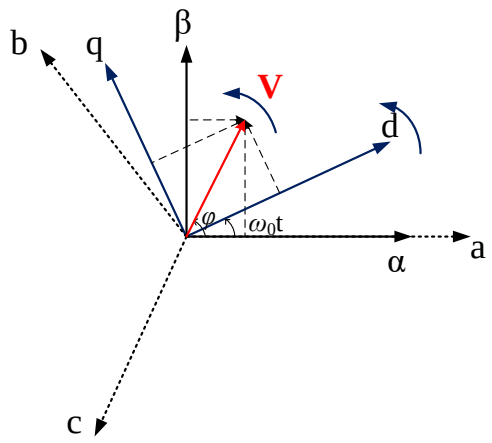

Figure 1.7 Definition of the stationary α β frame, rotating dq frame and three-phase abc frame

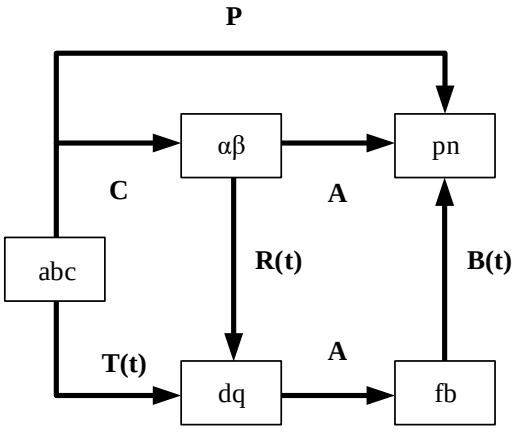

Figure 1.8 Transformation between different frames

1.5.1 abc frame to dq frame

Three-phase variables in abc frame can be transformed into the rotating dq

reference frame by the standard technique for the modeling of AC machines and converters [51]. Balanced three-phase quantities without harmonics can be assumed as constant DC values in a synchronously rotating reference frame. Hence, impedance modeling of three-phase VSC in the dq frame is relatively straightforward.

According to the definition of dq frame shown in Figure 1.7, the Park transformation **T(t)** in Figure 1.8 can be expressed as:

$$\mathbf{T(t)}=\frac{2}{3}\begin{bmatrix} \cos\omega_0 t & \cos(\omega_0 t-\frac{2\pi}{3}) & \cos(\omega_0 t+\frac{2\pi}{3}) \\ -\sin\omega_0 t & -\sin(\omega_0 t-\frac{2\pi}{3}) & -\sin(\omega_0 t+\frac{2\pi}{3}) \end{bmatrix} \tag{1.5}$$

In addition, the transformation from abc frame to dq frame can be obtained by the Clark transformation **C** and the rotating transformation **R(t)**, as:

$$\mathbf{T(t)}=\mathbf{R(t)C} \tag{1.6}$$

$$\mathbf{C}=\frac{2}{3}\begin{bmatrix} 1 & -\frac{1}{2} & -\frac{1}{2} \\ 0 & \frac{\sqrt{3}}{2} & -\frac{\sqrt{3}}{2} \end{bmatrix} \tag{1.7}$$

$$\mathbf{R(t)}=\begin{bmatrix} \cos(\omega_0 t) & \sin(\omega_0 t) \\ -\sin(\omega_0 t) & \cos(\omega_0 t) \end{bmatrix} \tag{1.8}$$

1.5.2 abc frame to pn frame

The method of symmetrical components was developed for investigation into the operation of an induction motor under unbalanced conditions and it has been extensively used in fault analysis [49][52]. Any unbalanced three-phase system can be expressed as the sum of a set of three balanced components, specifically, positive-sequence, negative-sequence, and zero-sequence as defined in Figure 1.9. The

subscript *p* denotes for positive-sequence components, a sum of three phasors equal in magnitude but 2π/3 apart in phase with a phase sequence of a-b-c as illustrated in Figure 1.9 (a). Similarly, the subscript *n* denotes for negative-sequence components, a sum of three phasors equal in magnitude but 2π/3 apart in phase with a phase sequence of a-c-b as illustrated in Figure 1.9 (b). The subscript *z* denotes for zero-sequence, a sum of three phasors equal in both magnitude and phase angle as illustrated in Figure 1.9 (c).

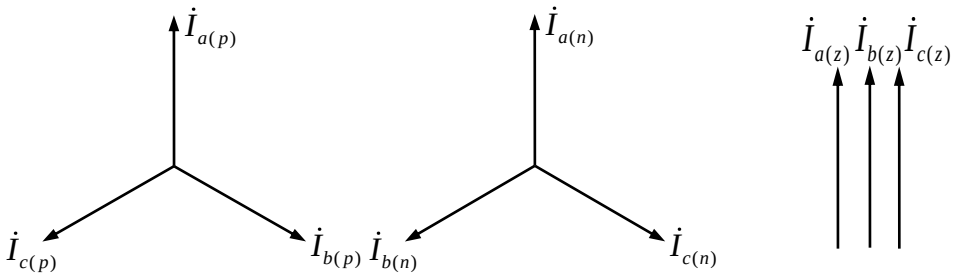

(a) Positive-sequence (b) Negative-sequence (c) Zero-sequence

Figure 1.9 Symmetrical components of three-phase phasors

According to the definition of pn frame, the transformation matrix **P** from abc frame to pn frame can be expressed as

$$\mathbf{P}=\begin{bmatrix} 1 & \alpha & \alpha^2 \\ 1 & \alpha^2 & \alpha \\ 1 & 1 & 1 \end{bmatrix} \tag{1.9}$$

where $\alpha = e^{j2\pi/3}$ and $\alpha^2 = e^{j4\pi/3}e^{4\pi/3}$.

1.5.3 dq frame to pn frame

In [53], the transformation matrix **A** from dq frame to fb frame in Figure 1.8 is expressed as

$$\mathbf{A} = \frac{1}{2}\begin{bmatrix} 1 & j \\ 1 & -j \end{bmatrix} \tag{1.10}$$

The frequency shift transformation matrix **B(t)** from fb frame to pn frame is derived in [49] as

$$\mathbf{B(t)} = \begin{bmatrix} e^{j\omega_0 t} & 0 \\ 0 & e^{-j\omega_0 t} \end{bmatrix} \tag{1.11}$$

Thus, according to Figure 1.8 and considering (1.10) and (1.11), the transformation matrix from dq frame to pn frame is obtained as

$$\begin{bmatrix} \triangle v_p(t) \\ \triangle v_n(t) \end{bmatrix} = \mathbf{B(t)A}\begin{bmatrix} \triangle v_d(t) \\ \triangle v_q(t) \end{bmatrix} \tag{1.12}$$

where $\Delta v_d(t)$ and $\Delta v_q(t)$ are the components in dq frame, and $\Delta v_p(t)$ and $\Delta v_n(t)$ are the corresponding components in pn frame.

1.6 Impedance modelling of grid-connected converter

For impedance-based stability analysis, an accurate impedance modelling of converters is required. Although two-level VSCs and MMCs share some similar characteristics, the complicated internal dynamics and the extra controllers of MMCs may make the conventional modelling method for VSC not applicable for MMC. In view of the distinguished features of the VSC and MMC, to explicitly assess the state-of-the-art of the two converters associated stability problems, the modeling methods of the two types of converters are illustrated separately in the following section.

1.6.1 Impedance modelling of a two-level VSC

According to the frame adopted in the modelling, the converter impedance can

be represented in the synchronous dq frame, the pn frame and the modified sequence frame, i.e. the fb frame in Figure 1.8.

1.6.1.1 Impedance modelling in dq frame

Under a three-phase balanced AC system, no DC component exits in the stationary frame. By transforming the stationary frame to synchronous dq frame, the grid-connected VSC system becomes two coupled DC systems with time invariant property, which indicates the system can be conducted with direct linearization in dq frame to derive the small-signal impedance. References [54][55] have derived the small-signal impedance of grid-connected converter with current control, PLL and power control. The effects of the VSC controllers such as the inner-loop current control, direct-voltage loop and PLL on the converter admittance are investigated in [54], and the following controllers design recommendations are provided to ensure the system stability:

- Use a PI controller with low integral gain or a direct P controller for the current loop.
- Select low bandwidths for the direct-voltage controller and PLL. Both bandwidths must be lower than one tenth of the current-loop bandwidth.
- Select low bandwidth of the voltage feedforward filter in current loop for normal mode of operation, but equal to the current-loop bandwidth or larger for short term transient-mode operation.

Reference [46] [47][55] focus on the impact of the PLL bandwidth and the power output of the converter on system stability based on the impedance model in dq frame. It concludes that higher PLL bandwidth will produce wider frequency range of negative resistance of Z_{qq} (q–q channel impedance) and higher power output of the converter results in a lower negative resistance of Z_{qq}. The negative resistance reduces system stability when the converter is working as a current source under weak grid.

For grid-connected VSC system, its impedance matrix in dq frame is actually 2×2 matrix with non-diagonal elements [54][55]. The off-diagonal terms in impedance matrix are nonzero, which indicates the system based on the impedance method is multiple input and multiple output (MIMO). Thus, generalized Nyquist criteria (GNC) for MIMO is required for the stability analysis. Moreover, because both grid impedance and VSC output impedance have off-diagonal elements, it cannot explain how the impedance characteristics of the grid and VSCs affect the oscillation frequencies [48].

1.6.1.2 Impedance modelling in pn frame

For the sequence impedance model in the pn frame, the grid-connected VSC inherently varies with time. Linearizing the time-varying system along a steady periodic trajectory yields a linear time periodic (LTP) system. To transform LTP systems into frequency-domain, the harmonic linearization method is introduced to obtain sequence impedances [56]-[60]. The model can be simplified as a diagonal transfer matrix and has two single-input single-output (SISO) transfer functions in the positive-sequence and negative-sequence. The system stability can be assessed by positive-sequence impedance and negative-sequence impedance individually.

Compared with the model in dq frame, the model in pn frame is beneficial for the stability analysis of multiple VSC systems since the overall system model is established in a common frame instead of multiple dq frames for multiple VSCs [58]. The stability can be analyzed directly through the impedance in pn frame, which is simpler and more straightforward than the method adopted in dq frame, i.e., GNC for MIMO. However, in [56][57], the SISO model is developed by ignoring the coupling components. Nevertheless, this kind of model ignores the small coupling term of converter pn sequence impedances, which may result in inaccurate stability estimation of power converters [61]. For example, a positive-sequence voltage perturbation

injected may lead to significant negative-sequence current perturbation. Hence, adopting diagonal impedance matrix to conduct stability analysis will be inaccurate theoretically.

The systematic methodology to derive the converter admittance in the pn frame is proposed in [62][63]. The admittance in the dq frame is derived firstly and is then transformed to the pn frame by applying the transformation matrices. The impact of the coupling between the positive- and the negative-sequence components of the converter admittance caused by negative-sequence compensator and the active power regulator on stability is assessed, whilst the impact of the negative-sequence compensator on the system stability is also studied.

1.6.1.3 Impedance modelling in modified sequence frame

To consider the frequency-coupling dynamics, a modified form of the sequence-domain impedance matrix is presented and the stability assessment are obtained in the modified sequence-domain based on GNC [48][64]. However, the modified sequence-domain model may yield a void sequence component without physical meaning. Reference [48] identifies the couplings between the mirror frequencies caused by PLL in grid-connected converters and proves that neglecting the admittance couplings can result in a wrong estimation of the system stability. In [65], a unified impedance model of VSC with PLL dynamic is derived based on complex space vectors. In addition, the mathematical relationship between the models in the dq frame and αβ frame is revealed. The frequency couplings effect on the stability of the grid-connected VSC is also studied. It is shown that the stability assessment not considering the coupling impedance in sequence domain created by the asymmetric controls in dq frame such as PLL, DC and power control, is not accurate.

1.6.2 Modelling for MMC

Due to the inherently complex behaviour of MMCs such as internal circulating current and submodule (SM) capacitor voltage ripple, the interactions between the MMC output impedance and grid impedance may lead to harmonic resonance and even instability [66]. Meanwhile, the complex internal dynamics of MMC makes modelling for stability analysis a challenging task [67][68]. In previous studies, several simplified equivalent models have been proposed to analyze the critical features of MMC [69].

1.6.2.1 Equivalent time-domain MMC models

The schematic diagram of an MMC was shown in Figure 1.4. In the early studies, simplified MMC model which does not contain the arm inductors and treated the SMs as switchable DC sources is considered [70]-[73]. The arm voltage is equivalent to a controlled and continuous voltage source consisted of many series-connected sub voltage sources as shown in Figure 1.10.

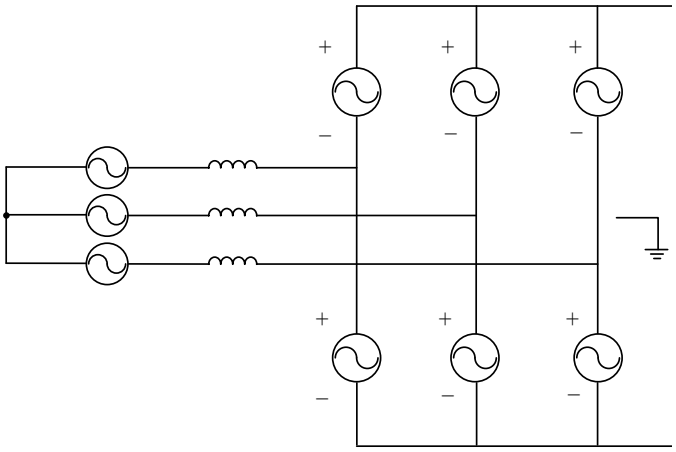

Figure 1.10 Early MMC equivalent circuit

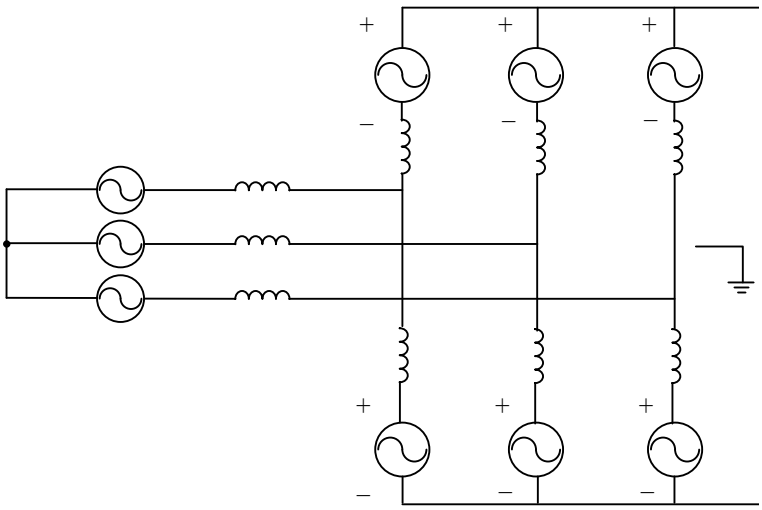

Figure 1.11 Equivalent circuit with arm inductors

MMC model with arm inductors to limit the arm current was late developed in [74]-[79], as shown in Figure 1.11. The arm voltage is still regarded as a controlled voltage source [80], which is only valid when the SM capacitors are large enough so the SM voltages are constant. Moreover, the number of SM is assumed to be large enough so the arm voltage can be regarded as continuous.

Although the above two equivalent models are simple and straightforward for MMC study, they have many drawbacks and limitations. Firstly, all the SMs in one arm are treated as a single unit, so the behaviour of each individual SM is lost [69]. Secondly, the dynamic of the coupling between the voltage of the SM capacitor and the arm current is ignored. Finally, the internal behaviour of the MMC such as circulating current is lost.

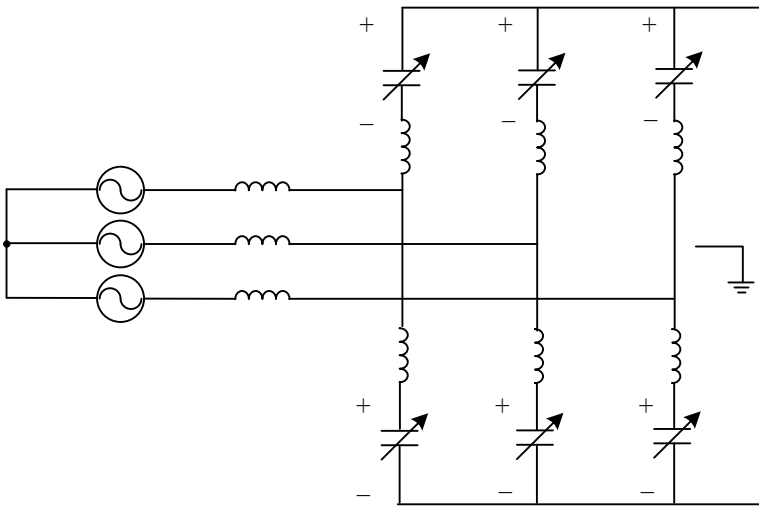

Figure 1.12 Equivalent circuit with nonlinear arm capacitors

The MMC model shown in Figure 1.12 is developed in [81]-[83]. The difference between this model and the previous models is that the arm voltage is equivalent to the voltage of a nonlinear capacitor with time variant sinusoidal capacitance. The capacitor voltage is still assumed a controlled voltage source. With this modeling approach the converter can be controlled by calculating the total capacitor energy in each arm in order to regulate the capacitor voltage, and the total energy of the upper and lower arm can be regulated to control the power delivery to the load. The difference between the upper and lower arm energies is then used to balance their respective voltages. With this model, the ripple voltage of the capacitor can be determined [84].

Since the SMs in an arm connected in series, the current flowing through each SM is the same. If each SM in one arm has the same duty ratio, the MMC can be represented as an averaged model [85]-[87], as shown in Figure 1.13.

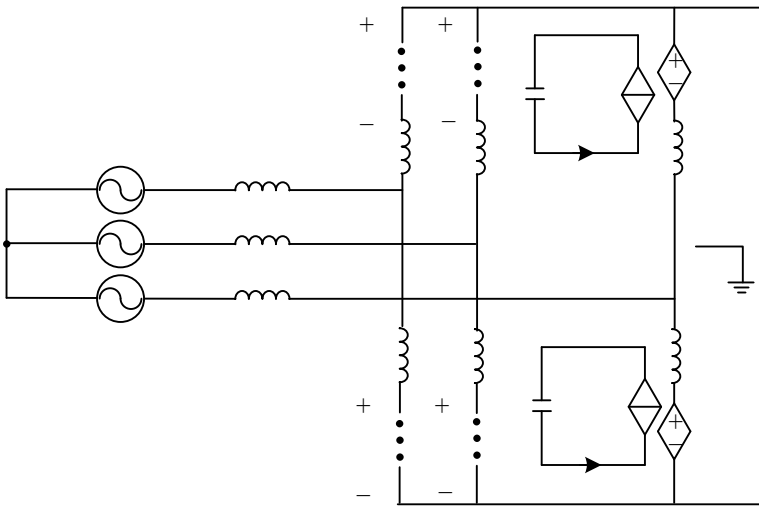

Figure 1.13 Equivalent circuit of averaged model

Compared to the previously described equivalent MMC models, the advantage of the averaged model is that the circulating current and the information of individual capacitors can be fully captured by this model. The limitation of this model is that the information of the individually SMs cannot be differentiated, as all of them are assumed to be identical. Another shortcoming is that the arm voltage is considered as continuous, which implies that the harmonics created by SM switching cannot be considered in the model. However, this is the common shortcoming of the four equivalent MMC models [69].

1.6.2.2 Impedance modelling of MMC

Since the impedance-based analysis is widely applied in grid-connected converter systems, various studies have been carried out to calculate the MMC impedance-based on the MMC averaged model shown in Figure 1.13.

In [88], an analytical sequence impedance model of a three-phase MMC is derived with the internal MMC dynamics, following the same approach used for two-level VSCs. However, the 2nd harmonic in the arm current and PLL are not considered

in the model. In [89], the AC side input admittances of the MMC under various control strategies are derived, though the circulating current controller is not included. Reference [90] focuses on the impact of different current control schemes on the shape of MMC admittance, considering the 2nd internal harmonic current. However, a large resistive load is added at the AC side to provide increased passive damping, so that high-order harmonics are not presented in the system and thus no need to be considered [90]. However, in real systems, such strong passive damping does not exist and harmonic or inter-harmonic resonances are a major concern and must be modelled.

The HSS method proposed to analyze linear time-periodic (LTP) system [91], models not only the steady-state harmonics in LTP systems, but also the dynamics of the harmonics during transients. Consequently, HSS method has been widely used to model power networks and converters, e.g., static synchronous compensators [92], LCC converters [91], transmission lines [93], and two-level VSCs [94]. Recently, HSS method has been used to model MMC impedance considering the impact of the internal harmonics [95]-[97]. Since the Fourier coefficients matrices in the HSS model are diagonal-constant matrices (Toeplitz matrices) [95], the MMC small-signal model based on HSS can be easily extended to any harmonic order. Hence, the dynamics of high-order harmonics in MMC can be fully considered.

However, various problems and limitations still exist in the proposed HSS-based MMC small-signal modelling methods [95]-[97]. In [95], a single-phase MMC model is developed and the impedance that reflects the voltage and current at the same frequency is derived but the couplings at different frequencies generated by the internal harmonics of MMC, are not taken into account. Impedance models of three-phase four-wire MMC systems, in which both the MMC DC mid-point and the AC neutral point are grounded providing a circulation path for the zero-sequence current, are derived in [96][97]. However, in reality, MMC systems are likely to be configured as an equivalent three-phase three-wire system without the low impedance path for the zero-

sequence current. To describe the MMC zero-sequence current on the MMC AC side in three-phase three-wire systems, zero-sequence voltage compensation is proposed to add into the single-phase model in [96] and the single-phase impedance is obtained for three-phase system stability assessment. The MMC controllers in the models also adopt the proportional resonant (PR) controller in the abc frame, implying that the controls for phase a, b, and c are totally independent and identical. However, for MMC controller implemented in αβ frame or dq frame, the single-phase modelling method is inadequate and is thus unsuitable for three-phase MMC system.

In the latest study on MMC impedance modelling, reference [98] provides a comprehensive three-phase HSS model of MMC. Similar to [96], the DC mid-point voltage is compensated using the AC neutral point voltage to eliminate the zero-sequence current. However, when developing the small-signal model, the expression of the neutral point voltage involves the steady-state value and the perturbation variables of three-phase voltages as well as the control signal of the arms, which lead to an extra complex calculation in the HSS model. In [98], the complex vector representation of the controllers in dq frame obtained based on the transfer function, has to be transformed to the αβ frame before being integrated into the MMC model to obtain the impedance in sequence frame, thus leading to complicated transformation and calculation.

In addition, the MMC impedance obtained in [98] is a 10 by 10 matrix. In order to simplify the process of stability assessment, a single input and single output (SISO) equivalent impedance of the MMC is derived by considering the grid side impedance. However, if the grid structure is more complex, e.g., there are other converters connected to the grid in close proximity, the grid impedance seen by the MMC will also become complicated. Thus it is difficult to simplify the 10 by 10 matrix of MMC impedance to a SISO equivalent. Therefore, a MMC impedance independent of the grid side impedance and in simple form is more beneficial for system stability

assessment with multiple converters. MMC represented by 2 by 2 impedance matrix in modified sequence-domain [99] is developed in [100][101]. However, in the modified sequence-domain the frequencies of the coupling admittance cannot be represented. Moreover, unlike the impedance in the sequence domain, the MMC impedance in the modified sequence domain cannot be measured directly in time-domain due to the existence of frequency shift between the modified sequence domain and sequence domain. In [102], a MMC 2 by 2 impedance matrix is derived to capture the characteristics of frequency coupling in sequence frame. However, the work focuses on the coupling between the AC system and DC system of the MMC and the dynamic of the PLL in AC side is not considered.

1.7 Current status and application of HVDC in UK and world-wide

Considering the increased network interconnections and connection of large offshore wind farms (e.g. in Europe) using HVDC links, many power networks have seen significant numbers of HVDC converters connected in close proximity. For example, as outlined in [103] and schematically shown in Figure 1.14, the GB network will have more than 20 HVDC connection by 2027, with a total transmission capacity of over 16 GW. Some studies have been carried out considering the interaction between LCC and VSC inverter stations and the parameters of the controllers are investigated based on the small-signal model [104][105]. In [106], the admittance-based stability assessment are adopted to studied the control interactions between two VSCs in frequency-domain. In [107], two MMCs connected to an AC grid system is studied based on MMC small-signal model. However, the model does not take into account the internal harmonics of MMC and thus the results are not representative. Therefore, further work to investigate the interaction between MMCs located in close proximity are required.

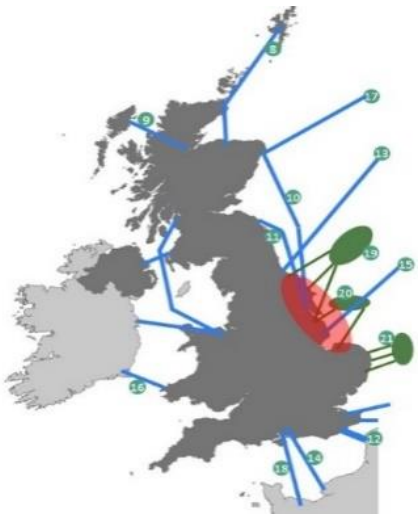

Figure 1.14 Outlook of HVDC connection in the GB power grid [103]

1.8 Motivation and aims of the work

1.8.1 Research motivation and objective

As discussed in Section 1.6.1, when asymmetric controller in dq frame [50] is adopted in two-level grid-connected VSC, the converter will generate coupling at different frequencies between positive- and negative-sequence components in pn frame. Reference [48][65] only conclude that ignoring this coupling may result in a wrong estimation of the system stability. The effect of the coupling impedance on system stability has not been investigated in detail. However, with the increase of grid-connected converters, e.g. wind farms and PV generation, the strength of grid becomes weaker and system stability becomes a serious problem [108]. The coupling impedance may have significant impact on system stability under weak grid.

According to the literature review on MMC impedance modelling, the main drawbacks of the existing MMC models are:

- The singe-phase model [95][96] cannot be used to describe three-phase MMC system since the model cannot deal with the zero-sequence current and cannot

model the controller adopted in three-phase MMC.

- The existing method adopted to deal with the zero-sequence current involves too many variables in three-phase model [98], which lead to an extra complex calculation in the model. Moreover, the model adopted has complicated transformation since the transfer function of the controller in dq frame is transformed to αβ frame and then further to pn frame by introducing the conjugate transfer function matrix.

- The calculated admittance matrix of MMC in pn frame has too high dimensions e.g., 10 by 10 matrix in [98], which brings great difficulty to system stability assessment.

Thus, it is necessary to develop an accurate and simplified impedance model of the MMC.

Considering the increased network interconnections and connection of large offshore wind farms (e.g. in Europe) using HVDC links, many power networks will see significant numbers of HVDC converters connected in close proximity. Therefore, further work to investigate the interaction between MMCs located in close proximity are required.

The main aims of this thesis are:

- to investigate the impedance couplings caused by the control in dq frame and improve the system stability based on the impedance model of grid-connected VSC in pn frame under weak grid;

- to develop an accurate and effective impedance mode of the MMC that is suitable for the practical application;

- to study the impact of different controller setting and control parameters on MMC system stability;

- to investigate the interaction of converters in close proximity.

1.8.2 Thesis contributions

The main contributions of this thesis can be summarized as:

- The stability problems associated with the coupling admittance in pn frame created by the PLL and outer-loop controller are studied based on the small-signal admittance of the VSC connected to a weak AC grid. An improved outer-loop controller is proposed to reduce the coupling admittance and improve system stability.

- A comprehensive impedance model of three-phase MMC is developed based on HSS theory. In the model proposed, the zero-sequence current is directly forced to zero to form a 3-phase 3-wire system. The model considers the impact of the internal harmonic on the impedance and also incorporates the effect of the controllers. The coupling between the positive-and negative-sequence brought by dq frame controller is also included in the model.

- With the impedance model, the impact of PLL bandwidth, the outer-loop controller, different operating point and different operating modes on the small-signal impedance and the stability of the MMC connected to the ac grid is fully investigated.

- Interaction of converters in close proximity is studied using the developed MMC models and system stability assessment in case of multiple MMCs in a network are carried out by introducing the multi-infeed interaction factor (MIIF).

1.9 Thesis outline

The work is composed of additional five Chapters, whose contents are outlined as follows.

Chapter 2 describes the procedure of deriving VSC admittance in pn sequence frame. Based on this, the stability problems associated with the coupling admittance created by the PLL and outer-loop controller of two-level VSCs are studied. An improved outer-loop controller that reduces the coupling admittance is proposed to improve the system stability.

Chapter 3 begins with a brief description of the HSS method and then presents a detailed procedure for deriving the small-signal model of single-phasor MMC system using HSS modelling approach. The small-signal HSS models of the MMC are developed, and the small-signal impedance of the MMC is obtained. The time-domain simulation results are provided to validate the developed MMC impedance models.

Chapter 4 describes the impedance modelling and validation of the three-phase MMC converter based on HSS. To realize the zero-sequence current control and capture the multi-frequency response of MMC in a 3-phase 3-wire system, the model of the three-phase MMC is developed in the pn frame. A complete model of a three-phase MMC with the description of various controllers are established by using the HSS method. The coupling between the positive and negative-sequence brought by the asymmetric dq controller are analyzed in the model. The small-signal impedances obtained from the developed analytical model are validated using time-domain models under various different scenarios in MATLAB/Simulink.

Chapter 5 carries out the stability assessment to show how the HSS-based MMC impedance model can be used in practical system analysis. Two specific scenarios, i.e., a single MMC connected to a weak grid and two MMCs connected to AC grids, are studied for the stability assessment. Based on the impedance-based analysis, the effect of different controllers, operating points and control modes on MMC impedance and system stability are investigated. Interaction of converters and stability of system with multiple converters in close proximity are studied using the developed models

considering multi-infeed interaction factors (MIIF). Time-domain simulations are carried out in MATLAB/Simulink to validate the theoretical analysis.

Chapter 6 concludes the thesis by summarising the major findings of this research and suggests for future work.

Chapter 2 Small-signal impedance model of the VSC connected to a weak grid system

In this chapter, the small-signal model of a grid connected VSC system is presented. The admittance of the VSC system in dq frame is derived and is used to carry out system stability assessment by applying the impedance-based method [41]. Since the admittance terms in dq frame are coupled, which increases difficulties of analyzing the system, in [48], the admittance in dq frame is mapped into the pn frame to simplify the stability analysis. However, in some cases the coupling admittance of VSC in pn frame can still impact on the system stability assessment. Based on the converter admittance in pn frame, the stability problems associated with the coupling admittance created by the PLL and outer-loop controller are studied separately. To overcome the disadvantage of the traditional outer-loop controller, an improved outer-loop controller that can reduce the coupling admittance is proposed to improve the system stability. VSC connected to a weak power grid system is modelled in MATLAB-SIMULINK® environment to validate the theoretical study.

2.1 Model of grid connected VSC system

The studied VSC system connected to AC grid is shown in Figure 2.1. As shown in Figure 2.1, the system consists of a VSC, an RLC-type (R_f L_f C) filter used to attenuate PWM harmonics generated by the converter, and an AC grid represented by a RL ($R_g L_g$) Thevenin equivalent circuit. The capacitor voltage v_{abc} and inverter current i_{abc} are measured and used for the VSC controller. Ignoring the voltage variation at the DC side, the DC link capacitor is replaced by an ideal DC voltage source. The electrical parameters of the studied system are listed in Table 2.1. Note that this studied system is modelled based on per unit system. The grid inductance L_g is equal to 0.5 p.u.

(SCR=2) indicating a weak AC grid.

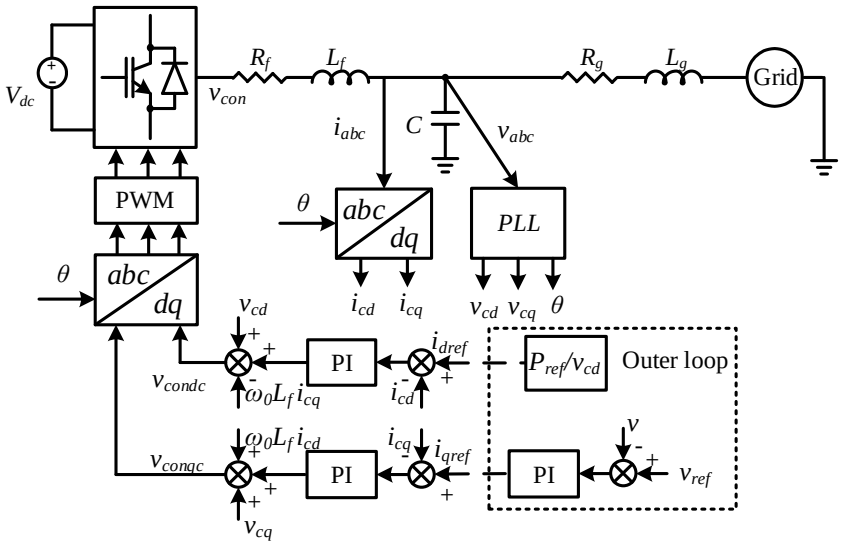

Figure 2.1 The configuration of a grid connected VSC system

Table 2.1 System and controller parameters of the grid-connected VSC system

AC nominal frequency f_0	50 Hz
Coupling inductance L_f	0.15 p.u.
Coupling Resistance R_f	0.01 p.u.
Filter Capacitance C	0.1 p.u.
Grid inductance L_g	0.5 p.u. (SCR=2)
Grid Resistance R_g	0.01 p.u.
Rated active power	2 MW.
VSC nominal voltage	690 V
Current-loop proportional gain K_p	0.36
Current-loop integral gain K_i	67.8584

A conventional dq frame based current control is implemented for the converter. For the converter circuit, the VSC current-loop dynamics in dq frame are expressed as

$$R_f i_d + L_f \frac{di_d}{dt} = v_{cond} - v_d + \omega_0 L_f i_q \tag{2.1}$$

$$R_f i_q + L_f \frac{di_q}{dt} = v_{conq} - v_q - \omega_0 L_f i_d \tag{2.2}$$

where ω_0 is fundamental angular velocity of the grid. With proportional-integral (PI) regulators, the current control loop is illustrated in Figure 2.1.

The PLL in the controller is used to estimate the angle of the AC grid. The input of the PLL loop is the measured capacitor voltage v_{abc}, and the output is the estimated angle θ which is used to transform the signals between abc and dq frames. As shown in Figure 2.2, a PI controller is used to control the q-axis voltage v_{cq} to 0 in the steady state so that the d-axis voltage is aligned to the phasor of the grid voltage.

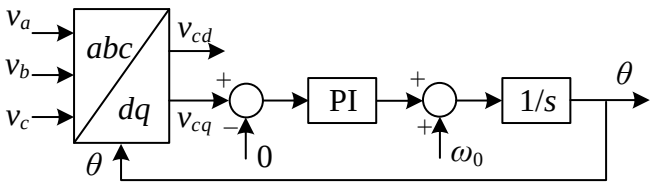

Figure 2.2 Block diagram of the PLL loop

The outer controller consists of two loops, the active power regulator, and the voltage regulator. The active power regulator controls the active power generated by converter, and the output of the regulator is the d-axis reference current i_{dref} as shown in Figure 2.1. The relationship between d-axis reference current i_{dref} and the reference of active power P_{ref} based on per unit system can be expressed as

$$i_{dref} = \frac{P_{ref}}{v_{cd}} \tag{2.3}$$

The AC voltage regulator provides the q-axis reference current i_{qref} of the current-loop and the magnitude of the measured AC voltage can be calculated by:

$$v = \sqrt{{v_{cd}}^2 + {v_{cq}}^2} \tag{2.4}$$

In the study, a PI regulator is considered for a zero tracking error under steady state conditions as shown in Figure 2.1.

2.2 VSC Small-signal impedance calculation

Generally, nonlinear systems are converted to linear systems so that classic control theory can be applied for stability analysis and controller design in the frequency-domain [50]. To linearize the studied system shown in Figure 2.1, the small signal theory is introduced. Based on the small-signal model, the small-signal impedance of the VSC including its controller can be derived.

2.2.1 Admittance in dq frame

Based on (2.1) and (2.2), the small-signal model of the system shown in Figure 2.1 can be derived as:

$$\begin{bmatrix} \triangle v_{cond} \\ \triangle v_{conq} \end{bmatrix} - \begin{bmatrix} \triangle v_d \\ \triangle v_q \end{bmatrix} = \begin{bmatrix} L_f s + R_f & -\omega_0 L_f \\ \omega_0 L_f & L_f s + R_f \end{bmatrix} \begin{bmatrix} \triangle i_d \\ \triangle i_q \end{bmatrix} \tag{2.5}$$

where Δv_{cond}, Δv_{conq}, Δv_d, Δv_q, Δi_d and Δi_q are the disturbance variables of the converter voltage, capacitor voltage and converter current in the grid dq frame, respectively. ω_0 is the fundamental angular velocity of the grid voltage.

When PLL is adopted to synchronize the converter to the grid, there exists two rotating frames. One frame is the actual system (grid) dq frame and the other is the dq frame of the controller defined by the PLL. During steady state, the control dq frame is aligned to the system dq frame, and the steady state voltage and current values are the same in the two frames. V_d, V_q, I_d, I_q, V_{cond} and V_{conq} are defined as the steady state values of the capacitor voltage, converter current and converter voltage in system dq frame, respectively.

During small-signal perturbations, the control dq frame is not aligned with the system dq frame anymore and an angle difference $\Delta\theta$ between the two frames appears. With the linearization of the PLL model presented in Figure 2.2, the relationship between the angle difference $\Delta\theta$ and q axis perturbation voltage Δv_q is obtained and shown in Figure 2.3 [41].

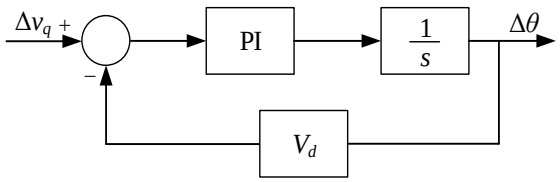

Figure 2.3 Relationship between $\Delta\theta$ and Δv_q

From Figure 2.3, the transfer function of PLL based on small-signal model can thus be expressed as:

$$\triangle\theta = G_{pll}(s)\triangle v_q \tag{2.6}$$

$$G_{pll}(s) = \frac{K_{ppll}s + K_{ipll}}{s^2 + V_d K_{ppll}s + V_d K_{ipll}} \tag{2.7}$$

where $G_{pll}(s)$ is the closed-loop transfer function of PLL, and K_{ppll} and K_{ipll} are the proportional and integral gains, respectively.

It can be observed that if there exists voltage perturbation in the terminal voltage of the VSC, there will be angle deviation $\Delta\theta$ extracted from PLL, which will further affect the frame transformation. During steady state, the relationship between voltage V_{cd} and V_{cq} in the control frame determined by PLL and V_d and V_q in the system frame can be expressed as:

$$\begin{bmatrix} V_{cd} \\ V_{cq} \end{bmatrix} = \begin{bmatrix} \cos(0) & \sin(0) \\ -\sin(0) & \cos(0) \end{bmatrix} \begin{bmatrix} V_d \\ V_q \end{bmatrix} \tag{2.8}$$

The voltage perturbations Δv_d and Δv_q passing through PLL results in:

$$\begin{bmatrix} V_{cd}+\triangle v_{cd} \\ V_{cq}+\triangle v_{cq} \end{bmatrix} = \begin{bmatrix} \cos(0+\triangle\theta) & \sin(0+\triangle\theta) \\ -\sin(0+\triangle\theta) & \cos(0+\triangle\theta) \end{bmatrix} \begin{bmatrix} V_d+\triangle v_d \\ V_q+\triangle v_q \end{bmatrix} \tag{2.9}$$

Subtracting the steady-state component (2.8) from (2.9) yields the voltage perturbation in PLL frame as:

$$\begin{bmatrix} \triangle v_{cd} \\ \triangle v_{cq} \end{bmatrix} = \begin{bmatrix} \triangle v_d+\triangle\theta V_q+\triangle\theta\triangle v_q \\ \triangle v_q-\triangle\theta V_d-\triangle\theta\triangle v_d \end{bmatrix} \tag{2.10}$$

Ignoring the second order terms $\triangle\theta\triangle v_q$ and $\triangle\theta\triangle v_d$, (2.10) can be rewritten as:

$$\begin{bmatrix} \triangle v_{cd} \\ \triangle v_{cq} \end{bmatrix} = \begin{bmatrix} \triangle v_d+\triangle\theta V_q \\ \triangle v_q-\triangle\theta V_d \end{bmatrix} \tag{2.11}$$

Substituting (2.6) into (2.11) yields:

$$\begin{bmatrix} \triangle v_{cd} \\ \triangle v_{cq} \end{bmatrix} = \begin{bmatrix} \triangle v_d+\triangle\theta V_q \\ \triangle v_q-\triangle\theta V_d \end{bmatrix} = \begin{bmatrix} 1 & V_q G_{pll}(s) \\ 0 & 1-V_d G_{pll}(s) \end{bmatrix} \begin{bmatrix} \triangle v_d \\ \triangle v_q \end{bmatrix} \tag{2.12}$$

The current perturbation in PLL frame can also be expressed in the similar form

as:

$$\begin{bmatrix} \triangle i_{cd} \\ \triangle i_{cq} \end{bmatrix} = \begin{bmatrix} \triangle i_d + \triangle \theta I_q \\ \triangle i_q - \triangle \theta I_d \end{bmatrix} = \begin{bmatrix} 0 & I_q G_{pll}(s) \\ 0 & -I_d G_{pll}(s) \end{bmatrix} \begin{bmatrix} \triangle v_d \\ \triangle v_q \end{bmatrix} + \begin{bmatrix} \triangle i_d \\ \triangle i_q \end{bmatrix} \tag{2.13}$$

where I_d and I_q are the d-axis and q-axis currents, respectively.

The small signal output voltage references by the current controller in system dq frame can be obtained as:

$$\begin{bmatrix} \triangle v_{cond} \\ \triangle v_{conq} \end{bmatrix} = \begin{bmatrix} \triangle v_{condc} - \triangle \theta V_{conqc} \\ \triangle v_{conqc} + \triangle \theta V_{condc} \end{bmatrix} = \begin{bmatrix} 0 & -V_{conq} G_{pll}(s) \\ 0 & V_{cond} G_{pll}(s) \end{bmatrix} \begin{bmatrix} \triangle v_d \\ \triangle v_q \end{bmatrix} + \begin{bmatrix} \triangle v_{condc} \\ \triangle v_{conqc} \end{bmatrix} \tag{2.14}$$

where V_{cond}, V_{conq}, Δv_{condc} and Δv_{condc} are the steady state and disturbance voltages of the current-loop output in the control frame, respectively.

Defining matrices: $\triangle \mathbf{v}_c = \begin{bmatrix} \triangle v_{cd} \\ \triangle v_{cq} \end{bmatrix}$, $\triangle \mathbf{i}_c = \begin{bmatrix} \triangle i_{cd} \\ \triangle i_{cq} \end{bmatrix}$, $\triangle \mathbf{v} = \begin{bmatrix} \triangle v_d \\ \triangle v_q \end{bmatrix}$, $\triangle \mathbf{i} = \begin{bmatrix} \triangle i_d \\ \triangle i_q \end{bmatrix}$, $\triangle \mathbf{v}_{conc} = \begin{bmatrix} \triangle v_{condc} \\ \triangle v_{conqc} \end{bmatrix}$, $\triangle \mathbf{v}_{con} = \begin{bmatrix} \triangle v_{cond} \\ \triangle v_{conq} \end{bmatrix}$, $\mathbf{A} = \begin{bmatrix} 1 & V_q G_{pll}(s) \\ 0 & 1 - V_d G_{pll}(s) \end{bmatrix}$, $\mathbf{B} = \begin{bmatrix} 0 & I_q G_{pll}(s) \\ 0 & -I_d G_{pll}(s) \end{bmatrix}$, $\mathbf{E} = \begin{bmatrix} 0 & -V_{conq} G_{pll}(s) \\ 0 & V_{cond} G_{pll}(s) \end{bmatrix}$, and $\mathbf{Z}_f = \begin{bmatrix} L_f s + R_f & -\omega_0 L_f \\ \omega_0 L_f & L_f s + R_f \end{bmatrix}$, equations (2.5), (2.12), (2.13) and (2.14) can be rewritten as

$$\triangle \mathbf{v}_{con} - \triangle \mathbf{v} = \mathbf{Z}_f \triangle \mathbf{i} \tag{2.15}$$

$$\triangle \mathbf{v}_c = \mathbf{A} \triangle \mathbf{v} \tag{2.16}$$

$$\triangle \mathbf{i}_c = \mathbf{B} \triangle \mathbf{v} + \triangle \mathbf{i} \tag{2.17}$$

$$\triangle \mathbf{v}_{conc} = \mathbf{E} \triangle \mathbf{v} - \triangle \mathbf{v}_{con} \tag{2.18}$$

When the VSC is controlled by the current loop directly, the current controller matrix is **C** and **D** is the decoupling term of the current controller, i.e.:

$$\mathbf{C}=\begin{bmatrix} K_{pi}+K_{ii}/s & 0 \\ 0 & K_{pi}+K_{ii}/s \end{bmatrix} \tag{2.19}$$

$$\mathbf{D}=\begin{bmatrix} 0 & -\omega_0 L_f \\ \omega_0 L_f & 0 \end{bmatrix} \tag{2.20}$$

where K_{pi} and K_{ii} are the proportional and integral gains of the current-loop PI controller, respectively. **F** is the matrix representing the time delay (T_{delay}) due to digital control and PWM [41], and is given as

$$\mathbf{F}=\begin{bmatrix} 1/(1+0.5T_{delay}s) & 0 \\ 0 & 1/(1+0.5T_{delay}s) \end{bmatrix} \tag{2.21}$$

Thus, the small perturbation voltage of the converter in the controller dq frame is derived as

$$\triangle\mathbf{v}_{conc}=\mathbf{F}(-\mathbf{C}\triangle\mathbf{i}_c+\mathbf{D}\triangle\mathbf{i}_c+\triangle\mathbf{v}_c) \tag{2.22}$$

According to (2.15)-(2.22), the small-signal admittance of VSC in system dq frame is obtained as

$$\mathbf{Y}_{vsc}=-\frac{\triangle\mathbf{i}}{\triangle\mathbf{v}}=\frac{\mathbf{E}-\mathbf{FCB}+\mathbf{FDB}+\mathbf{FA}-\mathbf{I}}{\mathbf{FD}-\mathbf{Z}_f-\mathbf{FC}} \tag{2.23}$$

$\mathbf{Y}_{vsc}$ is the transfer function matrix from disturbance voltage $[\Delta v_d,\ \Delta v_q]^{\mathrm{T}}$ to response current $[\Delta i_d,\ \Delta i_q]^{\mathrm{T}}$, and the form is shown as

$$\mathbf{Y}_{vsc}(s)=\begin{bmatrix} Y_{vscdd}(s) & Y_{vscdq}(s) \\ Y_{vscqd}(s) & Y_{vscqq}(s) \end{bmatrix} \tag{2.24}$$

When i_{dref} and i_{qref} are determined by the outer-loop controllers as described in Section 2.1, linearizing (2.3) and (2.4) yields the small-signal model of the outer-loop active power and AC voltage controllers as:

$$\begin{bmatrix} \triangle i_{dref} \\ \triangle i_{qref} \end{bmatrix}=\begin{bmatrix} 1 & 0 \\ 0 & K_{up}+K_{ui}/s \end{bmatrix}\begin{bmatrix} -P_{ref}/V_d^2 & 0 \\ V_d & V_q \end{bmatrix}\begin{bmatrix} \triangle v_{cd} \\ \triangle v_{cq} \end{bmatrix} \tag{2.25}$$

where K_{up} and K_{ui} are the proportional and integral coefficients of the AC voltage PI controller, respectively. P_{ref} is the power reference value.

Defining matrices $\mathbf{X}=\begin{bmatrix} 1 & 0 \\ 0 & K_{up}+K_{ui}/s \end{bmatrix}$ and $\mathbf{Z}=\begin{bmatrix} -P_{ref}/V_d^2 & 0 \\ V_d & V_q \end{bmatrix}$, the small-signal admittance of the VSC with PLL and the outer-loop controllers can be calculated as:

$$\mathbf{Y}_{vsc}=-\frac{\triangle \mathbf{i}}{\triangle \mathbf{v}}=\frac{\mathbf{E}-\mathbf{FCB}+\mathbf{FDB}+\mathbf{FA}+\mathbf{FCXZA}-\mathbf{I}}{\mathbf{FD}-\mathbf{Z}_f-\mathbf{FC}} \tag{2.26}$$

The schematic diagram for the calculation of the VSC admittance is shown in Figure 2.4. The small-signal converter admittance $\mathbf{Y}_{vsc}$ is defined as the transfer function from the small-perturbation voltage $\Delta\mathbf{v}$ to the response current $\Delta\mathbf{i}$. The mathematical expression of $\mathbf{Y}_{vsc}$ is derived above. It is noted that for the calculation of the VSC admittance the current direction is positive when the current $\Delta\mathbf{i}$ flows into VSC.

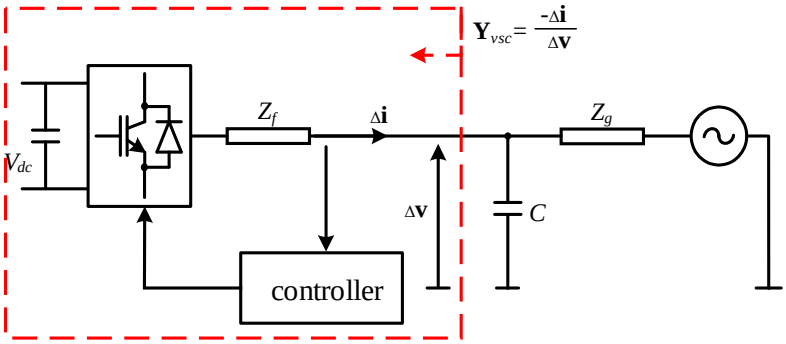

Figure 2.4 The schematic diagram for the calculation of the VSC admittance

When the VSC transmits 1 p.u. active power and 0.2 p.u. reactive power to the AC grid, and the current loop and PLL are adopted in the VSC controller, the calculated small-signal admittances of the the VSC using (2.23) are shown in Figure 2.5.

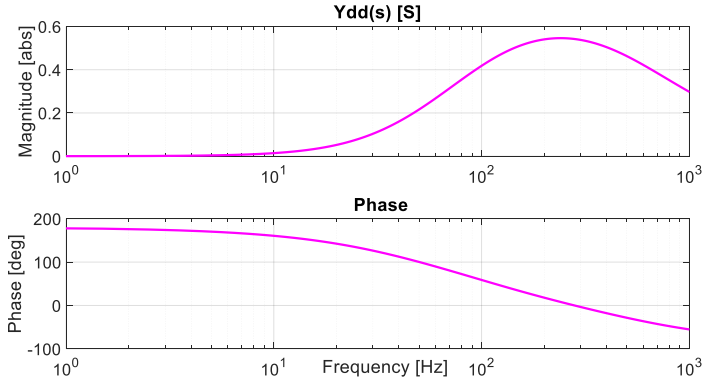

(a) $Y_{dd}(s)$

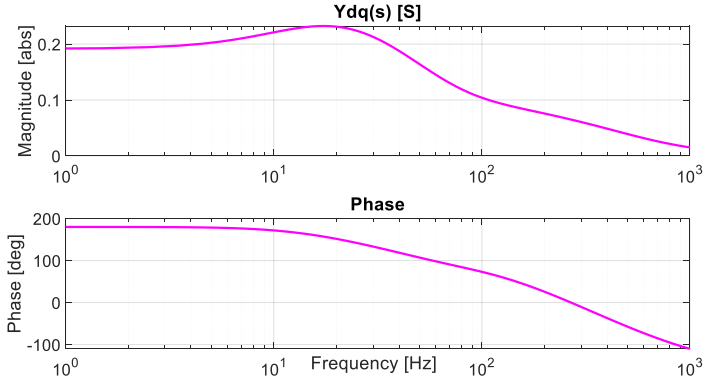

(b) $Y_{dq}(s)$

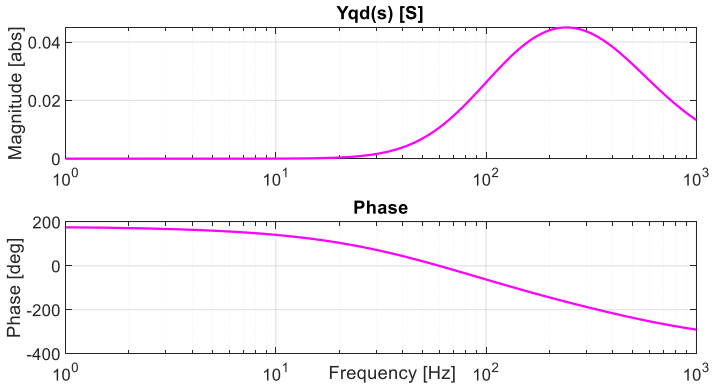

(c) $Y_{qd}(s)$

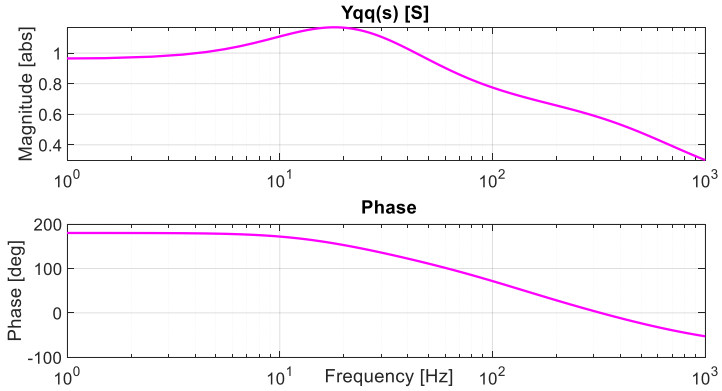

(d) $Y_{qq}(s)$

Figure 2.5 Calculated VSC admittance $\mathbf{Y}vsc$ in dq frame

2.2.2 Admittance in pn frame

The transformation matrices between different frames have been introduced in Section 1.5. Based on the application of the transformation matrices, the VSC small-signal admittances can be mapped from dq frame into pn frame. The pn frame has been chosen to study the system stability since in this frame the coupling caused by synchronous rotating does not exist, which simplifies the impedance analysis.

The pn frame small-signal admittance terms are related to the elements of the matrix $\mathbf{Y}_{vsc}$ in (2.24) as

$$Y_{vscpp}(s)=\frac{1}{2}(Y_{vscdd}(s-j\omega_0)+Y_{vscqq}(s-j\omega_0)+jY_{vscqd}(s-j\omega_0)-jY_{vscdq}(s-j\omega_0)) \tag{2.27}$$

$$Y_{vscpn}(s)=\frac{1}{2}(Y_{vscdd}(s+j\omega_0)-Y_{vscqq}(s+j\omega_0)+jY_{vscdq}(s+j\omega_0)+jY_{vscqd}(s+j\omega_0)) \tag{2.28}$$

$$Y_{vscnp}(s)=\frac{1}{2}(Y_{vscdd}(s-j\omega_0)-Y_{vscqq}(s-j\omega_0)-jY_{vscdq}(s-j\omega_0)-jY_{vscqd}(s-j\omega_0)) \tag{2.29}$$

$$Y_{vscnn}(s)=\frac{1}{2}(Y_{vscdd}(s+j\omega_0)+Y_{vscqq}(s+j\omega_0)+jY_{vscdq}(s+j\omega_0)-jY_{vscqd}(s+j\omega_0)) \tag{2.30}$$

The small-signal VSC admittance in pn frame can be expressed as [62]

$$\begin{bmatrix} \triangle i_p(s) \\ \triangle i_n(s-2j\omega_0) \end{bmatrix} = \mathbf{Y}_{vscPN}(s)\begin{bmatrix} \triangle v_p(s) \\ \triangle v_n(s-2j\omega_0) \end{bmatrix}$$
$$\mathbf{Y}_{vscPN}=\begin{bmatrix} Y_{vscpp}(s) & Y_{vscpn}(s) \\ Y_{vscnp}(s-2j\omega_0) & Y_{vscnn}(s-2j\omega_0) \end{bmatrix} \tag{2.31}$$

where $\mathbf{Y}_{vscPN}$(s) is the small-signal admittance of the converter in pn frame. $Y_{vscpp}(s)$, $Y_{vscpn}(s)$, $Y_{vscnp}(s)$ and $Y_{vscnn}(s)$ are the four elements of the matrix $\mathbf{Y}_{vscPN}$.

It is noted that there is no cross coupling between the input Δv_p, Δv_n and the output Δi_p, Δi_n under the same frequency f_p. However, couplings still exist among different frequencies. As indicated in (2.31), the positive-sequence disturbance voltage Δv_p at f_p not only generates the positive-sequence current Δi_p at f_p through $Y_{vscpp}(s)$ but also the negative-sequence current Δi_n at f_p-$2f_0$ through $Y_{vscnp}(s\text{-}2j\omega_0)$. Similarly, the negative-sequence disturbance voltage Δv_n at f_p will cause both the negative-sequence current Δi_n at f_p through $Y_{vscnn}(s\text{-}2j\omega_0)$ and the positive-sequence current Δi_p at f_p+$2f_0$ through $Y_{vscpn}(s)$.

When the VSC controller in dq frame is symmetric, there are Y_{vscdd}=Y_{vscqq} and Y_{vscdq}=-Y_{vscqd}. Consequently, Y_{vscpn} and Y_{vscnp} in (2.28) and (2.29) equal to 0. Under this condition, the small-signal positive and negative components of the converter are decoupled. Thus, the positive-sequence voltage Δv_p only generates the positive-sequence current Δi_p at f_p and the negative-sequence voltage Δv_p only generates

negative-sequence current Δi_p at f_p. However, the symmetry of the controller in dq frame is usually affected by PLL and the outer-loop control adopted in the system [109]. Therefore, the cross-coupling terms Y_{vscpn} and Y_{vscnp} may have significant impact on stability assessment, which will be studied in Section 2.6.

2.3 Admittance measuring method in time-domain

A time-domain simulation model of a grid connected VSC is established in MATLAB/Simulink to verify the small-signal admittance of VSC in pn frame. In order to extract the admittance in the time-domain simulation, a series of small-perturbation voltages (Δv_{pa}, Δv_{pb}, Δv_{pc}) at different frequencies are injected to the system at the point of common coupling (PCC) as shown in Figure 2.6. By measuring the response voltages (Δv_a, Δv_b, Δv_c) and currents (Δi_a, Δi_b, Δi_c) on the VSC side, the admittance of the converter in time-domain can be derived.

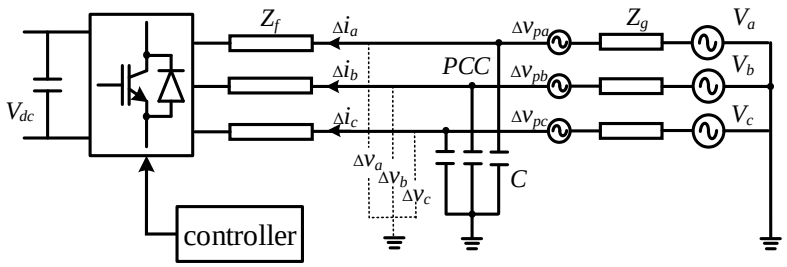

Figure 2.6 Simulation model with perturbation voltages injection

In order to derive the 2 by 2 matrix $\mathbf{Y}_{vscPN}$ in the time-domain simulation model, positive-sequence and negative-sequence voltages are injected into the system, separately.

For the positive-sequence voltage injection, the voltage is defined as:

$$
\begin{aligned}
\triangle v_{pa} &= \triangle v_p \cos(\omega_p t) \\
\triangle v_{pb} &= \triangle v_p \cos(\omega_p t - 2\pi/3) \\
\triangle v_{pc} &= \triangle v_p \cos(\omega_p t + 2\pi/3)
\end{aligned} \tag{2.32}
$$

where Δv_p is the amplitude of the small-signal perturbation voltage, and $\omega_p=2\pi f_p$ is the frequency of the perturbation voltage.

The response voltage Δv_a, Δv_b, and Δv_c on the VSC side consists of positive-sequence voltage at frequency ω_p and negative-sequence voltage at frequency ω_p-$2\omega_0$. The positive component at frequency ω_p is described as $\triangle v_{1p} \angle \triangle \theta_{v1p}(\omega_p)$, where $\triangle v_{1p}$ and $\triangle \theta_{v1p}$ are the amplitude and phase of the positive voltage, respectively. The negative-sequence component at frequency ω_p-$2\omega_0$ is described as $\triangle v_{1n} \angle \triangle \theta_{v1n}(\omega_p - 2\omega_0)$, where $\triangle v_{1n}$ and $\triangle \theta_{v1n}$ are the amplitude and phase of the negative voltage, respectively, and $(\omega_p - 2\omega_0)$ denotes the frequency of the negative-sequence voltage. In the time-domain simulation, $\triangle v_{1p}$, $\triangle \theta_{v1p}$, $\triangle v_{1n}$, and $\triangle \theta_{v1n}$ can be obtained by FFT analysis on the voltage $\triangle v_a$. Similarly, the positive-sequence and negative-sequence current responses $\triangle i_{1p} \angle \triangle \theta_{i1p}(\omega_p)$ and $\triangle i_{1n} \angle \triangle \theta_{i1n}(\omega_p - 2\omega_0)$ can be derived by FFT analysis of the current $\triangle i_a$.

According to (2.31), the response voltage and current at VSC terminal have the relationship shown as:

$$
\begin{aligned}
\begin{bmatrix} \triangle i_{1p} \angle \triangle \theta_{i1p}(\omega_p) \\ \triangle i_{1n} \angle \triangle \theta_{i1n}(\omega_p - 2\omega_0) \end{bmatrix} &= \begin{bmatrix} Y_{vscpp}(\omega_p) & Y_{vscpn}(\omega_p) \\ Y_{vscnp}(\omega_p - 2\omega_0) & Y_{vscnn}(\omega_p - 2\omega_0) \end{bmatrix} \begin{bmatrix} \triangle v_{1p} \angle \triangle \theta_{v1p}(\omega_p) \\ \triangle v_{1n} \angle \triangle \theta_{v1n}(\omega_p - 2\omega_0) \end{bmatrix} \\
&= \mathbf{Y}_{vscPN}(\omega_p) \begin{bmatrix} \triangle v_{1p} \angle \triangle \theta_{v1p}(\omega_p) \\ \triangle v_{1n} \angle \triangle \theta_{v1n}(\omega_p - 2\omega_0) \end{bmatrix}
\end{aligned} \tag{2.33}
$$

For the negative-sequence voltage injection, the perturbation voltage Δv_{pa}, Δv_{pb},

and Δv_{pc} are defined as:

$$\begin{aligned} \triangle v_{pa} &= \triangle v_n \cos[(\omega_p - 2\omega_0)t] \\ \triangle v_{pb} &= \triangle v_n \cos[(\omega_p - 2\omega_0)t + 2\pi/3] \\ \triangle v_{pc} &= \triangle v_n \cos[(\omega_p - 2\omega_0)t - 2\pi/3] \end{aligned} \tag{2.34}$$

where Δv_n is the amplitude of the small-signal perturbation voltage. The frequency of the negative-sequence perturbation voltage is ω_p-$2\omega_0$.

Similar to the positive-sequence voltage injection, the negative-sequence voltage injection generates not only negative-sequence voltage $\triangle v_{2n}\angle\triangle\theta_{v2n}(\omega_p - 2\omega_0)$ and current response $\triangle i_{2n}\angle\triangle\theta_{i2n}(\omega_p - 2\omega_0)$ at frequency ω_p-$2\omega_0$, but also positive-sequence voltage $\triangle v_{2p}\angle\triangle\theta_{v2p}(\omega_p)$ and current response $\triangle i_{2p}\angle\triangle\theta_{i2p}(\omega_p)$ at frequency ω_p. The amplitude and phase of the response voltage and current at VSC terminal can be obtained by FFT analysis and have the relationship shown as:

$$\begin{aligned} \begin{bmatrix} \triangle i_{2p}\angle\triangle\theta_{i2p}(\omega_p) \\ \triangle i_{2n}\angle\triangle\theta_{i2n}(\omega_p - 2\omega_0) \end{bmatrix} &= \begin{bmatrix} Y_{vscpp}(\omega_p) & Y_{vscpn}(\omega_p) \\ Y_{vscnp}(\omega_p - 2\omega_0) & Y_{vscnn}(\omega_p - 2\omega_0) \end{bmatrix} \begin{bmatrix} \triangle v_{2p}\angle\triangle\theta_{v2p}(\omega_p) \\ \triangle v_{2n}\angle\triangle\theta_{v2n}(\omega_p - 2\omega_0) \end{bmatrix} \\ &= \mathbf{Y}_{vscPN}(\omega_p) \begin{bmatrix} \triangle v_{2p}\angle\triangle\theta_{v2p}(\omega_p) \\ \triangle v_{2n}\angle\triangle\theta_{v2n}(\omega_p - 2\omega_0) \end{bmatrix} \end{aligned} \tag{2.35}$$

Combining (2.33) with (2.35) derives the VSC admittance $\mathbf{Y}_{vscPN}(\omega_p)$ at frequency ω_p as:

$$\mathbf{Y}_{vscPN}(\omega_p) = \begin{bmatrix} \triangle i_{1p}\angle\triangle\theta_{i1p}(\omega_p) & \triangle i_{2p}\angle\triangle\theta_{i2p}(\omega_p) \\ \triangle i_{1n}\angle\triangle\theta_{i1n}(\omega_p - 2\omega_0) & \triangle i_{2n}\angle\triangle\theta_{i2n}(\omega_p - 2\omega_0) \end{bmatrix} \begin{bmatrix} \triangle v_{1p}\angle\triangle\theta_{v1p}(\omega_p) & \triangle v_{2p}\angle\triangle\theta_{v2p}(\omega_p) \\ \triangle v_{1n}\angle\triangle\theta_{v1n}(\omega_p - 2\omega_0) & \triangle v_{2n}\angle\triangle\theta_{v2n}(\omega_p - 2\omega_0) \end{bmatrix}^{-1} \tag{2.36}$$

It is noteworthy that when ω_p is less than $2\omega_0$, the frequency (ω_p-$2\omega_0$) of injected negative-sequence voltage Δv_{pa}, Δv_{pb}, and Δv_{pc} is less than zero. However, in time-domain simulation, the voltage cannot have negative frequency. To solve this problem, the voltage expression in (2.34) is rewritten as

$$
\begin{aligned}
\triangle v_{pa} &= \triangle v_n \cos[(\omega_p - 2\omega_0)t] = \triangle v_n \cos[(2\omega_0 - \omega_p)t] \\
\triangle v_{pb} &= \triangle v_n \cos[(\omega_p - 2\omega_0)t + 2\pi/3] = \triangle v_n \cos[(2\omega_0 - \omega_p)t - 2\pi/3] \\
\triangle v_{pc} &= \triangle v_n \cos[(\omega_p - 2\omega_0)t - 2\pi/3] = \triangle v_n \cos[(2\omega_0 - \omega_p)t + 2\pi/3]
\end{aligned} \tag{2.37}
$$

According to (2.34), the negative frequency injected voltage is converted to the positive frequency injected voltage, which can be implemented in time-domain simulation. However, the sequence of the injected voltage is also changed in (2.37), i.e., the negative-sequence voltage becomes positive-sequence voltage.

In the same way, when ω_p is less than $2\omega_0$, the negative-sequence response voltage and current at frequency (ω_p-$2\omega_0$) become positive-sequence voltage and current at frequency ($2\omega_0$-ω_p) in time-domain simulation. Moreover, with the same mathematical operation in (2.37), the phases of the response voltage and current change from $\triangle\theta_{v1n}$, $\triangle\theta_{v2n}$, $\triangle\theta_{i1n}$ and $\triangle\theta_{i2n}$ to $-\triangle\theta_{v1n}$, $-\triangle\theta_{v2n}$, $-\triangle\theta_{i1n}$ and $-\triangle\theta_{i2n}$, that is, the phase becomes inverse.

Thus, when ω_p is less than $2\omega_0$ the VSC admittance $\mathbf{Y}_{vscPN}(\omega_p)$ at frequency ω_p shown in (2.36) is modified as

$$
\mathbf{Y}_{vscPN}(\omega_p) = \begin{bmatrix} \triangle i_{1p}\angle\triangle\theta_{i1p}(\omega_p) & \triangle i_{2p}\angle\triangle\theta_{i2p}(\omega_p) \\ \triangle i_{1n}\angle -\triangle\theta_{i1n}(\omega_p - 2\omega_0) & \triangle i_{2n}\angle -\triangle\theta_{i2n}(\omega_p - 2\omega_0) \end{bmatrix} \begin{bmatrix} \triangle v_{1p}\angle\triangle\theta_{v1p}(\omega_p) & \triangle v_{2p}\angle\triangle\theta_{v2p}(\omega_p) \\ \triangle v_{1n}\angle -\triangle\theta_{v1n}(\omega_p - 2\omega_0) & \triangle v_{2n}\angle -\triangle\theta_{v2n}(\omega_p - 2\omega_0) \end{bmatrix}^{-1} \tag{2.38}
$$

Figure 2.7 shows the flowchart of VSC small-signal admittance measurement in time-domain model.

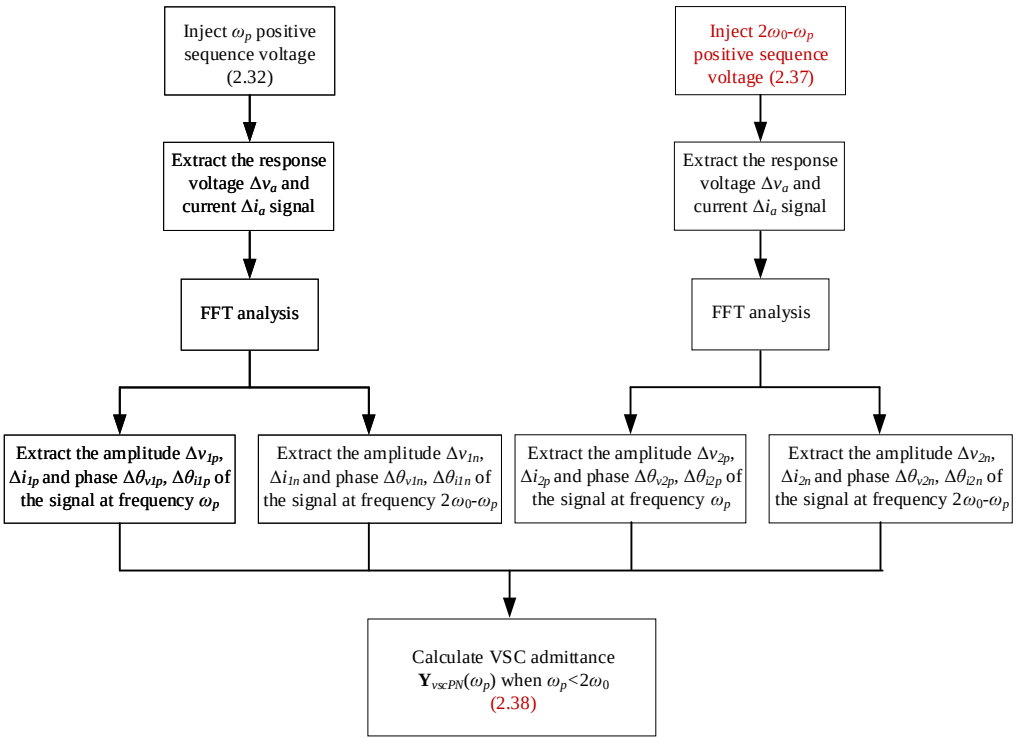

(a) $\omega_p<2\omega_0$

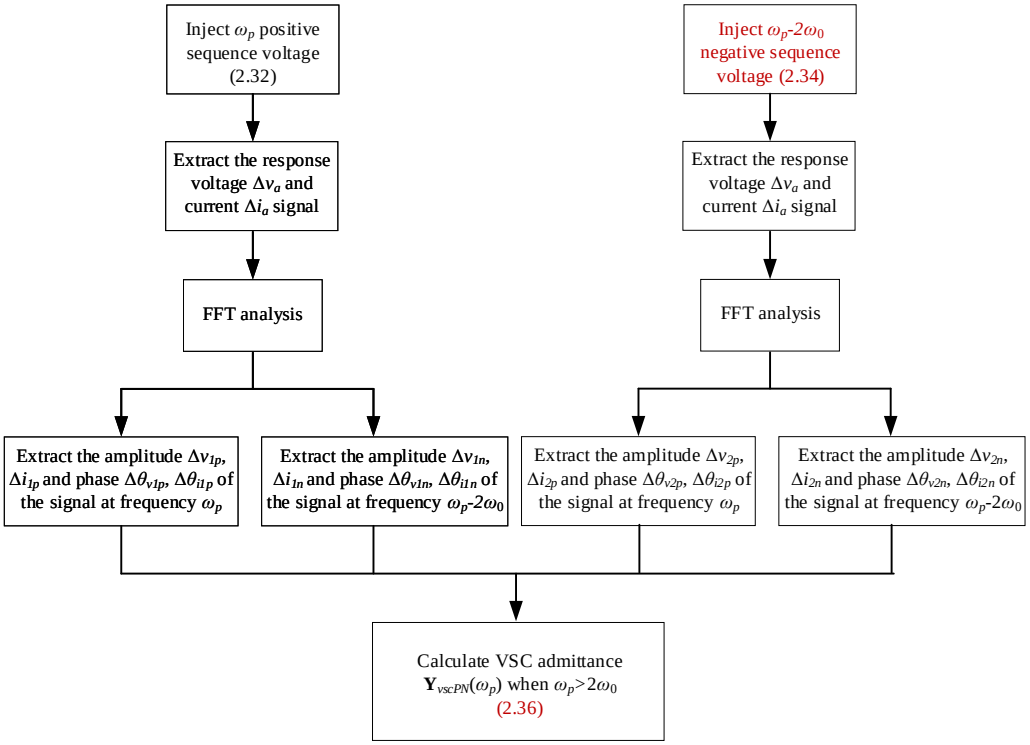

(b) $\omega_p>2\omega_0$

Figure 2.7 Flowchart of VSC small-signal admittance measurement in time-domain model

The time-domain simulation carries out a frequency sweep test where repeated measurements are taken with ω_p increasing from 2π rad/s to 2000π rad/s in the study.

2.4 Validation of analytical admittance

In the VSC-grid connected system, the VSC transmits 1 p.u. active power and 0.2 p.u. reactive power into the grid. Moreover, the VSC is controlled by the current loop and PLL. Figure 2.8 compares the analytical admittances and measured admittances of the VSC in time-domain, where the pink lines denote the analytical admittances and the blue dots are the admittances measured in time-domain. It can be seen that the analytical admittances match well with the measured ones, indicating the correctness of the analytical methods.

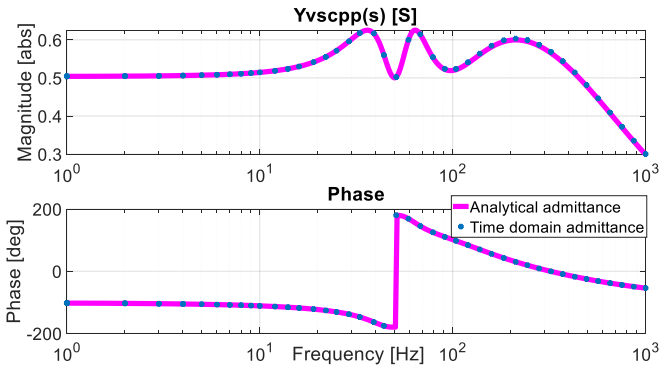

(a) $Y_{vscpp}(s)$

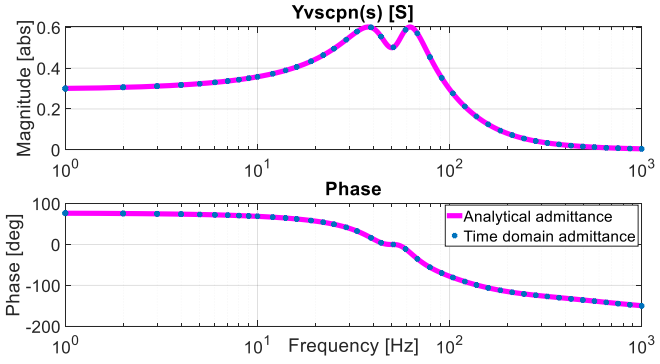

(b) $Y_{vscpn}(s)$

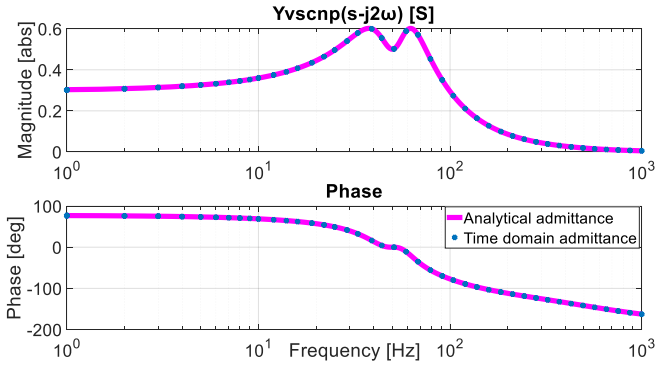

(c) $Y_{vscnp}(s\text{-}j2\omega_0)$

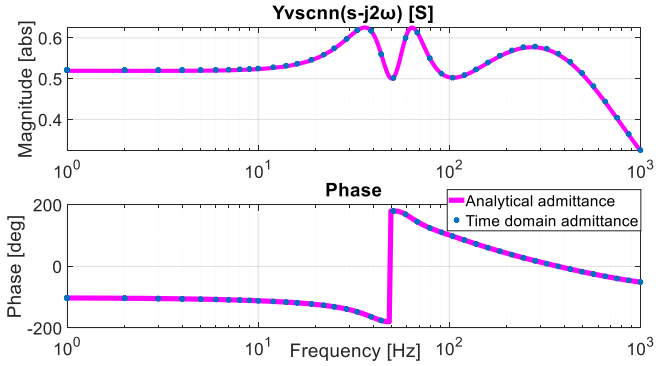

(d) $Y_{vscnn}(s\text{-}j2\omega_0)$

Figure 2.8 Converter admittance terms

2.5 Generalized Nyquist criterion for impedance-based stability analysis

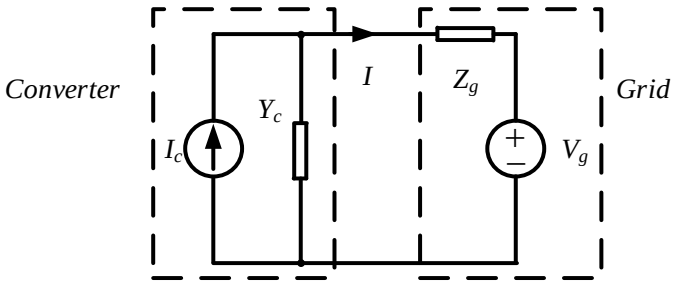

Figure 2.9 Small-signal equivalent circuit of the system studied

Figure 2.9 shows the small-signal equivalent circuit of the grid connected VSC system [41]. The converter is modelled in terms of Thevenin equivalent circuit using

the derived admittance Y_c, and the grid is described by its Norton equivalent circuit with the equivalent impedance Z_g. Based on the equivalent circuit, the inverter output current is:

$$I(s) = \frac{I_c(s)Z_c(s)}{Z_c(s)+Z_g(s)} - \frac{V_g(s)}{Z_c(s)+Z_g(s)} \tag{2.39}$$

Equation (2.39) can be rearranged as

$$I(s) = \left[I_c(s) - Y_c(s)V_g(s) \right] \frac{1}{1+Y_c(s)Z_g(s)} \tag{2.40}$$

Assuming that the open-loop transfer function $Y_c(s)Z_g(s)$ has no right half -plane poles (open-loop unstable processes in power electronics and systems are rare [109]), the grid-connected VSC system will be stable if $Y_c(s)Z_g(s)$ satisfies the generalized Nyquist criterion (GNC) i.e., it does not encircle (-1,0) for $s=\omega_p$, $-\infty<\omega_p<+\infty$.

For multivariable systems, stability-margin definitions were proposed in [110] and [111], which are complicated and time-consuming due to the introduction of complex numerical algorithms. Simpler definitions of gain margin and phase margin are thus adopted according to [109].

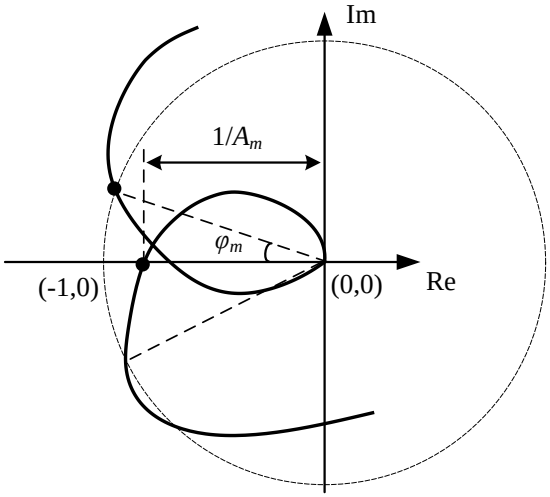

Figure 2.10 Definition of gain margin A_m and phase margin φ_m

The gain margin A_m is defined as the reciprocal of the distance between (0, 0) and the intersection closest to (−1,0) of the Nyquist curve with the real axis, as schematically shown in Figure 2.10. The phase margin φ_m is defined as the angle between the negative real axis and the intersection closest to (−1,0) of the Nyquist curve with the unit circle.

In the studied system, the open-loop transfer function matrix $\boldsymbol{Y}_{vscPN}\boldsymbol{Z}_{gPN}$ in pn frame is investigated for the stability analysis based on GNC.

2.6 Stability assessment of grid connected VSC system

Stability assessment of grid connected VSC system illustrated in Figure 2.1 is carried out here. The effect of coupling admittance resulting from PLL dynamic and outer-loop controller on system stability is analyzed. Based on the stability assessment results, an improved outer-loop controller is also proposed in this section to reduce the coupling admittance and improve system stability.

2.6.1 Coupling admittance created by PLL

For this study, the controller for the converter consists of the current loop and PLL but without the outer-loop control. The system and controller parameters are list in Table 2.1. Figure 2.11 (a) shows the Nyquist plots for 40Hz PLL bandwidth. $\boldsymbol{\lambda}_1$ and $\boldsymbol{\lambda}_2$ are the eigenvalues of $\mathbf{Y}_{vscPN}\mathbf{Z}_{gPN}$ considering the effect of VSC coupling admittances, while $\boldsymbol{\lambda}_{1p}$ and $\boldsymbol{\lambda}_{2n}$ are the eigenvalues in the case of ignoring coupling admittances. At the frequencies range higher than 99Hz, the differences between $\boldsymbol{\lambda}_1$ and $\boldsymbol{\lambda}_{1p}$ are smaller, indicating that the coupling admittance generated by PLL is small and thus has negligible impact on stability margin. Increasing the PLL bandwidth to 60Hz, the Nyquist curve shown in Figure 2.11(b) implies that the system becomes unstable and the coupling admittance generated by PLL will not impact on stability analysis. It can be concluded that the coupling admittance created by PLL has negligible impact on system stability even though the PLL has high control bandwidth.

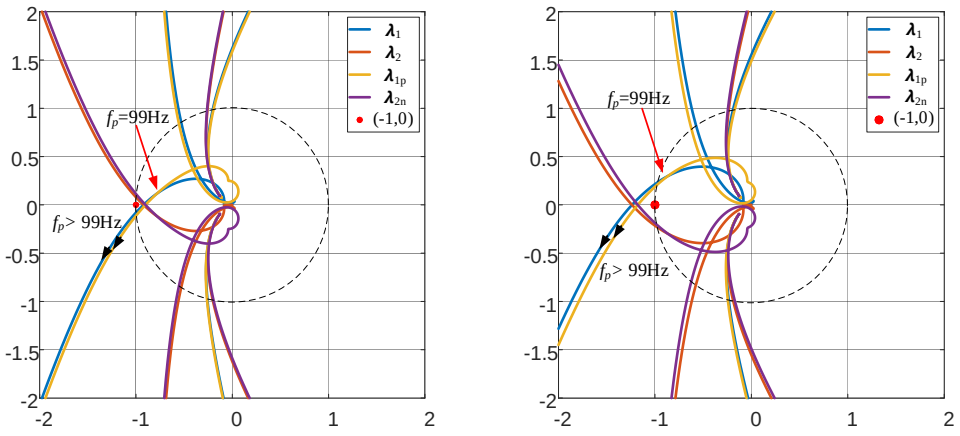

(a) PLL bandwidth of 40Hz (b) PLL bandwidth of 60Hz

Figure 2.11 Nyquist plot for different PLL bandwidth

Figure 2.12 shows the simulation results in time-domain when the PLL bandwidth is changed from 40 Hz to 60Hz at 7.0s. As can be seen, the system is stable for 40 Hz PLL bandwidth and but becomes unstable when PLL bandwidth is increased to 60 Hz. The simulation results match the analytical results in Figure 2.11, which verifies the

effectiveness and accuracy of the stability analysis method based on small-signal impedance.

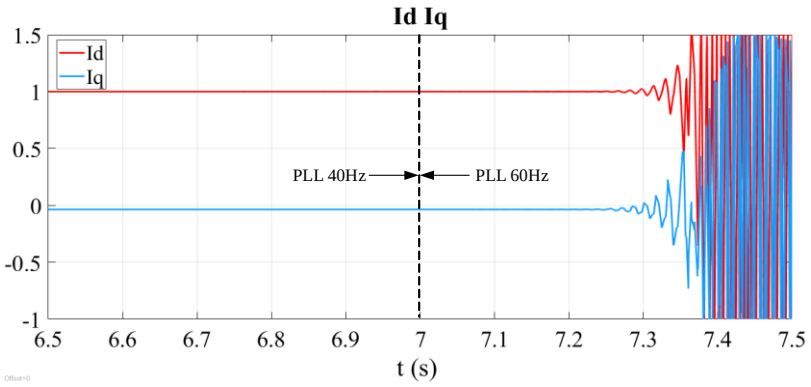

(a) I_d and I_q (p.u.)

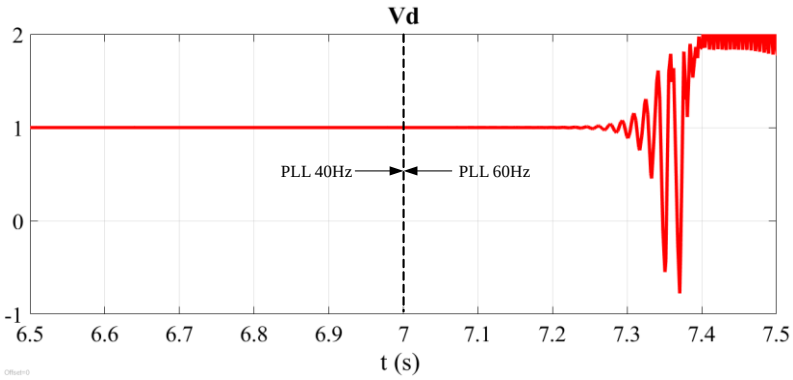

(b) Vd (p.u.)

Figure 2.12 Simulation results in time-domain

2.6.2 Coupling admittance created by outer-loop

The coupling admittances caused by the outer-loop controllers can also affect the system stability. The outer-loop controllers provide references for the current loop as shown in Figure 2.1. The PLL bandwidth is set to 40Hz in this study. The VSC coupling admittances terms $Y_{vscpn}(s)$ and $Y_{vscnp}(s\text{-}2j\omega_0)$ for two different AC voltage PI control parameters (in per unit terms) are compared in Figure 2.13. It can be seen that coupling admittances increase with the increase of the AC voltage control bandwidth (higher gains). The corresponding Nyquist plots for the two cases are shown in Figure

2.14 (a) and (b), respectively. In both Figure 2.14 (a) and (b), $\boldsymbol{\lambda}_1$ and $\boldsymbol{\lambda}_2$ are the eigenvalues considering the effect of VSC coupling admittances, while $\boldsymbol{\lambda}_{1p}$ and $\boldsymbol{\lambda}_{2n}$ are the eigenvalues when the coupling admittances are ignored. It can be seen in Figure 2.14 (a) that for the system with lower AC voltage control bandwidth, the system is considered to be stable regardless whether the coupling admittances are included in the analysis or not. However, for the system with higher AC voltage control bandwidth in Figure 2.14 (b), the system is considered to be stable if the coupling admittances are not included in the analysis, whilst the actual system is unstable when the full VSC admittances are considered. Thus it can be concluded that the coupling admittances can adversely affect the system stability, and its omitting in stability assessment could lead to wrong conclusion.

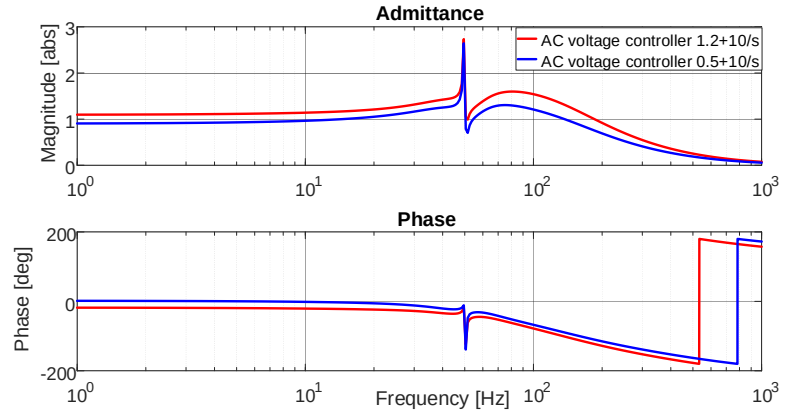

(a) $Y_{vscpn}(s)$

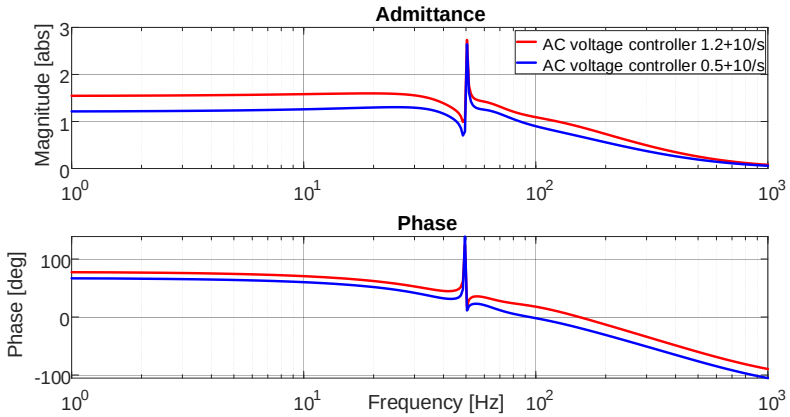

(b) $Y_{vscnp}(s\text{-}2j\omega_0)$

Figure 2.13 Coupling admittance with different controllers

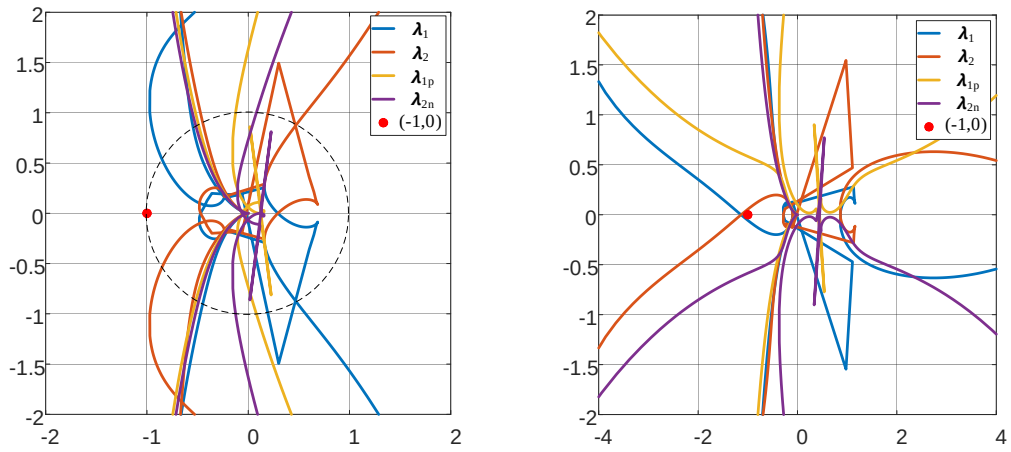

(a) With AC voltage PI controller gain: 0.5+10/s (b) With AC voltage PI controller gain: 1.2+10/s

Figure 2.14 Nyquist plot for different AC voltage controllers

2.6.3 Improvement of the outer-loop controller

When the model has the transfer function matrix $\mathbf{G}(s)$ as presented in (2.41) and the components of $\mathbf{G}(s)$ have the relationships of $G_{dd}(s)=G_{qq}(s)$ and $G_{dq}(s)=-G_{qd}(s)$, it is defined as symmetric model in dq frame, as proposed in [109].

$$\mathbf{G}(s)=\begin{bmatrix} G_{dd}(s) & G_{dq}(s) \\ G_{qd}(s) & G_{qq}(s) \end{bmatrix} \tag{2.41}$$

Obviously, the small-signal model of the outer-loop controller described in (2.25) is an asymmetric model in dq frame. The asymmetric will lead to the frequency coupling effect in pn frame [48], which can also be found according to (2.28) and (2.29). As the analysis result in Section 2.6.2, i.e., the coupling created by outer-loop control has negative impact on system stability, reducing the asymmetry between d-axis and q-axis in the frequency band where resonance may occur can improve system stability.

To decrease the coupling admittance generated by the outer-loop controller of the

VSC, an improved outer-loop controller is proposed as shown in Figure 2.15. Through lower-pass and high-pass filters, the compensation terms $k_1\Delta v_{cd}$ and $k_2\Delta v_{cq}$ are added to the *d*-axis and *q*-axis, respectively, so as to mitigate the coupling. The time constants of the low-pass filter T_1 and high-pass filter T_2 are adjusted to ensure that the potential resonance frequencies of the system are in the pass band of the filters. In this study, the potential resonance frequencies of the system are in the range from 50Hz to 200Hz in abc frame [112]. Therefore, T_1 and T_2 are set to 0.001s and 0.01s, respectively, to make the pass band of the filter from 66Hz to 209Hz in abc frame. The frequency range from 50Hz to 66Hz is not included to ensure that the control bandwidth of the outer-loop controller will not be affected by the compensation. In the pass band of the filters, the small-signal model of the outer-loop controller with the proposed compensation can be expressed as

$$\begin{bmatrix} \Delta i_{dref} \\ \Delta i_{qref} \end{bmatrix} = \begin{bmatrix} -P_{ref}/V_d^2 + k_1 & 0 \\ V_d(K_{up} + K_{ui}/s) & k_2 \end{bmatrix} \begin{bmatrix} \Delta v_{cd} \\ \Delta v_{cq} \end{bmatrix} \tag{2.42}$$

The gain k_1 ranges from 0 to 1 and k_2 is set to $(-P_{ref}/V_d^2+k_1)$ to make diagonal elements equal, i.e., $G_{dd}(s)=G_{qq}(s)$ in (2.41).

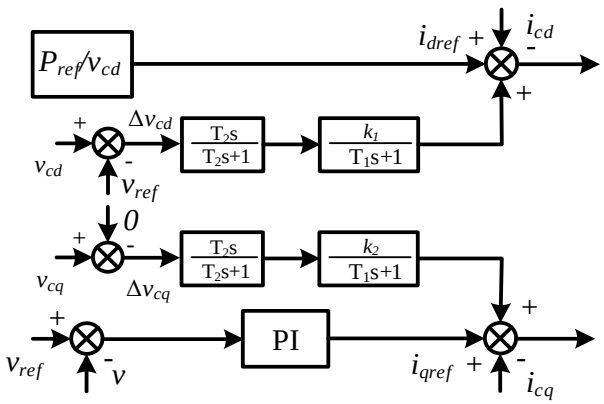

Figure 2.15 Improved outer-loop controller

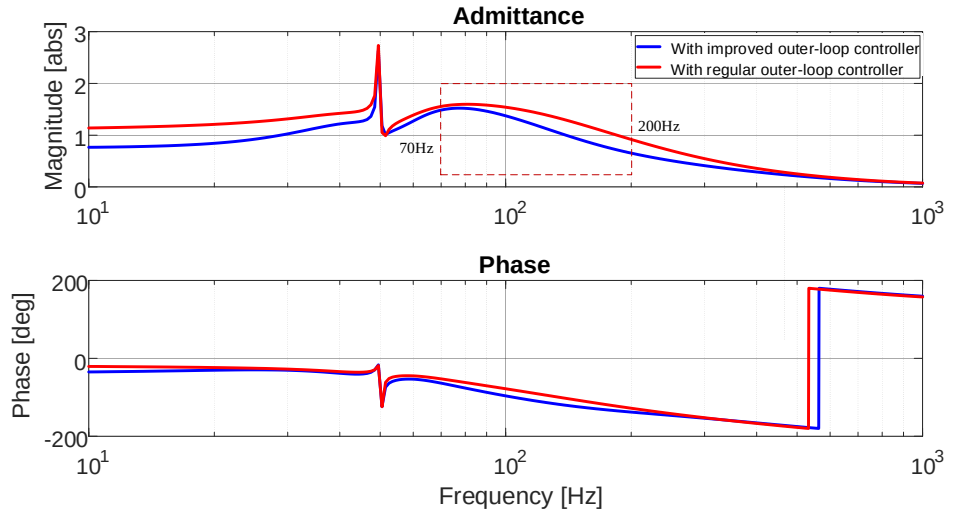

(a) $Y_{vscpn}(s)$

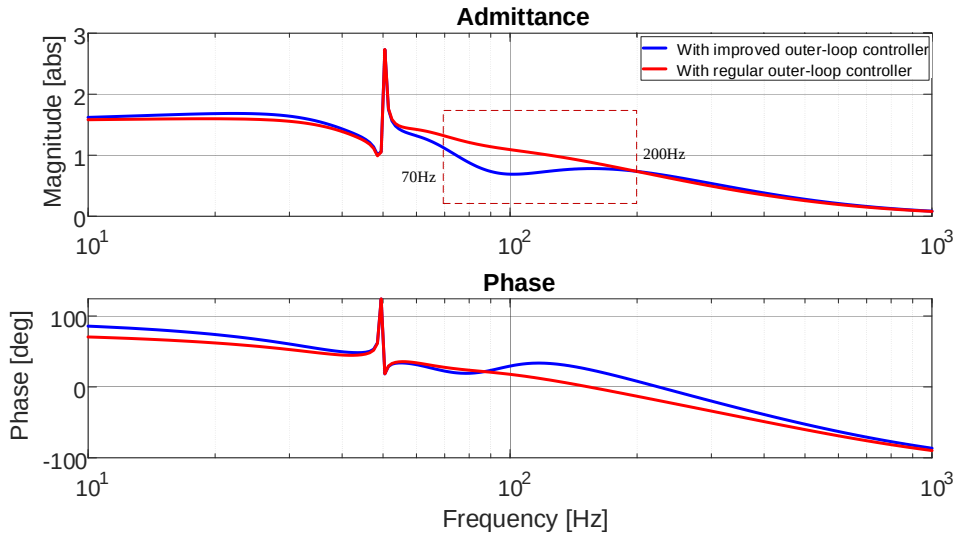

(b) $Y_{vscnp}(s\text{-}2j\omega_0)$

Figure 2.16 Coupling admittance with outer-loop controller

When k_1=0.5 and k_2=-0.5, the coupling admittances under traditional outer-loop controller and improved outer-loop controller are compared in Figure 2.16. It can be seen that, from 70Hz to 200Hz, both coupling admittance terms are reduced with improved outer-loop controller, which is beneficial to the system stability. However, the improved outer-loop controller increases the coupling admittance $Y_{vscpn}(s)$ near the

fundamental frequency, which could have negative impact on the stability. Hence, the parameters of the improved outer-loop controller should be redesigned according to different cases.

Figure 2.17 shows the Nyquist plot of the system with improved outer-loop controller and AC PI voltage controller parameters of 1.2+10/s. Comparing Figure 2.17 and Figure 2.14(b) with the original AC voltage controller, $\boldsymbol{\lambda}_1$ in the two plots has changed significant whereas $\boldsymbol{\lambda}_{1p}$ (without considering the coupling admittances) remains largely unchanged. In addition, $\boldsymbol{\lambda}_1$ in Figure 2.17 is closer to $\boldsymbol{\lambda}_{1p}$, indicating that the improved control reduces the coupling admittance to some degree. Meanwhile, $\boldsymbol{\lambda}_1$ does not encircle the point (-1, 0), so the system becomes stable and the system stability is improved. Simulation results in time-domain shown in Figure 2.18 verify the effectiveness of the proposed outer-loop controller. Before t=3.2s, the system adopts the improved outer-loop controller and is stable. However, the system becomes unstable when the outer-loop controller is shifted to the traditional design by setting the value of k_1 and k_2 to 0 after t=3.2s.

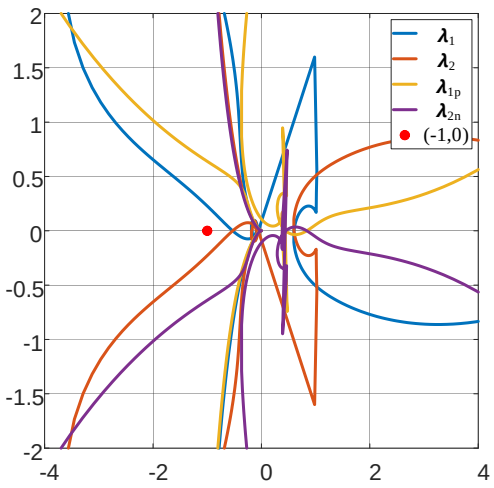

Figure 2.17 Nyquist plot for improved outer-loop controller

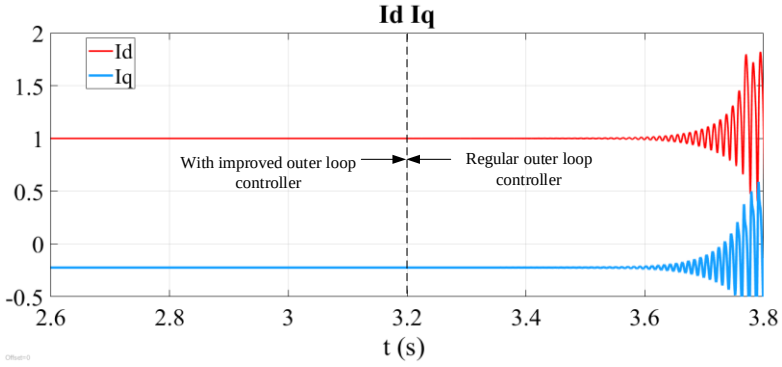

(a) I_d and I_q

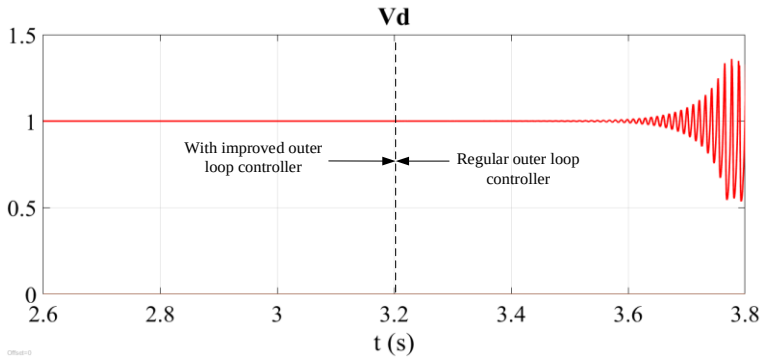

(b) V_d

Figure 2.18 Simulation results in time-domain

2.7 Summary

This chapter presents a methodology to calculate the small-signal admittance of grid connected VSC in the pn frame. The admittance in pn frame is obtained by applying the transformation equations between dq frame and pn frame. The method for measuring the VSC small-signal admittance in pn frame is also described in great detail. Based on the analysis of the obtained admittances, the influences of the pn coupling admittances generated by PLL and outer-loop controllers on system stability are investigated. The results indicate that:

- The VSC small-signal admittances from the analytical model accord well with the measured ones in the corresponding time-domain models.

- Under a weak grid, when the VSC is controlled by the current loop directly, the VSC coupling admittances in pn frame generated by PLL have negligible impact on system stability and thus can be ignored in system stability analysis.

- Traditional outer-loop controllers lead to an asymmetric model in dq frame and thus create high coupling admittance that has negative impact on system stability.

- Through lower-pass and high-pass filters, the improved outer-loop controller adds compensation terms into d axis and q axis at the potential resonance frequency range (66Hz-209Hz in the studied case) to reduce the asymmetry of the outer-loop controller in dq frame. Hence, the coupling admittance in pn frame caused by traditional outer-loop controller is reduced and the stability of system is enhanced.

Chapter 3 HSS modelling of single-phase MMC system

MMC technology is increasingly applied for high voltage and high power applications such as in HVDC systems for renewable energy integration, for its advantages of modularity, scalability, and high efficiency. However, the complex internal dynamics and its multifrequency response feature of MMC complicate its modeling and control. Analysis of complex dynamics and harmonic coupling of MMC is essential to identify potential system instability and to stable operation.

In this chapter, HSS modeling approach is introduced first due to its capability of accurate modelling of multiple frequency responses. It is then applied to characterize the multi-harmonic coupling behaviour of single-phase MMC to establish its small-signal impedance model covering all internal harmonics within the MMC. Different control schemes for the MMC, such as open-loop control, ac voltage control, and circulating current control, have also been incorporated in the model, which further reveals the impact of the MMC internal dynamics and control dynamics on the MMC impedance. Time-domain EMT simulation results are provided to validate the analytical MMC impedance models. Finally, the limitations and drawbacks of the single-phase MMC model are analyzed.

3.1 HSS modelling method

The harmonic balance method was proposed in 1886 and aimed to obtain the steady-state solution to nonlinear system [91]. This method transforms a Fourier series expansion of an input signal into a set of complex exponentials at harmonic frequencies. Given that both of the series expansions of the input signal and the system transfer function form an orthonormal basis, the resulting output is also an orthonormal set of complex exponentials. The mapping from a harmonic of the input signal through

a particular harmonic of the transfer function is unique to a single harmonic of the output signal, and therefore, every element of the output vector is linearly independent of each other. The basic idea of HSS is to derive a linear time-invariant (LTI) representation of the linear time-periodic (LTP) system in time domain, and thus the linear control theory can be used for stability analysis and controller design. The HSS modelling method is able to represent multiple frequency responses in each variable and build multidimensional harmonic transfer function based models.

A typical power system with connected power electronic converters is a LTP system in small-signal modelling due to the switching of converters derived from sinusoidal voltage waveforms is periodic. The LTP system in time-domain can be described by a set of first order linear state-space equations as

$$\dot{\mathbf{x}}(t) = \mathbf{A}(t)\mathbf{x}(t) + \mathbf{B}(t)\mathbf{u}(t) \tag{3.1}$$

$$\mathbf{y}(t) = \mathbf{C}(t)\mathbf{x}(t) + \mathbf{D}(t)\mathbf{u}(t) \tag{3.2}$$

Equation (3.1) is the state equation, in which $\mathbf{x}(t)$ is the state variables, $\mathbf{u}(t)$ is the inputs, $\mathbf{A}(t)$ is the state matrix, and $\mathbf{B}(t)$ is the input matrix. Equation (3.2) is the output equation, in which $\mathbf{y}(t)$ is the outputs, $\mathbf{C}(t)$ is the output matrix, and $\mathbf{D}(t)$ is the direct transmission matrix. $\mathbf{A}(t)$, $\mathbf{B}(t)$, $\mathbf{C}(t)$, and $\mathbf{D}(t)$ are all variant matrices. To be more precise they are time periodic matrices, i.e., $\mathbf{A}(t+T)=\mathbf{A}(t)$ and the same to $\mathbf{B}(t)$, $\mathbf{C}(t)$, and $\mathbf{D}(t)$, where T is the fundamental period.

If the state matrix, and the input and output signals vary, they cannot be solved by the general state-space equation. Hence, the model needs to be linearized according to the time-varying trajectories. Based on this, all the time-domain signals $\mathbf{x}(t)$ can be expressed using the Fourier series, as [113]

$$\mathbf{x}(t) = \sum_{n=-\infty}^{\infty} \mathbf{X}_n e^{jn\omega_0 t} \tag{3.3}$$

where n is the harmonic order and ω_0 is the fundamental frequency of the signal. $\mathbf{X}_n$ is the Fourier coefficient at the nth harmonic and is calculated as

$$\mathbf{X}_n = \frac{1}{T}\int_{t_0}^{t_0+T} \mathbf{x}(t) e^{-jn\omega_0 t} dt \tag{3.4}$$

Additionally, in order to include dynamic performance in the time and frequency-domain, the Exponentially Modulated Periodic (EMP) signal is introduced to represent the signals in an LTP system as

$$\mathbf{x}(t) = \sum_{n=-\infty}^{\infty} \mathbf{X}_n e^{jn\omega_0 t} e^{st} \tag{3.5}$$

where s is a complex number. The component e^{st} modulates each harmonic represented in the complex Fourier series, allowing the harmonics to vary with time, and hence describing the dynamics of harmonics under transient conditions.

The differential expression for $\mathbf{x}(t)$ in (3.5) is give as

$$\dot{\mathbf{x}}(t) = \sum_{n=-\infty}^{\infty} (jn\omega_0 + s)\mathbf{X}_n e^{jn\omega_0 + st} \tag{3.6}$$

Based on (3.3), the matrices $\mathbf{A}(t)$, $\mathbf{B}(t)$, $\mathbf{C}(t)$ and $\mathbf{D}(t)$ can be expanded in Fourier series as

$$\mathbf{A}(t) = \sum_{n=-\infty}^{\infty} \mathbf{A}_n e^{jn\omega_0 t} \tag{3.7}$$

Similarly for $\mathbf{B}(t)$, $\mathbf{C}(t)$ and $\mathbf{D}(t)$, the complex Fourier series can then be

substituted into the state equation in (3.1), and the Fourier form of the state dynamic equation can be described as

$$\begin{aligned}\sum_{n=-\infty}^{\infty}\left(jn\omega_0+s\right)\mathbf{X}_n e^{jn\omega_0 t+st} &= \sum_{n=-\infty}^{\infty}\mathbf{A}_n e^{jn\omega_0 t}\sum_{m=-\infty}^{\infty}\mathbf{X}_m e^{jm\omega_0 t+st}+\sum_{n=-\infty}^{\infty}\mathbf{B}_n e^{jn\omega_0 t}\sum_{m=-\infty}^{\infty}\mathbf{U}_m e^{jm\omega_0 t+st}\\ &= \sum_{n,m=-\infty}^{\infty}\mathbf{A}_n\mathbf{X}_m e^{j(n+m)\omega_0 t+st}+\sum_{n,m=-\infty}^{\infty}\mathbf{B}_n\mathbf{U}_m e^{j(n+m)\omega_0 t+st}\\ &= \sum_{n,m=-\infty}^{\infty}\mathbf{A}_{n-m}\mathbf{X}_m e^{jn\omega_0 t}e^{st}+\sum_{n,m=-\infty}^{\infty}\mathbf{B}_{n-m}\mathbf{U}_m e^{jn\omega_0 t}e^{st}\end{aligned} \tag{3.8}$$

where m denotes the set of harmonic frequencies of the state variable to represent frequency cross-coupling.

According to the harmonic balance theory, every harmonic at steady-state in a system is linearly independent. As a result, every harmonic of the gradient of the steady-state solution must also be linearly independent. For the nth harmonic, the steady-state solution can be rewritten as

$$s\mathbf{X}_n = \sum_{m=-\infty}^{\infty}\mathbf{A}_{n-m}\mathbf{X}_m - jn\omega_0\mathbf{X}_n + \sum_{m=-\infty}^{\infty}\mathbf{B}_{n-m}\mathbf{U}_m \tag{3.9}$$

Similarly, the output equation in (3.2) can be rewritten as

$$\mathbf{Y}_n = \sum_{m=-\infty}^{\infty}\mathbf{C}_{n-m}\mathbf{X}_m + \sum_{m=-\infty}^{\infty}\mathbf{D}_{n-m}\mathbf{U}_m \tag{3.10}$$

Equations (3.9) and (3.10) form the state-space equations, which can represent the dynamics of an LTP system in time-domain. To fully utilize the standard LTI techniques to analyze the LTP system, the LTP system should be transformed to an equivalent LTI system. Thus, the LTP system in the frequency-domain can be represented as a set of stead-state harmonics which are not functions of time, and consequently, the LTP system becomes a LTI system in frequency-domain.

The process of multiplying each single harmonic of the state variables $\mathbf{x}(t)$ or the input $\mathbf{u}(t)$ by the complex Fourier series of $\mathbf{A}(t)$, $\mathbf{B}(t)$, $\mathbf{C}(t)$, or $\mathbf{D}(t)$ is cumbersome, e.g., the component $\sum_{n=-\infty}^{\infty} \mathbf{A}_n e^{jn\omega_0 t} \sum_{m=-\infty}^{\infty} \mathbf{X}_m e^{jm\omega_0 t+st}$ in (3.8). The Toeplitz matrix is thus introduced to simplify the process which is given as:

$$\Gamma\{a_n\} = \begin{bmatrix} \ddots & \vdots & \vdots & \vdots & \\ \cdots & a_{+0} & a_{-1} & a_{-2} & \cdots \\ \cdots & a_{+1} & a_{+0} & a_{-1} & \cdots \\ \cdots & a_{+2} & a_{+1} & a_{+0} & \cdots \\ & \vdots & \vdots & \vdots & \ddots \end{bmatrix} \tag{3.11}$$

$\mathbf{A}(t)$, $\mathbf{B}(t)$, $\mathbf{C}(t)$, and $\mathbf{D}(t)$ are constructed in the form of a Toeplitz matrix filled with appropriate Fourier coefficients, whereas $\mathbf{x}(t)$ and $\mathbf{u}(t)$ are decomposed into column vectors with their Fourier coefficients. Because any LTP system exhibits a frequency coupling property, the introduction of Toeplitz matrices allows the input frequency to be shifted to the set of appropriate output frequencies, so as to fully describe the frequency coupling nature of LTP systems.

If a set of first-order differential equations for each state variable harmonic is expressed by Toeplitz matrices, the $-jn\omega_0$ component in (3.8) should be expanded and denoted by an appropriate matrix form. Thus, a diagonal matrix defined below is adopted to realize the expansion.

$$D\{a_n\} = \begin{bmatrix} \ddots & & & & \\ & a_{-1} & & & \\ & & a_{+0} & & \\ & & & a_{+1} & \\ & & & & \ddots \end{bmatrix} \tag{3.12}$$

Thus, the formal expression of the HSS framework in the frequency-domain can be defined as

$$\begin{cases} s\mathbf{X} = (\mathbf{A}\text{-}\mathbf{Q})\mathbf{X} + \mathbf{B}\mathbf{U} \\ \mathbf{Y} = \mathbf{C}\mathbf{X} + \mathbf{D}\mathbf{U} \end{cases} \tag{3.13}$$

where **A**, **B**, **C**, and **D** denote the Fourier coefficients of **A**(t), **B**(t), **C**(t) and **D**(t) established in the form of Toeplitz matrices, respectively. The variables of **X**, **Y**, **U**, **A**, **B** and **Q** are expressed as:

$$\mathbf{X}=\left[\mathbf{X}_{-h},\cdots,\mathbf{X}_{-1},\mathbf{X}_0,\mathbf{X}_1,\cdots,\mathbf{X}_h\right]^T;\quad \mathbf{Y}=\left[\mathbf{Y}_{-h},\cdots,\mathbf{Y}_{-1},\mathbf{Y}_0,\mathbf{Y}_1,\cdots,\mathbf{Y}_h\right]^T;\quad \mathbf{U}=\left[\mathbf{U}_{-h},\cdots,\mathbf{U}_{-1},\mathbf{U}_0,\mathbf{U}_1,\cdots,\mathbf{U}_h\right]^T$$

$$\mathbf{A}=\begin{bmatrix} \mathbf{A}_0 & \mathbf{A}_{-1} & \cdots & \mathbf{A}_{-h} & & & \\ \mathbf{A}_1 & \ddots & \ddots & \ddots & \ddots & & \\ \vdots & \ddots & \mathbf{A}_0 & \mathbf{A}_{-1} & \ddots & \ddots & \\ \mathbf{A}_h & \ddots & \mathbf{A}_1 & \mathbf{A}_0 & \mathbf{A}_{-1} & \ddots & \mathbf{A}_{-h} \\ & \ddots & \ddots & \mathbf{A}_1 & \mathbf{A}_0 & \ddots & \vdots \\ & & \ddots & \ddots & \ddots & \ddots & \mathbf{A}_{-1} \\ & & & A_h & \cdots & A_1 & A_0 \end{bmatrix}$$

$$\mathbf{B}=\begin{bmatrix} \mathbf{B}_0 & \mathbf{B}_{-1} & \cdots & \mathbf{B}_{-h} & & & \\ \mathbf{B}_1 & \ddots & \ddots & \ddots & \ddots & & \\ \vdots & \ddots & \mathbf{B}_0 & \mathbf{B}_{-1} & \ddots & \ddots & \\ \mathbf{B}_h & \ddots & \mathbf{B}_1 & \mathbf{B}_0 & \mathbf{B}_{-1} & \ddots & \mathbf{B}_{-h} \\ & \ddots & \ddots & \mathbf{B}_1 & \mathbf{B}_0 & \ddots & \vdots \\ & & \ddots & \ddots & \ddots & \ddots & \mathbf{B}_{-1} \\ & & & B_h & \cdots & B_1 & B_0 \end{bmatrix}$$

$$\mathbf{Q}=\begin{bmatrix} -jh\omega_0\cdot\mathbf{I} & & & & \\ & \ddots & & & \\ & & 0\cdot\mathbf{I} & & \\ & & & \ddots & \\ & & & & jh\omega_0\cdot\mathbf{I} \end{bmatrix}$$

The elements $\mathbf{X}_h$, $\mathbf{Y}_h$, $\mathbf{U}_h$, $\mathbf{A}_h$, and $\mathbf{B}_h$ are the corresponding h-th Fourier coefficients of **X**(t), **Y**(t), **U**(t), **A**(t) and **B**(t), respectively. Note that **A** and **B** are the

Toeplitz matrices in order to perform the frequency-domain convolution operation to obtain a clearer and more compact notation. **Q** is a diagonal matrix that represents the frequency information, **I** is an identity matrix having the same size with the number of state variables, and h is the harmonic order.

The general form of HSS in (3.13) illustrates the convolution of each harmonic of the state variable, and it equivalents to the first-order differential equation describing an LTI system. Therefore, a LTI representation of the LTP system can be achieved by HSS and the HSS model can also be easily extended to any number of harmonics.

The s operator is a complex phasor varying with time. During transient conditions, it describes the variation of each harmonic frequency with respect to time, and it vanishes as the harmonics reach steady state, i.e. no further variation in the harmonics. However, $s\mathbf{X}$ does not represent the gradient of the state variable's time-domain waveform, it rather strictly represents the variation of the harmonics over time.

A harmonic vector used to represent a signal in the HSS is filled with complex Fourier coefficients, and it comprises of both positive and negative frequency components, but they must be complex conjugate pairs for the signal to be real. Thus, the DC component in the harmonic vector should be a scalar, but for a uniform representation in this modelling, it is treated as a complex number with zero imaginary component.

3.2 HSS based impedance model of single-phase MMC

The structure of a 3-phase 4-wire MMC system is shown in Figure 3.1(a). Each phase of MMC consists of the upper and lower arms, which are in series with the DC power supply. Each arm has N sub-module (SM) in series with an arm reactor having equivalent resistance of R_m and inductance L_m. Providing the AC and DC sides are grounded, the three-phase MMC system can be considered as three independent single-

phase systems with 120° phase angle difference. Hence, the 3-phase 4-wire MMC system can be simplified and expressed with the single-phase system.

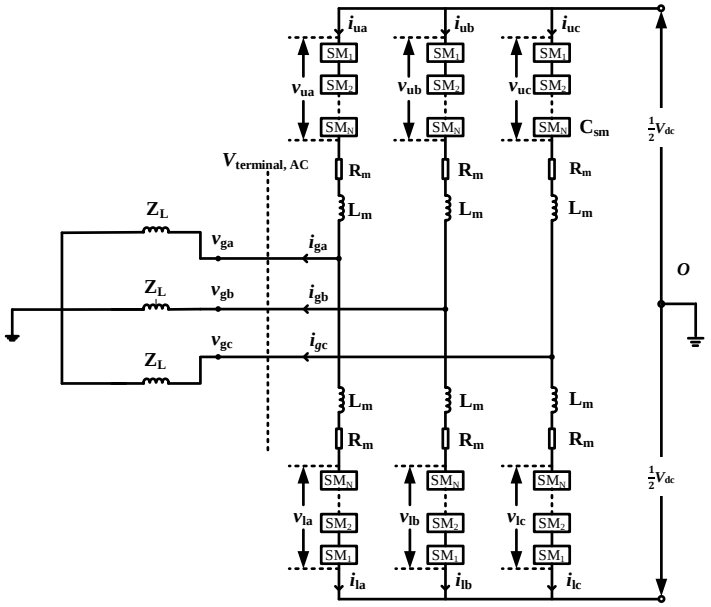

(a) Structure of a 3-phase 4-wire MMC

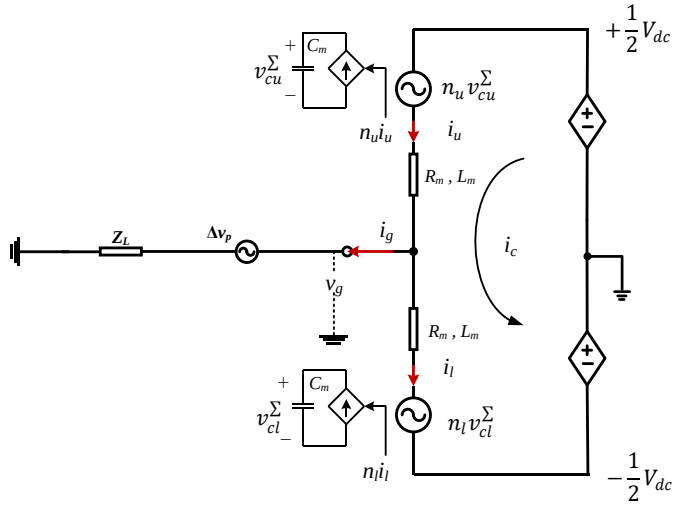

(b) Equivalent average model of single-phase MMC

Figure 3.1 Structure and equivalent circuit for 3-phase 4-wire MMC system

Considering the SM capacitor voltages are balanced and due to high number of SMs in each arm, the high frequency switching harmonics can be neglected. Thus each arm can be considered as a controllable voltage source and the equivalent average model of the single-phase MMC is shown in Figure 3.1(b). As shown in Figure 3.1(b), C_m is the equivalent capacitor in each arm and is given as C_m=C_{sm}/N. i_u and i_l are the current for the upper and lower arms, whereas v_{cu}^{Σ} and v_{cl}^{Σ} are the voltage of the equivalent upper and low arm capacitor C_m, respectively. n_u and n_l are the modulation ratios for the upper and lower arms, respectively. V_{dc} is the DC voltage and Z_L is the load impedance on the AC side. I_g and v_g are the voltage and current of the MMC AC terminal, and Δv_p is the perturbation voltage on the AC side. I_c is the internal common mode current given as

$$i_c = \frac{i_u + i_l}{2} \tag{3.14}$$

The AC-side current i_g can be obtained as

$$i_g = i_u - i_l \tag{3.15}$$

The terminal voltage v_g on the AC side is

$$v_g = Z_L i_g \tag{3.16}$$

According to Kirchhoff's voltage law, the following relationship can be obtained

$$v_g + L_m \frac{di_u}{dt} + R_m i_u + v_u = \frac{V_{dc}}{2} \tag{3.17}$$

$$v_g - L_m \frac{di_l}{dt} - R_m i_l - v_l = -\frac{V_{dc}}{2} \tag{3.18}$$

where v_n and v_l are the voltage for the upper and lower arms, which can be calculated using the capacitor voltage and the modulation ratio as

$$v_u = n_u v_{cu}^{\Sigma} \tag{3.19}$$

$$v_l = n_l v_{cl}^{\Sigma} \tag{3.20}$$

Substituting (3.19) and (3.20) into (3.17) and (3.18) yields

$$v_g + L_m \frac{di_u}{dt} + R_m i_u + n_u v_{cu}^{\Sigma} = \frac{V_{dc}}{2} \tag{3.21}$$

$$v_g - L_m \frac{di_l}{dt} - R_m i_l - n_l v_{cl}^{\Sigma} = -\frac{V_{dc}}{2} \tag{3.22}$$

Subtracting (3.22) from (3.21) and combining (3.14) yields

$$\frac{di_c}{dt} = -\frac{R_m}{L_m} i_c - \frac{n_u}{2L_m} v_{cu}^{\Sigma} - \frac{n_l}{2L_m} v_{cl}^{\Sigma} + \frac{1}{2L_m} V_{dc} \tag{3.23}$$

Adding (3.22) to (3.21) and combining (3.15) yields

$$\frac{di_g}{dt} = -\frac{n_u}{L_m} v_{cu}^{\Sigma} + \frac{n_l}{L_m} v_{cl}^{\Sigma} - \frac{R_m + 2Z_L}{L_m} i_g \tag{3.24}$$

According to the relationship between the capacitor voltage of the upper and lower arms and the arm current, there are

$$C_m \frac{dv_{cu}^{\Sigma}}{dt} = n_u i_u \tag{3.25}$$

$$C_m \frac{dv_{cl}^{\Sigma}}{dt} = n_l i_l \tag{3.26}$$

According to (3.12) and (3.15), (3.25), and (3.26) can be expressed as

$$\frac{dv_{cu}^{\Sigma}}{dt} = \frac{n_u}{C_m} i_c + \frac{n_u}{2C_m} i_g \tag{3.27}$$

$$\frac{dv_{cl}^{\Sigma}}{dt} = \frac{n_l}{C_m} i_c - \frac{n_l}{2C_m} i_g \tag{3.28}$$

Take the circulating current i_c, the capacitor voltage v_{cu}^{Σ} and v_{cl}^{Σ} of the upper and lower arms, and the current i_g on the AC side as the state variables, as

$$\mathbf{x}(t) = \begin{bmatrix} i_c(t) & v_{cu}^{\Sigma}(t) & v_{cl}^{\Sigma}(t) & i_g(t) \end{bmatrix}^T \tag{3.29}$$

and take the DC-side voltage as the input variable, as

$$\mathbf{u}(t) = \begin{bmatrix} V_{dc} \end{bmatrix} \tag{3.30}$$

The state-space equation of MMC can be derived using (3.23)，(3.24), (3.27), and (3.28) as

$$\frac{d\mathbf{x}(t)}{dt} = \mathbf{A}(t)\mathbf{x}(t) + \mathbf{B}(t)\mathbf{u}(t) \tag{3.31}$$

$$\mathbf{A}(t)=\begin{bmatrix} -\frac{R_m}{L_m} & -\frac{n_u}{2L_m} & -\frac{n_l}{2L_m} & 0 \\ \frac{n_u}{C_m} & 0 & 0 & \frac{n_u}{2C_m} \\ \frac{n_l}{C_m} & 0 & 0 & -\frac{n_l}{2C_m} \\ 0 & -\frac{n_u}{L_m} & \frac{n_l}{L_m} & -\frac{R_m+2Z_L}{L_m} \end{bmatrix} \tag{3.32}$$

$$\mathbf{B}(t)=\begin{bmatrix} \frac{1}{2L_m} & 0 & 0 & 0 \end{bmatrix}^T \tag{3.33}$$

where n_u and n_l are the modulation ratios for the upper and lower arms, which are determined by the MMC controller and can be expressed, when considering the DC, fundamental and 2nd harmonic output, as [95]

$$\begin{cases} n_u = 0.5 - n_1\cos(\omega_0 t+\theta_1) - n_2\cos(2\omega_0 t+\theta_2) \\ n_l = 0.5 + n_1\cos(\omega_0 t+\theta_1) - n_2\cos(2\omega_0 t+\theta_2) \end{cases} \tag{3.34}$$

where n_1 and θ_1 are the magnitude and phase angle of the modulation ratio at fundamental frequency ω_0 and are generated by the MMC AC current control. n_2 and θ_2 are at double-frequency and are determined by circulating current suppression controller (CCSC) [98].

3.2.1 HSS based MMC steady-state model

According to (3.34), during stable operation of MMC, the modulation ratio n_u and n_l contain the DC component, the fundamental frequency component and the double frequency component. For the state-variable in (3.29), the AC side current i_g of MMC comprises multiple odd harmonics. The circulating current i_c mainly contains even number harmonics. The capacitor voltage v_{cu}^{Σ} and v_{cl}^{Σ} of the upper and lower

arms also include various harmonics including fundamental and double frequency components [114]. To consider the interaction of the harmonics, transforming the state-space equation in time-domain in (3.31) into the frequency-domain and establish the HSS based MMC model in the form of (3.13) as

$$s\mathbf{X}_s = (\mathbf{A}_s - \mathbf{Q})\mathbf{X}_s + \mathbf{B}_s\mathbf{U}_s \tag{3.35}$$

where $\mathbf{X}_s$ is the state variable matrix at different harmonic frequencies and is expressed as

$$\mathbf{X}_s = \left[\mathbf{X}_{-h}, \cdots, \mathbf{X}_{-1}, \mathbf{X}_0, \mathbf{X}_1, \cdots, \mathbf{X}_h\right]^T \tag{3.36}$$

where the subscript h denotes the harmonic order. For example, the element $\mathbf{X}_h = \begin{bmatrix} i_{ch} & v_{cuh}^{\Sigma} & v_{clh}^{\Sigma} & i_{gh} \end{bmatrix}$ in the matrix $\mathbf{X}_s$ indicates that the state variable contains the h^{th} harmonic. Similarly, $\mathbf{X}_0 = \begin{bmatrix} i_{c0} & v_{cu0}^{\Sigma} & v_{cl0}^{\Sigma} & i_{g0} \end{bmatrix}^T$ is the DC component in the state variable.

The input matrix $\mathbf{U}_s$ at different harmonic frequency is given as

$$\mathbf{U}_s = \left[\mathbf{U}_{-h}, \cdots, \mathbf{U}_{-1}, \mathbf{U}_0, \mathbf{U}_1, \cdots, \mathbf{U}_h\right]^T \tag{3.37}$$

Since the load is connected on the AC side without power supply and the DC-side has a stable DC voltage, the matrix elements in (3.37) can be expressed as $\mathbf{U}_0 = [V_{dc}]$ and $\mathbf{U}_1 = \mathbf{U}_{-1} = \cdots = \mathbf{U}_h = \mathbf{U}_{-h} = [0]$.

$\mathbf{A}_s$ and $\mathbf{B}_s$ are the Toeplitz matrices and can be denoted as

$$\mathbf{A}_s=\begin{bmatrix} \mathbf{A}_0 & \mathbf{A}_{-1} & \cdots & \mathbf{A}_{-h} & & & \\ \mathbf{A}_1 & \ddots & \ddots & \ddots & \ddots & & \\ \vdots & \ddots & \mathbf{A}_0 & \mathbf{A}_{-1} & \ddots & \ddots & \\ \mathbf{A}_h & \ddots & \mathbf{A}_1 & \mathbf{A}_0 & \mathbf{A}_{-1} & \ddots & \mathbf{A}_{-h} \\ & \ddots & \ddots & \mathbf{A}_1 & \mathbf{A}_0 & \ddots & \vdots \\ & & \ddots & \ddots & \ddots & \ddots & \mathbf{A}_{-1} \\ & & & \mathbf{A}_h & \cdots & \mathbf{A}_1 & \mathbf{A}_0 \end{bmatrix} \tag{3.38}$$

$$\mathbf{B}_s=\begin{bmatrix} \mathbf{B}_0 & \mathbf{B}_{-1} & \cdots & \mathbf{B}_{-h} & & & \\ \mathbf{B}_1 & \ddots & \ddots & \ddots & \ddots & & \\ \vdots & \ddots & \mathbf{B}_0 & \mathbf{B}_{-1} & \ddots & \ddots & \\ \mathbf{B}_h & \ddots & \mathbf{B}_1 & \mathbf{B}_0 & \mathbf{B}_{-1} & \ddots & \mathbf{B}_{-h} \\ & \ddots & \ddots & \mathbf{B}_1 & \mathbf{B}_0 & \ddots & \vdots \\ & & \ddots & \ddots & \ddots & \ddots & \mathbf{B}_{-1} \\ & & & \mathbf{B}_h & \cdots & \mathbf{B}_1 & \mathbf{B}_0 \end{bmatrix} \tag{3.39}$$

where the elements in the matrices are attached in the appendix A

Assuming $s\mathbf{X}_s$=0 in (3.35) for the system in steady state, the steady-state state variables of MMC at different harmonic frequencies under the input DC voltage V_{dc} can be expressed as

$$\mathbf{X}_s=-(\mathbf{A}_s-\mathbf{Q})^{-1}\mathbf{B}_s\mathbf{U}_s \tag{3.40}$$

3.2.2 HSS based MMC small-signal model

The response of MMC can be considered as the superposition of various harmonics at the fundamental frequency ω_0. The steady-state model of MMC is derived using HSS in Section 3.2.1, which includes $-h$, …, -1, 0, 1, …, h order harmonics. MMC steady-state response has periodical and time-variant features, whereas the stability analysis is conducted on the premise of time-invariant model. In this section, the linearized small-signal model of MMC using HSS is derived.

Linearizing (3.23), (3.24), (3.27) and (3.28) yields

$$\begin{cases} \dfrac{d\Delta i_c}{dt} = -\dfrac{R_m}{L_m}\Delta i_c - \dfrac{N_u}{2L_m}\Delta v_{cu}^{\Sigma} - \dfrac{N_l}{2L_m}\Delta v_{cl}^{\Sigma} - \dfrac{V_{cu}^{\Sigma}}{2L_m}\Delta n_u - \dfrac{V_{cl}^{\Sigma}}{2L_m}\Delta n_l \\ \dfrac{d\Delta v_{cu}^{\Sigma}}{dt} = \dfrac{N_u}{C_m}\Delta i_c + \dfrac{N_u}{2C_m}\Delta i_g + \dfrac{2I_c + I_g}{2C_m}\Delta n_u \\ \dfrac{d\Delta v_{cl}^{\Sigma}}{dt} = \dfrac{N_l}{C_m}\Delta i_c - \dfrac{N_l}{2C_m}\Delta i_g + \dfrac{2I_c - I_g}{2C_m}\Delta n_l \\ \dfrac{d\Delta i_g}{dt} = -\dfrac{R_m + 2Z_L}{L_m}\Delta i_g - \dfrac{N_u}{L_m}\Delta v_{cu}^{\Sigma} + \dfrac{N_l}{L_m}\Delta v_{cl}^{\Sigma} - \dfrac{V_{cu}^{\Sigma}}{L_m}\Delta n_u + \dfrac{V_{cl}^{\Sigma}}{L_m}\Delta n_l - \dfrac{2\Delta v_p}{L_m} \end{cases} \tag{3.41}$$

where Δ denotes small-signal perturbation. N_u and N_l are the steady-state upper and lower arm modulation rations. I_c, I_g, V_{cu}^{Σ} and V_{cl}^{Σ} are the steady-state internal circulating current, the AC-side terminal current, and capacitor voltage for the upper and lower arms. The steady-state components include -h, …, -1, 0, 1, …, h order harmonics.

Equation (3.41) can be written in matrix form and the small-signal state equation of MMC can be expressed as

$$\Delta \dot{\mathbf{x}}(t) = \mathbf{A}_p(t)\Delta\mathbf{x}(t) + \mathbf{B}_p\Delta\mathbf{u}(t) \tag{3.42}$$

where the small-signal state variables are

$$\Delta\mathbf{x}(t) = \begin{bmatrix} \Delta i_c(t) & \Delta v_{cu}^{\Sigma}(t) & \Delta v_{cl}^{\Sigma}(t) & \Delta i_g(t) \end{bmatrix}^T \tag{3.43}$$

The perturbation input $\Delta\mathbf{u}(t)$ is

$$\Delta\mathbf{u}(t) = \begin{bmatrix} \Delta n_u & \Delta n_l & \Delta v_p \end{bmatrix} \tag{3.44}$$

where Δn_u and Δn_l are the perturbation for the upper and lower modulation ratios, respectively, Δv_p is the perturbation voltage injected into the AC terminal of the MMC.

The coefficient matrices can be written as

$$\mathbf{A}_p(t) = \begin{bmatrix} -\frac{R_m}{L_m} & -\frac{N_u}{2L_m} & -\frac{N_l}{2L_m} & 0 \\ \frac{N_u}{C_m} & 0 & 0 & \frac{N_u}{2C_m} \\ \frac{N_l}{C_m} & 0 & 0 & -\frac{N_l}{2C_m} \\ 0 & -\frac{N_u}{L_m} & \frac{N_l}{L_m} & -\frac{R_m + 2Z_L}{L_m} \end{bmatrix} \tag{3.45}$$

$$\mathbf{B}_p(t) = \begin{bmatrix} -\frac{V_{cu}^{\Sigma}}{2L_m} & -\frac{V_{cl}^{\Sigma}}{2L_m} & 0 \\ \frac{2I_c + I_g}{2C_m} & 0 & 0 \\ 0 & \frac{2I_c - I_g}{2C_m} & 0 \\ -\frac{V_{cu}^{\Sigma}}{L_m} & \frac{V_{cl}^{\Sigma}}{L_m} & -\frac{2}{L_m} \end{bmatrix} \tag{3.46}$$

3.2.3 Small-signal model of MMC with controllers

A. Circulating current suppression controller (CCSC)

As the dominant component in the circulating current is the 2nd order harmonic, CCSC for three-phase MMC can be designed using either PI controller in dq frame (rotating at double frequency) or PR controller in abc frame, and both designs can effectively suppress the second harmonic circulating current in the MMC arms. Here

the PR controller in abc stationary frame is adopted. For three-phase PR controller in the abc frame, each phase control is identical and independent. Therefore, a single-phase controller can be adopted in the analysis, as shown in Figure 3.2

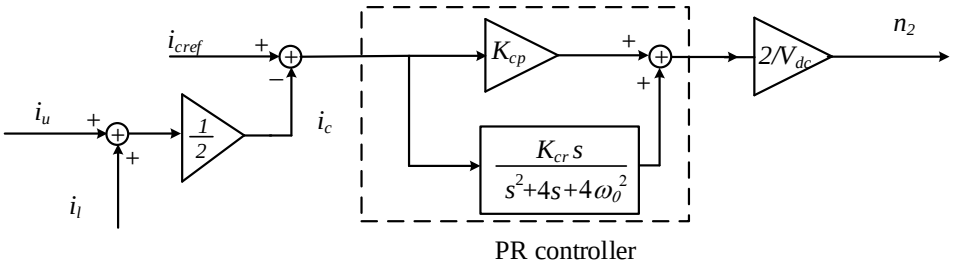

Figure 3.2 Diagram of the circulating current control with PR controller

The common mode current i_c as depicted in (3.14) mainly contains the DC component and the second harmonic circulating current. As shown in Figure 3.2, the DC current component is removed by adding the steady-state DC current reference i_{cref}=P/3/V_{dc}, where P denotes the output active power of MMC. K_{cp} and K_{cr} are the proportional and resonant coefficients of the PR controller, respectively, and the resonant frequency is $2\omega_0$. The output of the CCSC is the modulation ratio n_2 at double frequency in (3.34).

According to the small-signal model of the circulating current controller, the perturbation of the modulation ratio Δn_2 and the circulating current Δi_c can be expressed as

$$\Delta n_2 = G_{cc}(t)\Delta i_c \tag{3.47}$$

where $G_{cc}(t)$ is the gain of the controller and the transfer function in frequency-domain is

$$G_{cc} = -\frac{2K_{cp}}{V_{dc}} - \frac{2K_{cr}s}{V_{dc}(s^2 + 4s + 4\omega_0^2)} \tag{3.48}$$

B. MMC AC current controller

As single-phase MMC model is considered here, the MMC AC-side current controller also employs the PR controller in abc frame. The single-phase control diagram is shown in Figure 3.3.

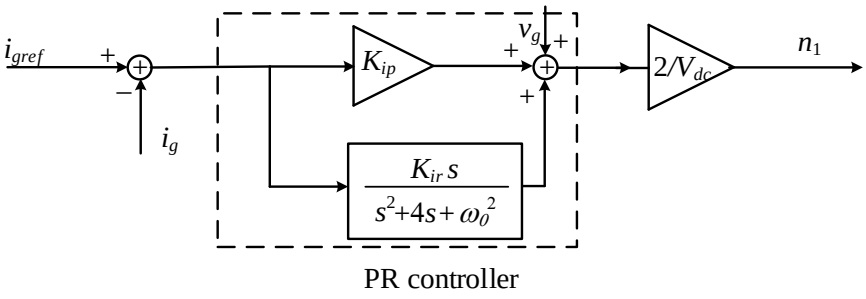

Figure 3.3 Diagram of the fundamental current control with PR controller

In Figure 3.3, i_{gref} is the current reference for the MMC AC side output, and the resonant frequency of the PR controller is the fundamental frequency ω_0. K_{ip} and K_{ir} are the proportional and resonant coefficients of the PR controller, respectively. The output n_1 is the fundamental frequency component in (3.34).

According to the small-signal model of the AC-side current controller, the perturbation of the fundamental frequency modulation ratio Δn_1 and the AC current Δi_g can be expressed as

$$\Delta n_1 = G_i(t)\Delta i_g \tag{3.49}$$

where $G_i(t)$ is the gain of the AC current controller and the transfer function in frequency-domain is

$$G_i = -\frac{2K_{ip}}{V_{dc}} - \frac{2K_{ir}s}{V_{dc}(s^2 + 4s + \omega_0^2)} \tag{3.50}$$

Moreover, when the controller has the voltage feed forward, the terminal voltage perturbation Δv_g of MMC can also affect the perturbation of the fundamental frequency modulation ratio Δn_1 as

$$\Delta n_1 = G_v(t)\Delta v_g \tag{3.51}$$

where $G_v(t)$ is the gain from the perturbation voltage to the AC controller output.

The total fundamental frequency perturbation Δn_1 is the sum of the components in (3.49) and (3.51), and the double-frequency perturbation Δn_2 of the modulation ratio can be determined by (3.47). According to (3.34), the perturbation for the upper and lower arms can thus be expressed as

$$\begin{cases} \Delta n_u = -G_i(t)\Delta i_g - G_v(t)\Delta v_g - G_{cc}(t)\Delta i_c \\ \Delta n_l = G_i(t)\Delta i_g + G_v(t)\Delta v_g - G_{cc}(t)\Delta i_c \end{cases} \tag{3.52}$$

Substituting the modulation ratio perturbation (3.52) into the small-signal model (3.44) derives the small-signal state equations of MMC with controllers, shown as the matrix form in (3.42), where $\Delta\mathbf{u}(t)$, $\mathbf{A}_\mathrm{p}(t)$ and $\mathbf{B}_\mathrm{p}(t)$ are rewritten as

$$\Delta\mathbf{u}(t) = \begin{bmatrix} \Delta v_p \end{bmatrix} \tag{3.53}$$

$$\mathbf{A}_p(t)=\begin{bmatrix} \dfrac{-G_{cc}(t)(V_{cu}^{\Sigma}+V_{cl}^{\Sigma})}{2L_m}-\dfrac{R_m}{L_m} & -\dfrac{N_u}{2L_m} & -\dfrac{N_l}{2L_m} & \dfrac{(G_v(t)Z_L+G_i(t))(V_{cu}^{\Sigma}-V_{cl}^{\Sigma})}{2L_m} \\ \dfrac{N_u+G_{cc}(t)(I_c+0.5I_g)}{C_m} & 0 & 0 & \dfrac{N_u-(G_v(t)Z_L+G_i(t))(2I_c+I_g)}{2C_m} \\ \dfrac{N_l+G_{cc}(t)(I_c-0.5I_g)}{C_m} & 0 & 0 & \dfrac{-N_l+(G_v(t)Z_L+G_i(t))(2I_c-I_g)}{2C_m} \\ \dfrac{-G_{cc}(t)(V_{cu}^{\Sigma}-V_{cl}^{\Sigma})}{L_m} & -\dfrac{N_u}{L_m} & \dfrac{N_l}{L_m} & -\dfrac{R_m+2Z_L}{L_m}+\dfrac{(G_v(t)Z_L+G_i(t))(V_{cu}^{\Sigma}+V_{cl}^{\Sigma})}{L_m} \end{bmatrix} \tag{3.54}$$

$$\mathbf{B}_p(t)=\begin{bmatrix} \dfrac{G_v(t)Z_L(V_{cu}^{\Sigma}-V_{cl}^{\Sigma})}{2L_m} \\ \dfrac{-G_v(t)Z_L(2I_c+I_g)}{2C_m} \\ \dfrac{G_v(t)Z_L(2I_c-I_g)}{2C_m} \\ -\dfrac{2}{L_m}+\dfrac{G_v(t)Z_L(V_{cu}^{\Sigma}+V_{cl}^{\Sigma})}{L_m} \end{bmatrix} \tag{3.55}$$

Transforming the above small-signal state equation into frequency-domain and establishing the model with HSS yield

$$s\Delta\mathbf{X}_s=(\mathbf{A}_{ps}-\mathbf{Q})\Delta\mathbf{X}_s+\mathbf{B}_{ps}\Delta\mathbf{U}_s \tag{3.56}$$

where the state variable matrix $\Delta\mathbf{X}_s$ can be expressed as

$$\Delta\mathbf{X}_s=\left[\Delta\mathbf{X}_{p-h},\cdots,\Delta\mathbf{X}_{p-1},\Delta\mathbf{X}_p,\Delta\mathbf{X}_{p-1},\cdots,\Delta\mathbf{X}_{p+h}\right]^T \tag{3.57}$$

where $\Delta\mathbf{X}_{p-h}=\left[\Delta i_{cp-h}\quad \Delta v_{cup-h}^{\Sigma}\quad \Delta v_{clp-h}^{\Sigma}\quad \Delta i_{gp-h}\right]$, the subscript p denotes the perturbation component injected at frequency ω_p, and the subscript p-h denotes the response at ω_p-$h\omega_0$. Similarly, $\Delta\mathbf{X}_{p+h}=\left[\Delta i_{cp+h}\quad \Delta v_{cup+h}^{\Sigma}\quad \Delta v_{clp+h}^{\Sigma}\quad \Delta i_{gp+h}\right]$ represents the response at ω_p+$h\omega_0$.

The small-signal perturbation input matrix $\Delta\mathbf{U}_s$ is expressed as

$$\Delta\mathbf{U}_s = \left[\Delta\mathbf{U}_{p-h}, \cdots, \Delta\mathbf{U}_{p-1}, \Delta\mathbf{U}_p, \Delta\mathbf{U}_{p-1}, \cdots, \Delta\mathbf{U}_{p+h}\right]^T \tag{3.58}$$

The perturbation voltage Δv_p injected at ω_p is written as $\Delta\mathbf{U}_p = \left[\Delta v_p\right]$, and $\Delta\mathbf{U}_{p-h} = \Delta\mathbf{U}_{p+h} = 0 \quad (h \geq 1)$. The frequency matrix $\mathbf{Q}$ is

$$\mathbf{Q} = \begin{bmatrix} -jh\omega_0\mathbf{I} & & & & \\ & \ddots & & & \\ & & j0\omega_0\mathbf{I} & & \\ & & & \ddots & \\ & & & & jh\omega_0\mathbf{I} \end{bmatrix} \tag{3.59}$$

where $\mathbf{I}$ is a 4 by 4 identify matrix.

Equation (3.52) can be expressed in frequency-domain as

$$\begin{cases} \Delta n_u(s) = -G_i(s)\Delta i_g(s) - G_v(s)\Delta v_g(s) - G_{cc}(s)\Delta i_c(s) \\ \Delta n_l(s) = G_i(s)\Delta i_g(s) + G_v(s)\Delta v_g(s) - G_{cc}(s)\Delta i_c(s) \end{cases} \tag{3.60}$$

Note that in (3.60), $s=j\omega_p$. This equation indicates that the modulation ratio generated by the controller at the perturbation frequency ω_p. While for the perturbation variable at $\omega_p+h\omega_0$, the controller transfer function can be expressed as

$$\begin{cases} \Delta n_u(s+jh\omega_0) = -G_i(s+jh\omega_0)\Delta i_g(s+jh\omega_0) - G_v(s+jh\omega_0)\Delta v_g(s+jh\omega_0) - G_{cc}(s+jh\omega_0)\Delta i_c(s+jh\omega_0) \\ \Delta n_l(s+jh\omega_0) = G_i(s+jh\omega_0)\Delta i_g(s+jh\omega_0) + G_v(s+jh\omega_0)\Delta v_g(s+jh\omega_0) - G_{cc}(s+jh\omega_0)\Delta i_c(s+jh\omega_0) \end{cases} \tag{3.61}$$

Hence, for different order harmonics, the transfer function for different controller should conduct corresponding frequency shift and the coefficient matrix $\mathbf{A}_{ps}$ can be written as

$$\mathbf{A}_{ps}=\begin{bmatrix}
\mathbf{A}_0(s-jh\omega_0) & \mathbf{A}_{-1}(s-j(h-1)\omega_0) & \cdots & \mathbf{A}_{-h}(s) & & & & \\
\mathbf{A}_1(s-jh\omega_0) & \ddots & \ddots & \ddots & \ddots & & & \\
\vdots & \ddots & \mathbf{A}_0(s-j\omega_0) & \mathbf{A}_{-1}(s) & \ddots & \ddots & & \\
\mathbf{A}_h(s-jh\omega_0) & \ddots & \mathbf{A}_1(s-j\omega_0) & \mathbf{A}_0(s) & \mathbf{A}_{-1}(s+j\omega_0) & \ddots & \mathbf{A}_{-h}(s+jh\omega_0) & \\
 & \ddots & \ddots & \mathbf{A}_1(s) & \mathbf{A}_0(s+j\omega_0) & \ddots & \vdots & \\
 & & \ddots & \ddots & \ddots & \ddots & \mathbf{A}_{-1}(s+jh\omega_0) & \\
 & & & \mathbf{A}_h(s) & \cdots & \mathbf{A}_1(s+j(h-1)\omega_0) & \mathbf{A}_0(s+jh\omega_0) &
\end{bmatrix} \tag{3.62}$$

Due to the transfer function of the controller at different harmonic frequency, the matrix $\mathbf{A}_{ps}$ will not be the Toeplitz matrix, and every element matrix will also be different. Appendix A lists the expression of the middle row matrix $\mathbf{A}_{-h}(s)$, $\mathbf{A}_{-1}(s)$, $\mathbf{A}_0(s)$, $\mathbf{A}_1(s)$, $\mathbf{A}_h(s)$ of $\mathbf{A}_{ps}$ and other elements in $\mathbf{A}_{ps}$ can be derived through the frequency shift of these matrices.

Similarly, matrix $\mathbf{B}_{\mathrm{ps}}$ can be derived as

$$\mathbf{B}_{ps}=\begin{bmatrix}
\mathbf{B}_0(s-jh\omega_0) & \mathbf{B}_{-1}(s-j(h-1)\omega_0) & \cdots & \mathbf{B}_{-h}(s) & & & & \\
\mathbf{B}_1(s-jh\omega_0) & \ddots & \ddots & \ddots & \ddots & & & \\
\vdots & \ddots & \mathbf{B}_0(s-j\omega_0) & \mathbf{B}_{-1}(s) & \ddots & \ddots & & \\
\mathbf{B}_h(s-jh\omega_0) & \ddots & \mathbf{B}_1(s-j\omega_0) & \mathbf{B}_0(s) & \mathbf{B}_{-1}(s+j\omega_0) & \ddots & \mathbf{B}_{-h}(s+jh\omega_0) & \\
 & \ddots & \ddots & \mathbf{B}_1(s) & \mathbf{B}_0(s+j\omega_0) & \ddots & \vdots & \\
 & & \ddots & \ddots & \ddots & \ddots & \mathbf{B}_{-1}(s+jh\omega_0) & \\
 & & & \mathbf{B}_h(s) & \cdots & \mathbf{B}_1(s+j(h-1)\omega_0) & \mathbf{B}_0(s+jh\omega_0) &
\end{bmatrix} \tag{3.63}$$

where the element matrices $\mathbf{B}_{-h}(s)$, $\mathbf{B}_{-1}(s)$, $\mathbf{B}_0(s)$, $\mathbf{B}_1(s)$, and $\mathbf{B}_h(s)$ are given in Appendix A.

3.2.4 Small-signal impedance of MMC

If a perturbation voltage Δv_p is injected into the AC terminal of MMC at ω_{p} as shown in Figure 3.1 (b), the AC terminal will generate the voltage Δv_g and the current Δi_g at ω_{p}. The positive current direction is defined as flowing out of MMC. Thus, the ratio of the small-signal response voltage and current denotes the small-signal impedance of MMC seen from the AC terminal as

$$Z_{MMC} = -\frac{\Delta v_g}{\Delta i_g} \tag{3.64}$$

When the perturbation voltage Δv_p is injected, due to the existence of Z_L, the terminal voltage perturbation Δv_g of the MMC is described as

$$\Delta v_g = \Delta v_p + Z_L \Delta i_g \tag{3.65}$$

According to (3.64) and (3.65), the small-signal impedance Z_{MMC} of MMC can be written as

$$Z_{MMC} = -\frac{\Delta v_p}{\Delta i_g} - Z_L \tag{3.66}$$

In the subsection 3.2.3, the HSS based small-signal model of MMC is described by (3.56), where Δv_p is the input voltage, and the AC-side current perturbation Δi_g is one of the state variables. Through solving the state equation (3.56), the relationship between the input variable Δv_p and the state variable Δi_g can be obtained. The solution of (3.56) can be expressed as

$$\Delta \mathbf{X}_s = (s\mathbf{I} - \mathbf{A}_{ps} + \mathbf{Q}) \cdot \mathbf{B}_{ps} \Delta \mathbf{U}_s = \mathbf{H}_{hss} \Delta \mathbf{U}_s \tag{3.67}$$

where $\mathbf{I}$ is the identity matrix, and $\mathbf{H}_{hss}$ reflects the relationship between the input and state variables. Extracting the input variable Δv_p and the state variable Δi_g and then combining with (3.66) yield the small-signal impedance of MMC.

3.3 Verification of small-signal impedance of MMC

To validate the small-signal model of MMC, a time-domain EMT simulation model in the form of Figure 3.1 is established in Matlab/Simulink. The load impedance is $Z_L = R_L + j\omega_0 L_L = 90 + j0.06\Omega$ and the related parameters of the MMC are listed in

Table 3.1.

Table 3.1 Main electrical parameters of the MMC

Parameters	Value
MMC rated apparent power (S_n)	1044 MVA
MMC rated active power (P)	±1000 MW
MMC rated reactive power(Q)	±300 MVar
MMC nominal DC Voltage (V_{dc})	640 kV(±320 kV)
MMC rated AC output voltage (L-L) (V_{nl})	360 kV
Arm resistance (R_m)	0.08 Ω
Arm inductance (L_m)	0.042 H
Cell capacitance (C_m)	31.4 μF
Nominal Frequency (f_0)	50 Hz

To derive the small-signal impedance of the MMC in time-domain, frequency sweeping method is used. The voltage perturbation Δv_p at ω_p is injected into the AC side of MMC with the magnitude of 1kV. The voltage v_g and the current i_g measured at the AC-side terminal of the MMC are handled by FFT to extract the small-signal voltage Δv_g and current Δi_g at ω_p. Using (3.64), the small-signal impedance of MMC in time-domain can be obtained at ω_p. ω_p can then be set to different frequencies and the corresponding MMC impedances cross a wide frequency range can be obtained.

3.3.1 Open loop MMC impedance model validation

In the open-loop model, i.e. no AC current controller or CCSC, the magnitude and phase of the given modulation ratio at fundamental frequency are fixed at n_1=0.45 and θ_1=0.01, whilst n_2=0 and θ_2=0 for double frequency. In addition, the modulation

ratio perturbation Δn_u and Δn_l for upper and lower arms in (3.52) are 0. With the HSS based MMC model established, the impedance can be calculated as shown in Figure 3.4 by considering the harmonic order h with 0, 1, 2, 3 and 4 in the model. In addition, the small-signal impedance of MMC measured in time-domain is also compared in Figure 3.4.

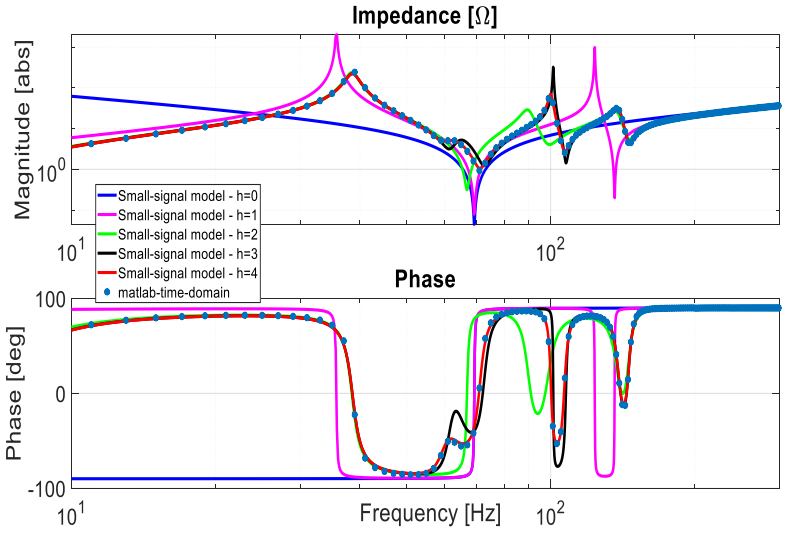

Figure 3.4 The impedance plot of HSS model and time-domain simulation model

It can be observed that the harmonic order considered in the HSS model of the MMC has a great impact on the accuracy of the analytical impedance model. Since significant steady-state harmonic components exist in the MMC arm current and capacitor voltage, the higher the harmonic order is considered in the HSS model, the more accurate the analytical impedance model is. In the impedance magnitudes shown in Figure 3.4, the solid red line which represents the magnitude of the HSS impedance model with h=4 overlap with that of the time-domain simulation model which is shown as blue dots in the figure. In the impedance phases shown in Figure 3.4, close match between those two models can also be observed. Based on those observations, it can be indicated that the analytical model with h=4 matches well with the measured results in the time-domain simulation.

3.3.2 Impedance model validation of the MMC with CCSC

In this part, the analytical model of the MMC system with CCSC is validated against the Matlab/Simulink time-domain model. The CCSC adopts the control design shown in Figure 3.2. The harmonic order *h* of the analytical model is selected as 2. As shown in Figure 3.5, the analytical impedance has a good agreement with the measured results in the simulation, which validates the analytical MMC impedance model. Moreover, it is worth noting that the high order harmonic components are well suppressed by CCSC so the analytical model with *h*=2 is sufficient, i.e. with h=3 and 4 the calculated impedances are largely identical to those shown in Figure 3.5.

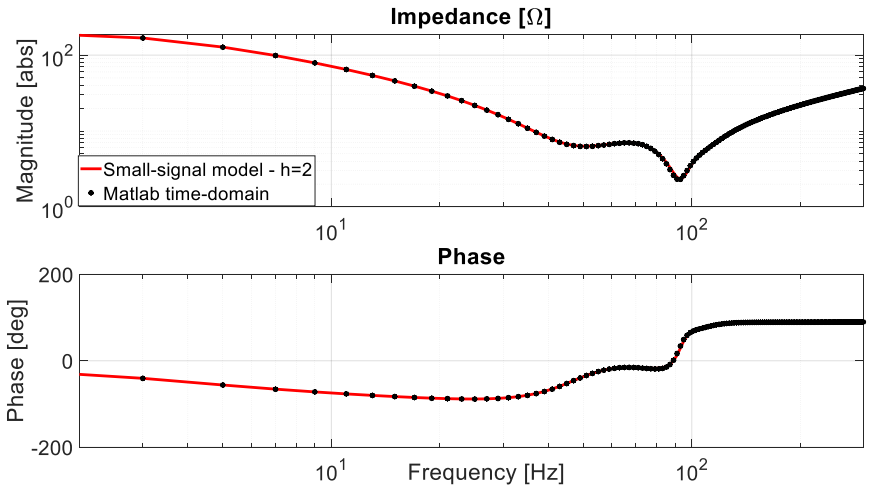

Figure 3.5 Analytical and simulation measured impedances of the MMC with CCSC

3.3.3 Impedance model validation of the MMC with full control

With the CCSC and the AC current controller included, Figure 3.6 compares the measured and calculated small-signal impedance of the MMC using the developed HSS analytical model with *h*=2. It can be observed that the two impedances match well, which verifies that the small-signal model established can produce accurate the small-signal MMC impedance with the controllers.

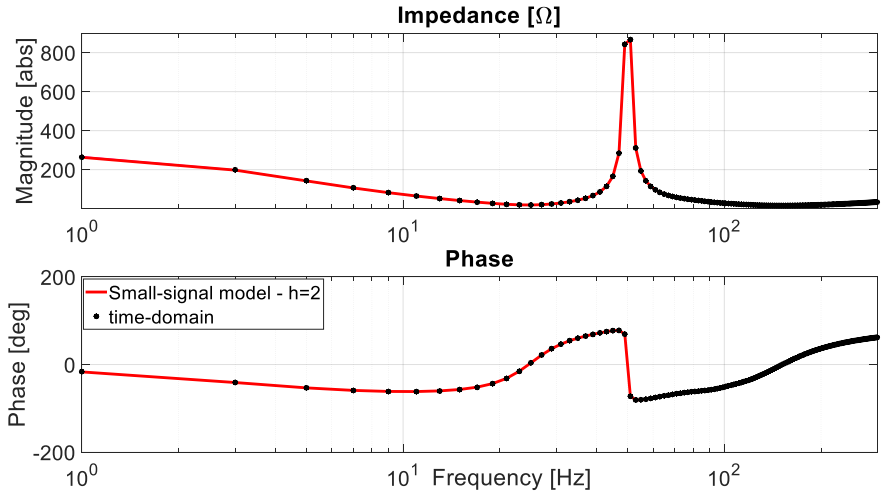

Figure 3.6 Analytical and simulation measured impedances of the MMC with full control

3.4 Problems existing in the single-phase MMC model

If the system uses the 3-phase 4-wire configuration, the three-phase MMC system can be analysed using single-phase systems. However, practical MMC systems normally do not have solid grounding on the DC mid-point employ and thus effectively resemble a 3-phase 3-wire connection. For the 3-phase 4-wire system, common AC and DC grounding allows common mode current to flow, e.g. third harmonic current. While for the 3-phase 3-wire system, there is no common mode current flowing through the AC and DC sides. The existence of the third harmonic in the 4-wire system can significantly affect the impedance of MMC, as will be discussed in detail in the next Chapter. Therefore, the single-phase modelling method for MMC proposed in this chapter cannot represent the true MMC impendence in real systems.

The MMC model established chooses the voltage on the AC-side ground point as reference. In order to obtain the operating point of the MMC terminal voltage, the load impedance Z_L needs to be included in the small-signal model of MMC. In the case of complex AC grid configuration, the mathematical expression of Z_L is difficult to obtain and thus this complicates the small-signal modelling of MMC. Nevertheless, if the

MMC terminal voltage is chosen as the reference point, the small-signal model developed will not depend on the impedance on the AC side.

When the MMC adopts the PR control in abc frame, the transfer function of the control for phase a, b and c is independent and identical. Take the AC-side current loop for example

$$\begin{bmatrix} \Delta n_{1a} \\ \Delta n_{1b} \\ \Delta n_{1c} \end{bmatrix} = \begin{bmatrix} G(s) & 0 & 0 \\ 0 & G(s) & 0 \\ 0 & 0 & G(s) \end{bmatrix} \begin{bmatrix} \Delta i_{ga} \\ \Delta i_{gb} \\ \Delta i_{gc} \end{bmatrix} \tag{3.68}$$

It can be seen that the modulation ratio Δn_{1a} for phase a is only associated with phase a current Δi_{ga}. Thus the transfer function for three-phase controller can be simplified into single-phase ones. Note that in Section 3.2, both the CCSC and the AC-side current control adopt the PR control in abc frame. If other controls are employed, for example, the PR control in αβ frame, the transfer function is given as

$$\begin{bmatrix} \Delta n_{1\alpha} \\ \Delta n_{1\beta} \end{bmatrix} = \begin{bmatrix} G(s) & 0 \\ 0 & G(s) \end{bmatrix} \begin{bmatrix} \Delta i_{g\alpha} \\ \Delta i_{g\beta} \end{bmatrix} \tag{3.69}$$

Transforming into the abc frame yields

$$\begin{aligned} \begin{bmatrix} \Delta n_{1a} \\ \Delta n_{1b} \\ \Delta n_{1c} \end{bmatrix} &= \frac{2}{3} \begin{bmatrix} 1 & 0 \\ -\frac{1}{2} & \frac{\sqrt{3}}{2} \\ -\frac{1}{2} & -\frac{\sqrt{3}}{2} \end{bmatrix} \begin{bmatrix} G(s) & 0 \\ 0 & G(s) \end{bmatrix} \begin{bmatrix} 1 & -\frac{1}{2} & -\frac{1}{2} \\ 0 & \frac{\sqrt{3}}{2} & -\frac{\sqrt{3}}{2} \end{bmatrix} \begin{bmatrix} \Delta i_{ga} \\ \Delta i_{gb} \\ \Delta i_{gc} \end{bmatrix} \\ &= \frac{2}{3} \begin{bmatrix} G(s) & -\frac{1}{2}G(s) & -\frac{1}{2}G(s) \\ -\frac{1}{2}G(s) & G(s) & -\frac{1}{2}G(s) \\ -\frac{1}{2}G(s) & -\frac{1}{2}G(s) & G(s) \end{bmatrix} \begin{bmatrix} \Delta i_{ga} \\ \Delta i_{gb} \\ \Delta i_{gc} \end{bmatrix} \end{aligned} \tag{3.70}$$

For (3.58), it can be seen that phase a modulation ratio Δn_{1a} is not only associated with phase a current Δi_{ga} but also phase b and c current Δi_{gb} and Δi_{gc}. Therefore, the modulation ratio Δn_1 for any phase cannot be represented by only its own phase current perturbation. In this situation, the controller transfer function cannot be acquired accurately. Thus, the impedance obtained from the single-phase modelling method is only valid and suitable for the MMC using PR control in abc frame.

The small-signal impedance of MMC derived reflects the relationship of the terminal voltage Δv_g and the resulting current Δi_g at the same frequency. However, as documented in literatures and from the time-domain simulation model, perturbation at one frequency can generate multiple frequency responses. Figure3.7 shows the measured FFT results for the terminal voltage v_g and current i_g from the time-domain model where the perturbation voltage Δv_p at 40Hz is injected.

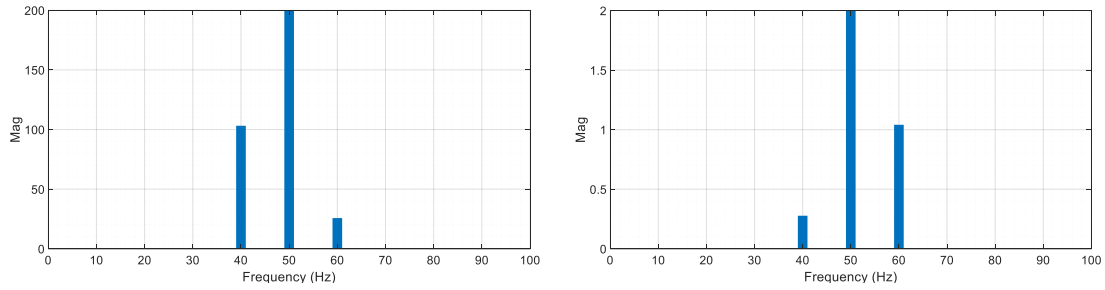

(a) v_g (b) i_g

Figure3.7 FFT analysis result for the terminal voltage and current with perturbation injection

According to the FFT results, it is obvious that the perturbation voltage at 40Hz not only causes the current response at 40Hz but also the voltage and current at 60Hz. In fact, different frequency coupling exists in the input and the response is generated by the internal harmonics of MMC, which is an important feature of MMC. However, the impedance modelling method for MMC in this chapter only reflects the AC

terminal voltage and current at the same frequency without considering different frequency coupling characteristics, which may lead to inaccurate stability analysis if such impedance models are used.

3.5 Summary

The HSS modeling approach is adopted for developing three-phase MMC impedance based on the single-phase equivalent circuit. The developed small-signal MMC impedance models includes all the internal harmonics within the MMC under various control strategies. The results show that the HSS modeling method can effectively explore both steady-state frequency coupling and dynamic harmonic interactions in power electronics based systems. Close matches have been observed between the impedances calculated from the developed analytical model and measured ones using frequency sweeping method from the time-domain EMT models. However, the study has also found that the single-phase modelling approach, which considers the system as an equivalent 3-phase 4-wire system, is not entirely effective for modelling practical MMC systems due to the absence of common AC and DC grounding point in practical installations. The controller adopted for the single-phase model cannot represent the actual control applied at the three-phase system. In addition, the MMC impedance only accounts for the voltage and current at the same frequency without considering different frequency coupling characteristics. Chapter 4 will further modelling method for addressing such problems.

Chapter 4 Harmonic state-space modelling of three-phase MMC

This chapter focuses on developing an accurate small signal impedance model of the three-phase MMC using the HSS method based on the developed single-phase MMC model in Chapter 3. The MMC model established represents a practical 3-phase 3-wire MMC system. The detailed modelling procedure is described using the HSS theory. To accommodate multiple harmonics in the linearization process, a matrix formulation is introduced and used to model both the converter power stage and its control including the PLL, the circulating current suppression control, AC current control and outer-loop power and AC voltage control. It further reveals the impact of the MMC internal dynamics and control dynamics on the MMC impedance. The derived impedance models are then verified by comparing the frequency responses of the developed analytical model with the impedances measured from a nonlinear time-domain simulation model in MATLAB/Simulink.

4.1 Linearizing the model of MMC in abc frame

The structure of a three-phase MMC is shown in Figure 4.1(a). Take phase *a* for example, V_a and Z_L represent the AC grid voltage and AC impedance used to determine the steady-state operating point, respectively. The upper and lower arms are connected in series to form one phase-leg with the upper and lower arm current being i_{ua} and i_{la}, the voltage v_{ua} and v_{la} , and modulation control signal n_{ua} and n_{la}. Each arm includes N sub-modules (SMs) with the capacitance of C_{sm}, and an arm reactor with inductance L_m and resistance R_m. The average-value modelling method is used [87], in which it is assumed that the capacitor voltages in the SMs are balanced and the high-order switching harmonics of arms are negligible.

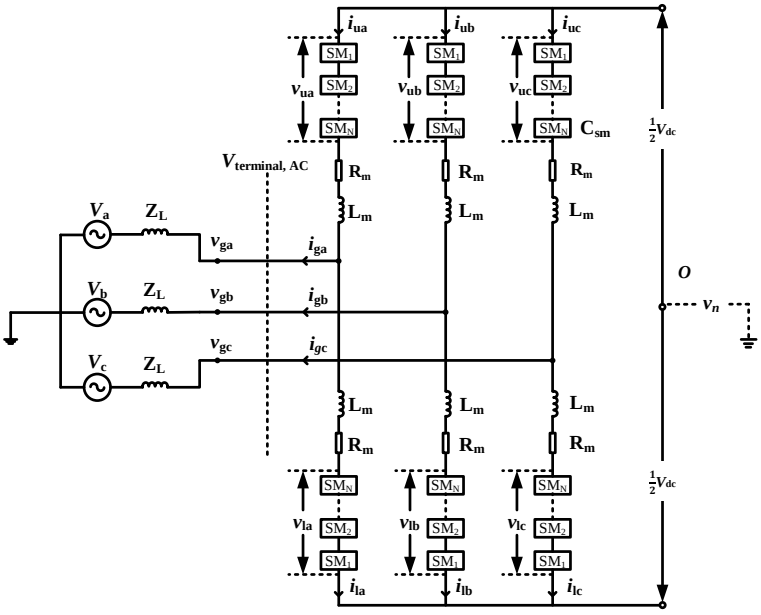

(a) Structure of a three-phase MMC

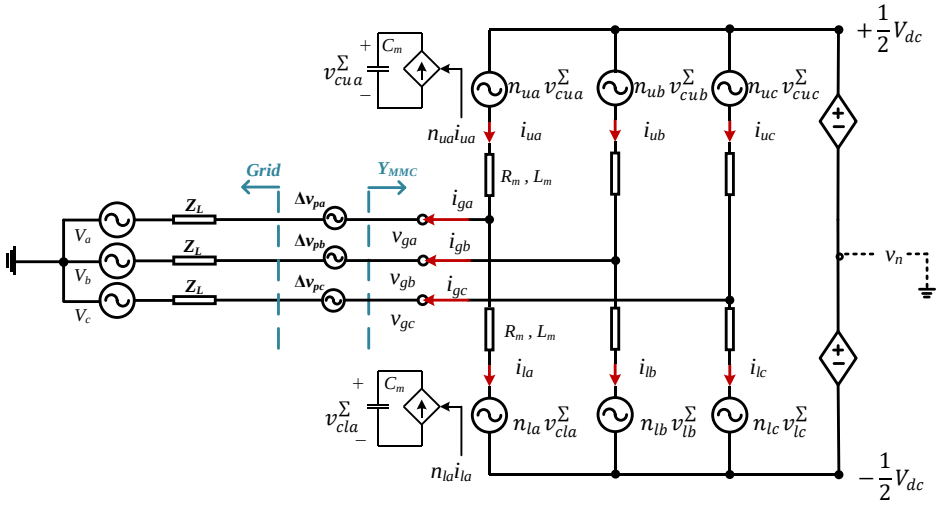

(b) Averaged equivalent circuit of a three-phase MMC

Figure 4.1 Structure and equivalent circuit of a three-phase MMC

The equivalent circuit of the MMC average model is depicted in Figure 4.1(b). A lumped equivalent capacitor C_m is used to represent the capacitors of all SMs in one arm and equals to C_{sm}/N. v_{cua}^{Σ} and v_{cla}^{Σ} denote the sum of the capacitor voltages of

SMs in the upper and lower arms, respectively, and v_{ga} and i_{ga} are the respective voltage and current on the MMC AC side. V_{dc} is the DC side voltage and is assumed to be constant. Since the system is in a 3-phase 3-wire connection, the voltage of the DC neutral point is v_n.

For ease of analysis, the three-phase quantities are defined in 3 by 1 matrices as $\mathbf{v}_{gabc}$, $\mathbf{i}_{gabc}$, $\mathbf{v}_{cuabc}^{\Sigma}$, $\mathbf{v}_{clabc}^{\Sigma}$, $\mathbf{v}_{uabc}$, $\mathbf{i}_{uabc}$, $\mathbf{v}_{labc}$, $\mathbf{i}_{labc}$, $\mathbf{i}_{cabc}$, $\mathbf{V}_{dc}$ and $\mathbf{v}_n$, whereas $\mathbf{n}_{uabc}$ and $\mathbf{n}_{uabc}$ are 3 by 3 diagonal matrices.

For a three-phase MMC, the relationship between the arm voltage and the equivalent capacitor voltage of the SMs can be expressed as

$$\begin{cases} \mathbf{v}_{uabc} = \mathbf{n}_{uabc} \cdot \mathbf{v}_{cuabc}^{\Sigma} \\ \mathbf{v}_{labc} = \mathbf{n}_{labc} \cdot \mathbf{v}_{clabc}^{\Sigma} \end{cases} \tag{4.1}$$

The internal dynamics between equivalent capacitor voltage of SMs and the arm current are depicted as

$$\begin{cases} C_m \cdot \dfrac{d\mathbf{v}_{cuabc}^{\Sigma}}{dt} = \mathbf{n}_{uabc} \cdot \mathbf{i}_{uabc} \\ C_m \cdot \dfrac{d\mathbf{v}_{clabc}^{\Sigma}}{dt} = \mathbf{n}_{labc} \cdot \mathbf{i}_{labc} \end{cases} \tag{4.2}$$

Both the arm voltage $\mathbf{v}_{abc}$ and capacitor voltage $\mathbf{v}_{cabc}^{\Sigma}$ contain multiple harmonics under steady-state. It indicates that MMC has multi-frequency response due to its significant steady-state harmonic components in the arm voltage and capacitor voltage.

The common mode current which circulates inside the MMC arms without appearing on the AC terminal is denoted as

$$\mathbf{i}_{cabc}=\frac{\mathbf{i}_{uabc}+\mathbf{i}_{labc}}{2} \tag{4.3}$$

The current on the AC side can be calculated as

$$\mathbf{i}_{gabc}=\mathbf{i}_{uabc}-\mathbf{i}_{labc} \tag{4.4}$$

According to the Kirchhoff's law, the voltage on the AC terminal of MMC and the current and voltage of the arm have the following relationship

$$\begin{cases} \mathbf{v}_{gabc}+L_m\cdot\dfrac{d\mathbf{i}_{uabc}}{dt}+R_m\cdot\mathbf{i}_{uabc}+\mathbf{v}_{uabc}=\dfrac{\mathbf{V}_{dc}}{2}+\mathbf{v}_n \\ \mathbf{v}_{gabc}-L_m\cdot\dfrac{d\mathbf{i}_{labc}}{dt}-R_m\cdot\mathbf{i}_{labc}-\mathbf{v}_{labc}=-\dfrac{\mathbf{V}_{dc}}{2}+\mathbf{v}_n \end{cases} \tag{4.5}$$

Combining (4.1), (4.2), (4.3), (4.4) with (4.5) derives the state-space equation of MMC as

$$\begin{cases} \dfrac{d\mathbf{i}_{cabc}}{dt}=-\dfrac{R_m}{L_m}\mathbf{i}_{cabc}-\dfrac{\mathbf{n}_{uabc}}{2L_m}\mathbf{v}^{\Sigma}_{cuabc}-\dfrac{\mathbf{n}_{labc}}{2L_m}\mathbf{v}^{\Sigma}_{clabc}+\dfrac{\mathbf{V}_{dc}}{2L_m} \\ \dfrac{d\mathbf{i}_{gabc}}{dt}=-\dfrac{R_m}{L_m}\mathbf{i}_{gabc}-\dfrac{\mathbf{n}_{uabc}}{L_m}\mathbf{v}^{\Sigma}_{cuabc}+\dfrac{\mathbf{n}_{labc}}{L_m}\mathbf{v}^{\Sigma}_{clabc}-\dfrac{2}{L_m}\mathbf{v}_{gabc}+\dfrac{2\mathbf{v}_n}{L_m} \\ \dfrac{d\mathbf{v}^{\Sigma}_{cuabc}}{dt}=\dfrac{\mathbf{n}_{uabc}}{C_m}\mathbf{i}_{cabc}+\dfrac{\mathbf{n}_{uabc}}{2C_m}\mathbf{i}_{gabc} \\ \dfrac{d\mathbf{v}^{\Sigma}_{clabc}}{dt}=\dfrac{\mathbf{n}_{labc}}{C_m}\mathbf{i}_{cabc}-\dfrac{\mathbf{n}_{labc}}{2C_m}\mathbf{i}_{gabc} \end{cases} \tag{4.6}$$

Introducing the small perturbation analysis to linearize (4.6) yields the small-signal state-space model of three-phase MMC in abc frame as

$$\begin{cases} \dfrac{d\triangle\mathbf{i}_{cabc}}{dt} = -\dfrac{R_m}{L_m}\triangle\mathbf{i}_{cabc} - \dfrac{\mathbf{N}_{uabc}}{2L_m}\triangle\mathbf{v}^{\Sigma}_{cuabc} - \dfrac{\mathbf{N}_{labc}}{2L_m}\triangle\mathbf{v}^{\Sigma}_{clabc} - \dfrac{\mathbf{V}^{\Sigma}_{cuabc}}{2L_m}\triangle\mathbf{n}_{uabc} - \dfrac{\mathbf{V}^{\Sigma}_{clabc}}{2L_m}\triangle\mathbf{n}_{labc} \\ \dfrac{d\triangle\mathbf{i}_{gabc}}{dt} = -\dfrac{R_m}{L_m}\triangle\mathbf{i}_{gabc} - \dfrac{\mathbf{N}_{uabc}}{L_m}\triangle\mathbf{v}^{\Sigma}_{cuabc} + \dfrac{\mathbf{N}_{labc}}{L_m}\triangle\mathbf{v}^{\Sigma}_{clabc} - \dfrac{\mathbf{V}^{\Sigma}_{cuabc}}{L_m}\triangle\mathbf{n}_{uabc} + \dfrac{\mathbf{V}^{\Sigma}_{clabc}}{L_m}\triangle\mathbf{n}_{labc} - \dfrac{2}{L_m}\triangle\mathbf{v}_{pabc} + \dfrac{2}{L_m}\triangle\mathbf{v}_n \\ \dfrac{d\triangle\mathbf{v}^{\Sigma}_{cuabc}}{dt} = \dfrac{\mathbf{N}_{uabc}}{C_m}\triangle\mathbf{i}_{cabc} + \dfrac{\mathbf{N}_{uabc}}{2C_m}\triangle\mathbf{i}_{gabc} + \dfrac{\mathbf{I}_{cabc}}{C_m}\triangle\mathbf{n}_{uabc} + \dfrac{\mathbf{I}_{gabc}}{2C_m}\triangle\mathbf{n}_{uabc} \\ \dfrac{d\triangle\mathbf{v}^{\Sigma}_{clabc}}{dt} = \dfrac{\mathbf{N}_{labc}}{C_m}\triangle\mathbf{i}_{cabc} - \dfrac{\mathbf{N}_{labc}}{2C_m}\triangle\mathbf{i}_{gabc} + \dfrac{\mathbf{I}_{cabc}}{C_m}\triangle\mathbf{n}_{labc} - \dfrac{\mathbf{I}_{gabc}}{2C_m}\triangle\mathbf{n}_{labc} \end{cases} \tag{4.7}$$

where variables in capital form denote the values at the steady-state operation point and variables with $\triangle$ denote the corresponding small perturbations. $\triangle\mathbf{v}_{pabc}$ is the injected small perturbation voltage at the MMC AC terminal.

4.2 Transforming the small-signal model of MMC in abc frame to pn frame

The pn frame has been chosen to study the system stability since it enables any number of harmonics to be effectively tracked for three-phase system [25]. The matrix **P** is adopted to realize the frame transformation from abc coordinate to the pn frame whereas $\mathbf{P}^{-1}$ is the inverse matrix, as

$$\mathbf{P}=\begin{bmatrix} 1 & e^{j2\pi/3} & e^{j4\pi/3} \\ 1 & e^{j4\pi/3} & e^{j2\pi/3} \\ 1 & 1 & 1 \end{bmatrix} \tag{4.8}$$

Apply the transformation for the current, voltage and modulation signals, as

$$\triangle\mathbf{i}_{cabc}=\mathbf{P}^{-1}\cdot\triangle\mathbf{i}_{cPN0};\ \triangle\mathbf{i}_{gabc}=\mathbf{P}^{-1}\cdot\triangle\mathbf{i}_{gPN0};\ \triangle\mathbf{v}^{\Sigma}_{cuabc}=\mathbf{P}^{-1}\cdot\triangle\mathbf{v}^{\Sigma}_{cuPN0};\ \triangle\mathbf{v}^{\Sigma}_{clabc}=\mathbf{P}^{-1}\cdot\triangle\mathbf{v}^{\Sigma}_{clPN0}$$

$$\triangle\mathbf{n}_{uabc}=\mathbf{P}^{-1}\cdot\triangle\mathbf{n}_{uPN0};\ \triangle\mathbf{n}_{labc}=\mathbf{P}^{-1}\cdot\triangle\mathbf{n}_{lPN0};\ \triangle\mathbf{v}_{pabc}=\mathbf{P}^{-1}\cdot\triangle\mathbf{v}_{pPN0}.$$

Thus, (4.7) can be rewritten in the pn coordinate frame as

$$\begin{cases} \dfrac{d\triangle \mathbf{i}_{cPN0}}{dt} = -\dfrac{R_m}{L_m}\triangle \mathbf{i}_{cPN0} - \dfrac{\mathbf{PN}_{uabc}\mathbf{P}^{-1}}{2L_m}\triangle \mathbf{v}^{\Sigma}_{cuPN0} - \dfrac{\mathbf{PN}_{labc}\mathbf{P}^{-1}}{2L_m}\triangle \mathbf{v}^{\Sigma}_{clPN0} - \dfrac{\mathbf{PV}^{\Sigma}_{cuabc}\mathbf{P}^{-1}}{2L_m}\triangle \mathbf{n}_{uPN0} - \dfrac{\mathbf{PV}^{\Sigma}_{clabc}\mathbf{P}^{-1}}{2L_m}\triangle \mathbf{n}_{lPN0} \\ \dfrac{d\triangle \mathbf{i}_{gPN0}}{dt} = -\dfrac{R_m}{L_m}\mathbf{C}_z\triangle \mathbf{i}_{gPN0} - \dfrac{\mathbf{PN}_{uabc}\mathbf{P}^{-1}}{L_m}\triangle \mathbf{v}^{\Sigma}_{cuPN0} + \dfrac{\mathbf{PN}_{labc}\mathbf{P}^{-1}}{L_m}\triangle \mathbf{v}^{\Sigma}_{clPN0} - \dfrac{\mathbf{PV}^{\Sigma}_{cuabc}\mathbf{P}^{-1}}{L_m}\triangle \mathbf{n}_{uPN0} + \dfrac{\mathbf{PV}^{\Sigma}_{clabc}\mathbf{P}^{-1}}{L_m}\triangle \mathbf{n}_{lPN0} - \dfrac{2}{L_m}\triangle \mathbf{v}_{pPN0} \\ \dfrac{d\triangle \mathbf{v}^{\Sigma}_{cuPN0}}{dt} = \dfrac{\mathbf{PN}_{uabc}\mathbf{P}^{-1}}{C_m}\triangle \mathbf{i}_{cPN0} + \dfrac{\mathbf{PN}_{uabc}\mathbf{P}^{-1}}{2C_m}\mathbf{C}_z\triangle \mathbf{i}_{gPN0} + \dfrac{\mathbf{PI}_{cabc}\mathbf{P}^{-1}}{C_m}\triangle \mathbf{n}_{uPN0} + \dfrac{\mathbf{PI}_{gabc}\mathbf{P}^{-1}}{2C_m}\triangle \mathbf{n}_{uPN0} \\ \dfrac{d\triangle \mathbf{v}^{\Sigma}_{clPN0}}{dt} = \dfrac{\mathbf{PN}_{labc}\mathbf{P}^{-1}}{C_m}\triangle \mathbf{i}_{cPN0} - \dfrac{\mathbf{PN}_{labc}\mathbf{P}^{-1}}{2C_m}\mathbf{C}_z\triangle \mathbf{i}_{gPN0} + \dfrac{\mathbf{PI}_{cabc}\mathbf{P}^{-1}}{C_m}\triangle \mathbf{n}_{lPN0} - \dfrac{\mathbf{C}_m^{-1}\mathbf{PI}_{gabc}\mathbf{P}^{-1}}{2C_m}\triangle \mathbf{n}_{lPN0} \end{cases} \tag{4.9}$$

Due to the three-phase three-wire system, no zero-sequence current circulation path exists at MMC AC side [96]. Note that in (4.7), $\triangle \mathbf{v}_n$ is a zero-sequence compensation voltage and is inserted into the AC side to eliminate the zero-sequence grid current in abc frame [98]. However, to simplify the analysis, a matrix $\mathbf{C}_z$ is introduced here in the analytical model in pn frame to force the zero-sequence grid current zero and thus $\triangle \mathbf{v}_n$ can be ignored in (4.9), as

$$\mathbf{C}_z = \begin{bmatrix} 1 & 0 & 0 \\ 0 & 1 & 0 \\ 0 & 0 & 0 \end{bmatrix} \tag{4.10}$$

The small-signal model of the three-phase MMC around an operation trajectory in pn frame, characterized by $\triangle \mathbf{i}_{cPN0}$, $\triangle \mathbf{i}_{gPN0}$, $\triangle \mathbf{v}^{\Sigma}_{cuPN0}$ and $\triangle \mathbf{v}^{\Sigma}_{clPN0}$, can be derived in matrix form as

$$\triangle \dot{\mathbf{x}}_{PN0} = \mathbf{A}_s \triangle \mathbf{x}_{PN0} + \mathbf{M}\triangle \mathbf{n}_{PN0} + \mathbf{B}\triangle \mathbf{v}_{pPN0} \tag{4.11}$$

where

$$\mathbf{A}_s=\begin{bmatrix} -\dfrac{R_m}{L_m}\mathbf{I} & \mathbf{0} & -\dfrac{\mathbf{PN}_{uabc}\mathbf{P}^{-1}}{2L_m} & -\dfrac{\mathbf{PN}_{labc}\mathbf{P}^{-1}}{2L_m} \\ \mathbf{0} & -\dfrac{R_m}{L_m}\cdot\mathbf{C}_z & -\dfrac{\mathbf{PN}_{uabc}\mathbf{P}^{-1}}{L_m} & \dfrac{\mathbf{PN}_{labc}\mathbf{P}^{-1}}{L_m} \\ \dfrac{\mathbf{PN}_{uabc}\mathbf{P}^{-1}}{C_m} & \dfrac{\mathbf{PN}_{uabc}\mathbf{P}^{-1}}{2C_m}\cdot\mathbf{C}_z & \mathbf{0} & \mathbf{0} \\ \dfrac{\mathbf{PN}_{labc}\mathbf{P}^{-1}}{C_m} & -\dfrac{\mathbf{PN}_{labc}\mathbf{P}^{-1}}{2C_m}\cdot\mathbf{C}_z & \mathbf{0} & \mathbf{0} \end{bmatrix}$$

$$\mathbf{M}=\begin{bmatrix} -\dfrac{\mathbf{PV}^{\Sigma}_{cuabc}\mathbf{P}^{-1}}{2L_m} & -\dfrac{\mathbf{PV}^{\Sigma}_{clabc}\mathbf{P}^{-1}}{2L_m} \\ -\dfrac{\mathbf{PV}^{\Sigma}_{cuabc}\mathbf{P}^{-1}}{L_m} & \dfrac{\mathbf{PV}^{\Sigma}_{cuabc}\mathbf{P}^{-1}}{L_m} \\ \dfrac{(2\mathbf{PI}_{cabc}\mathbf{P}^{-1}+\mathbf{PI}_{gabc}\mathbf{P}^{-1})}{2C_m} & \mathbf{0} \\ \mathbf{0} & \dfrac{(2\mathbf{PI}_{cabc}\mathbf{P}^{-1}-\mathbf{PI}_{gabc}\mathbf{P}^{-1})}{2C_m} \end{bmatrix}$$

$$\mathbf{B}=\begin{bmatrix}\mathbf{0} & -2\mathbf{I}/L_m & \mathbf{0} & \mathbf{0}\end{bmatrix}^T,\ \triangle\mathbf{n}_{PN0}=\begin{bmatrix}\triangle\mathbf{n}_{uPN0} & \triangle\mathbf{n}_{lPN0}\end{bmatrix}^T$$

$$\triangle\mathbf{x}_{PN0}=\begin{bmatrix}\triangle\mathbf{i}_{cPN0} & \triangle\mathbf{i}_{gPN0} & \triangle\mathbf{v}^{\Sigma}_{cuPN0} & \triangle\mathbf{v}^{\Sigma}_{clPN0}\end{bmatrix}^T.$$

In (4.11), $\mathbf{A}_s$ is the coefficient matrix, determined by L_m, R_m, C_m and the steady-state variables $\mathbf{N}_{labc}$ and $\mathbf{N}_{uabc}$ of the modulation ratio. $\mathbf{B}$ is the coefficient matrix of the input variables and is only related with the arm inductor L_m. In order to derive the state equation of the system, the relationship among the modulation ratio $\Delta\mathbf{n}_{PN0}$, the state variable $\Delta\mathbf{x}_{PN0}$ and the input variable $\Delta\mathbf{v}_{pPN0}$ should be identified in pn frame.

When the MMC controller is considered, the variation $\Delta\mathbf{n}_{PN0}$ of the modulation ratio depends on the control variables of the controller. The control variables of the MMC generally include the AC current and voltage as well as the internal circulating current. Thus $\Delta\mathbf{n}_{PN0}$ can be expressed as

$$\begin{cases} \triangle \mathbf{n}_{uPN0} = -\mathbf{G}_{iPN0} \cdot \triangle \mathbf{i}_{gPN0} - \mathbf{G}_{vPN0} \cdot \triangle \mathbf{v}_{gPN0} - \mathbf{G}_{ccPN0} \cdot \triangle \mathbf{i}_{cPN0} \\ \triangle \mathbf{n}_{lPN0} = \mathbf{G}_{iPN0} \cdot \triangle \mathbf{i}_{gPN0} + \mathbf{G}_{vPN0} \cdot \triangle \mathbf{v}_{gPN0} - \mathbf{G}_{ccPN0} \cdot \triangle \mathbf{i}_{cPN0} \end{cases} \tag{4.12}$$

where $\mathbf{G}_{iPN0}$, $\mathbf{G}_{vPN0}$ and $\mathbf{G}_{ccPN0}$ are the gain matrices of the relevant controllers.

Rewriting (4.12) in matrix form yields the relationship among the modulation ratio $\triangle \mathbf{n}_{PN0}$, the state variable $\triangle \mathbf{x}_{PN0}$, and the voltage $\triangle \mathbf{v}_{gPN0}$ as

$$\begin{bmatrix} \triangle \mathbf{n}_{uPN0} \\ \triangle \mathbf{n}_{lPN0} \end{bmatrix} = \begin{bmatrix} -\mathbf{G}_{ccPN0} & -\mathbf{G}_{iPN0} & 0 & 0 \\ -\mathbf{G}_{ccPN0} & \mathbf{G}_{iPN0} & 0 & 0 \end{bmatrix} \begin{bmatrix} \triangle \mathbf{i}_{cPN0} \\ \triangle \mathbf{i}_{gPN0} \\ \triangle \mathbf{v}^{\Sigma}_{cuPN0} \\ \triangle \mathbf{v}^{\Sigma}_{clPN0} \end{bmatrix} + \begin{bmatrix} -\mathbf{G}_{vPN0} \\ \mathbf{G}_{vPN0} \end{bmatrix} \cdot \triangle \mathbf{v}_{gPN0} \tag{4.13}$$

Equation (4.13) can be depicted in simple forms as

$$\triangle \mathbf{n}_{PN0} = \mathbf{G}_A \cdot \triangle \mathbf{x}_{PN0} + \mathbf{G}_B \cdot \triangle \mathbf{v}_{gPN0} \tag{4.14}$$

where $\mathbf{G}_A = \begin{bmatrix} -\mathbf{G}_{ccPN0} & -\mathbf{G}_{iPN0} & \mathbf{0} & \mathbf{0} \\ -\mathbf{G}_{ccPN0} & \mathbf{G}_{iPN0} & \mathbf{0} & \mathbf{0} \end{bmatrix}$ and $\mathbf{G}_B = \begin{bmatrix} -\mathbf{G}_{vPN0} \\ \mathbf{G}_{vPN0} \end{bmatrix}$.

Substituting (4.14) into (4.11) derives the small-signal state-space equation of the three-phase MMC in pn frame as

$$\triangle \dot{\mathbf{x}}_{PN0} = (\mathbf{A}_s + \mathbf{M}\mathbf{G}_\mathbf{A}) \triangle \mathbf{x}_{PN0} + (\mathbf{B} + \mathbf{M}\mathbf{G}_\mathbf{B}) \triangle \mathbf{v}_{pPN0} \tag{4.15}$$

4.3 MMC modelling using HSS method

All the state variables in (4.15) are periodic signals in the steady state, and the MMC is deemed essentially a time periodic system. Based on the HSS modelling method, the time-domain state-space equation (4.15) of the MMC is transformed to the small-signal HSS model expressed as

$$s\triangle\mathbf{x}_{\mathbf{PN0}}=(\mathbf{A}_s+\mathbf{M}\cdot\mathbf{G}_{\mathbf{A}}-\mathbf{Q})\cdot\triangle\mathbf{x}_{\mathbf{PN0}}+(\mathbf{M}\cdot\mathbf{G}_{\mathbf{B}}+\mathbf{B})\cdot\triangle\mathbf{v}_{p\mathbf{PN0}} \tag{4.16}$$

According to the general equation of HSS, Fourier expansion of (4.16) can be written as

$$s\triangle\mathbf{X}_{PN0}=(\Gamma[\mathbf{A}_s]+\Gamma[\mathbf{M}]\cdot\mathbf{HG}_A-\mathbf{Q})\cdot\triangle\mathbf{X}_{PN0}+\left(\Gamma[\mathbf{B}]+\Gamma[\mathbf{M}]\cdot\mathbf{HG}_B\right)\cdot\triangle\mathbf{V}_{pPN0} \tag{4.17}$$

where $\Gamma[\mathbf{A}_s]$, $\Gamma[\mathbf{B}]$ and $\Gamma[\mathbf{M}]$ are Toeplitz matrices, which are related with the MMC parameters L_{m}, R_{m}, C_{m} and the harmonic components at the steady-state operation point of the MMC. $\mathbf{HG}_A$ is the control transfer matrix associated with the harmonic state variables, and $\mathbf{HG}_B$ is the one with the harmonic input variables. Their specific expressions are decided by the controller. $\triangle\mathbf{X}_{PN0}$ and $\triangle\mathbf{V}_{pPN0}$ are the harmonic state variable matrices and the input matrix in harmonic frequency, respectively. These matrices $\Gamma[\mathbf{A}_s]$, $\Gamma[\mathbf{B}]$, $\Gamma[\mathbf{M}]$, $\mathbf{HG}_A$, $\mathbf{HG}_B$, $\triangle\mathbf{X}_{PN0}$, and $\triangle\mathbf{V}_{gPN0}$ are given as in the Appendix B.

4.4 Small-signal modelling of MMC control

To establish a complete small-signal model of MMC, its control needs to be included in the modelling. As shown in the state-space equation (4.17), $\mathbf{HG}_A$ and $\mathbf{HG}_B$ are the transfer function matrices determined by the controller in pn frame. Therefore, to derive the small-signal impedance of MMC, the transfer function of specific controllers should be achieved in corresponding frame and then the frame transformation should be carried out to obtain the transfer function in pn frame.

4.4.1 Circulating current suppression controller (CCSC)

The circulating current flows within the arms and transfers charge between the SM capacitors, which plays a very important role in MMC internal dynamics.

Therefore, the circulating current control has significant impacts on the converter impedance response. The implementation of a PR controller in the circulating current suppression control is depicted in Figure 4.2. In general, since the circulating current contains a series of even-harmonic components, in which the second-order harmonic currents are the dominant components in the circulating current, the objective is to suppress the dominant second order harmonic circulating currents by setting the references to zero and $2\omega_0$ to be twice of the fundamental frequency. The circulating current signal is obtained by filtering out the DC component from the common mode current in (4.3) using high pass filters (HPF), as shown in Figure 4.2. Since this controller acts on the common-mode component of the modulation functions of the upper and lower arms in each phase leg, its output is added with the same sign to the modulation functions of the upper and lower arms.

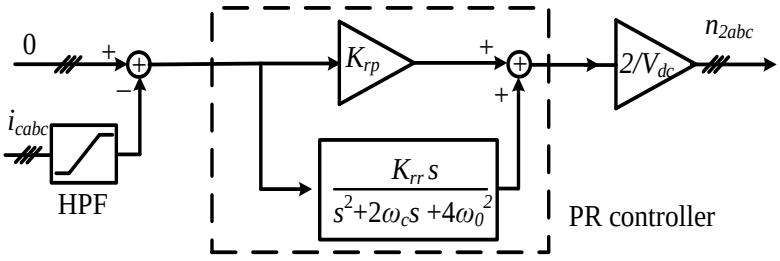

Figure 4.2 Diagram of circulating current suppression controller

The transfer function of the PR controller can be expressed as [115]

$$G_{PR}(s) = K_{rp} + \frac{K_{rr}}{s^2 + 2\omega_c s + 4\omega_0^2} \tag{4.18}$$

where K_{rp} and K_{rr} are the proportional and resonant coefficients of the PR controller, respectively. ω_c is the cutoff frequency and ω_0 is the fundamental frequency.

The transfer function of HPF is

$$G_{HPF}(s) = \frac{s^2}{s^2 + 2\zeta\omega_n s + \omega_n^2} \tag{4.19}$$

where ω_n is the un-damped natural frequency and ζ is the damping factor [116].

Thus, the double frequency output modulation signal by the CCSC and the circulating current have the following relationship

$$\begin{bmatrix} \triangle n_{2a} \\ \triangle n_{2b} \\ \triangle n_{2c} \end{bmatrix} = \mathbf{G}_{ccabc}(s) \begin{bmatrix} \triangle i_{ca} \\ \triangle i_{cb} \\ \triangle i_{cc} \end{bmatrix} \tag{4.20}$$

where $\mathbf{G}_{ccabc}(s)$ is the circulating current transfer function matrix in abc frame, and is given as

$$\mathbf{G}_{ccabc}(s) = \frac{-2}{V_{dc}} \begin{bmatrix} G_{HPF}(s)G_{PR}(s) & 0 & 0 \\ 0 & G_{HPF}(s)G_{PR}(s) & 0 \\ 0 & 0 & G_{HPF}(s)G_{PR}(s) \end{bmatrix} \tag{4.21}$$

The corresponding CCSC transfer function in pn frame $\mathbf{G}_{ccPN0}(s)$, as part of $\mathbf{HG}_A$ in (4.17), can be derived as

$$\mathbf{G}_{ccPN0}(s) = \mathbf{P} \cdot \mathbf{G}_{ccabc}(s) \cdot \mathbf{P}^{-1} \tag{4.22}$$

4.4.2 Current control at MMC AC terminal

The current control loop has fast response and the capability of limiting the current when system faults occur. The block diagram of an inner current loop including the PLL is presented in Figure 4.3.

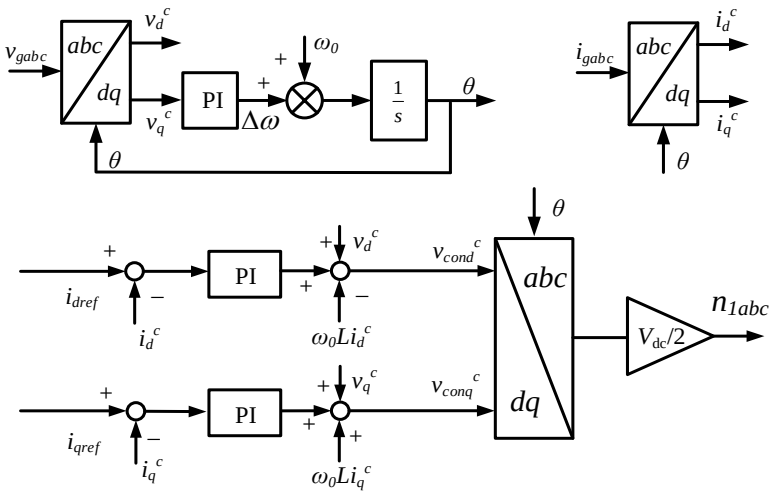

Figure 4.3 The block diagram of an inner current loop

As shown, v_{gabc} and i_{gabc} are the actual network voltage and current at the MMC AC terminal, respectively. The PLL extracts the voltage phase angle through three-phase voltage v_{abc} to be used for abc to dq frame transformation of voltage and current. L is the equivalent input AC inductance and equals to half of the inductance of the arm reactor L_m. The output of the current control loop is the fundamental frequency modulation ratio n_{1abc}. When the voltage perturbation occurs, the dynamics of the PLL can be described as [41]

$$\Delta\theta = G_{pll}\,\Delta v_q \tag{4.23}$$

where G_{pll} is the transfer function of the PLL and is expressed as

$$G_{pll}(s) = \frac{K_{ppll}s + K_{ipll}}{s^2 + V_d K_{ppll}s + V_d K_{ipll}} \tag{4.24}$$

where K_{ppll} and K_{ipll} are the proportional and integral coefficients of the PLL PI controller, respectively.

It can be observed that if there exists voltage perturbation in the terminal voltage

of MMC, there will be angle deviation $\triangle\theta$ extracted from PLL, and consequently, $\triangle\theta$ will further affect the frame transformation.

During steady state, the relationship between voltage V_d^c and V_q^c in the control frame determined by PLL and V_d and V_q in the system frame can be written as:

$$\begin{bmatrix} V_d^c \\ V_q^c \end{bmatrix} = \begin{bmatrix} \cos(0) & \sin(0) \\ -\sin(0) & \cos(0) \end{bmatrix} \begin{bmatrix} V_d \\ V_q \end{bmatrix} \tag{4.25}$$

The voltage perturbations $\triangle v_d$ and $\triangle v_q$ passing through PLL result in

$$\begin{bmatrix} V_d^c + \triangle v_d^c \\ V_q^c + \triangle v_q^c \end{bmatrix} = \begin{bmatrix} \cos(0+\triangle\theta) & \sin(0+\triangle\theta) \\ -\sin(0+\triangle\theta) & \cos(0+\triangle\theta) \end{bmatrix} \begin{bmatrix} V_d + \triangle v_d \\ V_q + \triangle v_q \end{bmatrix} \tag{4.26}$$

Subtracting the steady-state component (4.25) from (4.26) yields the voltage perturbation in PLL frame as

$$\begin{bmatrix} \triangle v_d^c \\ \triangle v_q^c \end{bmatrix} = \begin{bmatrix} \triangle v_d + \triangle\theta V_q + \triangle\theta\triangle v_q \\ \triangle v_q - \triangle\theta V_d - \triangle\theta\triangle v_d \end{bmatrix} \tag{4.27}$$

Ignoring the second order terms $\triangle\theta\triangle v_q$ and $\triangle\theta\triangle v_d$, (4.27) can be rewritten as

$$\begin{bmatrix} \triangle v_d^c \\ \triangle v_q^c \end{bmatrix} = \begin{bmatrix} \triangle v_d + \triangle\theta V_q \\ \triangle v_q - \triangle\theta V_d \end{bmatrix} \tag{4.28}$$

Substituting (4.23) into (4.28) yields

$$\begin{bmatrix} \Delta v_d^c \\ \Delta v_q^c \end{bmatrix} = \begin{bmatrix} \Delta v_d + \Delta\theta V_q \\ \Delta v_q - \Delta\theta V_d \end{bmatrix} = \begin{bmatrix} 1 & V_q G_{pll} \\ 0 & 1 - V_d G_{pll} \end{bmatrix} \begin{bmatrix} \Delta v_d \\ \Delta v_q \end{bmatrix} \tag{4.29}$$

The current perturbation in PLL frame can also be expressed in the similar form

as

$$\begin{bmatrix} \Delta i_d^c \\ \Delta i_q^c \end{bmatrix} = \begin{bmatrix} \Delta i_d + \Delta\theta I_q \\ \Delta i_q - \Delta\theta I_d \end{bmatrix} = \begin{bmatrix} 0 & I_q G_{pll} \\ 0 & -I_d G_{pll} \end{bmatrix} \begin{bmatrix} \Delta v_d \\ \Delta v_q \end{bmatrix} + \begin{bmatrix} \Delta i_d \\ \Delta i_q \end{bmatrix} \tag{4.30}$$

where I_d and I_q are the d-axis and q-axis currents, respectively.

The voltage reference value in system dq frame can be obtained as

$$\begin{bmatrix} \Delta v_{cond} \\ \Delta v_{conq} \end{bmatrix} = \begin{bmatrix} \Delta v_{cond}^c - \Delta\theta V_{conq}^c \\ \Delta v_{conq}^c + \Delta\theta V_{cond}^c \end{bmatrix} = \begin{bmatrix} \Delta v_{cond}^c \\ \Delta v_{conq}^c \end{bmatrix} + \begin{bmatrix} 0 & -V_{conq} G_{pll} \\ 0 & V_{cond} G_{pll} \end{bmatrix} \begin{bmatrix} \Delta v_d \\ \Delta v_q \end{bmatrix} \tag{4.31}$$

where V_{cond} and V_{conq} are the output d-axis and q-axis voltage of the current control loop, respectively.

To derive a simplified matrix form, we can define the following matrices: $A = \begin{bmatrix} 1 & V_q G_{pll} \\ 0 & 1 - V_d G_{pll} \end{bmatrix}$, $B = \begin{bmatrix} 0 & I_q G_{pll} \\ 0 & -I_d G_{pll} \end{bmatrix}$, $C = \begin{bmatrix} G_{iPI} & 0 \\ 0 & G_{iPI} \end{bmatrix}$, $D = \begin{bmatrix} 0 & -\omega_0 L_m \\ \omega_0 L_m & 0 \end{bmatrix}$, and $E = \begin{bmatrix} 0 & -V_{conq} G_{pll} \\ 0 & V_{cond} G_{pll} \end{bmatrix}$.

The inner current controller for small-signal perturbation can be depicted using the blocks shown in Figure 4.4.

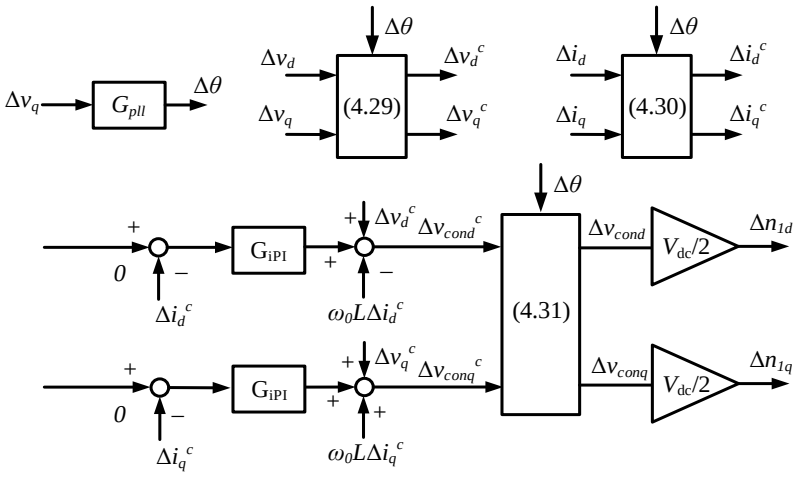

Figure 4.4 Block diagram of an inner current controller for small-signal perturbation

According to Figure 4.4, the perturbation relationship between the modulation ratio and voltage and current can be written as

$$\triangle\mathbf{n}_{dq} = \frac{2}{V_{dc}}(\mathbf{D}-\mathbf{C})\triangle\mathbf{i}_{\mathbf{dq}} + \frac{2}{V_{dc}}(\mathbf{DB}+\mathbf{E}+\mathbf{A}-\mathbf{CB})\triangle\mathbf{v}_{dq} \tag{4.32}$$

Thus, in dq frame, the transfer functions between the perturbations of the modulation ratio and the current and voltage can be expressed respectively as

$$\mathbf{G}_{idq} = \frac{2}{V_{dc}}(\mathbf{D}-\mathbf{C}) \tag{4.33}$$

$$\mathbf{G}_{vdq} = \frac{2}{V_{dc}}(\mathbf{DB}+\mathbf{E}+\mathbf{A}-\mathbf{CB}) \tag{4.34}$$

The controller transfer functions in dq frame can generally be expressed as

$$\mathbf{G}_{idq}(s) = \begin{bmatrix} G_{idd}(s) & G_{idq}(s) \\ G_{iqd}(s) & G_{iqq}(s) \end{bmatrix} \tag{4.35}$$

$$\mathbf{G}_{vdq}(s)=\begin{bmatrix} G_{vdd}(s) & G_{vdq}(s) \\ G_{vqd}(s) & G_{vqq}(s) \end{bmatrix} \tag{4.36}$$

Since $\mathbf{G}_{idq}$ and $\mathbf{G}_{vdq}$ are matrices in dq frame, they need be transformed into pn frame using (4.37).

$$\begin{cases} G_{iPP}(s)=\dfrac{1}{2}\left[G_{idd}(s-j\omega_0)+G_{iqq}(s-j\omega_0)-jG_{idq}(s-j\omega_0)+G_{iqd}(s-j\omega_0)\right] \\ G_{iPN}(s)=\dfrac{1}{2}\left[G_{idd}(s+j\omega_0)-G_{iqq}(s+j\omega_0)+jG_{idq}(s+j\omega_0)+G_{iqd}(s+j\omega_0)\right] \\ G_{iNP}(s)=\dfrac{1}{2}\left[G_{idd}(s-j\omega_0)-G_{iqq}(s-j\omega_0)-jG_{idq}(s-j\omega_0)-G_{iqd}(s-j\omega_0)\right] \\ G_{iNN}(s)=\dfrac{1}{2}\left[G_{idd}(s+j\omega_0)+G_{iqq}(s+j\omega_0)+jG_{idq}(s+j\omega_0)-G_{iqd}(s+j\omega_0)\right] \end{cases} \tag{4.37}$$

After transformation, the controller transfer functions in pn frame are depicted as

$$\begin{bmatrix} \triangle n_{iP}(s) \\ \triangle n_{iN}(s) \\ \triangle n_{i0}(s) \end{bmatrix}=\begin{bmatrix} G_{iPP}(s) & G_{iPN}(s) & 0 \\ G_{iNP}(s) & G_{iNN}(s) & 0 \\ 0 & 0 & 0 \end{bmatrix}\begin{bmatrix} \triangle i_P(s) \\ \triangle i_N(s) \\ \triangle i_0(s) \end{bmatrix} \tag{4.38}$$

$$\begin{bmatrix} \triangle n_{vP}(s) \\ \triangle n_{vN}(s) \\ \triangle n_{v0}(s) \end{bmatrix}=\begin{bmatrix} G_{vPP}(s) & G_{vPN}(s) & 0 \\ G_{vNP}(s) & G_{vNN}(s) & 0 \\ 0 & 0 & 0 \end{bmatrix}\begin{bmatrix} \triangle v_P(s) \\ \triangle v_N(s) \\ \triangle v_0(s) \end{bmatrix} \tag{4.39}$$

The coupling relation generated by the controller at different frequency in pn frame has been studied in Chapter 2, and specifically:

- $G_{iPP}(s)$ in the current transfer function $\mathbf{G}_{iPN0}(s)$ indicates that the positive-sequence current $\triangle i_p(s)$ at frequency f_p produces the positive-sequence control signal $\triangle n_{iP}(s)$ at the same frequency f_p;
- $G_{iNP}(s)$ indicates that the positive-sequence current $\triangle i_p(s)$ generates the negative-sequence $\triangle n_{iN}(s\text{-}2j\omega_0)$ at frequency $f_p\text{-}2\omega_0$;

- $G_{iPN}(s)$ indicates that the negative-sequence current $\Delta i_N(s)$ at frequency f_p generates the positive-sequence $\Delta n_{iP}(s+2j\omega_0)$ at frequency $f_p+2\omega_0$;
- $G_{iNN}(s)$ indicates that the negative-sequence current $\Delta i_N(s)$ at frequency f_p produces the negative-sequence control signal $\Delta n_{iN}(s)$ at the same frequency.

As describe above, the input $\Delta i_p(s)$ generates two control signals $\Delta n_{iP}(s)$ and $\Delta n_{iN}(s-2j\omega_0)$. These two signals are represented by the same symbol $\Delta n_{iP}(s)$ in (4.38) by ignoring the frequency shift. However, when the transfer function of controller is introduced into the HSS model, the relationship between each input and output needs to be expressed clearly and accurately. Therefore, the control signals $\Delta n_{iP}(s)$ and $\Delta n_{iN}(s-2j\omega_0)$ created by $\Delta i_p(s)$ need to be separated. The same procedure is carried out for $\Delta n_{iN}(s)$ and $\Delta n_{iP}(s+2j\omega_0)$ created by $\Delta i_N(s)$. For accurate expression, (4.38) is rewritten as:

$$\begin{bmatrix} \Delta\mathbf{n}_{iPN0}(s-j2\omega_0) \\ \Delta\mathbf{n}_{iPN0}(s-j\omega_0) \\ \Delta\mathbf{n}_{iPN0}(s) \\ \Delta\mathbf{n}_{iPN0}(s+j\omega_0) \\ \Delta\mathbf{n}_{iPN0}(s+j2\omega_0) \end{bmatrix} = \begin{bmatrix} \mathbf{GNP}_{iPN0}(s) \\ \mathbf{0} \\ \mathbf{G}_{iPN0}(s) \\ \mathbf{0} \\ \mathbf{GPN}_{iPN0}(s) \end{bmatrix} \left[\Delta\mathbf{i}_{iPN0}(s)\right] \tag{4.40}$$

where $\mathbf{G}_{iPN0}(s) = \begin{bmatrix} G_{iPP}(s) & 0 & 0 \\ 0 & G_{iNN}(s) & 0 \\ 0 & 0 & 0 \end{bmatrix}$, $\mathbf{GNP}_{iPN0}(s) = \begin{bmatrix} 0 & 0 & 0 \\ G_{iPN0}(s) & 0 & 0 \\ 0 & 0 & 0 \end{bmatrix}$,

$\mathbf{GPN}_{iPN0}(s) = \begin{bmatrix} 0 & G_{iPN0}(s) & 0 \\ 0 & 0 & 0 \\ 0 & 0 & 0 \end{bmatrix}$, $\Delta\mathbf{n}_{iPN0}(s) = \begin{bmatrix} \Delta n_{iP}(s) \\ \Delta n_{iN}(s) \\ \Delta n_{i0}(s) \end{bmatrix}$, $\Delta\mathbf{i}_{iPN0}(s) = \begin{bmatrix} \Delta i_P(s) \\ \Delta i_N(s) \\ \Delta i_0(s) \end{bmatrix}$

$\Delta\mathbf{n}_{iPN0}(s\pm j\omega_0) = \begin{bmatrix} \Delta n_{iP}(s\pm j\omega_0) \\ \Delta n_{iN}(s\pm j\omega_0) \\ \Delta n_{i0}(s\pm j\omega_0) \end{bmatrix}$, $\Delta\mathbf{n}_{iPN0}(s\pm j2\omega_0) = \begin{bmatrix} \Delta n_{iP}(s\pm j2\omega_0) \\ \Delta n_{iN}(s\pm j2\omega_0) \\ \Delta n_{i0}(s\pm j2\omega_0) \end{bmatrix}$.

Combining $\mathbf{G}_{ccPN0}(s)$ derived in Section 4.4.1 with $\mathbf{G}_{iPN0}(s)$ yields the transfer

function $\mathbf{G}_A(s)$ for the modulation ratio of the upper and lower arms in (4.16) as

$$\begin{bmatrix} \triangle\mathbf{n}_{uPN0}(s) \\ \triangle\mathbf{n}_{lPN0}(s) \end{bmatrix} = \mathbf{G}_A(s) \begin{bmatrix} \triangle\mathbf{i}_{cPN0}(s) \\ \triangle\mathbf{i}_{gPN0}(s) \\ \triangle\mathbf{v}^{\Sigma}_{cuPN0}(s) \\ \triangle\mathbf{v}^{\Sigma}_{clPN0}(s) \end{bmatrix} \tag{4.41}$$

where $\mathbf{G}_A(s) = \begin{bmatrix} -\mathbf{G}_{ccPN0}(s) & -\mathbf{G}_{iPN0}(s) & \mathbf{0} & \mathbf{0} \\ -\mathbf{G}_{ccPN0}(s) & \mathbf{G}_{iPN0}(s) & \mathbf{0} & \mathbf{0} \end{bmatrix}$.

The modulation ratio of the upper and lower arms brought by the coupling shown in (4.40) can be expressed as

$$\begin{bmatrix} \triangle\mathbf{n}_{uPN0}(s - j2\omega_0) \\ \triangle\mathbf{n}_{lPN0}(s - j2\omega_0) \end{bmatrix} = \mathbf{GNP}_A(s) \begin{bmatrix} \triangle\mathbf{i}_{cPN0}(s) \\ \triangle\mathbf{i}_{gPN0}(s) \\ \triangle\mathbf{v}^{\Sigma}_{cuPN0}(s) \\ \triangle\mathbf{v}^{\Sigma}_{clPN0}(s) \end{bmatrix} \tag{4.42}$$

$$\begin{bmatrix} \triangle\mathbf{n}_{uPN0}(s + j2\omega_0) \\ \triangle\mathbf{n}_{lPN0}(s + j2\omega_0) \end{bmatrix} = \mathbf{GPN}_A(s) \begin{bmatrix} \triangle\mathbf{i}_{cPN0}(s) \\ \triangle\mathbf{i}_{gPN0}(s) \\ \triangle\mathbf{v}^{\Sigma}_{cuPN0}(s) \\ \triangle\mathbf{v}^{\Sigma}_{clPN0}(s) \end{bmatrix} \tag{4.43}$$

where

$$\mathbf{GNP}_{\mathrm{A}}(s) = \begin{bmatrix} \mathbf{0} & -\mathbf{GNP}_{iPN0}(s) & \mathbf{0} & \mathbf{0} \\ \mathbf{0} & \mathbf{GNP}_{iPN0}(s) & \mathbf{0} & \mathbf{0} \end{bmatrix}, \quad \mathbf{GPN}_{\mathrm{A}}(s) = \begin{bmatrix} \mathbf{0} & -\mathbf{GPN}_{iPN0}(s) & \mathbf{0} & \mathbf{0} \\ \mathbf{0} & \mathbf{GPN}_{iPN0}(s) & \mathbf{0} & \mathbf{0} \end{bmatrix}.$$

Considering other harmonic inputs, matrix $\mathbf{HG}_A$ in the Appendix is modified as

$$\mathbf{HG_A}=\begin{bmatrix} \ddots & \vdots & \vdots & \vdots & \vdots & \vdots & \iddots \\ \cdots & \mathbf{G_A}(s-j2\omega_0) & \mathbf{0} & \mathbf{GNP_A}(s) & \mathbf{0} & \mathbf{0} & \cdots \\ \cdots & \mathbf{0} & \mathbf{G_A}(s-j\omega_0) & \mathbf{0} & \mathbf{GNP_A}(s+j\omega_0) & \mathbf{0} & \cdots \\ \cdots & \mathbf{GPN_A}(s-j2\omega_0) & \mathbf{0} & \mathbf{G_A}(s) & \mathbf{0} & \mathbf{GNP_A}(s+j2\omega_0) & \cdots \\ \cdots & 0 & \mathbf{GPN_A}(s-j\omega_0) & \mathbf{0} & \mathbf{G_A}(s+j\omega_0) & \mathbf{0} & \cdots \\ \cdots & 0 & \mathbf{0} & \mathbf{GPN_A}(s) & \mathbf{0} & \mathbf{G_A}(s+j2\omega_0) & \cdots \\ \iddots & \vdots & \vdots & \vdots & \vdots & \vdots & \ddots \end{bmatrix} \quad (4.48)$$

The matrix $\mathbf{HG}_B$ can also be derived following the above procedure.

$$\mathbf{HG_B}=\begin{bmatrix} \ddots & \vdots & \vdots & \vdots & \vdots & \vdots & \iddots \\ \cdots & \mathbf{G_B}(s-j2\omega_0) & \mathbf{0} & \mathbf{GNP_B}(s) & \mathbf{0} & \mathbf{0} & \cdots \\ \cdots & \mathbf{0} & \mathbf{G_B}(s-j\omega_0) & \mathbf{0} & \mathbf{GNP_B}(s+j\omega_0) & \mathbf{0} & \cdots \\ \cdots & \mathbf{GPN_B}(s-j2\omega_0) & \mathbf{0} & \mathbf{G_B}(s) & \mathbf{0} & \mathbf{GNP_B}(s+j2\omega_0) & \cdots \\ \cdots & 0 & \mathbf{GPN_B}(s-j\omega_0) & \mathbf{0} & \mathbf{G_B}(s+j\omega_0) & \mathbf{0} & \cdots \\ \cdots & 0 & \mathbf{0} & \mathbf{GPN_B}(s) & \mathbf{0} & \mathbf{G_B}(s+j2\omega_0) & \cdots \\ \iddots & \vdots & \vdots & \vdots & \vdots & \vdots & \ddots \end{bmatrix} \quad (4.49)$$

where

$$\mathbf{G}_B(s)=\begin{bmatrix} -\mathbf{G}_{vPN0}(s) \\ \mathbf{G}_{vPN0}(s) \end{bmatrix}, \mathbf{GNP_B}(s)=\begin{bmatrix} -\mathbf{GNP}_{vPN0}(s) \\ \mathbf{GNP}_{vPN0}(s) \end{bmatrix}, \mathbf{GPN_B}(s)=\begin{bmatrix} -\mathbf{GPN}_{vPN0}(s) \\ \mathbf{GPN}_{vPN0}(s) \end{bmatrix}$$

$$\mathbf{G}_{vPN0}(s)=\begin{bmatrix} G_{vPP}(s) & 0 & 0 \\ 0 & G_{vNN}(s) & 0 \\ 0 & 0 & 0 \end{bmatrix}, \quad \mathbf{GNP}_{vPN0}(s)=\begin{bmatrix} 0 & 0 & 0 \\ G_{vPN0}(s) & 0 & 0 \\ 0 & 0 & 0 \end{bmatrix},$$

$$\mathbf{GPN}_{vPN0}(s)=\begin{bmatrix} 0 & G_{vPN0}(s) & 0 \\ 0 & 0 & 0 \\ 0 & 0 & 0 \end{bmatrix}.$$

4.4.3 Outer-loop controller

The outer-loop controller is designed to set the current reference i_{dref} and i_{qref} for the inner-loop current controller. Two outer-loop control schemes, i.e., PV control with active power and AC voltage control, and PQ control with active and reactive power control, are shown in Figure 4.5.

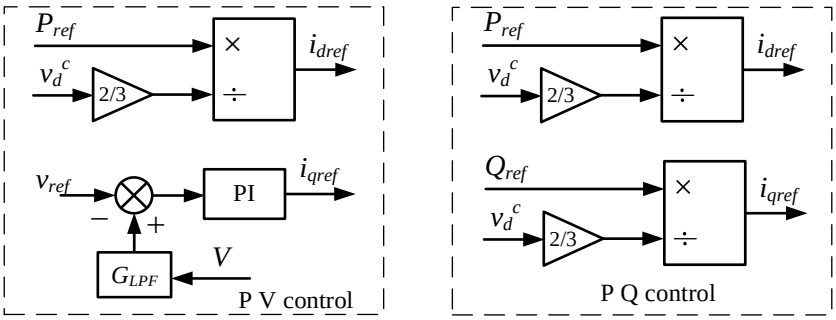

Figure 4.5 Outer-loop: PV and PQ control

When the outer-loop adopts the PV control , V is the terminal voltage magnitiude of MMC expressed as

$$V = \sqrt{v_d^{c2} + v_q^{c2}} \tag{4.44}$$

Linearizing (4.44) yields

$$\Delta v = \frac{V_d \Delta v_d^c + V_q \Delta v_q^c}{\sqrt{V_d{}^2 + V_q{}^2}} \tag{4.45}$$

The q-axis current perturbation can be depicted as

$$\Delta i_{qref} = G_{LPF} G_{vPI} \frac{V_d \Delta v_d^c + V_q \Delta v_q^c}{\sqrt{V_d{}^2 + V_q{}^2}} \tag{4.46}$$

where G_{LPF} is the transfer funtion of the low pass filter in the AC voltage measurement and G_{vPI} denotes the transfer funtion for the voltage -loop PI controller, as

$$G_{LPF} = \frac{1}{sT+1}, \qquad G_{vPI} = K_{vp} + \frac{K_{vi}}{s} \tag{4.47}$$

where T is the time constant of the low pass filter [116], K_{vp} and K_{vi} are the proportional and integral coefficients of the AC voltage control loop.

For the active power control, the current reference can be obtained as

$$i_{dref} = \frac{2P_{ref}}{3v_d^c} \tag{4.48}$$

After linearization, there is

$$\Delta i_{dref} = -\frac{2P_{ref}}{3V_d^2}\Delta v_d^c \tag{4.49}$$

Rewriting (4.46) and (4.49) in the matrix form yields

$$\begin{bmatrix} \Delta i_{dref} \\ \Delta i_{qref} \end{bmatrix} = \begin{bmatrix} 1 & 0 \\ 0 & G_{LPF}G_{vPI} \end{bmatrix} \begin{bmatrix} -2P_{ref}/3V_d^2 & 0 \\ V_d/\sqrt{V_d^2+V_q^2} & V_q/\sqrt{V_d^2+V_q^2} \end{bmatrix} \begin{bmatrix} \Delta v_d^c \\ \Delta v_q^c \end{bmatrix} \tag{4.50}$$

Defining $\mathbf{X} = \begin{bmatrix} 1 & 0 \\ 0 & G_{LPF}G_{vPI} \end{bmatrix}$ and $\mathbf{Z} = \begin{bmatrix} -2P_{ref}/3V_d^2 & 0 \\ V_d & V_q \end{bmatrix}$, and according to the current inner-loop control in Section 4.4.2, there is

$$\begin{aligned} \mathbf{G}_{idq} &= \frac{2}{V_{dc}}(\mathbf{D}-\mathbf{C}) \\ \mathbf{G}_{vdq} &= \frac{2}{V_{dc}}(\mathbf{DB}+\mathbf{E}+\mathbf{A}-\mathbf{CB}+\mathbf{CXZA}) \end{aligned} \tag{4.51}$$

When the outer-loop adopts the PQ control, the q-axis current reference derived from the reactive power is

$$i_{qref} = \frac{2Q_{ref}}{3v_d^c} \tag{4.52}$$

After linearizing (4.52), there is

$$\Delta i_{qref} = -\frac{2Q_{ref}}{3V_d^2}\Delta v_d^c \tag{4.53}$$

Combining (4.53) with the active power linearization in (4.49) yields

$$\begin{bmatrix}\Delta i_{dref}\\ \Delta i_{qref}\end{bmatrix} = \begin{bmatrix}-2P_{ref}/3V_d^2 & 0\\ -2Q_{ref}/3V_d^2 & 0\end{bmatrix}\begin{bmatrix}\Delta v_{cd}\\ \Delta v_{cq}\end{bmatrix} \tag{4.54}$$

Define $\mathbf{Y} = \begin{bmatrix}-2P_{ref}/3V_d^2 & 0\\ -2Q_{ref}/3V_d^2 & 0\end{bmatrix}$ and the transfer function of controller under PQ control can be expressed as

$$\begin{aligned}\mathbf{G}_{\text{idq}} &= \frac{2}{\text{V}_{\text{dc}}}(\mathbf{D}-\mathbf{C})\\ \mathbf{G}_{\text{vdq}} &= \frac{2}{\text{V}_{\text{dc}}}(\mathbf{DB}+\mathbf{E}+\mathbf{A}-\mathbf{CB}+\mathbf{CYA})\end{aligned} \tag{4.55}$$

After obtaining $\mathbf{G}_{idq}$ and $\mathbf{G}_{vdq}$, the same procedure in Section 4.4.2 can be applied to determine $\mathbf{HG}_{\mathbf{A}}$ and $\mathbf{HG}_{\mathbf{B}}$.

4.5 Small-signal admittance of MMC in pn frame

The solution of (4.17) can be calculated as

$$\begin{aligned}\Delta\mathbf{X}_{PN0} &= (s\mathbf{I}-\Gamma[\mathbf{A}_s]-\Gamma[\mathbf{M}]\cdot\mathbf{HG}_A+\mathbf{Q})^{-1}\cdot\left(\Gamma[\mathbf{B}]+\Gamma[\mathbf{M}]\cdot\mathbf{HG}_B\right)\cdot\Delta\mathbf{V}_{pPN0}\\ &= \mathbf{H}_{\text{hss}}\cdot\Delta\mathbf{V}_{pPN0}\end{aligned} \tag{4.56}$$

where the matrix $\mathbf{H}_{\text{hss}}$ reflects the relationship between the input variable $\Delta\mathbf{V}_{pPN0}$ and state variables $\Delta\mathbf{X}_{PN0}$.

The admittance matrix of MMC is calculated as

$$\mathbf{Y}_{MMC} = \frac{\triangle \mathbf{i}_{gPN}}{\triangle \mathbf{v}_{pPN}} \tag{4.57}$$

In pn frame, the current perturbation matrix $\triangle \mathbf{i}_{gPN}$ at the MMC AC terminal is part of the state variable matrix $\triangle \mathbf{X}_{PN0}$, whereas $\triangle \mathbf{v}_{pPN}$ is part of the input matrix $\triangle \mathbf{V}_{pPN0}$. Consequently, the small-signal admaittance matrix $\mathbf{Y}_{\mathrm{MMC}}$ can be extracted from the matrix $\mathbf{H}_{\mathrm{hss}}$.

As for the MMC, the *h*th harmonics in the upper and lower arms of any phase have the same magnitude and phase (called a common mode (CM) harmonic) if *h* is an even number, and the same magnitude but 180° phase difference (called a differential-mode (DM) harmonic) if *h* is an odd number [117]. Thus, the CM components circulate in the arms while the DM components ouput to the MMC AC terminals. If a positive-sequence perturbation $\triangle \mathbf{v}_{pabc}$ at ω_p is injected into the MMC AC terminal, the upper and lower arm equivalent capacitors $\mathrm{C_m}$ will have positive-sequence response voltage $\triangle \mathbf{v}_{cuabc}^{\Sigma}$ and $\triangle \mathbf{v}_{clabc}^{\Sigma}$ at ω_p, respectively. Because the upper and lower arms are symmetraical, the perturbation voltage $\triangle \mathbf{v}_{cuabc}^{\Sigma}$ and $\triangle \mathbf{v}_{clabc}^{\Sigma}$ are DM components, i.e., the same magnitude but 180° phase difference. Taking the positive-sequence capactior voltage perturbations $\triangle \mathbf{v}_{cuabc}^{\Sigma}$ and $\triangle \mathbf{v}_{clabc}^{\Sigma}$ for the upper and lower arms as an example, they can be expressed as

$$\triangle \mathbf{v}_{cuabc}^{\Sigma} = -\triangle \mathbf{v}_{clabc}^{\Sigma} = \begin{bmatrix} \triangle m_c \cos(\omega_p t + \triangle \theta_c) \\ \triangle m_c \cos(\omega_p t + \triangle \theta_c - 2\pi/3) \\ \triangle m_c \cos(\omega_p t + \triangle \theta_c + 2\pi/3) \end{bmatrix} \tag{4.58}$$

where $\triangle m_c$ and $\triangle \theta_c$ are the magnitude and phase angle of the perturbation voltage, respectively.

The steady-state values of the modulation ratio for the upper and lower arms are

$\mathbf{N}_{uabc}$ and $\mathbf{N}_{labc}$, including only the DC, fundamental and double-frequency components. Considering the DC components of $\mathbf{N}_{uabc}$ and $\mathbf{N}_{labc}$, both $\Delta\mathbf{v}_{cuabc}^{\Sigma}\mathbf{N}_{uabc0}$ and $\Delta\mathbf{v}_{clabc}^{\Sigma}\mathbf{N}_{labc0}$ are positive-sequence variables with the same frequency ω_p but opposite sign, resulting in positive-sequence voltage at ω_p generated at the MMC terminal. Consequently, positve-sequence current at ω_p is generated at the MMC AC terminal.

Consider that the fundamental frequency component of the upper and lower arm modulation ratio are DM components, i.e., $\mathbf{N}_{uabc1}$=-$\mathbf{N}_{labc1}$. Thus, $\mathbf{N}_{uabc1}\Delta\mathbf{v}_{cuabc}^{\Sigma}$ equals $\mathbf{N}_{labc1}\Delta\mathbf{v}_{clabc}^{\Sigma}$, and the two appear as MMC internal CM components. Thus, no current or voltage response at the MMC AC terminal will be observed.

For the double-frequency component $\mathbf{N}_{uabc2}$ and $\mathbf{N}_{labc2}$, they are CM components and identical, as

$$\begin{aligned}&\mathbf{N}_{uabc2}=\mathbf{N}_{labc2}\\&=\begin{bmatrix}N_2\cos(2\omega_0 t+\theta_2) & & \\ & N_2\cos(2\omega_0 t+\theta_2+2\pi/3) & \\ & & N_2\cos(2\omega_0 t+\theta_2-2\pi/3)\end{bmatrix}\end{aligned} \tag{4.59}$$

The product of the perturbation arm capacitor voltage $\Delta\mathbf{v}_{cuabc}^{\Sigma}$ and $\mathbf{N}_{uabc2}$ is

$$\begin{aligned}&\mathbf{N}_{uabc2}\Delta\mathbf{v}_{cuabc}^{\Sigma}=-\mathbf{N}_{labc2}\Delta\mathbf{v}_{clabc}^{\Sigma}\\&=\frac{\Delta m_c N_2}{2}\begin{bmatrix}\cos[(\omega_p+2\omega_0)t+(\Delta\theta_c+\theta_2)]+\cos[(\omega_p-2\omega_0)t+(\Delta\theta_c-\theta_2)]\\ \cos[(\omega_p+2\omega_0)t+(\Delta\theta_c+\theta_2)]+\cos[(\omega_p-2\omega_0)t+(\Delta\theta_c-\theta_2)+2\pi/3]\\ \cos[(\omega_p+2\omega_0)t+(\Delta\theta_c+\theta_2)]+\cos[(\omega_p-2\omega_0)t+(\Delta\theta_c-\theta_2)-2\pi/3]\end{bmatrix}\end{aligned} \tag{4.60}$$

According to (4.60), the interaction between the two yields the zero-sequence voltage at ω_p+$2\omega_0$ with opposite direction for the upper and lower arms. For a three-wire system with no zero-sequence current path, such zero-sequence voltage only exists in the internal MMC, and thus, there is no zero-sequence current or voltage at

ω_p+2ω_0 on the MMC AC terminal. However, the generated negative-sequence voltages at ω_p-2ω_0 for the upper and lower arms are DM component, and hence, will appear at the MMC AC terminal together with the corresponding current.

Generally, the interaction of CM and DM results in DM components which appear on the AC terminal side. Consequently, for non-even order harmonics, the interaction will not generate AC response. Similarly to h=2, with h=4, there exists only ω_p+4ω_0 at the MMC terminal but can be neglected due to its very small magnitude. Whereas for h>4, the hth harmonics in the MMC are all very small and the response at $\omega_p \pm h\omega_0$ can be ignored.

Therefore, based on the above observation, the specific form of the small-signal admittance $\mathbf{Y_{MMC}}$ at the MMC terminal can be simplified as a 2 by 2 matrix expressed as

$$\begin{bmatrix} \triangle i_{gP}(s) \\ \triangle i_{gN}(s-j2\omega_0) \end{bmatrix} = \begin{bmatrix} Y_{PP}(s) & Y_{PN}(s) \\ Y_{NP}(s-j2\omega_0) & Y_{NN}(s-j2\omega_0) \end{bmatrix} \begin{bmatrix} \triangle v_{pP}(s) \\ \triangle v_{pN}(s-j2\omega_0) \end{bmatrix} \tag{4.61}$$

where $Y_{PP}(s)$, $Y_{PN}(s)$, $Y_{NP}(s\text{-}j2\omega_0)$, and $Y_{NN}(s\text{-}j2\omega_0)$ are the four elements extracting from the matrix $\mathbf{H_{hss}}$. When $s=j\omega_p$, the followings can be observed from (4.63):

- $Y_{PP}(s)$ denotes the relationship between the positive-sequence voltage perturbation $\Delta v_{pP}(s)$ at ω_p and the positive-sequence current response $\Delta i_{gP}(s)$ at ω_p;
- $Y_{NP}(s\text{-}j2\omega_0)$ denotes that the positive-sequence voltage $\Delta v_{pP}(s)$ at frequency ω_p leads to negative-sequence current $\Delta i_{gN}(s\text{-}j2\omega_0)$ at ω_p-2ω_0;
- $Y_{NN}(s\text{-}j2\omega_0)$ denotes the relationship between the negative-sequence voltage perturbation $\Delta v_{pN}(s\text{-}j2\omega_0)$ at ω_p-2ω_0 and negative-sequence current response $\Delta i_{gN}(s\text{-}j2\omega_0)$ at ω_p-2ω_0;
- $Y_{PN}(s)$ denotes that the voltage perturbation $\Delta v_{pN}(s\text{-}j2\omega_0)$ at frequency ω_p-2ω_0 leads to the positive-sequence current $\Delta i_{gP}(s)$ at frequency ω_p.

4.6 Small-signal admittance validation and analysis

In order to validate the HSS model developed in this work, a comparison between the impedance plots from the HSS model and the time-domain model has been carried out. The time-domain model is implemented in MATLAB/Simulink, and the HSS model as described in this section is implemented using an m.file in MATLAB. To ensure the small-signal admittance of MMC can be measured under various operating modes, a strong and stable external AC system is used. Thus, the grid-side resistance and inductance are set to R_L=1.02Ω and L_L=0.0324H, and the corresponding SCR is 12. The ac-side small-signal impedance of the MMC is measured by injecting a series of small perturbations Δv_{pa}, Δv_{pb}, Δv_{pc} with peak value of 3kV at the ac-side of the MMC at different frequencies, as shown in Figure 4.6. The ac-side current responses Δi_{ga}, Δi_{gb}, Δi_{gc} under each specific frequency is measured and the impedance under this frequency is calculated by applying (4.61). The main electrical parameters of the MMC system are listed in Table 4.1.

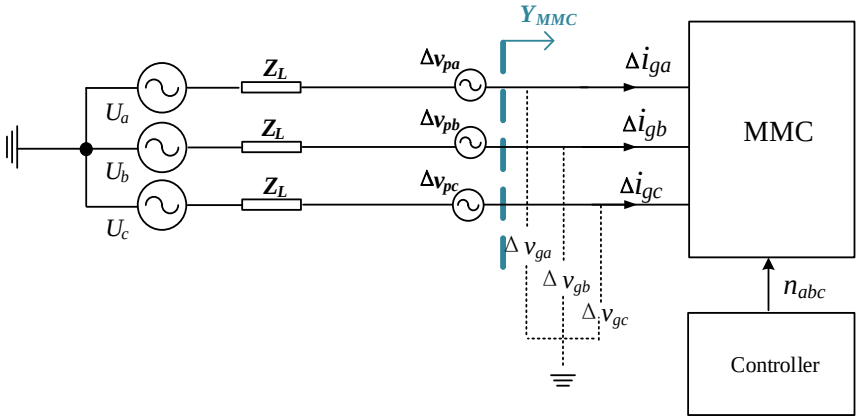

Figure 4.6 The ac-side small-signal impedance of the MMC

Table 4.1 Main electrical parameters of the MMC system

Parameters	Value
Rated active and reactive power (P, Q)	1000 MW, ±300 MVar
Nominal DC Voltage (V_{dc})	±320 kV
Rated AC voltage (L-L) (V_{nl})	360 kV
Arm resistance and inductance (R_m L_m)	0.08 Ω, 0.042 H
Cell capacitance (C_m)	31.4 μF
Nominal Frequency (f_0)	50 Hz
Transformer rated apparent power (St)	1265 MVA
Transformer voltage ratio (kt)	400/360 kV
Transformer leakage reactance Xt*	0.18 p.u.

4.6.1 Admittance validation for open-loop control

Initial tests in the time-domain model with the MMC under open-loop control is carried out. The three-phase modulation ratio for the upper arm under open-loop control is assigned as:

$$n_{ua}=0.5-0.46[\cos(\omega_0 t+0.07)]+0.01[\cos(2\omega_0 t+0.07)],$$

$$n_{ub}=0.5-0.46[\cos(\omega_0 t+0.07)-2pi/3]+0.01[\cos(2\omega_0 t+0.07)+2pi/3],$$

$$n_{uc}=0.5-0.46[\cos(\omega_0 t+0.07)+2pi/3]+0.01[\cos(2\omega_0 t+0.07)-2pi/3],$$

where the modulation ratio at fundamental frequency is the positive-sequence component, and the one at double frequency is the negative-sequence component. Voltage perturbations of 40Hz positive and negative-sequence are injected at the MMC AC terminal, separately. FFT analysis is conducted on the phase ‘a’ current and voltage

and selected spectra are shown in Figure 4.7 in which the 50Hz fundamental frequency components have been omitted for clarity.

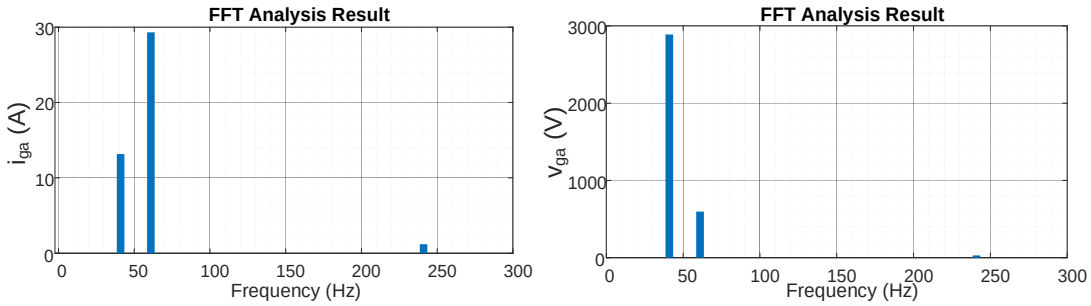

(a) With 40Hz positive-sequence voltage injection

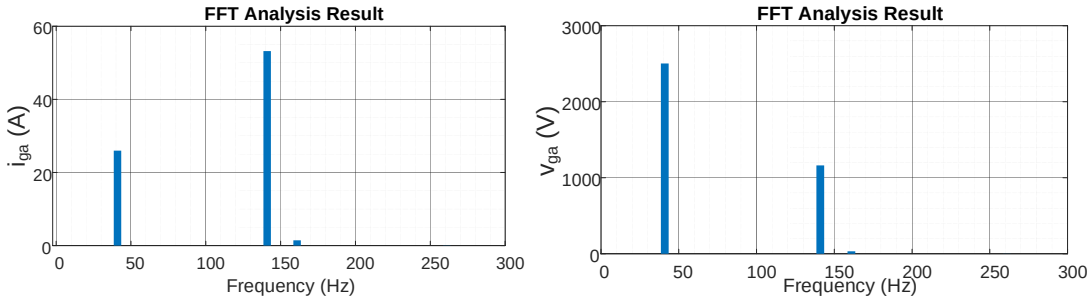

(b) With 40Hz negative-sequence voltage injection

Figure 4.7 FFT results with voltage perturbation

Table 4.2 Phase angles of the 3-phase voltage and current with 40Hz positive- and negative-sequence voltage injections (degree)

	Positive sequence 40Hz			Negative sequence 40Hz		
	40Hz	60Hz	240Hz	40Hz	140Hz	160Hz
Δv_{ga}	85.3	-63.5	71.9	93.6	80.7	241.1
Δv_{gb}	-34.7	176.5	191.9	213.6	-39.3	1.1
Δv_{gc}	205.3	56.5	-48.1	-26.4	200.7	121.1
Δi_{ga}	150.4	105.9	214.9	64.5	236.9	34.4

Δi_{gb}	30.4	-14.1	-25.1	184.5	116.9	154.4
Δi_{gc}	-89.6	225.9	94.9	-55.5	-3.1	-85.6

Figure 4.7 (a) shows that under 40Hz positive-sequence voltage perturbation, there are multiple frequency responses in the voltage and current at 40Hz, 60Hz and 240Hz.

Table 4.2 shows the phase angles for the voltage and current responses. It can be observed that:

- The voltage and current responses are positive-sequence at 40Hz and 60Hz, and negative-sequence at 240Hz.

- The resulted positive-sequence response at 60Hz can also be considered as negative-sequence at -60Hz, as -60Hz negative-sequence indicates 60Hz positive-sequence in time-domain [118].

- Thus, it can be concluded that the injected positive-sequence voltage perturbation at ω_p leads to a positive-sequence response at ω_p and negative-sequence responses at ω_p-2ω_0 and ω_p+4ω_0, though the negative-sequence response at ω_p+4ω_0 is very small.

For 40Hz negative-sequence voltage perturbation, Figure 4.7 (b) shows the voltage and current responses at 40Hz, 140Hz and 160Hz, in which the response at 160Hz is negligible.

Table 4.2 shows the corresponding voltage and current the phase angles. It can be observed that:

- The response is negative-sequence at 40Hz, positive-sequence at 140Hz, and negative-sequence at 160Hz.

- According to the analysis in Section 4.5, the negative-sequence input at ω_p causes the negative-sequence at ω_p (40Hz) and positive-sequence response at $\omega_p+2\omega_0$ (140Hz) and $\omega_p-4\omega_0$ (-160Hz).
- Positive-sequence -160Hz is deemed negative-sequence at 160Hz in time-domain.

The above simulation results verify the theoretical analysis in Section 4.5, and the small-signal model of MMC in pn frame is properly captured by the four admittance elements in (4.61).

Figure 4.8 compares the admittance elements $Y_{PP}(s)$, $Y_{PN}(s)$, $Y_{NP}(s-2j\omega_0)$, and $Y_{NN}(s-2j\omega_0)$ in matrix $\mathbf{Y_{MMC}}$ derived from the HSS model with different harmonic orders considered, and those obtained from the time-domain model. The MMC exports 1000 MW / 0 MVar to the AC grid and the AC terminal voltage is 1 p.u.. Comparing the different admittace curves, it is found that higher harmonic order considered in the analytical HSS model leads to more accurate model, and for h=4 the analytical admittances match well with those of the time-domain simulation models. It also implies that the internal harmonics of MMC has a significant impact on the AC side small-signal admittance, and need to be considered in the modelling.

In order to ensure the accuracy of the analytical model, h is set to 4 in the following analysis.

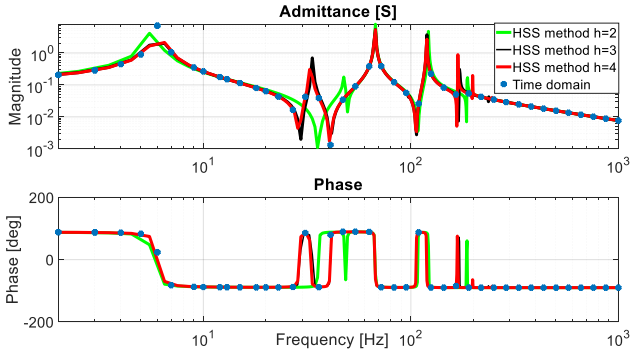

(a) $Y_{PP}(s)$

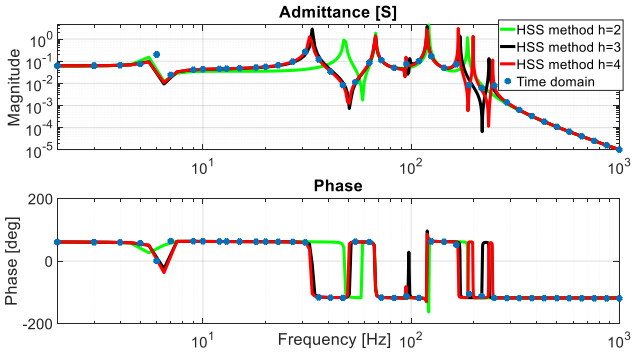

(b) $Y_{PN}(s)$

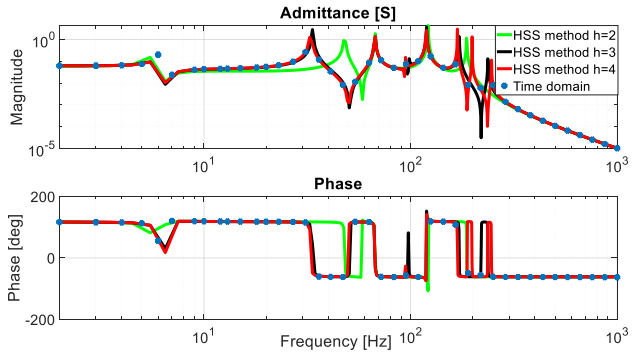

(c) $Y_{NP}(s\text{-}j2\omega_0)$

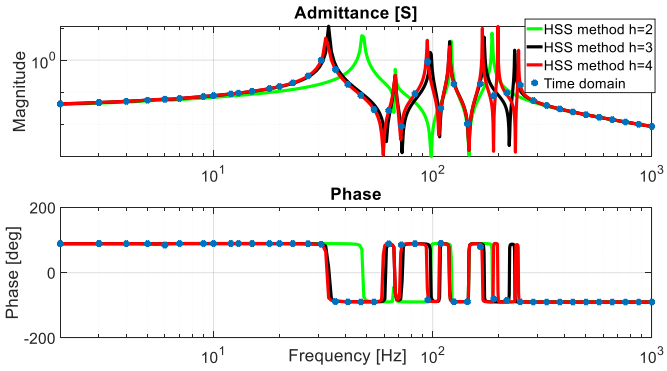

(d) $Y_{NN}(s\text{-}j2\omega_0)$

Figure 4.8 Validation of the admittance for the open loop control

4.6.2 Admittance validation with CCSC

In this case, the CCSC is imposed on the open loop control to analyze its influence. The DC and fundamental modulation ratio are assigned directly, and their magnitude and the phase are the same to those in Section 4.6.1. For the 2nd order harmonic modulation ratio, it is from the CCSC. Figure 4.9 compares the MMC admittances calculated from the HSS analytical model and measured from the time-domain model. As can be seen, the calculated and measured MMC admittances with the added CCSC match well.

Comparing the admittances in Figure 4.8 and Figure 4.9, it is seen that the resonant points are significantly reduced after adding the CCSC, which suppresses the internal 2nd harmonic current. Meanwhile, the 2nd harmonic voltage in the arm capacitors is also reduced. Consequently, the response at other frequencies resulting from the 2nd harmonic is considerably weaken and the resonant points of MMC impedance reduced. In addition, it can be observed that the CCSC reduces the magnitude of Y_{NP} and Y_{PN} around 50 Hz. This can be explained by considering that a perturbation at ω_p results in the generation of CM component at $\omega_p+\omega_0$ in the internal MMC. If ω_p is close to 50 Hz, the CM response is around 100 Hz, which is suppressed by the CCSC. Hence, the response at $\omega_p+\omega_0$ is low, and when it interacts with the steady-state component, the current responses at $\omega_p+2\omega_0$ and $\omega_p-2\omega_0$ at the AC terminal of MMC are thus further reduced and so as the admittance magnitude. Similarly, the CCSC reduces the positve-sequence admittance Y_{PP} and the negative-sequence admittance Y_{NN} at 0 Hz and 100 Hz, respectively, when compared to open loop MMC admittance shown in Figure 4.8.

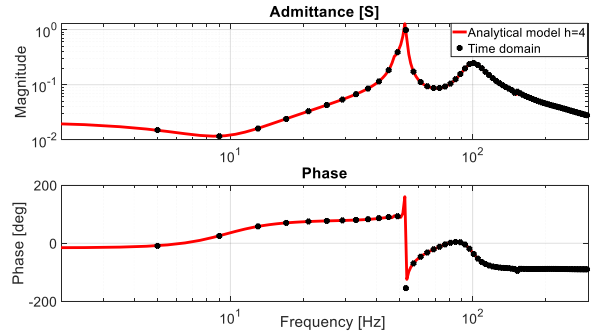

(a) $Y_{PP}(s)$

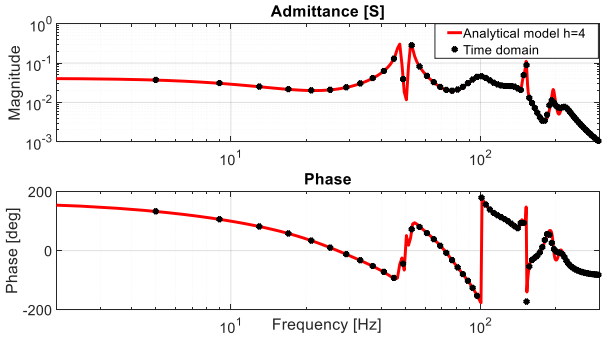

(b) $Y_{PN}(s)$

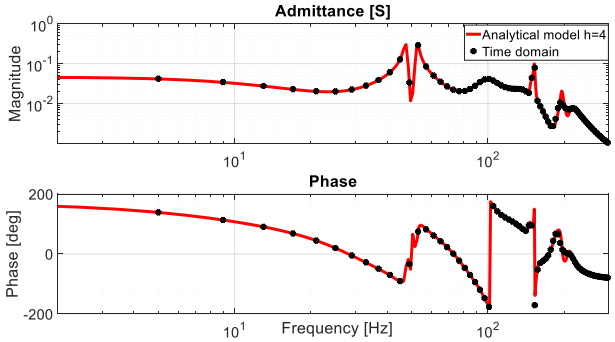

(c) $Y_{NP}(s\text{-}j2\omega_0)$

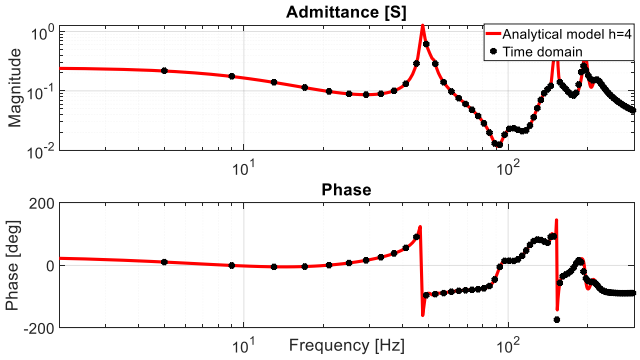

(d) $Y_{NN}(s\text{-}j2\omega_0)$

Figure 4.9 Admittance of MMC with CCSC

4.6.3 Admittance with the AC current loop

Assume the MMC operates in inverter mode and transfers active power from DC to AC. The active current assigned to the current loop is i_{dref}=2268 A (corresponding to 1 p.u. active power) and the reactive power current i_{qref}=0 A. The calculated and measured small-signal admittances of the MMC are compared in Figure 4.10.

It is shown in Figure 4.10 (a) and (b) that the phasor of Y_{PP} and Y_{NN} at 50 - 130 Hz is larger than 90°, indicating the existence of negative resistance effect and negative damping to the system. Thus, the system tends to be unstable in this frequency range. For frequencies above 130 Hz, the phases of the two admittances approach to 0, indicating strong positive damping. The existence of Y_{PN} and Y_{NP} with non-negligible magnitude indicates strong coupling between the positive- and negative-sequence components and therefore, for accurate stability analysis, they must be included and more details will be given in Chapter 5.

Assume the MMC operates in rectifier mode and transmit power from AC to the DC. The references for the current loop are i_{dref}=-2268 A and i_{qref}=0 A, respectively. The small-signal admittance of the MMC is shown in Figure 4.11. Comparing Figure 4.11 and Figure 4.10, it can be found that the magnitude of the correspondence admittances for inverter and rectifier operation are identical but the phasor is almost opposite. In Figure 4.11, the phases of Y_{PP} and Y_{NN} above 130 Hz range from 90° to 270° implying negative resistance effect and potentially leading to unstable system.

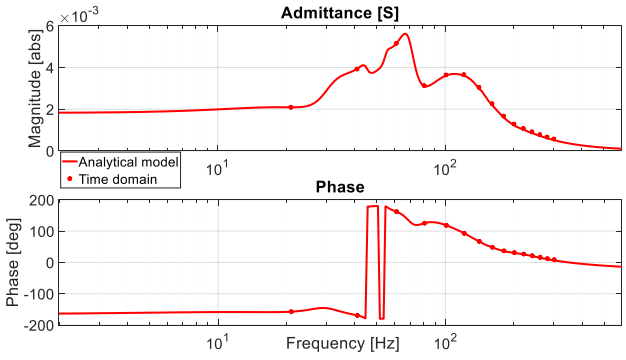

(a) $Y_{PP}(s)$

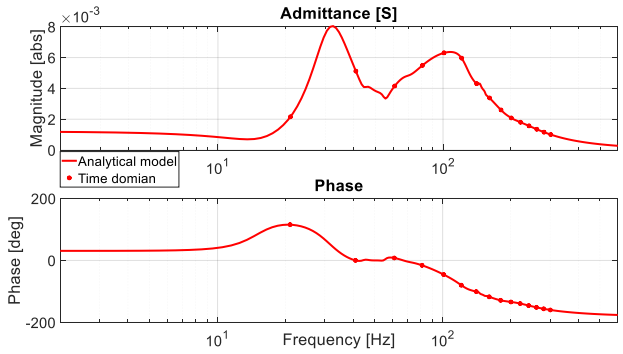

(b) $Y_{PN}(s)$

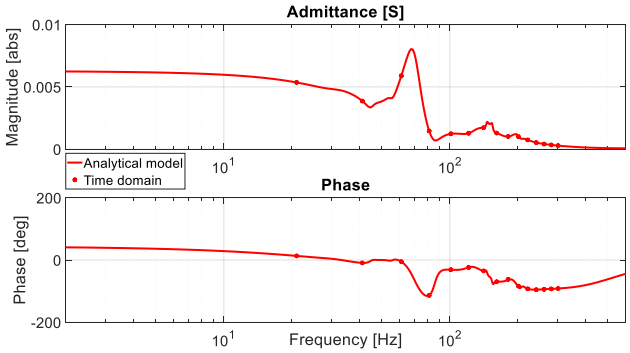

(c) $Y_{NP}(s\text{-}j2\omega_0)$

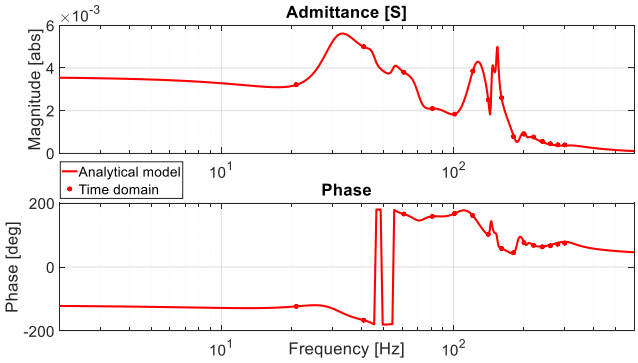

(d) $Y_{NN}(s\text{-}j2\omega_0)$

Figure 4.10 Admittance when the MMC operates in inverter mode.

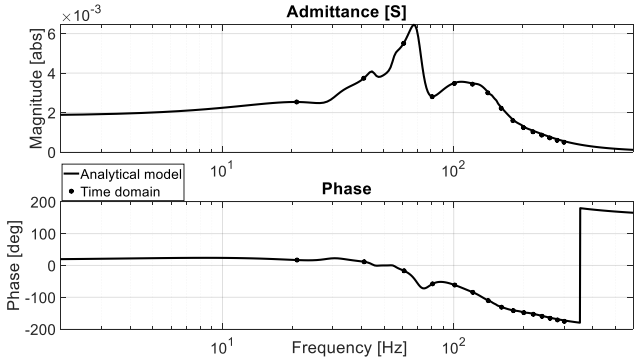

(a) $Y_{PP}(s)$

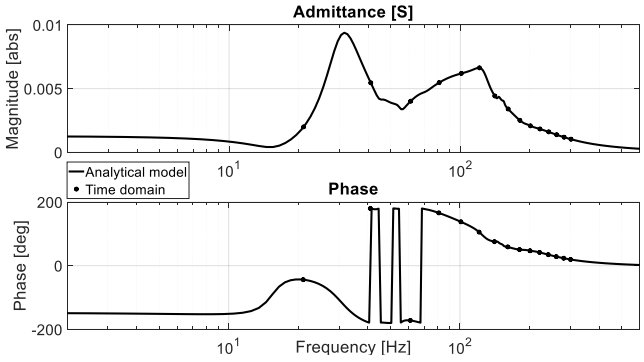

(b) $Y_{PN}(s)$

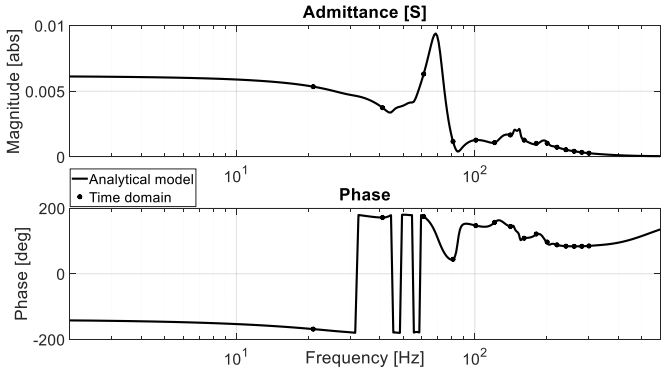

(c) $Y_{NP}(s\text{-}j2\omega_0)$

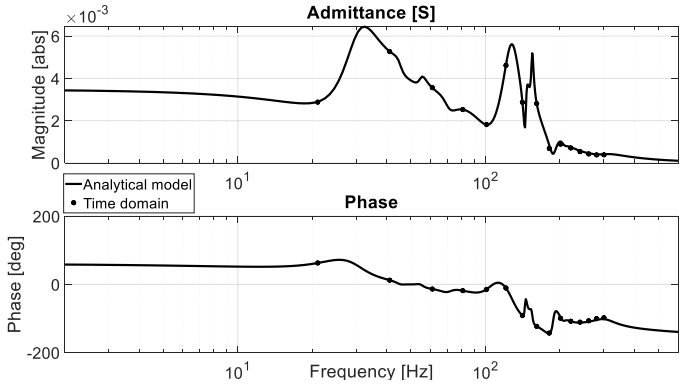

(d) $Y_{NN}(s\text{-}j2\omega_0)$

Figure 4.11 Admittance when the MMC operates in rectifier mode.

For both inverter and rectifier operation, the small-signal MMC model using the HSS method can accurately calculate the impedance of the MMC. Considering the positive- and negative-sequence impedance, the system is more likely to become unstable at lower frequency in inverter mode whereas at higher frequency in rectifier mode.

4.6.4 Admittance with the outer-loop

When the MMC operates in inverter mode and outputs 1GW active power, the small-signal admittances of the MMC with the PV and PQ outer-loop are compared in Figure 4.12.

It can be seen in Figure 4.12 that the admittance measured in the time-domain accords well with that derived from the HSS based MMC analytical model. In the case of PQ outer-loop control, the magnitude of Y_{PP} and Y_{NN} at 50 -100 Hz is smaller than those in PV control, which contributes to improved system stability. Moreover, the phase of Y_{PP} with PQ control is closer to zero than that with PV control indicating better damping. Under both controls, the phase of Y_{PP} and Y_{NN} among 90-270° implies the negative resistance effect and tends to oscillate. In this scenario, the PQ control is better that PV control. While the frequency is above 100 Hz, the admittance with the two controls is almost the same.

When the MMC operates in rectifier mode and absorbs 1 GW active power, the small-signal admittances of MMC with the PV and PQ outer-loop are compared in Figure 4.13.

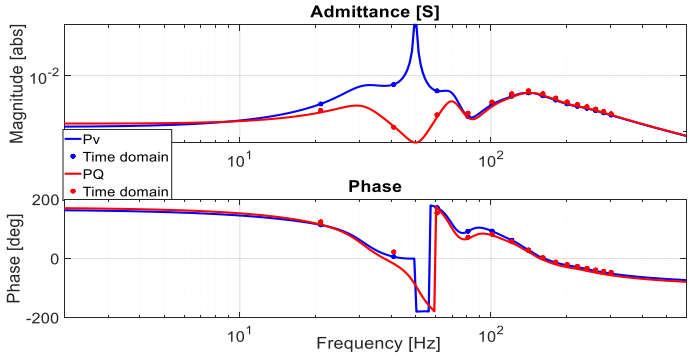

(a) $Y_{PP}(s)$

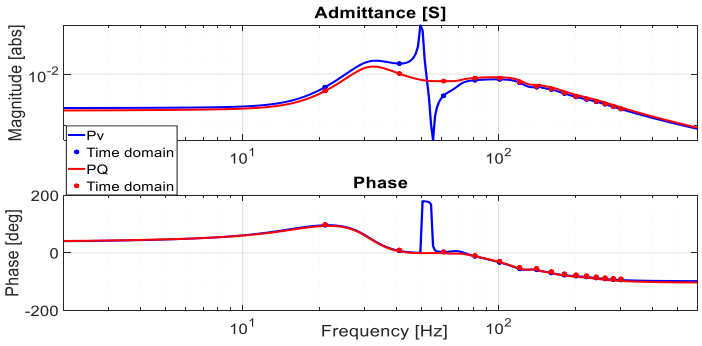

(b) $Y_{PN}(s)$

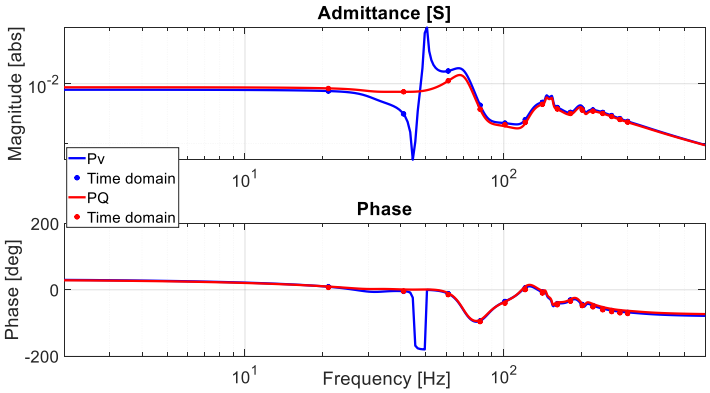

(c) $Y_{NP}(s\text{-}j2\omega_0)$

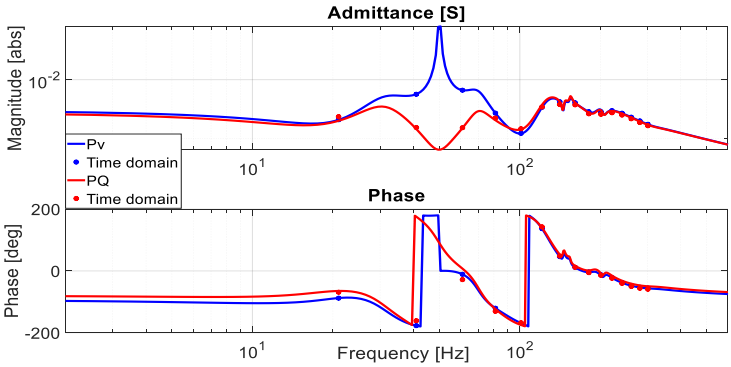

(d) $Y_{NN}(s\text{-}j2\omega_0)$

Figure 4.12 Admittance when MMC outputs 1GW active power

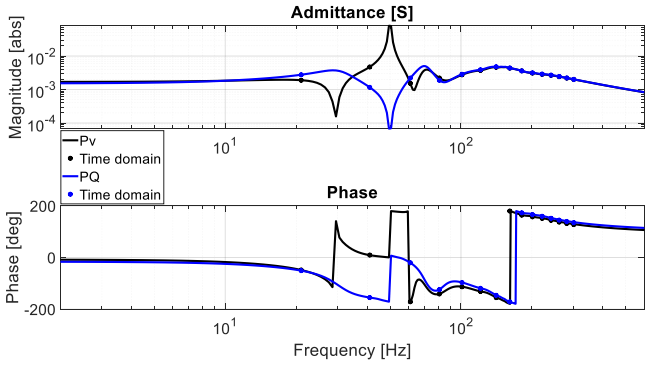

(a) $Y_{PP}(s)$

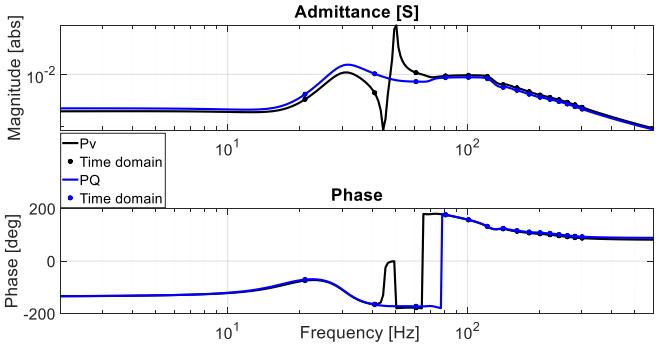

(b) $Y_{PN}(s)$

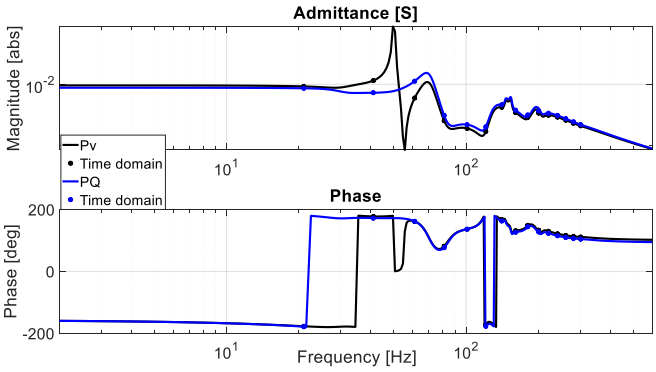

(c) $Y_{NP}(s\text{-}j2\omega_0)$

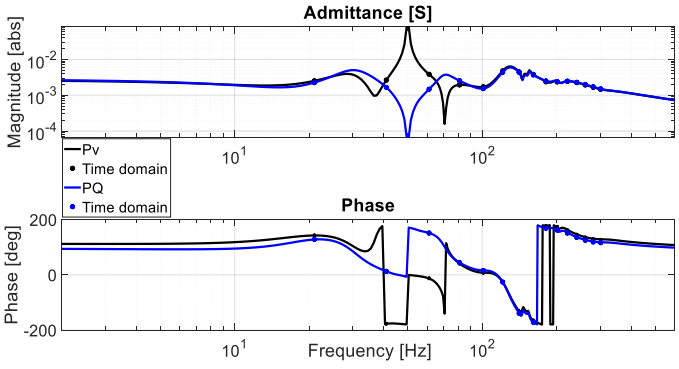

(d) $Y_{NN}(s\text{-}j2\omega_0)$

Figure 4.13 Admittance when MMC absorbs 1GW active power

Considering Y_{PP} and Y_{NN} for frequencies above 130 Hz the phases are in the range from 90° to 270°, again indicating negative damping and potential instability. Furthermore, the admittances under the two controls are almost the same in this frequency range and thus result in similar stability margin.

4.7 Summary

This chapter has described the impedance modelling and validation of the MMC in 3-phase 3-wire system based on HSS. The detailed mathematical expressions of HSS modelling for MMC have been derived considering the integration of circulating current control, the inner-loop AC current control, and the outer-loop power and AC voltage control. The coupling between the positive- and negative-sequence components are considered and analyzed in the model. The small-signal impedances obtained from the developed analytical model have been validated using measurements from time-domain models under various scenarios in MATLAB/Simulink. It has shown that:

- Various validations show that the admittance measured in the time-domain accords well with that derived from HSS based MMC. The proposed modular modelling concept allows modifications of control systems to be easily implemented into the small signal model without the need to recalculate the various state matrix.

- For open loop MMC system, it is important that higher order harmonics (e.g. h=4) are considered in order to accurately model the impedance behaviour of the MMC. This is due to the fact that for open loop MMC system, there exist strong couplings among the harmonics and high harmonic order is thus required to accurately represent the system dynamics in the small signal model.

- Once the circulating current controller and AC current controller are included, due to the largely eliminated circulating current, the harmonic interaction of MMC is

reduced.

- After adding the CCSC, the response at other frequency resulting from the 2th harmonics is considerably weakened and the number of resonant points of MMC impedance is significantly reduced.

- With the AC current control, the small-signal model of HSS based MMC can accurately calculate the impedance of the MMC. From observing the positive- and negative-sequence impedances, inverter mode tends to have reduced stability at lower frequency range than rectifier mode, and vice versa at higher frequency range.

- The admittance under the two outer-loop controls (PV and PQ) is almost the same at high frequency and thus the similar control effect.

Chapter 5 Stability assessment of grid connected MMC system

The HSS-based small-signal impedance model of MMC derived in Chapter 4 is applied in this chapter for stability assessment of AC network connected with MMC-HVDC transmission systems. The stability is assessed by examining the locus described by the ratio of the source and load impedances in the complex plane via the Nyquist stability criterion. Stability of single MMC connected to an AC grid is carried out first. The AC cable has significant impact on the grid impedance, which will result in a weak grid, therefore the impedance of AC cable is considered in MMC connected to the grid system. The impact of PLL bandwidth, the outer-loop controller, and different operating points on the stability of the grid connected MMC is also studied. The impact of multiple converters in close electrical proximity on system stability is then investigated considering cases with different multi-infeed impact factors (MIIF). System stability of two MMCs with different MIIF is assessed with different outer-loop controls using Nyquist criterion, and the results validated using time-domain simulations in MATLAB/Simulink.

5.1 Single MMC connected to an AC grid

5.1.1 System configuration

Figure 5.1 shows the simplified configuration of the grid connected MMC system. In the analysis, the influence of the DC voltage on the MMC AC side is not considered and the DC voltage is maintained at a constant value-640kV. The AC grid is modelled equivalently with a voltage source V_g and the grid-side resistor R_g and inductor L_g. The cable is represented by an equivalent π-type model and the equivalent RLC parameters

are obtained by considering the frequency response of the frequency dependent cables model that has been discussed in [119]. For a 60km AC cable, the parameters for the simplified PI section are R_{cable}=1.8792Ω, L_{cable}=0.0228H and C_{cable}=6.75μF. The specific parameters have been listed in Table 4.1 in Chapter 4. The transformer is represented by the inductor L_t. The equivalent inductor value of the transformer seen from the secondary side can be calculated as

$$L_t = \frac{X_t^*(V_{nl})^2}{2\pi f_0 S_t} = 0.0587H \tag{5.1}$$

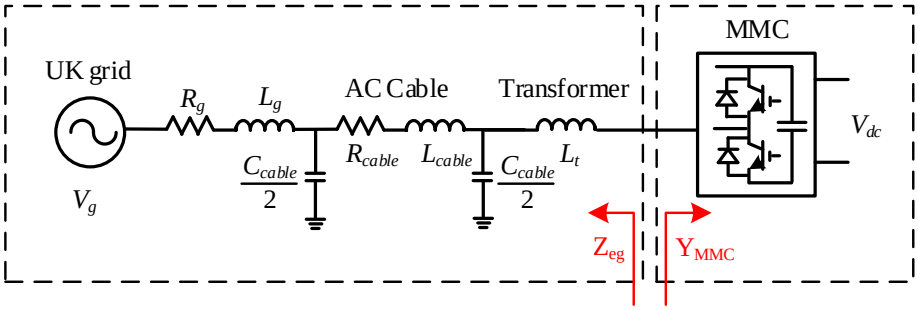

Figure 5.1 The simplified circuit for MMC based grid

5.1.2 Equivalent AC network model

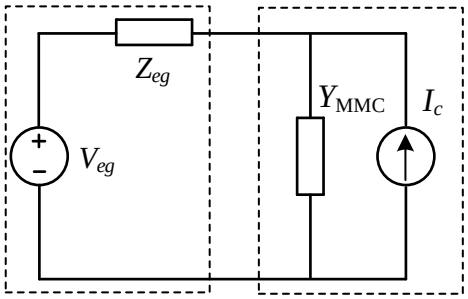

Figure 5.2 Small-signal impedance representation of MMC-grid

The small-signal impedance equivalent circuit of the MMC-grid system is depicted as Figure 5.2. As can be seen, the MMC side is equivalent using Norton circuit,

in which the MMC is represented by the current source I_c in parallel with MMC small-signal admittance $\mathbf{Y}_{\mathrm{MMC}}$ calculated in Chapter 4. The AC network adopts the Thevenin equivalent circuit with a voltage source V_{eg} in series with the impedance $\boldsymbol{Z}_{eg}$.

The grid impedance $Z_g(s)$ in the frequency-domain can be denoted as $Z_g(s)=R_g+sL_g$ and the impedance of the transformer referring to the converter side in frequency-domain is $X_t(s)=sL_t$. The capacitor and the inductor in the equivalent circuit of the AC cable in the frequency-domain can be expressed as $X_c(s)=2/(sC_{cable})$ and $X_{cable}(s)=sL_{cable}$. Thus, the equivalent AC network impedance seen from the transformer secondary side can be obtained as

$$Z_{eg}(s)=\frac{1}{k_t^2}\left[(Z_g(s)\,||\,X_c(s)+R_{cable}+X_{cable}(s))\,||\,X_c(s)\right]+X_t(s) \tag{5.2}$$

where k_t is the transformer ratio.

With $s=\mathrm{j}\omega_0$, the grid short circuit ratio (SCR) is derived as

$$SCR=\frac{k_t^2V_{nl}^2}{P\left[Z_g(s)+R_{cable}+X_{cable}(s)\right]} \tag{5.3}$$

Therefore, the whole system stability can be assessed by the product of the AC-side equivalent impedance $Z_{eg}(s)$ and the MMC admittance $Y_{\mathrm{MMC}}(s)$, which has been discussed in detail in Section 2.5.

5.1.3 Stability assessment

Stability of the MMC grid system shown in Figure 5.1 is carried out using the developed small signal impedances considering the impact of the control strategy and different operating point. To validate the analytical results, a time-domain simulation model of the same system is carried out in Matlab/simulink. The AC cable length

considered is 60km. The block-diagram of the MMC control structure is illustrated in Figure 5.3, which has been discussed in detail in Section 4.4, and the related control parameters can be found in Table 5.1. As shown, the MMC AC current is controlled by the current controller in dq frame in Figure 5.3 (a), and the PLL provides the phase angle for transformation between abc and dq frames. The current references can be assigned directly or by the outer-loop controller in Figure 5.3 (b), depending on the specific cases considered. The circulating current suppression controller is presented in Figure 5.3 (c). Noted that the output of circulating current suppression controller is negative sequence.

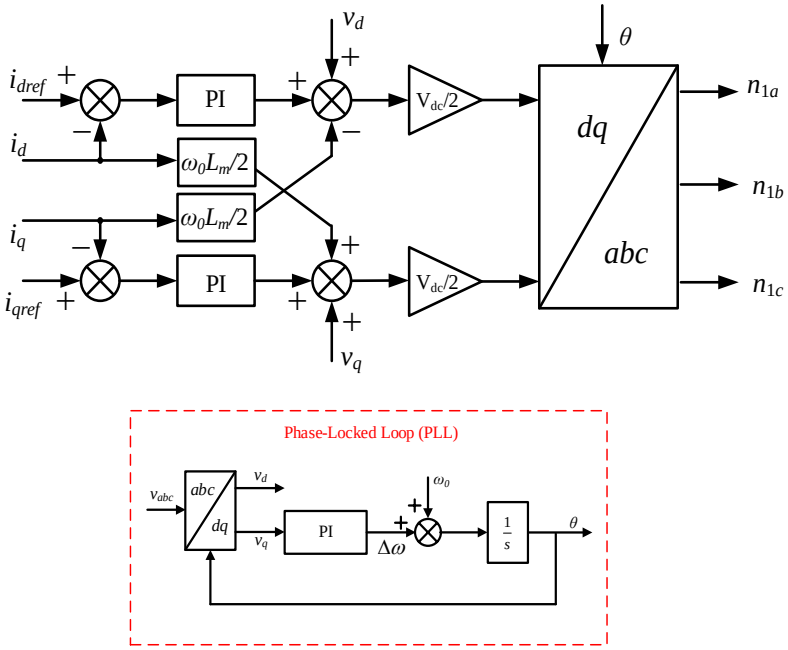

(a) Control block for the current loop

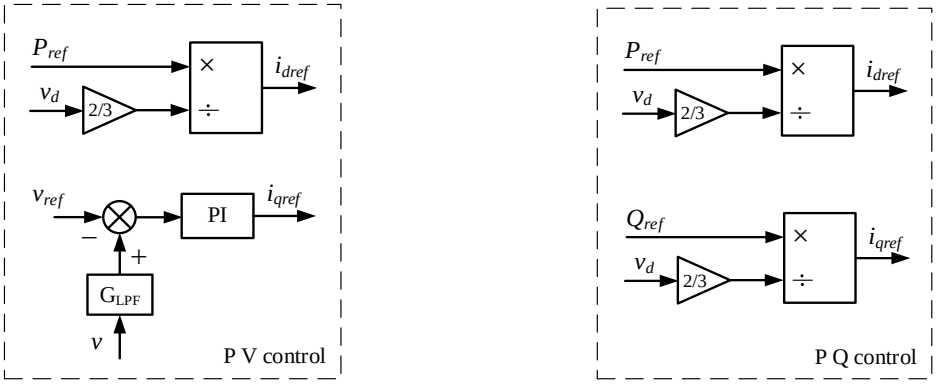

(b) Outer-loop: PV and PQ control

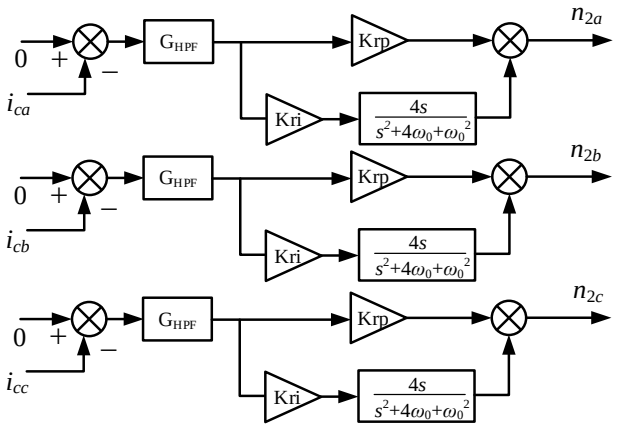

(c) Internal circulating current control

Figure 5.3 MMC control structure

Table 5.1 Controller parameters for current controller

Parameters	Value
Current loop proportional gain K_{ip}	15.8 Ω
Current loop integral gain K_{ii}	2980 Ω/s
PLL proportional gain K_{pllp}	0.0013 rad/(sV)
PLL integral gain K_{plli}	0.1209 rad/(s^2V)
PR controller proportional gain K_{rp}	63.3 Ω
PR controller integral gain K_{rr}	11200 Ω/s

5.1.3.1 Impact of different PLL bandwidth on system stability

(a) MMC operates as an inverter

In this case, the outer-loop control is not considered and the grid SCR is 2.27 (indicating a weak grid) calculated according to (5.3). The d-axis current reference for the current controller is set to 2268A (1.0 p.u.), which refers to 1GW output power of MMC to the grid while the q-axis current reference is -40A to maintain the terminal voltage of MMC at 360kV.

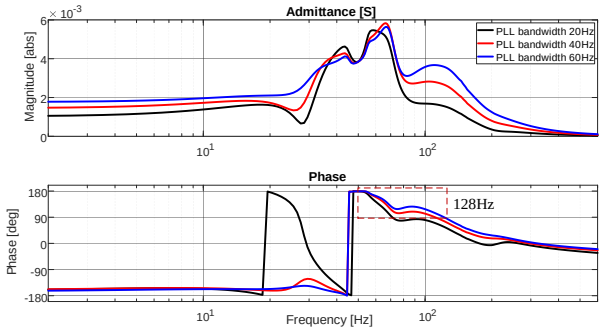

(a) $Y_{pp}(s)$

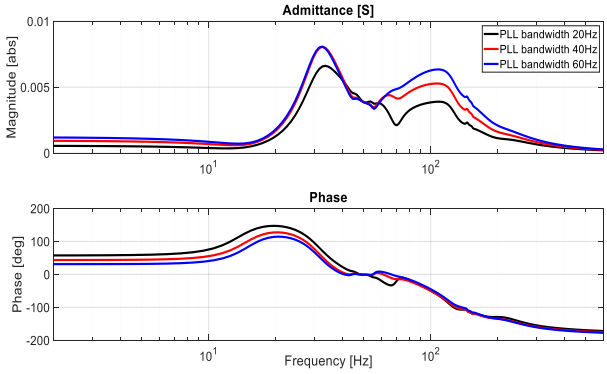

(b) $Y_{pn}(s)$

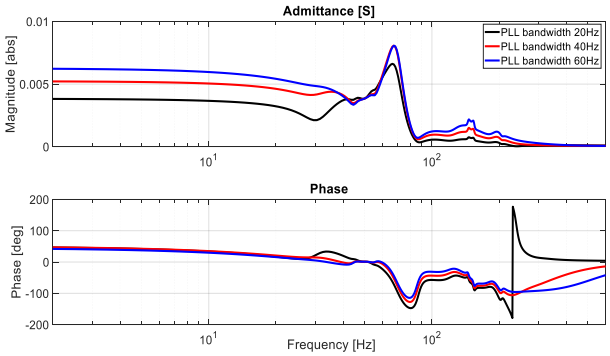

(c) $Y_{np}(s\text{-}2j\omega_0)$

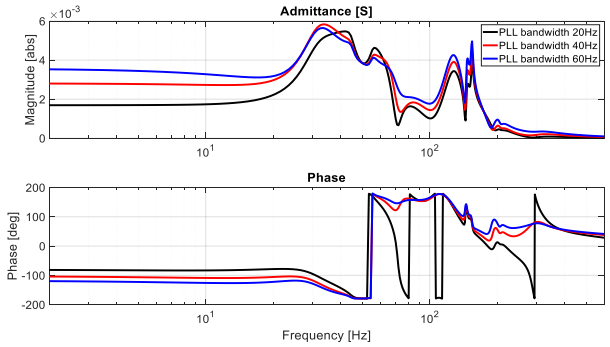

(d) $Y_{nn}(s\text{-}2j\omega_0)$

Figure 5.4 Admittances under different PLL bandwidths

Using the model developed in Chapter 4, the small-signal admittances under different PLL bandwidths can be obtained as shown in Figure 5.4. The black line, red line and blue line denote the MMC admittances with 20Hz, 40Hz, and 60Hz PLL bandwidths, respectively. As can be seen, lower bandwidth generally leads to smaller magnitude of the admittance, which is beneficial for the system stability as the equivalent impedance in parallel with the current source has large magnitude [41]. In addition, in terms of the phase of the positive-sequence admittance $Y_{pp}(s)$, lower PLL bandwidth makes the phase approach to 0, which indicates improved damping for the MMC system and thus is beneficial to the stability improvement. From the point of the small-signal impedance of MMC, it can be concluded that the lower PLL control bandwidth leads to a more stable system.

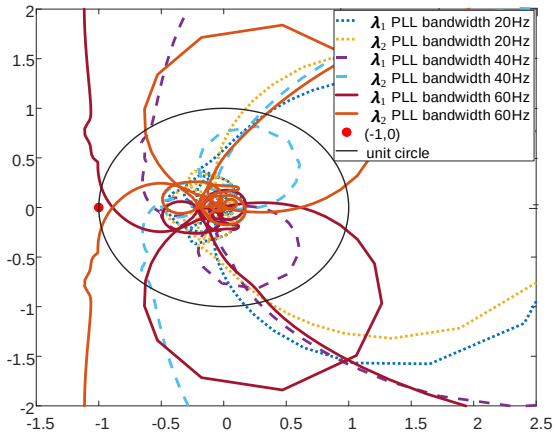

Figure 5.5 Nyquist plots with different PLL bandwidth

Figure 5.5 presents the Nyquist plots for the eigenvalues of $\mathbf{Z}_{eg}\mathbf{Y}_{MMC}$ under different PLL bandwidths of 20Hz, 40Hz, and 60Hz, respectively. As can been, all the plots do not encircle the point (−1, 0), which indicates that the interconnected system is stable under the 3 different PLL bandwidths. However, system stability is decreased by increasing the bandwidth as Nyquist plots get closer to the point (−1, 0). With 60Hz bandwidth, both the magnitude and phase margins are relatively lower and stability is weaker than with 20Hz bandwidth. In practical system, many aspects need be considered when selecting control parameters, e.g., small signal system stability, system response during large transients. For example, converters with lower PLL bandwidth are less able to limit/control the AC current during external AC system fault potentially resulting in overcurrent, when compared to converters with higher PLL bandwidth.

In order to validate the above theoretical analysis in frequency-domain, the time-domain simulation results for the same condition are shown in Figure 5.6. At 4s, a small perturbation is induced on the d-axis current reference, i.e., i_{dref} is stepped up from 2268A to 2288A. With 20Hz bandwidth, the responses of I_d and V_d have smaller overshoots than those with 40Hz bandwidth, whereas with 60Hz bandwidth, the current and voltage contain significant oscillations although the system remains stable.

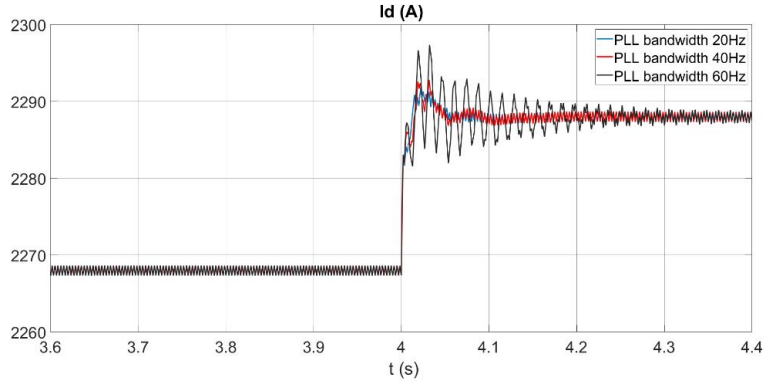

(a) d-axis current I_d

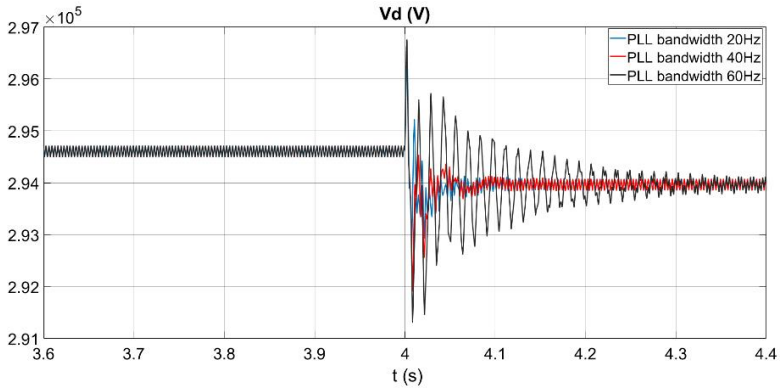

(b) d-axis voltage V_d

Figure 5.6 Simulation results under different PLL bandwidth

(b) MMC operates as rectifier

The AC grid SCR is set to 3.0 by reducing R_g and L_g to ensure the system stable. The d-axis current reference for the active power is i_{dref}=-2268A, i.e., -1p.u., indicating that the MMC absorbs 1GW active power from the AC grid. Meanwhile, the q-axis current reference for the reactive power sets to i_{qref}=-291A to maintain the MMC terminal voltage at 360kV.

The MMC admittances under different PLL bandwidths are shown in Figure 5.7, where the black, red and blue curves denote admittances under 20Hz, 30Hz and 40Hz PLL bandwidths, respectively. The positive-sequence admittance Y_{pp} and the negative-sequence admittance Y_{nn} in the range of frequency above 150Hz with the phase

between -90º~-180º imply negative resistor effect and thus leading to potential instability [120]. In addition, the increase of the PLL bandwidth leads to the magnitude increase of the positive-sequence admittance Y_{pp}, which has negative effect on system stability. In the meantime, the phase is further away from 90º and the negative damping becomes more severe, which deteriorates system stability. Therefore, in terms of MMC admittance, the increase of PLL bandwidth will weaken system stability.

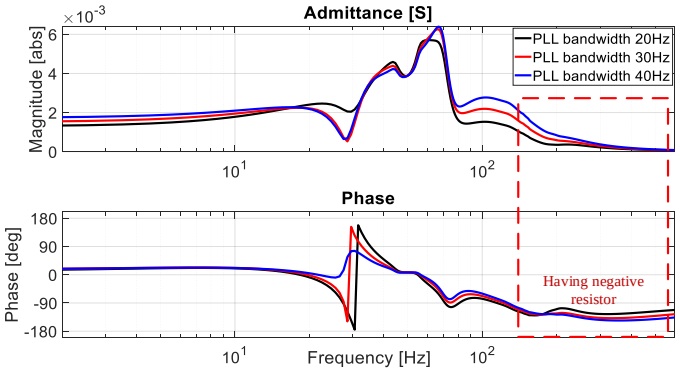

(a) $Y_{pp}(s)$

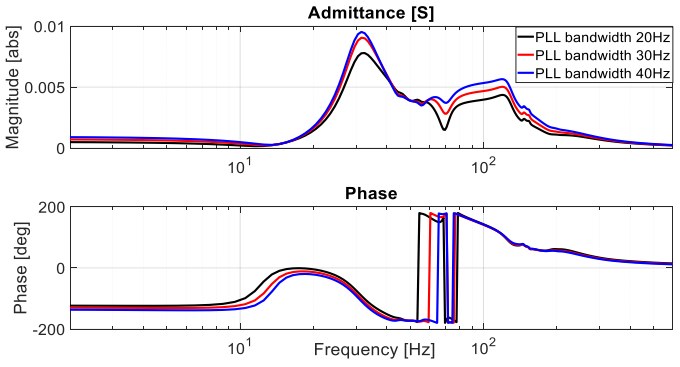

(b) $Y_{pn}(s)$

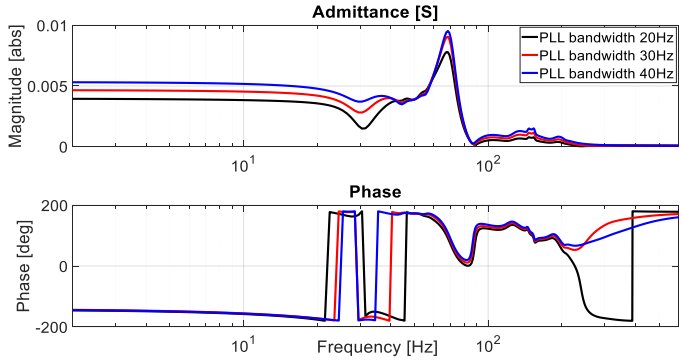

(c) $Y_{np}(s\text{-}2j\omega_0)$

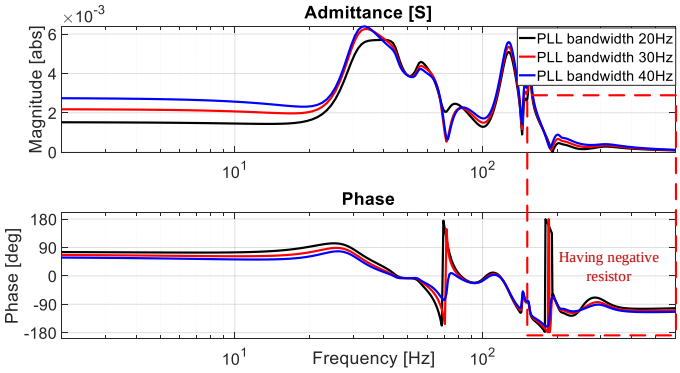

(d) $Y_{nn}(s\text{-}2j\omega_0)$

Figure 5.7 Admittance under different PLL bandwidth

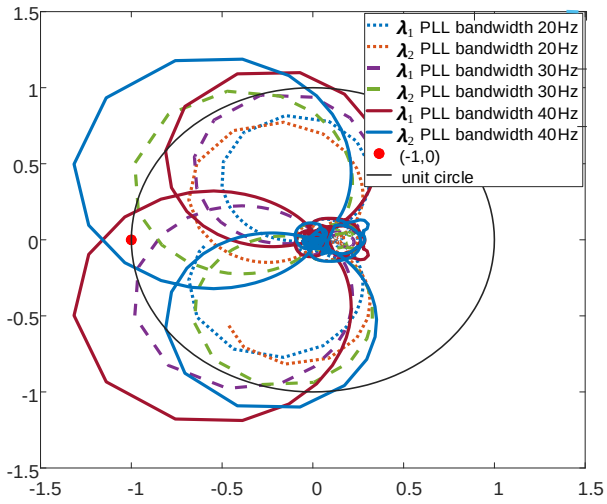

Figure 5.8 Nyquist plots with different PLL bandwidth

The Nyquist plot of corresponding eigenvalues is presented in Figure 5.8. It can be seen that PLL bandwidths of 20Hz and 30Hz result in no encirclement of (-1,0) and thus indicating stable systems. With the 20Hz PLL bandwidth, a larger stability margin can be achieved than the 30Hz case. In the case of 40Hz, the plot encircling (-1,0) implies an unstable system.

To verify the frequency-domain analysis results, time-domain simulations are conducted. In the simulation results compared in Figure 5.9 with PLL bandwidths of 20Hz to 30Hz, the d-axis current reference i_{dref} steps up from -2268A to -2288A at 5s. As can be seen, although the current responses are similar for the two bandwidths when the perturbation is imposed, the difference of the voltage responses is significant. When the PLL bandwidth is 20Hz, the system can be stabilized quicker than with 30Hz bandwidth.

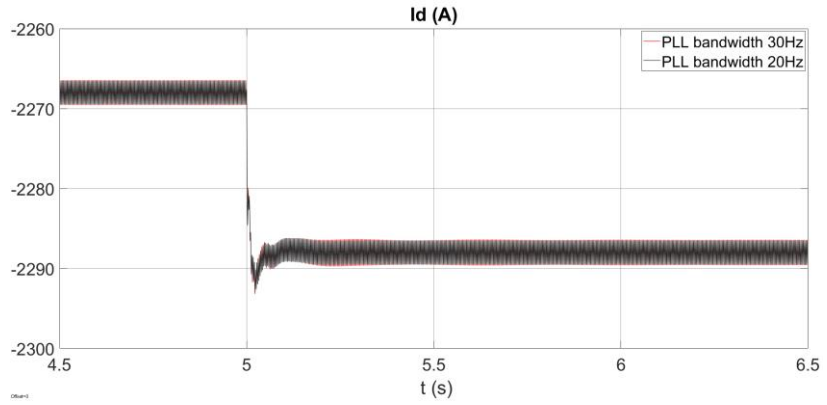

(a) d-axis current Id

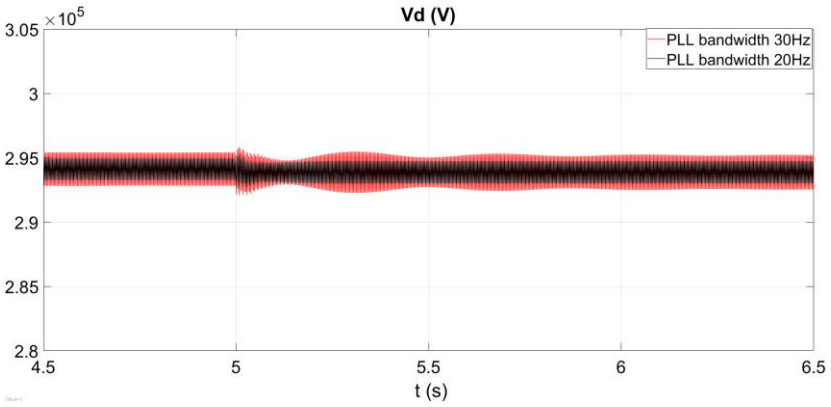

(b) d-axis voltage Vd

Figure 5.9 Simulation results under 20Hz and 30 Hz PLL bandwidth

Further studies when the PLL bandwidth increases from 30Hz to 40Hz at 5s are carried out and the response results are shown in Figure 5.10. As seen in Figure 5.10 (a) and (b), the system is stable before 5s. However, when the bandwidth changes to 40Hz, the system begins to oscillate. Figure 5.10 (c) shows that the three-phase voltage waveform during 6.0s-6.2s contains significant 7th harmonic, as indicated in the FFT analysis in Figure 5.10 (d). The time-domain simulation results show that the system becomes unstable as the bandwidth increases from 30Hz to 40Hz, which is in accordance with the frequency-domain analysis.

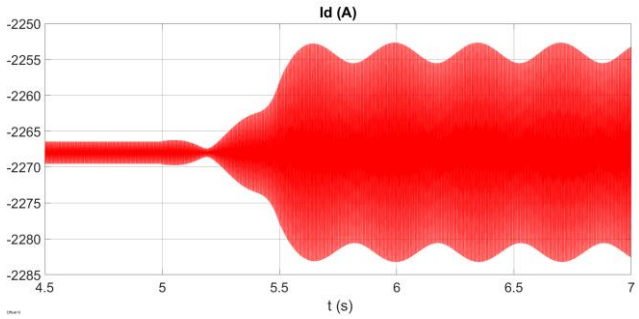

(a) d-axis current I_d

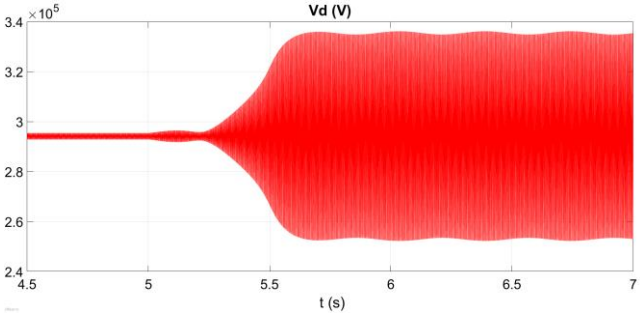

(b) d-axis voltage V_d

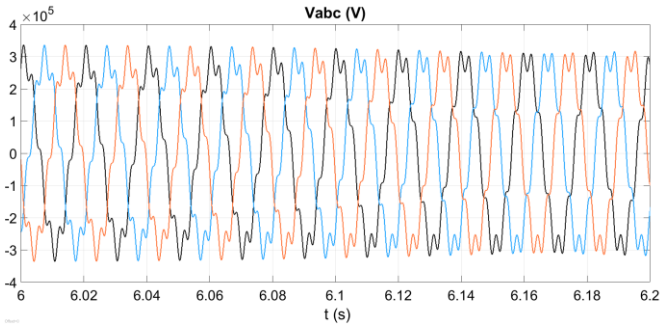

(c) Three-phase voltage during 6-6.2s

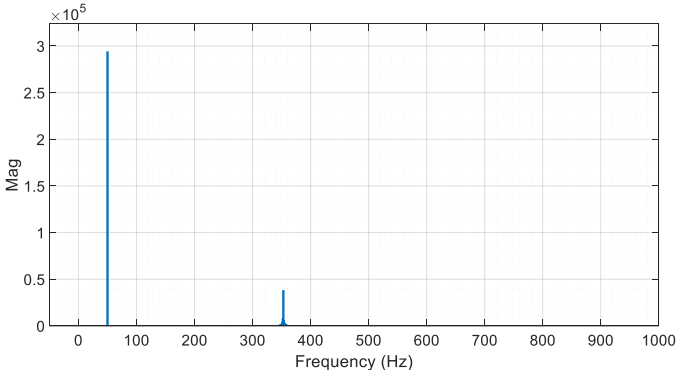

(d) FFT analysis for a-phase voltage

Figure 5.10 PLL bandwidth increases from 30Hz to 40Hz

It can be concluded that for both inverter and rectifier modes, when the MMC is connected to a relatively weak grid, reducing the PLL bandwidth improves system stability. Comparing MMC in inverter and rectifier modes, the system tends to be less stable in rectifier mode due to the negative resistance effect (negative damping) in the MMC admittance, than in inverter mode.

5.1.3.2 Impact of different outer-loop controller on system stability

The effect of different outer-loop controllers on the stability of the MMC system is investigated. The system operating point keeps unchanged as previous studies and the PLL bandwidth is set to 60Hz. Different outer-loop controllers shown in Figure 5.3 are applied to the MMC controller.

When using outer active power and AC voltage control, the references for d-axis and q-axis current components are given as

$$\begin{cases} i_{dref} = \dfrac{2P_{ref}}{3v_d} \\ i_{qref} = k_{vp}(v - v_{ref}) + k_{vi}\int (v - v_{ref})dt \end{cases} \tag{5.4}$$

where $v = \sqrt{v_d{}^2 + v_q{}^2}$ is the three-phase AC voltage amplitude at the MMC terminal and is passed through a LPF and before sending to the outer-loop control. The voltage reference is $v_{ref} = \sqrt{2} \times 360kV / \sqrt{3} = 293.9kV$, k_{vp}=0.005 A/V and k_{vi}=0.5A/(s·V).

When using outer active power and reactive power control, the current references are assigned as

$$\begin{cases} i_{dref} = \dfrac{2P_{ref}}{3v_d} \\ i_{qref} = \dfrac{2Q_{ref}}{3v_d} \end{cases} \tag{5.5}$$

(a) MMC in inverter mode

With grid SCR of 2.27, active power reference P_{ref}=1GW, and reactive power Q_{ref}=-13.2MVar, which keeps the three-phase voltage constant at 360kV, the small-signal positive-sequence admittance of the MMC under the outer-loop PV and PQ control are shown in Figure 5.11. Only the positive-sequence admittance is presented here as the others has similar trend. However, the Nyquist curves presented use the full admittances.

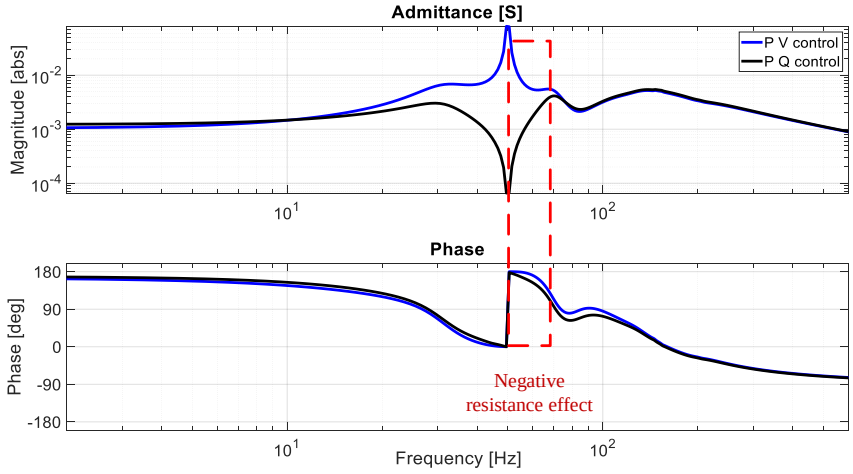

Figure 5.11 Small-signal admittance Y_{pp} of MMC with PV and PQ control

In Figure 5.11, the admittances under PV and PQ control mainly distinct in 20-70Hz frequency range. The implementation of the voltage control means the voltage variation during a 50Hz current perturbation to the MMC is minimized resulting in the maximum admittance around 50Hz. Note that both the admittances under PV and PQ control have negative resistance between 50Hz and 70Hz shown in Figure 5.11, which indicate potential resonance in this frequency range. In comparison with the PV control, the magnitude of the MMC admittance with PQ control around 50Hz is much smaller. The phase of the positive-sequence admittance Y_{pp} is also smaller around 50~70Hz under PQ control than PV control, indicating larger damping and thus larger stability

margin.

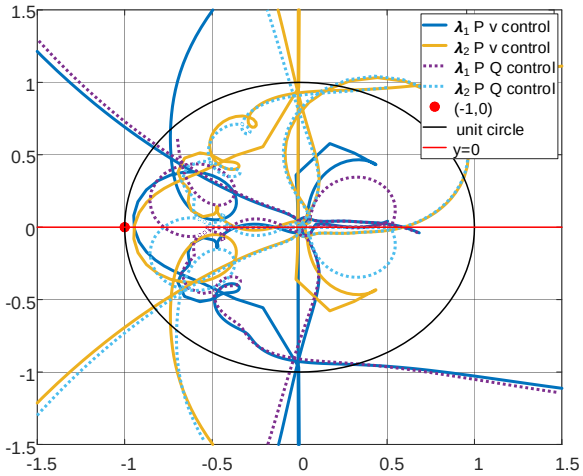

Figure 5.12 Nyquist plots with PV and PQ outer-loop control

Figure 5.12 compares the Nyquist plots for system eigenvalue loci with the two outer-loop controls. All four curves do not encircle the point (-1, 0) and thus both are stable. Moreover, with the two controls, the intersections of the Nyquist plots and the unit circle are almost identical, indicating similar phase margins. As the intersection with the x-axis being far away from (-1, 0) means a large magnitude margin, it can be observed that PQ control has larger magnitude margin and thus better stability than PV control.

The time-domain simulations are conducted to confirm the frequency-domain analysis results. At 4s, a small perturbation is injected to the active power reference and the simulation results are shown in Figure 5.13. Comparing the two outer-loop controllers, it can be observed that the system is stabilized quicker with smaller overshoot in the case of PQ control. This indicates that the system is more stable with PQ control than PV control, which matches well with the frequency-domain analysis. The oscillation frequency of the voltage and the current in dq frame is about 10 Hz, i.e., 60Hz in abc frame. It is in accordance with the frequency range in Figure 5.11 that

the MMC admittance exists obvious distinction.

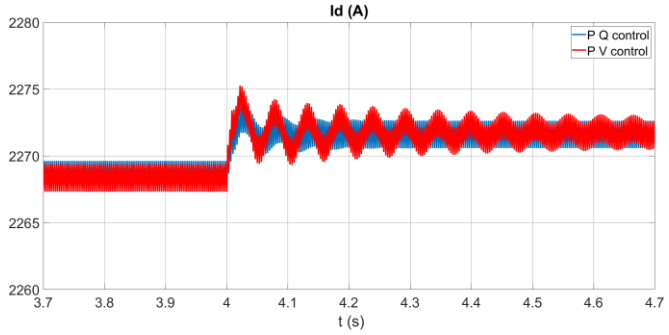

(a) d-axis current Id

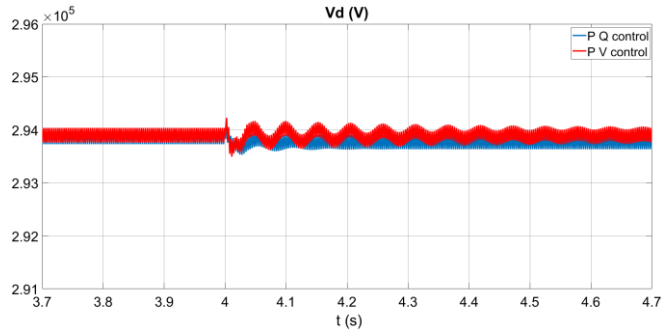

(b) d-axis voltage V_d

Figure 5.13 Simulation results under two outer-loop controllers

In addition, without the outer-loop voltage control, the oscillation frequency for the voltage and current response in Figure 5.6 was about 125Hz with 60Hz PLL bandwidth. When the outer-loop is added the oscillation frequency becomes 60Hz. Observe the positive-sequence admittance Y_{pp} in the case with only the current control and 60Hz PLL bandwidth shown in Figure 5.4 (a), the phase above 90º in 50-128Hz frequency range indicates negative resistance effect and the oscillation frequency lies in this range. As the outer-loop is added, the phase in 70-128Hz has reduced to be less than 90º, which implies the negative resistance decrease and the system becomes more stable in this frequency range. However, in the range 50~70Hz, the phase is still above 90º and the oscillation is likely to occur in this frequency range.

(b) MMC in the rectifier mode

When the grid SCR is 3.0, the terminal voltage is kept at 360kV and the PLL bandwidth is 60Hz. The grid absorbs 0.5GW active power from the grid. The same outer-loop in case (a) is adopted, and the small-signal admittance of the MMC is shown in Figure 5.14.

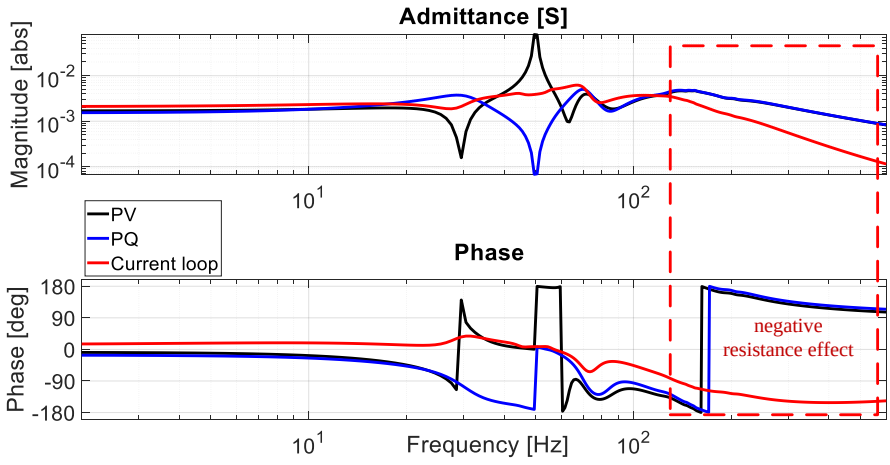

Figure 5.14 Admittance Y_{pp} with different outer-loop in the rectifier mode

Above 200Hz, the admittance is almost identical under PV and PQ outer-loop controls. The phase of Y_{pp} is larger than 90º, indicating negative resistance effect. This is similar to the case with only the current controller shown in Figure 5.14. Figure 5.15 shows the Nyquist plots and it can be seen that with only the current loop, the system is stable. However, the added outer-loop will lead to unstable system with similar effects from the PV and PQ controls.

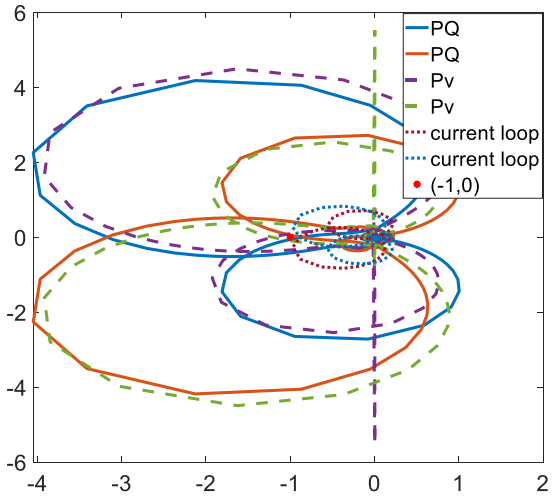

Figure 5.15 The Nyquist plot with different control loop in the rectifier mode

The time-domain simulation result is presented in Figure 5.16 which show that the active power response when the MMC ramps down power from 0 to -0.5GW. Without the outer-loop, the system is stable, whereas with either PV or PQ outer-loop controller, the system becomes unstable at -0.5GW with the oscillation frequency around 380Hz.

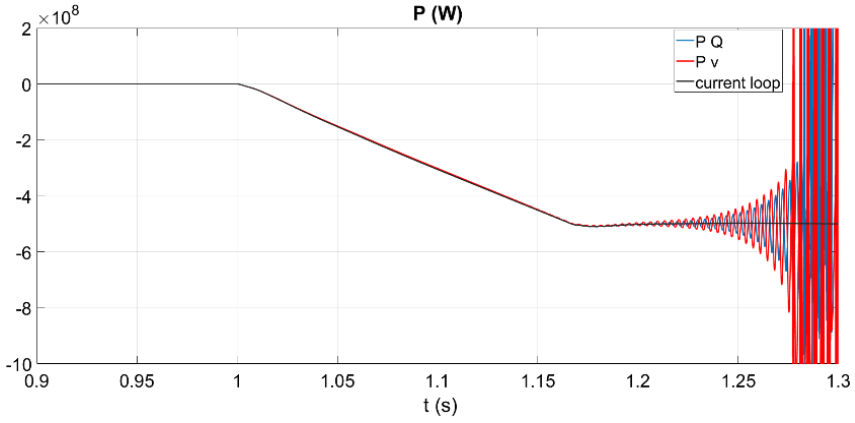

Figure 5.16 The active power when the MMC absorbs 0.5GW active power

The above analysis indicates that in inverter mode, the outer-loop is beneficial for the stability of the system and the system oscillation frequency is low. Moreover, PQ

control is superior to PV control for the system stability. However, in rectifier mode, the addition of the outer-loop deteriorates the system stability and the system tends to oscillate in relatively high frequency range. Moreover, the effects of PV and PQ controls on system stability are similar.

5.1.3.3 Impact of different SCR on system stability

In this section, the impact of the AC grid strength on the stability of the MMC system when it is in inverter operation is investigated. With the same operating conditions as previous inverter operation cases, the grid impedance Z_g is varied whilst keeping the cable length at 60km. The SCR of the two cases considered here are 3.57 and 1.87, respectively. Since the active power and AC voltage of the MMC are kept unchanged, the active current i_d remains constant, whilst different SCR affects MMC reactive current i_q, i.e., the reactive power operating point. The q-axis currents are 61.5A and -67.5A for SCR=3.57 and SCR=1.87, respectively. The small-signal admittance of MMC are compared in Figure 5.17 with SCR=3.57 and SCR=1.87, where the small difference is purely caused by the different reactive power/current operating point.

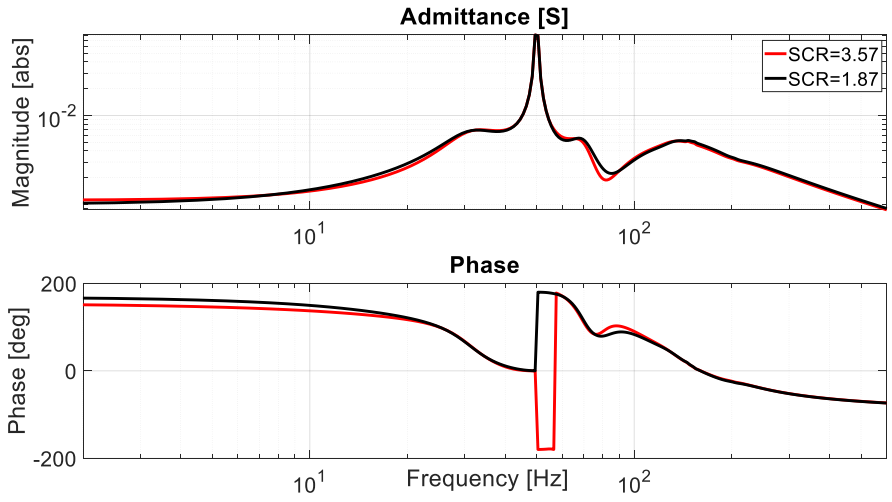

Figure 5.17 Small-signal admittance Y_{pp} with different SCR

The impedances Z_{eg} on the AC side (including the 60 km AC cable) are presented in Figure 5.18 and there is obvious difference between the two SCR. As the SCR decreases, the resonant point of the impedance will move toward lower frequency.

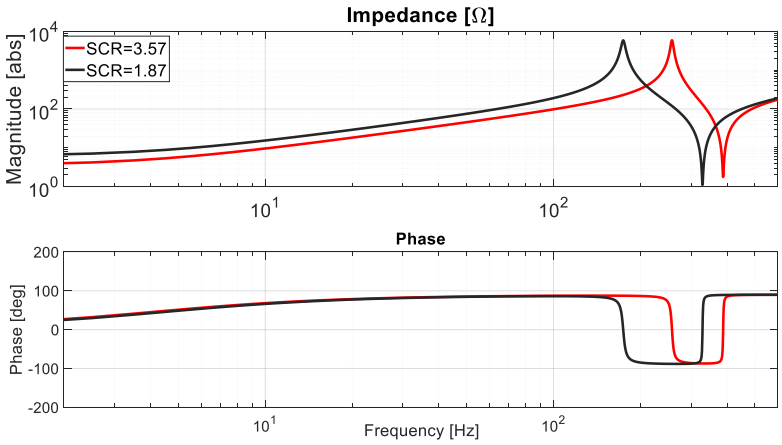

Figure 5.18 Impedance $Z_{eg}(s)$ on the AC side

Figure 5.19 demonstrates the Nyquist plots of the eigenvalues of $Z_{eg}Y_{MMC}$ under different SCR. In the case of SCR=1.87, the dashed lines encircle the point (-1, 0), which indicate that the interconnected system is unstable. In the case of strong AC grid with SCR=3.57, the solid lines do not encircle (-1, 0), indicating stable operation.

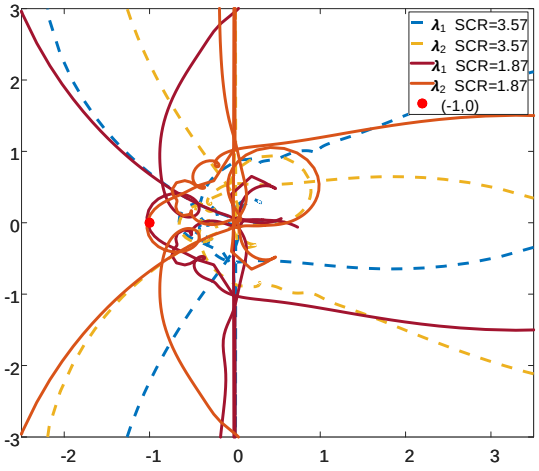

Figure 5.19 Nyquist plots with different SCR

The corresponding time-domain simulation results are shown in Figure 5.20. It is observed that the system is stable when SCR=3.57 and oscillation occurs for SCR=1.87. The time-domain analysis is consistent with the frequency-domain analysis based on small-signal impedance.

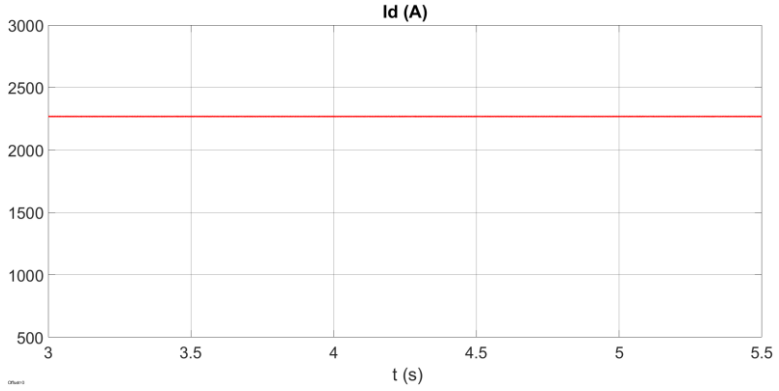

(a) SCR=3.57

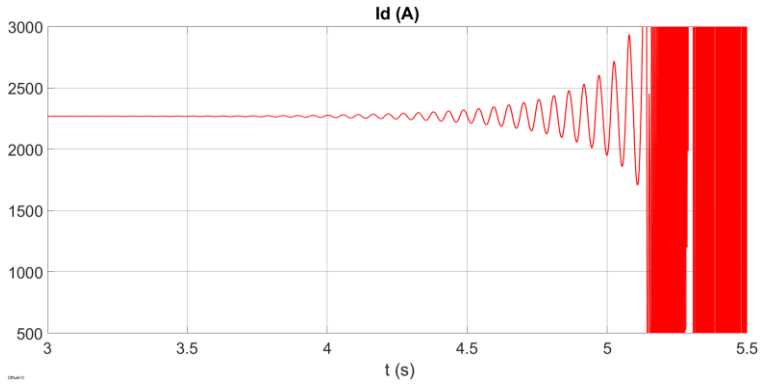

(b) SCR=1.87

Figure 5.20 Simulation results of d-axis current I_d for different SCR values.

5.1.3.4 Impact of different active power with PV outer-loop controller on system stability

Tests on the impact of different active power output on system stability are carried out. The AC grid SCR is 1.87 and the MMC is in inverter mode. The MMC admittances are compared in Figure 5.21 for active power of 1GW and 0.5GW, respectively. As can be seen, when the active power is reduced by half, the MMC admittance magnitude

also decreases, implies better system stability. The Nyquist plots in Figure 5.22 also confirms that the system is unstable with 1GW output active power while the system becomes stable with 0.5GW active power.

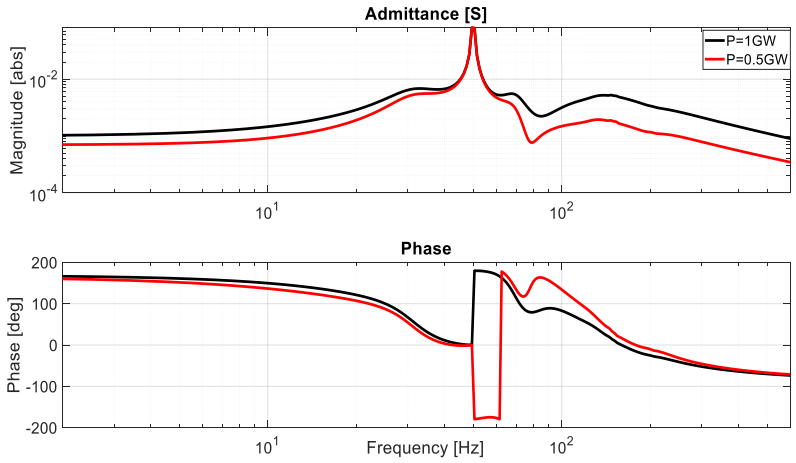

Figure 5.21 Small-signal admittance Y_{pp} for different active power of 0.5GW and 1GW

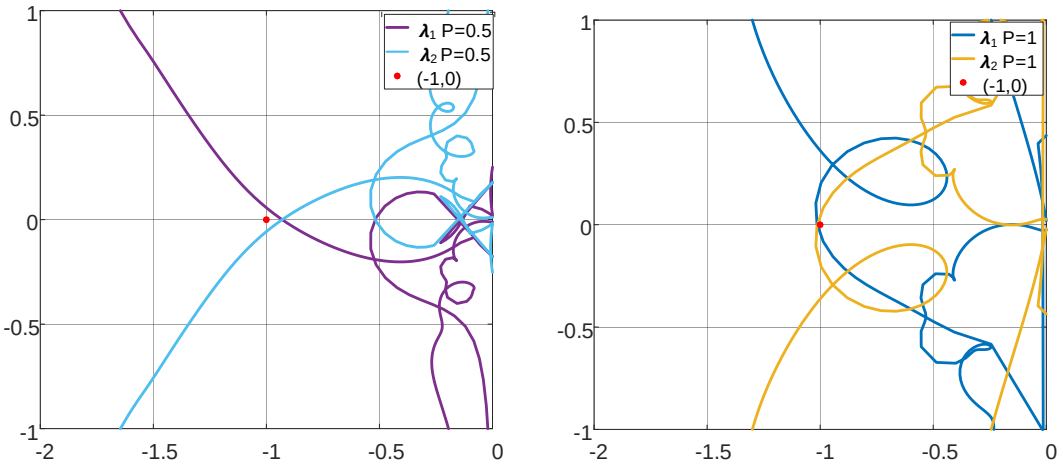

(a) P=0.5GW (b) P=1GW

Figure 5.22 Nyquist plots with different active power

For the time-domain simulation shown in Figure 5.23, the active power output of the MMC is ramped up from 0.5GW to 1GW at 3s. As can be seen, the system becomes oscillatory after the active power increase, which is in good agreement with the

analytical results in Figure 5.22.

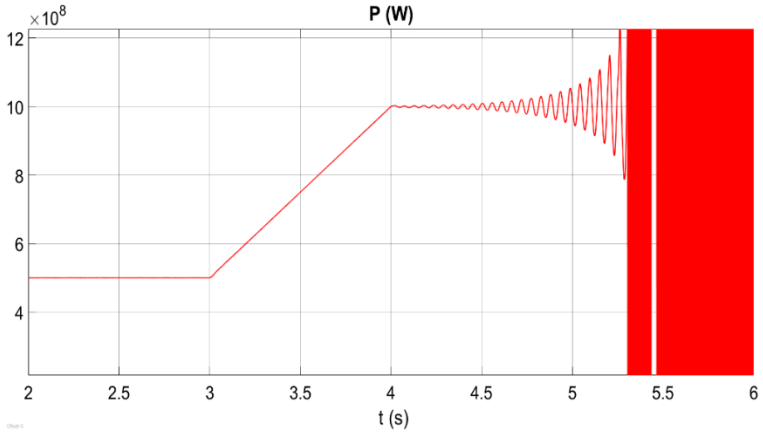

Figure 5.23 Simulation results with active power increased from 0.5GW to 1GW

Further studies with the change of active power direction, i.e., between inverter and rectifier operation, have been carried out. With AC grid SCR of 4.0, two cases of MMC operating at inverter (P=0.5GW) and rectifier (P=-0.5GW) modes are investigated and the corresponding Nyquist plots are depicted in Figure 5.24. As can be seen, MMC operating at inverter mode results in better stability compared with that in rectifier mode. The time-domain simulation results are compared in Figure 5.25 in which a small perturbation is added at 4.5s. The system can be stabilized quicker in the case of inverter operation than rectifier operation, in which the voltage undergoes considerable oscillation at about 300Hz. This conclusion is in line with previous assessments.

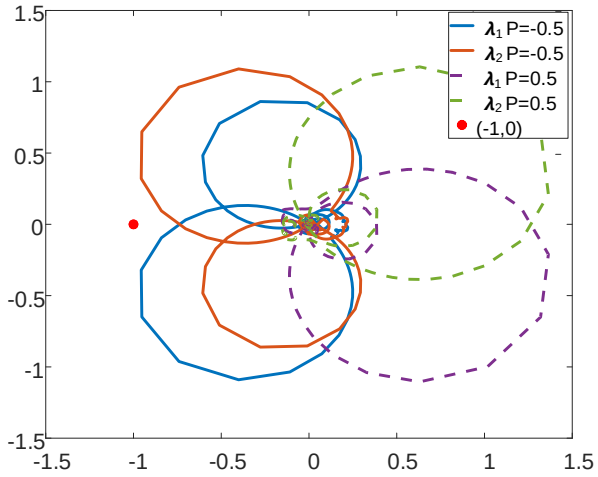

Figure 5.24 Nyquist plot in the case of MMC outputting and absorbing power

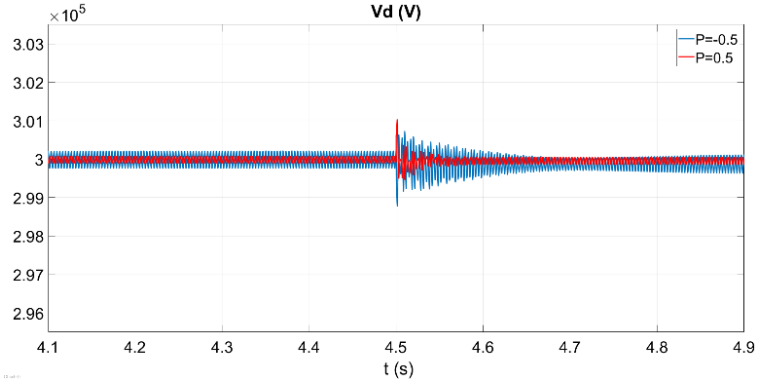

Figure 5.25 The d-axis voltage response in the case of MMC outputting and absorbing power

5.2 Network with two MMCs

5.2.1 System configuration

Considering increased network interconnections and connection of large offshore wind farms (e.g. in Europe) using HVDC links, many power networks in Europe will see significant numbers of HVDC converters connected in close proximity. For example, as outlined in [103] and schematically shown in Figure 5.26, the GB network will have more than 20 HVDC connection by 2027, with a total transmission capacity

of over 16GW. When multiple converters are considered for studying converter interaction, shown in RED area in Figure 5.26 as an example, the network admittance seen at each of the converter connection points will need to be considered together with the electrical coupling between the converters. In order to perform an analytical study on system stability and interaction, a simplified network structure is required. In this thesis, the so-called multi-infeed interaction factor (MIIF) between the converters [121], proposed by CIGRE WG B4 is used to quantify the simplified system structures. Converter AC busses electrically far apart will have low MIIF, while MIIF is high when the AC busses are very close and the interaction is strong between the converters.

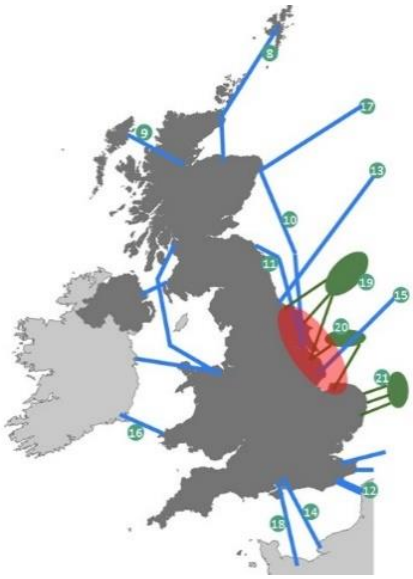

Figure 5.26 Example of multiple converters in close proximity

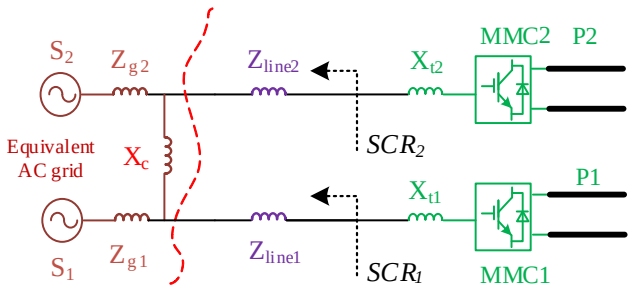

Figure 5.27 Equivalent circuit configuration for analytical studies

5.2.1.1 Equivalent AC network

Considering the case with two MMCs, each of the MMC can be equivalent to connection with an AC source through a certain impedance to emulate the network condition at the MMC connection point, and the two AC sources are interconnected (within the same AC network). Thus, a simplified network configuration as shown in Figure 5.27 can be developed. Z_{line1} and Z_{line2} in Figure 5.27 are considered as the impedances of two 60km cables connecting the MMCs to the existing network. Applying the MIIF concept, the followings are considered when setting the network parameters:

- MMC_1 infeed is considered as an existing HVDC link, and thus Z_{g1} is pre-determined.

- When there exists strong electrical coupling between MMC_1 and MMC_2, i.e. the two converters are in close proximity (or high MIIF), X_c is set to a low value while Z_{g2} is set to a high value, so that MMC_2 can be deemed close to AC system S_1 while being further away from S_2.

- When there only exists weak electrical coupling between MMC_1 and MMC_2 (i.e. low MIIF), X_c is set to a high value while Z_{g2} is set to a low value, so that MMC_2 can be deemed close to the AC system S_2 and far away from S_1.

5.2.1.2 Equivalent SCR and MIIF

The equivalent impedance on the AC side of MMC1 seen from PCC1 is shown in Figure 5.28. The equivalent impedance for MMC_1 can be calculated as $Z_{SCR1} = (Z_{g2} + X_c) \,||\, Z_{g1} + Z_{line1}$. Thus, the SCR can be obtained as $SCR_1 = Z_n / Z_{SCR1}$ where $Z_n = V_n^2 / S_n$. Similarly, the equivalent impedance on the AC side of MMC_2 connected at PCC2 and the SCR for MMC2 can be calculated as $Z_{SCR2} = (Z_{g1} + X_c) \,||\, Z_{g2} + Z_{line1}$ and $SCR_2 = Z_n / Z_{SCR2}$.

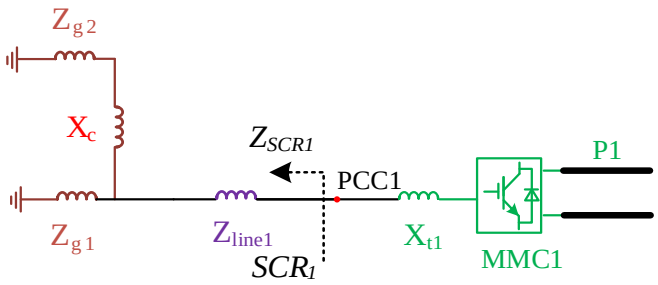

Figure 5.28 Equivalent impedance on the AC side of MMC1

The general formula for calculating $MIIF_{e,n}$ is expressed as [121]

$$MIIF_{e,n} = \Delta V_e / \Delta V_n \tag{5.6}$$

where ΔV_e is the observed voltage change at bus e when a small voltage change ΔV_n is induced at bus n.

To represent cases where the two MMCs have strong or weak coupling, the system parameters considered in this thesis are shown in Table 5.2. The corresponding SCR and MIIF are presented in Table 5.3.

Table 5.2 The system parameter in the case of weak coupling and strong coupling

Parameters	Weak coupling	Strong coupling
L_{t1}	0.0587H	0.0587H
L_{t2}	0.0587H	0.0587H
Cable1 length	60 km	60 km
Cable2 length	60 km	60 km
R_{g1}	4.08Ω	4.08Ω
L_{g1}	0.1296H	0.1296H
R_{g2}	4.08Ω	10.2 Ω

L_{g2}	0.1296H	0.324H
L_c	0.3H	0.01H

Table 5.3 SCR and MIIF in the case of weak coupling and strong coupling

	Weak coupling	Strong coupling
SCR1	2.59	2.74
SCR2	2.59	2.64
$MIIF_{1,2}$	0.26	0.78
$MIIF_{2,1}$	0.26	0.81

5.2.2 AC network impedance calculation for stability analysis

To assess the stability of the grid system with two MMCs, if MMC1 is the converter under consideration, the small-signal impedance $Z_{MMC2}(s)=1/Y_{MMC2}(s)$ of MMC2 should be included when calculating the equivalent grid impedance. According to Figure 5.27 and considering the voltages for sources S_1 and S_2 are the same, the two power sources can be equivalent to one power source as shown in Figure 5.29 (a) and then the three impedance $Z_{g1}(s)$, $Z_{g2}(s)$, and $X_c(s)$ form a delta connection. Furthermore, the delta connection can be transformed to Y connection as shown in Figure 5.29 (b).

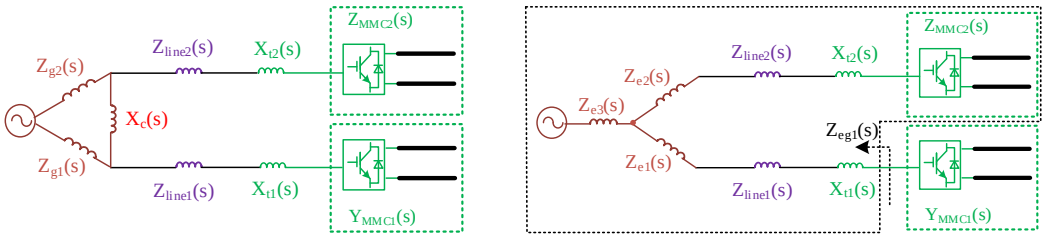

(a) The power source equivalent circuit

(b) The delta – Y connection transformation

Figure 5.29 Small-signal impedance equivalent circuit

Therefore, the impedance denoted in Figure 5.29 (b) can be depicted as

$$Z_{e1}(s) = \frac{Z_{g1}(s)X_c(s)}{Z_{g1}(s) + Z_{g2}(s) + X_c(s)} \tag{5.7}$$

$$Z_{e2}(s) = \frac{Z_{g2}(s)X_c(s)}{Z_{g1}(s) + Z_{g2}(s) + X_c(s)} \tag{5.8}$$

$$Z_{e3}(s) = \frac{Z_{g1}(s)Z_{g2}(s)}{Z_{g1}(s) + Z_{g2}(s) + X_c(s)} \tag{5.9}$$

As a result, the equivalent impedance $Z_{eg1}(s)$ can be derived using $Z_{e1}(s)$, $Z_{e2}(s)$ and $Z_{e3}(s)$ as

$$Z_{eg1}(s) = [Z_{e3}(s) \| (Z_{e2}(s) + Z_{line2}(s) + X_{t2}(s) + Z_{MMC2}(s)] + Z_{e1}(s) + Z_{line1}(s) + X_{t1}(s) \tag{5.10}$$

Thus, the system stability can be assessed based on Nyquist curve for eigenvalue loci of $Z_{eg1}(s)Y_{MMc1}(s)$.

5.2.3 Stability analysis

5.2.3.1 PQ outer-loop control for both MMCs

MMC_1 and MMC_2 adopt the control shown in Figure 5.3 and the outer-loop employ PQ control with P_{ref1}=1GW and P_{ref2}=1GW. The reactive power of MMC can be regulated to maintain the terminal voltage of MMC at 360kV and the same control parameters are adopted as listed in Table 5.1.

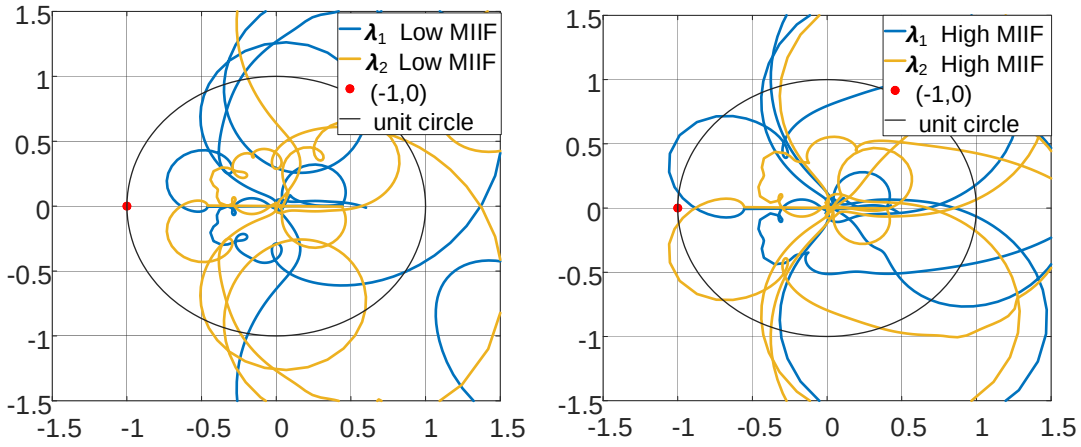

(a) Low MIIF (b) High MIIF

Figure 5.30 Nyquist plots in the case of low MIIF and high MIIF using PQ outer-loop control

To assess the system stability in terms of MMC1, under different MIIF, the Nyquist plots for eigenvalue loci of $Z_{eg1}Y_{MMC1}$ are shown in Figure 5.30. For both high and low MIIF values, they do not cause encirclement of the point (-1, 0) and thus both systems can always remain stable. In the case of low MIIF value, the interaction of the two MMCs are weak and the Nyquist plots imply that the system has high phase margin and magnitude margin, and the stability is strong. In contrast, in the case of high MIIF value, the system stability is weak with low phase margin and magnitude margin.

The corresponding time-domain simulation results are given in Figure 5.31 with a perturbation injected into the active power reference of MMC1 at 12s. As seen in Figure 5.31 (a), the d-axis current of MMC1 with low MIIF has small overshoot and can reach stable quickly. However, under the high MIIF, the system is prone to oscillation as shown in Figure 5.31 (b). The time-domain simulation results accord well with the Nyquist analysis.

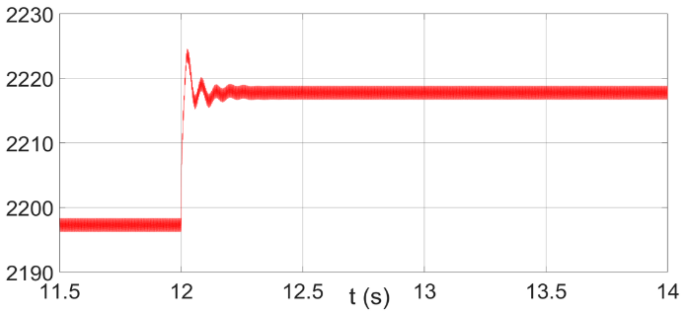

(a) Low MIIF

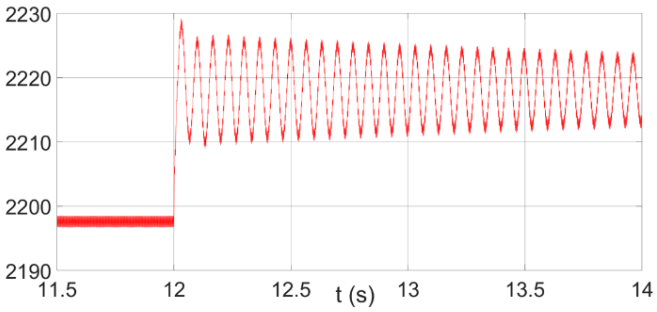

(b) High MIIF

Figure 5.31 The d-axis current of MMC1 with different MIIF from the Simulink model

Despite of the grid strength with SCR1=2.59 is weak, in the case of low $MIIF_{2,1}$=0.26, the system still has favorable stability. However, when the coupling of the two MMCs is strong with $MIIF_{2,1}$=0.81, the system stability is weak.

5.2.3.2 PQ outer-loop for MMC1 and PV outer-loop for MMC2

The effect of different outer-loop control on the stability of the interconnection system is investigated, with MMC1 adopting PQ control and MMC2 PV control. Under different MIIF, the frequency analysis is depicted in Figure 5.32. As seen, the system can maintain sufficient stability with low MIIF. Whereas with high MIIF, the system becomes unstable. The time-domain simulation results shown in Figure 5.33 also validate the analytical results. The results indicate that the use of PV control at MMC2, the stability of the system is reduced when compared to PQ control. Therefore, it is important the impact of outer-loop on system stability is fully considered.

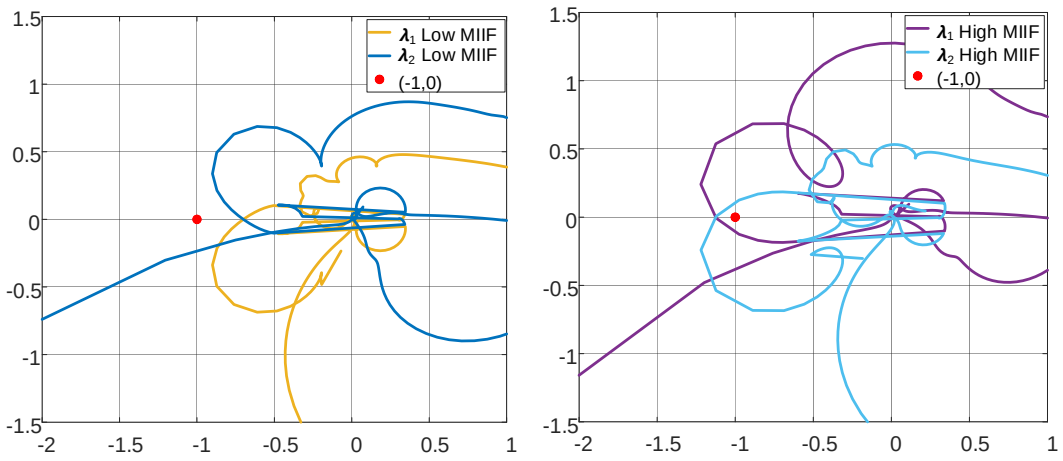

(a) Low MIIF (b) High MIIF

Figure 5.32 Nyquist plot with different MIIF using PQ and PV control

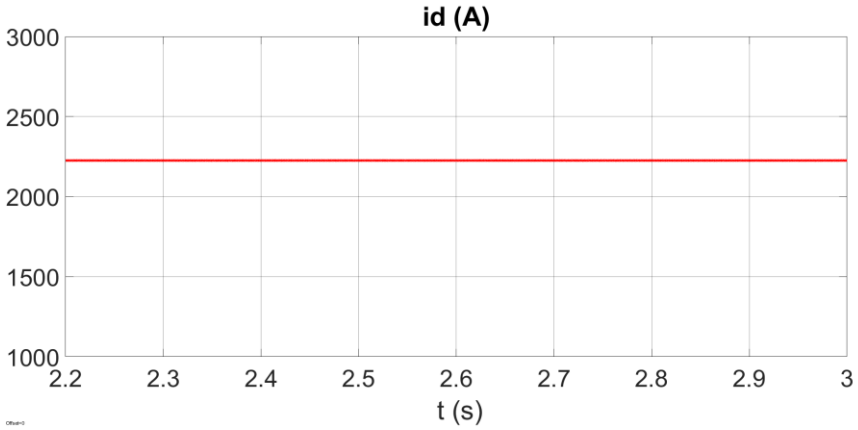

(a) d-axis current with low MIIF

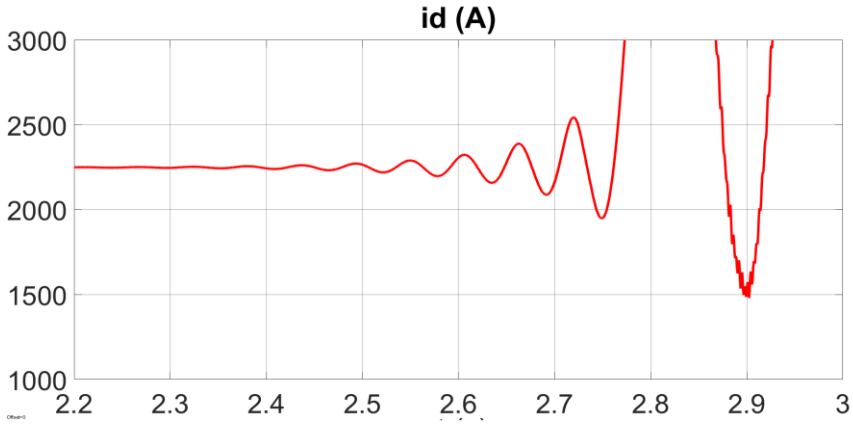

(b) d-axis current with high MIIF

Figure 5.33 The d-axis current of MMC1 with different MIIF

5.2.3.3 MMC1 in rectifier mode and MMC2 in inverter mode

With MMC1 importing active power from the grid (rectifier) and MMC2 exporting active power to the grid (inverter), system stability analysis is conducted with different MIIF. Both MMCs adopt PV outer-loop control and MMC2 exports fixed 1GW active power. With a low MIIF, Figure 5.34 compares the Nyquist plots for MMC1 importing 0.24GW and 0.26GW active power. As seen, with MMC1 importing 0.24GW from the AC grid, the plot does not encircle (-1,0) and thus the system is stable. However, when MMC1 importing power increases to 0.26GW, the Nyquist plot shows an unstable system.

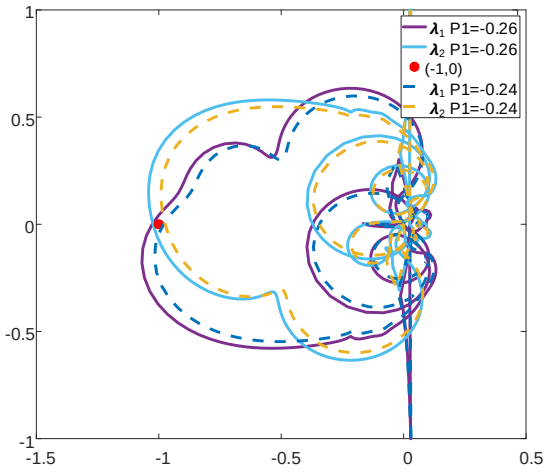

Figure 5.34 Nyquist plot when MMC1 absorbs different power with low MIIF

The time-domain simulation results shown in Figure 5.35 indicate the same conclusion. At seen, after the imported active power by MMC1 increases from 0.24GW to 0.26GW at 2.5s, the system gradually becomes unstable.

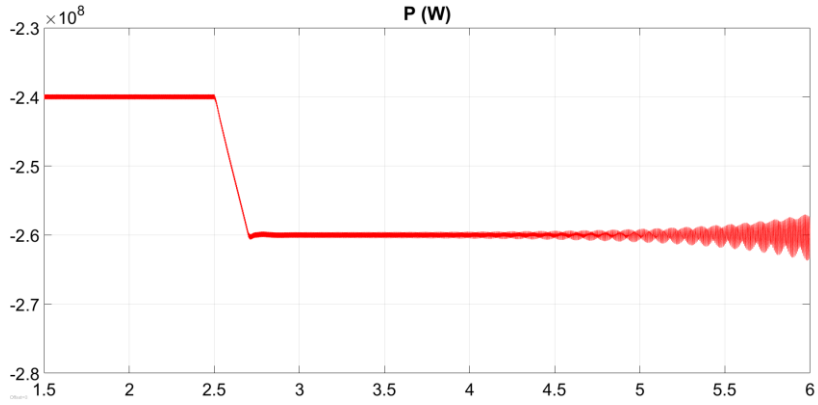

(a) Active power

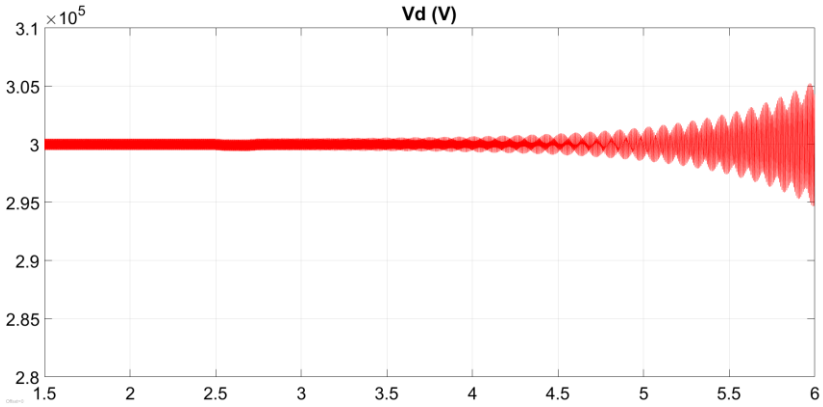

(b) d-axis voltage

Figure 5.35 Simulation results when MMC1 absorbs different power with low MIIF

Previous results when both MMCs operated in inverter mode showed that the system oscillated at lower-frequency of around 10-20Hz. However, in this case, the system oscillates at high frequency, caused by the negative damping at high frequency in MMC1's admittance in rectifier mode.

With high MIIF, the Nyquist plot is presented in Figure 5.36. In this case, MMC1 imports 0.73GW active power from AC and the system is proven to be stable whereas the case with 0.75GW imported power indicates an unstable system. Again, time-domain simulation results shown in Figure 5.37 validate the conclusion derived from Nyquist plot.

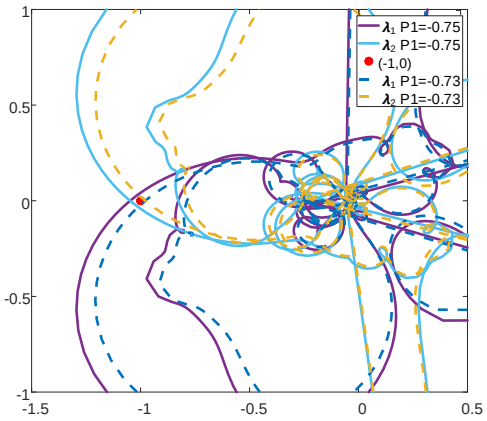

Figure 5.36 Nyquist plot when MMC1 absorbs different power with low MIIF

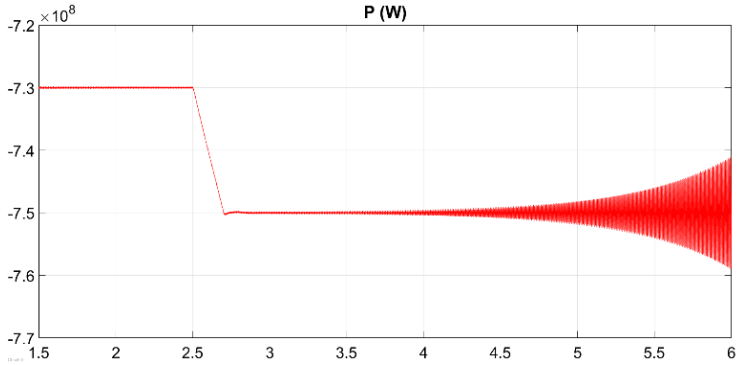

(a) Active power

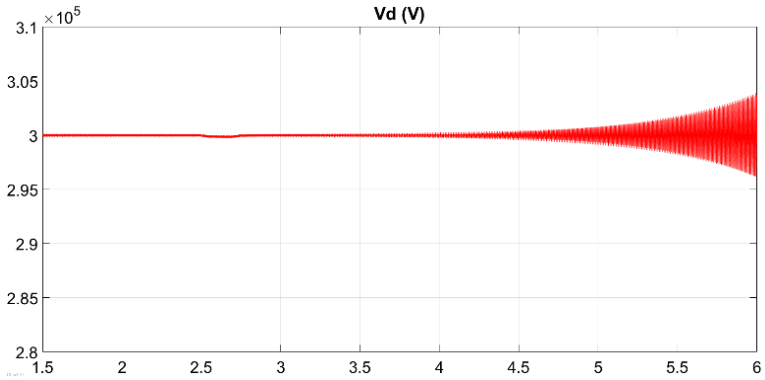

(b) d-axis voltage

Figure 5.37 Simulation results when MMC1 absorbs different power with high MIIF

5.3 Summary

This chapter has carried out stability assessment of AC network connected with MMC-HVDC transmission systems by using Nyquist stability criterion. The impacts

of AC cable length, MMC PLL bandwidth, outer-loop controller, and operating points on system stability have been studied. System stability of multiple converters in close electrical proximity has also been investigated. All cases are validated using time-domain simulation. It is found that:

1 For AC grid with single MMC, high PLL bandwidth leads to less stable system. Consequently, when the grid is weak and encounters stability problem, the reduction of the PLL bandwidth is beneficial to the system stability and may be considered.

2 In inverter mode, MMC has better stability with PQ outer-loop control than with PV control, whereas in the rectifier mode, both outer-loop controls have similar effect on stability. Compared with only current-loop control, the addition of the outer-loop control deteriorates system stability when MMC works in rectifier mode.

3 Compared with inverter mode, MMC in rectifier mode is more likely to induce system instability. Moreover, the resonance frequency usually locates in high frequency, .e.g., above 150Hz for the case studied.

4 High MMC active power results in increased MMC admittance magnitude and consequently, reduced system stability. This applied to both rectifier and inverter operation.

5 Interaction of converters in close proximity can be studied using the impedance model and the multi-infeed interaction factor (MIIF). Stability analysis and simulation results show that system with high MIIF where strong couplings between the two MMCs exist may lead to unstable system.

Chapter 6 Conclusions and future work

6.1 General conclusions

This thesis has developed accurate small-signal frequency-domain models of grid-connected converters for stability analysis, including the two-level VSC, single-phase and three-phase MMC. The developed models have then been applied for stability assessments.

For the grid connected two-level VSC, the derivation of its small-signal admittance in pn frame is presented. Based on the analytical admittance, influences of the coupling admittance that generated by the PLL and outer-loop controllers on system stability are investigated. The results indicate that under a weak grid the traditional outer-loop active power and AC voltage controller creates coupling admittance that has negative impact on system stability. To reduce the coupling admittance and improve system stability, an improved outer-loop controller is proposed which adds compensation terms into the d- and q-axis current in the form of $k_1\Delta v_{cd}$ and $k_2\Delta v_{cq}$ at the potential resonance frequency range through lower-pass and high-pass filters. Simulation results in time-domain verify the correctness of small-signal admittance in frequency-domain and the effectiveness of the proposed controller.

The small-signal impedance model of the single-phase MMC is established based on the HSS modelling method, which is capable of covering all internal harmonics within the MMC. Different MMC control schemes, such as the AC current control and circulating current control, have also been incorporated in the model. The impact of the MMC internal dynamics and control dynamics on MMC impedance is investigated. The simulation results are provided to validate the proposed MMC impedance models. It is found that for open loop MMC system, it is important that higher order harmonics

(e.g. h=4) are considered in the HSS model for accurate MMC impedance model. However, whereas once the circulating current controller and AC current controller are included, the MMC harmonic interaction is reduced and HSS model with h=2 generally provide adequate results.

As the modelling method for single-phase MMC cannot represent the true behaviour of three-phase MMC systems, especially the zero-sequence current system and control system implementation, an accurate model of the grid-connected three-phase MMC in sequence frame using the HSS modelling method is developed. Detailed procedures of the modelling is described including the transformation from abc frame into pn frame and various controls that have been incorporated in its small-signal model. The coupling between the positive- and negative-sequence components brought by the external control loops and PLL are analyzed in the model. The small-signal impedances obtained from the developed analytical model have been validated using time-domain models under different scenarios. It is found that the HSS model presents a promising tool to achieve efficient system control design and analysis, particularly where harmonic coupling may be an issue. Moreover, different control loops, e.g., PLL, AC voltage control, power control etc., can be easily incorporated into the impedance model. The modelling method proposed allows modifications on control system to be easily implemented into the small signal models without the need to recalculate the various state matrix.

This developed analytical MMC model is used for assessing system stability considering both single MMC case and multiple MMCs operating in close vicinity. For single MMC connected to a weak grid, system stability is reduced with high PLL bandwidth and operating at high active power. When the MMC operating as an inverter, PQ outer-loop control leads to better system stability than PV control. However, for rectifier operation, PV outer-loop control is superior to PQ control in terms of stability. With the impedance model, interaction of converters in close proximity is studied

considering different multi-infeed interaction factor (MIIF). Considering the case with two MMCs, a simplified AC network configuration is developed which can be easily configured to cater for different MIIFs and network strengths. Stability analysis and simulation results show that system with high MIIF where strong couplings between the two MMCs exist may lead to system instability.

6.2 Future work

The proposed three-phase MMC impedance does not consider the DC bus dynamics as the DC side is assumed an ideal voltage source. However, the perturbation voltage at the MMC AC terminal will cause voltage fluctuation at the DC terminal, which in turn will affect the modulation signal on the MMC arm and the AC terminal current. This means there is strong interaction between the MMC AC and DC terminals and implies the DC side perturbation will affect the AC side impedance of the MMC. Therefore, it is necessary to consider the DC side dynamics for developing a more accurate impedance model of the complete MMC-HVDC system. Moreover, the small-signal impedance of MMC with different control structures such as negative-sequence controller will need to be studied for a full understanding of the MMC impedance characteristics and further optimize system control to improve stability.

Significant numbers of LCC-HVDC systems currently exist in power networks and in some cases, additional VSC based power generation plants and interconnections are being built in close proximity. Therefore, the interaction between the existing LCC-HVDC systems and VSC converters needs to be studied. For LCC-HVDC systems, due to the existence of significant 11^{th} and 13^{th} harmonic current in the LCC converter, there potentially can have significant harmonic interactions at relatively high frequency, i.e. around 600Hz for 50Hz AC system. Thus, the small-signal impedance model of LCC converter using the HSS method needs to be developed, and stability assessment considering both grid-connected LCC and VSC systems conducted.

The future work can be concluded as:

- Develop the more accurate small-signal impedance model of the MMC-HVDC system in which the dynamics of DC side is considered.

- Negative-sequence controller of MMC-HVDC system in dq frame will be modelled for the MMC impedance model. Further, the impact caused by negative-sequence controller on system stability will be studied.

- Develop the small-signal impedance model of the LCC-HVDC system based on HSS method. The significant 11th and 13th harmonic will be included in the model.

- When different type of converters such as two-level VSC, MMC and LCC are connected in close proximity. The interactions between them will be analyzed based on the developed impedance models.

References

[1] European Commission, “The Revised Renewable Energy Directive,” https://eur-lex.europa.eu/legal-content/EN/TXT/PDF/?uri=CELEX:32018L2001&from=EN, 2020.

[2] J. Dorn, H. Gambach and D. Retzmann, “HVDC transmission technology for sustainable power supply,” International Multi-Conference on Systems, Signals & Devices, Chemnitz, 2012, pp. 1-6.

[3] F. M. Khan, A. Abbasi, M. A. Khan and M. I. Khan, “General overview of using High Voltage Direct Current (HVDC) transmission in Pakistan for maximum efficiency and performance,” 2015 Power Generation System and Renewable Energy Technologies (PGSRET), Islamabad, 2015, pp. 1-5.

[4] O. E. Oni, I. E. Davidson and K. N. I. Mbangula, “A review of LCC-HVDC and VSC-HVDC technologies and applications,” 2016 IEEE 16th International Conference on Environment and Electrical Engineering (EEEIC), Florence, 2016, pp. 1-7.

[5] Chunyi Guo, Yi Zhang, A. Gole and Chengyong Zhao, “Analysis of dual-infeed HVDC with LCC-HVDC and VSC-HVDC,” 2013 IEEE Power & Energy Society General Meeting, Vancouver, BC, 2013, pp. 1-1.

[6] L. Xu, L. Yao, and C. Sasse, “Grid Integration of Large DFIG-Based Wind Farms Using VSC Transmission,” IEEE Transactions on Power Systems, vol. 22, pp. 976-984, 2007.

[7] J.-H. Ying, H. Duchen, M. Karlsson, L. Ronstrom, and B. Abrahamsson, “HVDC with voltage source converters - a powerful standby black start facility,” in 2008 IEEE/PES Transmission and Distribution Conference and Exposition, 2008, pp. 1-9.

[8] K. Friedrich, “Modern HVDC PLUS application of VSC in Modular Multilevel Converter topology,” in 2010 IEEE International Symposium on Industrial Electronics, 2010, pp. 3807-3810.

[9] L. Jian, Y. Jianguo, W. Di, W. Chuanxin, Y. Shenchun, and L. Ji, “Application research on VSC-HVDC in urban power network,” in 2011 IEEE Power Engineering and Automation Conference, 2011, pp. 115-119.

[10] P. Hurtuk, R. Radvan, and M. Frivaldský, “Investigation of possibilities to increasing efficiency of full bridge converter designed for low output voltage and high output current applications,” in 2012 ELEKTRO, 2012, pp. 129-132.

[11] R. Zeng, “Design, analysis and operation of hybrid modular multilevel converters for HVDC applications,” University of Strathclyde, 2015.

[12] A. Lesnicar and R. Marquardt, “An innovative modular multilevel converter topology suitable for a wide power range,” in 2003 IEEE Bologna Power Tech Conference Proceedings, 2003, p. 6 pp. Vol.3.

[13] S. Allebrod, R. Hamerski, and R. Marquardt, “New transformer less scalable Modular Multilevel Converters for HVDC-transmission,” in 2008 IEEE Power Electronics Specialists Conference, 2008, pp. 174-179.

[14] R. Marquardt, “Modular Multilevel Converter topologies with DC-Short circuit current limitation,” in 8th International Conference on Power Electronics - ECCE Asia, 2011, pp. 1425-1431.

[15] R. Marquardt, “Modular Multilevel Converter: An universal concept for HVDC-Networks and extended DC-Bus-applications,” in The 2010 International Power Electronics Conference - ECCE ASIA -, 2010, pp. 502-507

[16] H. Liu, K. Ma, Z. Qin, P. C. Loh and F. Blaabjerg, “Lifetime Estimation of MMC for Offshore Wind Power HVDC Application,” in IEEE Journal of Emerging and Selected Topics in Power Electronics, vol. 4, no. 2, pp. 504-511, June 2016.

[17] A. Rodríguez-Cabero, J. Roldán-Pérez, M. Prodanovic, J. A. Suul and S. D'Arco, "Coupling of AC Grids via VSC-HVDC Interconnections for Oscillation Damping Based on Differential and Common Power Control," in IEEE Transactions on Power Electronics, vol. 35, no. 6, pp. 6548-6558, June 2020.

[18] H. C. Liu and J. Sun, "Voltage stability and control of offshore windfarms with AC collection and HVDC transmission," IEEE Journal of Emerging and Selected Topics in Power Electronics, vol. 2, no. 4, pp.1181–1189, Dec. 2014.

[19] C. Zou, H. Rao, S. Xu, Y. Li., "Analysis of Resonance Between a VSC-HVDC Converter and the AC Grid," in IEEE Transactions on Power Electronics, vol. 33, no. 12, pp. 10157-10168, Dec. 2018.

[20] J. L. Agorreta, M. Borrega, J. López, and L. Marroyo, "Modeling and control of n-paralleled grid-connected inverters with LCL filter coupled due to grid impedance in PV plants," in IEEE Transactions on Power Electronics,vol.26, no. 3, pp. 770–785, Mar. 2011.

[21] C. Guo, C. Zhao, R. Iravani, H. Ding and X. Wang, "Impact of phase-locked loop on small-signal dynamics of the line commutated converter-based high-voltage direct-current station," in IET Generation, Transmission & Distribution, vol. 11, no. 5, pp. 1311-1318.

[22] A. M. C. Buchhagen, M. Greve, and J. Jung, "Harmonic stability-practical experience of a TSO," in Proc. Wind Integr. Workshop, Nov.2016, pp.1–6.

[23] Y. Zhang, C. Hong, L. Tu, T. Zhou and J. Yang, "Research on High-frequency Resonance Mechanism and Active Harmonic Suppression Strategy of Power Systems with Power Electronics," 2018 International Conference on Power System Technology (POWERCON), Guangzhou, 2018, pp. 2350-2356.

[24] W. Ren and E. Larsen, "A refined frequency scan approach to sub-synchronous control interaction (SSCI) study of wind farms," IEEE Trans. Power Syst., vol. 31, no. 5, pp. 3904-3912, Sep. 2016.

[25] J. Sun, “Small-signal methods for AC distributed power systems—A review,” IEEE Trans. Power Electron., vol. 24, no. 11, pp. 2545–2554, Nov. 2009.

[26] G. Pinares and M. Bongiorno, “Modeling and analysis of VSC-based HVDC systems for dc network stability studies,” IEEE Trans. Power Del., vol. 31, no. 2, pp. 848-856, April 2016.

[27] D. Maksimovic, A. M. Stankovic, V. J. Thottuvelil, and G. C. Verghese, “Modeling and simulation of power electronic converters,” Proc. IEEE, vol. 89, no. 6, 2001, pp. 898-912.

[28] V. J. Thottuvelil, D. Chin, and G. C. Verghese, “Hierarchical approaches to modeling high-power factor ac-dc converters,” IEEE Trans. Power Electron., vol. 6, no. 2, pp. 179-187, April 1991.

[29] R. W. Erickson and D. Maksimovic, Fundamentals of Power Electronics, 2nd Ed. New York, NY, USA: Kluwer Academic, 2001.

[30] F. Milano, Power System Modelling and Scripting. London, U.K.: Springer-Verlag, 2010.

[31] J.J.Chavez,A.Ramirez,V.Dinavahi,R.Iravani,J.Martinez,J.Jatskevitch, and G. Chang, “Interfacing techniques for time-domain and frequency-domainsimulationmethods,”IEEETrans.PowerDel.,vol.25, no. 3, pp. 1796–1807, Jul. 2010.

[32] D. N. Zmood, D. G. Holmes, and G. H. Bode, “Frequency-domain analysis of three-phase linear current regulators,” IEEE Trans. Ind. Appl., vol. 37, no. 2, pp. 601–610, Mar./Apr. 2001.

[33] A. Ramirez, A. Semlyen, and R. Iravani, “Harmonic domain characterization of the resonant interaction between generator and transmission line,” IEEE Trans. Power Del., vol. 20, no. 2, pt. 2, pp. 1753–1762, Apr. 2005.

[34] J. R. C. Orillaza and A. R. Wood, “Harmonic State-Space Model of a Controlled TCR,” IEEE Transactions on Power Delivery, vol. 28, pp. 197-205, 2013.

[35] G. Love and A. Wood, “Harmonic state space model of power electronics,” presented at the 13th IEEE Conf. Harmonics Power Qual., Wollongong, Australia, 2008.

[36] M. Amin, and M. Molinas, “Small-signal stability assessment of power electronics based power systems: a discussion of impedance- and eigenvalue-based methods,” IEEE Trans. Ind. Appl., vol. 53, no. 5, pp. 5014–5030, Sept. 2017.

[37] Y. Mishra, S. Mishra, F. Li, Z. Y. Dong and R. C. Bansal, “Small-Signal Stability Analysis of a DFIG-Based Wind Power System Under Different Modes of Operation,” in IEEE Transactions on Energy Conversion, vol. 24, no. 4, pp. 972-982, Dec. 2009.

[38] G. O. Kalcon, G. P. Adam, O. Anaya-Lara, S. Lo, and K. Uhlen, “Small-signal stability analysis of multi-terminal VSC-based DC transmission systems,” IEEE Trans. Power Syst., vol. 27, no. 4, pp. 1818–1830, Nov. 2012.

[39] G. Pinares and M. Bongiorno, “Modeling and analysis of VSC-based HVDC systems for DC network stability studies,” IEEE Trans. Power Del., vol. 31, no. 2, pp. 848–856, Apr. 2016.

[40] R. D. Middlebrook, “Input filter considerations in design and application of switching regulators,” in Proc. IEEE Ind. Appl. Soc. Annu. Meeting, 1976, pp. 366-382.

[41] J. Sun, “Impedance-based stability criterion for grid-connected inverters,” IEEE Trans. Power Electron., vol. 26, no. 11, pp. 3075–3078, Nov. 2011

[42] B. Wen, D. Boroyevich, R. Burgos, P. Mattavelli, and Z. Shen, “Small-signal stability analysis of three-phase AC systems in the presence of constant power loads based on measured d-q, frame impedances,” IEEE Trans. Power Electron.,

vol. 30, no. 10, pp. 5952–5963, Oct. 2015.

[43] D. Dong, B. Wen, D. Boroyevich, P. Mattavelli, and Y. Xue, “Analysis of phase-locked loop low-frequency stability in three-phase grid-connected power converters considering impedance interactions,” IEEE Trans. Ind. Electron., vol. 62, no. 1, pp. 310–321, Jan. 2015.

[44] L. Harnefors, A. G. Yepes, A. Vidal, and J. Doval-Gandoy, “Passivity-based controller design of grid-connected VSCs for prevention electrical resonance instability,” IEEE Trans. Ind. Electron., vol. 62, no. 2, pp. 702–710, Feb. 2015.

[45] X. Wang, F. Blaabjerg, and W. Wu, “Modeling and analysis of harmonic stability in ac power-electronics-based power system,” IEEE Trans. Power Electron., vol. 29, no. 12, pp. 6421–6432, Dec. 2014.

[46] B. Wen, D. Dong, D. Boroyevich, R. Burgos, P. Mattavelli, and Z. Shen, “Impedance-based analysis of grid-synchronization stability for three phase paralleled converters,” IEEE Trans. Power Electron., vol. 31, no. 1, pp. 26–38, Jan. 2015.

[47] B. Wen, D. Boroyevich, R. Burgos, P. Mattavelli, and Z. Shen, “Influence of phase-locked loop on dq frame impedance of three-phase voltage-source converters and the impact on system stability,” presented at the CPES Power Electronics Conf., Blacksburg, VA, USA, Apr. 6–8, 2013.

[48] A. Rygg, M. Molinas, C. Zhang and X. Cai, “A Modified Sequence-Domain Impedance Definition and Its Equivalence to the dq-Domain Impedance Definition for the Stability Analysis of AC Power Electronic Systems,” in IEEE Journal of Emerging and Selected Topics in Power Electronics, vol. 4, no. 4, pp. 1383-1396, Dec. 2016.

[49] G. C. Paap, “Symmetrical components in the time domain and their application to power network calculations,” in *IEEE Transactions on Power Systems*, vol. 15, no. 2, pp. 522-528, May 2000.

[50] G. Amico, “Wind farm high frequency electrical resonances: impedance-based stability analysis and mitigation techniques,” Ph.D. dissertation, Dept. Electrical and Electronic Engineering, University of Strathclyde, Glasgow, UK, 2019.

[51] S. Shah, and L. Parsa, “Impedance modeling of three-phase voltage source converters in dq, sequence, and phasor domains,” IEEE Energy Convers., vol. 32, no.3, pp. 1139–1150, Sept. 2017.

[52] W. V. Lyon, Applications of the method of symmetrical components. McGraw-Hill book company, inc., 1937.

[53] S. Shah, “Small and large signal impedance modeling for stability analysis of grid-connected voltage source converters,” Department of Electrical Engineering，Rensselaer Polytechnic Institute，Troy, New York，2018.

[54] L. Harnefors, M. Bongiorno, and S. Lundberg, “Input-admittance calculation and shaping for controlled voltage-source converters,” IEEE Trans. Ind. Electron., vol. 54, no. 6, pp. 3323–3334, Dec. 2007.

[55] B. Wen, D. Boroyevich, R. Burgos, P. Mattavelli, and Z. Shen, “Analysis of D-Q small-signal impedance of grid-tied inverters,” IEEE Trans. Power Electron., vol. 31, no. 1, pp. 675–687, Jan. 2016.

[56] M. Cespedes and J. Sun, “Impedance modeling and analysis of grid-connected voltage-source converters,” IEEE Trans. Power Electron., vol. 29, no. 3, pp. 1254–1261, Mar. 2014.

[57] M. Cespedes and J. Sun, “Modeling and mitigation of harmonic resonance between wind turbines and the grid,” 2011 IEEE Energy Conversion Congress and Exposition, Phoenix, AZ, 2011, pp. 2109-2116.

[58] M. Cespedes and J. Sun, “Renewable Energy Systems Instability Involving Grid-Parallel Inverters,” 2009 Twenty-Fourth Annual IEEE Applied Power Electronics Conference and Exposition, Washington, DC, 2009.

[59] H. Nian , L. Chen, Y. Xu, H. Huang, and J. Ma, “Sequences domain impedance modeling of three-phase grid-connected converter using harmonic transfer matrices,” IEEE Energy Convers., vol. 33, no. 2, pp. 627–638, Jun. 2018.

[60] I Vieto, and J. Sun, “Sequence impedance modelling and converter-grid resonance analysis considering DC bus dynamics and mirrored harmonics,” 2018 IEEE 19th Workshop on Control and Modeling for Power Electronics.

[61] M. K. Bakhshizadeh et al., “Couplings in phase domain impedance modeling of grid-connected converters,” IEEE Trans. Power Electron, vol. 31, no. 10, pp. 6792–6796, Oct. 2016.

[62] G. Amico, A. Egea-Àlvarez, P. Brogan and S. Zhang, “Small-Signal Converter Admittance in the pn-Frame: Systematic Derivation and Analysis of the Cross-Coupling Terms,” in IEEE Transactions on Energy Conversion, vol. 34, no. 4, pp. 1829-1838, Dec. 2019.

[63] G. Amico, A. Egea-`lvarez, L. Xu and P. Brogan, “Stability margin definition for a converter-grid system based on diagonal dominance property in the sequence-frame,” 2019 21st European Conference on Power Electronics and Applications (EPE '19 ECCE Europe), Genova, Italy, 2019, pp. P.1-P.10.

[64] S. Shah and L. Parsa, “Sequence domain transfer matrix model of three-phase voltage source converters,” in Proc. IEEE Power Energy Soc. General Meet., 2016, pp. 1–5.

[65] X. Wang, L. Harnefors, and F. Blaabjerg, “Unified impedance model of grid-connected voltage-source converters,” IEEE Trans. Power Electron., vol. 33, no.

[66] H. Saad, J. Peralta, S. Dennetiere, and J. Mahseredjian,”Dynamic averaged and simplified models for MMC-based HVDC transmission systems,” IEEE Trans. Power Del., vol. 28, no. 3, pp. 1723–1730, Jul. 2013.

[67] A. Jamshidifar, and D. Jovcic, “Small-signal dynamic dq model of modular

multilevel converter for system studies," IEEE Trans. Power Del., vol. 31, no. 1, pp. 1991–1999, Feb. 2016.

[68] Y. Li, G. Tang, J. Ge, Z. He, H. Pang, J. Yang, and Y. Wu, "Modeling and damping control of modular multilevel converter based dc grid," IEEE Trans. Power Syst., vol. 31, no. 1, pp. 723–735, Jan. 2018.

[69] J. Wang, R. Burgos and D. Boroyevich, "A survey on the modular multilevel converters — Modeling, modulation and controls," 2013 IEEE Energy Conversion Congress and Exposition, Denver, CO, 2013, pp. 3984-3991.

[70] A. Lesnicar and R. Marquardt, "An innovative modular multilevel converter topology suitable for a wide power range," 2003 IEEE Bologna Power Tech Conference Proceedings, Bologna, Italy, 2003, pp. 6 pp. Vol.3.

[71] M. Glinka, "Prototype of multiphase modular-multilevel-converter with 2 MW power rating and 17-level-output-voltage," 2004 IEEE 35th Annual Power Electronics Specialists Conference (IEEE Cat. No.04CH37551), Aachen, Germany, 2004, pp. 2572-2576 Vol.4.

[72] M. Glinka and R. Marquardt, "A new AC/AC multilevel converter family," in IEEE Transactions on Industrial Electronics, vol. 52, no. 3, pp. 662-669, June 2005.

[73] S. Allebrod, R. Hamerski and R. Marquardt, "New transformer less scalable Modular Multilevel Converters for HVDC-transmission," 2008 IEEE Power Electronics Specialists Conference, Rhodes, 2008, pp. 174-179.

[74] H. M. Pirouz, M. T. Bina and K. Kanzi, "A New Approach to the Modulation and DC-Link Balancing Strategy of Modular Multilevel AC/AC Converters," 2005 International Conference on Power Electronics and Drives Systems, Kuala Lumpur, 2005, pp. 1503-1507.

[75] G. Ding, G. Tang, Z. He and M. Ding, "New technologies of voltage source

converter (VSC) for HVDC transmission system based on VSC," 2008 IEEE Power and Energy Society General Meeting - Conversion and Delivery of Electrical Energy in the 21st Century, Pittsburgh, PA, 2008, pp. 1-8.

[76] K. Friedrich, "Modern HVDC PLUS application of VSC in Modular Multilevel Converter topology," 2010 IEEE International Symposium on Industrial Electronics, Bari, 2010, pp. 3807-3810.

[77] Q. Tu, Z. Xu and J. Zhang, "Circulating current suppressing controller in modular multilevel converter," IECON 2010 - 36th Annual Conference on IEEE Industrial Electronics Society, Glendale, AZ, 2010, pp. 3198-3202.

[78] C. D. Barker and N. M. Kirby, "Reactive power loading of components within a modular multi-level HVDC VSC converter," 2011 IEEE Electrical Power and Energy Conference, Winnipeg, MB, 2011, pp. 86-90.

[79] M. A. Pérez and J. Rodríguez, "Generalized modeling and simulation of a modular multilevel converter," 2011 IEEE International Symposium on Industrial Electronics, Gdansk, 2011, pp. 1863-1868.

[80] M. Hiller, D. Krug, R. Sommer and S. Rohner, "A new highly modular medium voltage converter topology for industrial drive applications," 2009 13th European Conference on Power Electronics and Applications, Barcelona, 2009, pp. 1-10.

[81] A. Antonopoulos, L. Angquist and H. Nee, "On dynamics and voltage control of the Modular Multilevel Converter," 2009 13th European Conference on Power Electronics and Applications, Barcelona, 2009, pp. 1-10.

[82] L. Angquist, A. Antonopoulos, D. Siemaszko, K. Ilves, M. Vasiladiotis and H. Nee, "Open-Loop Control of Modular Multilevel Converters Using Estimation of Stored Energy," in IEEE Transactions on Industry Applications, vol. 47, no. 6, pp. 2516-2524, Nov.-Dec. 2011.

[83] L. Harnefors, S. Norrga, A. Antonopoulos and H. Nee, "Dynamic modeling of

modular multilevel converters," Proceedings of the 2011 14th European Conference on Power Electronics and Applications, Birmingham, 2011, pp. 1-10.

[84] M. Hagiwara, K. Nishimura and H. Akagi, "A Medium-Voltage Motor Drive With a Modular Multilevel PWM Inverter," in IEEE Transactions on Power Electronics, vol. 25, no. 7, pp. 1786-1799, July 2010.

[85] J. Reed, G. Venkataramanan and F. Martínez, "Complex phasor modeling and control of modular multilevel inverters," 2011 IEEE Energy Conversion Congress and Exposition, Phoenix, AZ, 2011, pp. 4013-4020.

[86] D. C. Ludois, J. K. Reed and G. Venkataramanan, "Hierarchical Control of Bridge-of-Bridge Multilevel Power Converters," in IEEE Transactions on Industrial Electronics, vol. 57, no. 8, pp. 2679-2690, Aug. 2010.

[87] D. C. Ludois and G. Venkataramanan, "Modular multilevel converter as a low inductance machine drive," 2012 IEEE Power and Energy Conference at Illinois, Champaign, IL, 2012, pp. 1-4.

[88] J. Lyu, X. Cai, and M. Molinas, "Frequency domain stability analysis of MMC-based HVDC for wind farm integration," IEEE J. Emerg. Sel.Topics Power Electron., vol. 4, no. 1, pp. 141–151, Mar. 2016.

[89] M. Beza, M. Bongiorno, and G. Stamatiou, "Analytical derivation of the ac-side input admittance of a modular multilevel converter with open- and closed-loop control strategies," IEEE Trans. Power Del., vol. 33, no. 1, pp. 248–256, Feb. 2018.

[90] L. Bessegato, K. Ilves, L. Harnefors, and S. Norrga, "Effects of control on the ac-side admittance of a modular multilevel converter", IEEE Trans. Power Electron., vol. 34, no. 8, pp. 7206–7220, Aug. 2019.

[91] S. Hwang, "Harmonic state-space modelling of an hvdc converter with closed-loop control," Department of Electrical and Computer Engineering，University of Canterbury, Christchurch, New Zealand，2013.

[92] J. J. Rico, M. Madrigal and E. Acha, “Dynamic harmonic evolution using the extended harmonic domain,” IEEE Trans. Power Del., vol. 18, no. 2, pp. 587-594, April 2003.

[93] J. J. Chavez and A. Ramirez, “Dynamic Harmonic Domain Modelling of Transients in Three-Phase Transmission Lines,” IEEE Trans. Power Del., vol. 23, no. 4, pp. 2294-2301, Oct. 2008.

[94] J. B. Kwon, X. Wang, F. Blaabjerg, C. L. Bak, A. R. Wood and N. R. Watson, “Harmonic instability analysis of a single-phase grid-connected converter using a harmonic state-space modelling method,” IEEE Trans. Ind. Appl., vol. 52, no. 5, pp. 4188-4200, Sept.-Oct. 2016.

[95] J. Lyu, X. Zhang, X. Cai, and M. Molinas, “Harmonic state-space based small-signal impedance modelling of modular multilevel converter with consideration of internal harmonic dynamics,” IEEE Trans. Power Electron., vol. 34, no. 3, pp. 2134–2148, Mar. 2019.

[96] Z. Xu, B. Li, S. Wang, S. Zhang and D. Xu, “Generalised Single-Phase Harmonic State Space Modelling of the Modular Multilevel Converter With Zero-Sequence Voltage Compensation,” IEEE Trans. Ind. Electron., vol. 66, no. 8, pp. 6416-6426, Aug. 2019.

[97] H. Wu, X. Wang and Ł. Kocewiak, “Impedance-Based Stability Analysis of Voltage-Controlled MMCs Feeding Linear AC Systems,” IEEE J. Emerg. Sel. Topics Power Electron., early access, 2019.

[98] H. Wu and X. Wang, “Dynamic Impact of Zero-Sequence Circulating Current on Modular Multilevel Converters: Complex-Valued AC Impedance Modelling and Analysis,” IEEE J. Emerg. Sel. Topics Power Electron., vol. 8, no. 2, pp. 1947-1963, June 2020.

[99] A. Rygg, M. Molinas, C. Zhang and X. Cai, “A Modified Sequence-Domain Impedance Definition and Its Equivalence to the dq-Domain Impedance

Definition for the Stability Analysis of AC Power Electronic Systems," IEEE J. Emerg. Sel. Topics Power Electron., vol. 4, no. 4, pp. 1383-1396, Dec. 2016.

[100] H. Zong, J. Lyu, C. Zhang, X. Cai, M. Molinas and F. Rao, "MIMO impedance based stability analysis of DFIG-based wind farm with MMC-HVDC in modified sequence domain," in Proc. 8th Int. Conf. Renew. Power Gener. (RPG), Shanghai, China, 2019, pp. 1-7.

[101] H. Zong, C. Zhang, J. Lyu, X. Cai, M. Molinas and F. Rao, "Generalized MIMO Sequence Impedance Modeling and Stability Analysis of MMC-HVDC With Wind Farm Considering Frequency Couplings," IEEE Access, vol. 8, pp. 55602-55618, 2020.

[102] K. Ji, G. Tang, H. Pang and J. Yang, "Impedance Modeling and Analysis of MMC-HVDC for Offshore Wind Farm Integration," IEEE Trans. Power Del., vol. 35, no. 3, pp. 1488-1501, June 2020.

[103] "GB National Electricity System Seven Year Statement", National Grid, 2011

[104] C. Guo, W. Liu, J. Zhao and C. Zhao, "Impact of control system on small-signal stability of hybrid multi-infeed HVDC system," in IET Generation, Transmission & Distribution, vol. 12, no. 19, pp. 4233-4239, 30 10 2018.

[105] G., Chunyi, W. Liu, C. Zhao, and X. Ni. "Small-signal dynamics and control parameters optimization of hybrid multi-infeed HVDC system." International Journal of Electrical Power & Energy Systems, 2018, pp.409-418.

[106] A. Bayo-Salas, J. Beerten, J. Rimez and D. Van Hertem, "Analysis of control interactions in multi-infeed VSC HVDC connections," in IET Generation, Transmission & Distribution, vol. 10, no. 6, pp. 1336-1344, 21 4 2016.

[107] G. Grdenić, M. Delimar and J. Beerten, "Comparative Analysis on Small-Signal Stability of Multi-Infeed VSC HVDC System With Different Reactive Power Control Strategies," in IEEE Access, vol. 7, pp. 151724-151732, 2019.

[108] A. Egea-Alvarez, C. Barker, F. Hassan and O. Gomis-Bellmunt, “Capability curves of a VSC-HVDC connected to a weak AC grid considering stability and power limits,” 11th IET International Conference on AC and DC Power Transmission, Birmingham, 2015, pp. 1-5.

[109] L. Harnefors, “Modeling of Three-Phase Dynamic Systems Using Complex Transfer Functions and Transfer Matrices,” IEEE Trans. Ind. Electron., vol. 54, no. 4, pp. 2239-2248, Aug. 2007.

[110] J. R. Bar-on and E. A. Jonckheere, “Phase margins for multivariable control systems,” Int. J. Control, vol. 52, no. 2, pp. 485–498, 1990.

[111] J. R. Bar-on and E. A. Jonckheere, “Multivariable gain margin,” Int. J. Control, vol. 54, no. 2, pp. 337–365, 1991.

[112] E. Ebrahimzadeh, F. Blaabjerg, X. Wang and C. L. Bak, “Modeling and identification of harmonic instability problems in wind farms,” 2016 IEEE Energy Conversion Congress and Exposition (ECCE), Milwaukee, WI, 2016, pp. 1-6.

[113] V. Salis, A. Costabeber, S. M. Cox, P. Zanchetta and A. Formentini, “Stability Boundary Analysis in Single-Phase Grid-Connected Inverters With PLL by LTP Theory,” in IEEE Transactions on Power Electronics, vol. 33, no. 5, pp. 4023-4036, May 2018.

[114] R. Li, L. Xu and D. Guo, “Accelerated switching function model of hybrid MMCs for HVDC system simulation,” IET Power Electron., vol. 10, no. 15, pp. 2199-2207, 15 12 2017.

[115] D. N. Zmood and D. G. Holmes, “Stationary frame current regulation of PWM inverters with zero steady-state error,” IEEE Trans. Power Electron., vol. 18, no. 3, pp. 814-822, May. 2003.

[116] O. Katsuhiko and Y. Yang, Modern Control Engineering, 5ed. Upper Saddle River, NJ: Prentice hall, 2010.

[117] J. Sun and H. Liu, “Sequence Impedance Modelling of Modular Multilevel Converters,” IEEE J. Emerg. Sel. Topics Power Electron., vol. 5, no. 4, pp. 1427-1443, Dec. 2017.

[118] M. Cespedes and J. Sun, “Impedance Modelling and Analysis of Grid-Connected Voltage-Source Converters,” IEEE Trans. Power Electron., vol. 29, no. 3, pp. 1254-1261, March. 2014.

[119] The National HVDC Centre and the University of Strathclyde, “Stability Assessment and Mitigation of Converter Interactions – Phase 2”

[120] M. Cespedes, L. Xing and J. Sun, “Constant-power load system stabilisation by passive damping,” IEEE Trans. Power Electron., vol. 26, no. 7, pp. 1832-1836, July 2011.

[121] B. Davies et al., Systems with multiple dc infeed, CIGRE Working Group B4.41, Paris, France, pp. 12–14, Dec. 2008.

Appendix A Matrix elements for MMC single-phase HSS equation

$$A_0=\begin{bmatrix} -\frac{R_m}{L_m} & -\frac{1}{4L_m} & -\frac{1}{4L_m} & 0 \\ \frac{1}{2C_m} & 0 & 0 & \frac{1}{4C_m} \\ \frac{1}{2C_m} & 0 & 0 & -\frac{1}{4C_m} \\ 0 & -\frac{1}{2L_m} & \frac{1}{2L_m} & -\frac{R_m+2Z_L}{L} \end{bmatrix};\ A_1=\begin{bmatrix} 0 & \frac{n_1e^{j\theta_1}}{8L_m} & -\frac{n_1e^{j\theta_1}}{8L_m} & 0 \\ -\frac{n_1e^{j\theta_1}}{4C_m} & 0 & 0 & -\frac{n_1e^{j\theta_1}}{8C_m} \\ \frac{n_1e^{j\theta_1}}{4C_m} & 0 & 0 & -\frac{n_1e^{j\theta_1}}{8C_m} \\ 0 & \frac{n_1e^{j\theta_1}}{4L_m} & \frac{n_1e^{j\theta_1}}{4L_m} & 0 \end{bmatrix};$$

$$A_{-1}=\begin{bmatrix} 0 & \frac{n_1e^{-j\theta_1}}{8L_m} & -\frac{n_1e^{-j\theta_1}}{8L_m} & 0 \\ -\frac{n_1e^{-j\theta_1}}{4C_m} & 0 & 0 & -\frac{n_1e^{-j\theta_1}}{8C_m} \\ \frac{n_1e^{-j\theta_1}}{4C_m} & 0 & 0 & -\frac{n_1e^{-j\theta_1}}{8C_m} \\ 0 & \frac{n_1e^{-j\theta_1}}{4L_m} & \frac{n_1e^{-j\theta_1}}{4L_m} & 0 \end{bmatrix};\ A_2=\begin{bmatrix} 0 & \frac{n_2e^{j\theta_2}}{8L_m} & \frac{n_2e^{j\theta_2}}{8L_m} & 0 \\ -\frac{n_2e^{j\theta_2}}{4C_m} & 0 & 0 & -\frac{n_2e^{j\theta_2}}{8C_m} \\ -\frac{n_2e^{j\theta_2}}{4C_m} & 0 & 0 & \frac{n_2e^{j\theta_2}}{8C_m} \\ 0 & \frac{n_2e^{j\theta_2}}{4L_m} & -\frac{n_2e^{j\theta_2}}{4L_m} & 0 \end{bmatrix};$$

$$A_{-2}=\begin{bmatrix} 0 & \frac{n_2e^{-j\theta_2}}{8L_m} & \frac{n_2e^{-j\theta_2}}{8L_m} & 0 \\ -\frac{n_2e^{-j\theta_2}}{4C_m} & 0 & 0 & -\frac{n_2e^{-j\theta_2}}{8C_m} \\ -\frac{n_2e^{-j\theta_2}}{4C_m} & 0 & 0 & \frac{n_2e^{-j\theta_2}}{8C_m} \\ 0 & \frac{n_2e^{-j\theta_2}}{4L_m} & -\frac{n_2e^{-j\theta_2}}{4L_m} & 0 \end{bmatrix};\ A_h=A_{-h}=\begin{bmatrix} 0 & 0 & 0 & 0 \\ 0 & 0 & 0 & 0 \\ 0 & 0 & 0 & 0 \\ 0 & 0 & 0 & 0 \end{bmatrix} \qquad (h\geq 3)$$

where $A_{-h}\ldots A_{-2}$, A_{-1}, A_0, A_1, $A_2\ldots A_h$ are the elements of the matrix $\mathbf{A_s}$ in (3.38).

$$B_0=\begin{bmatrix} \frac{1}{2L_m} & 0 & 0 & 0 \end{bmatrix}^T;\ B_h=B_{-h}=\begin{bmatrix} 0 & 0 & 0 & 0 \end{bmatrix} \qquad (h\geq 1)\ .$$

where $B_{-h}\ldots B_0, \ldots B_h$ are the elements of the matrix $\mathbf{B_s}$ in (3.39).

Appendix B Matrices for MMC three-phase HSS equation

$$\mathbf{v}_{gabc}=\begin{bmatrix} v_{ga} \\ v_{gb} \\ v_{gc} \end{bmatrix},\quad \mathbf{i}_{gabc}=\begin{bmatrix} i_{ga} \\ i_{gb} \\ i_{gc} \end{bmatrix},\quad \mathbf{v}^{\Sigma}_{cuabc}=\begin{bmatrix} v^{\Sigma}_{cua} \\ v^{\Sigma}_{cub} \\ v^{\Sigma}_{cuc} \end{bmatrix},\ \mathbf{v}^{\Sigma}_{clabc}=\begin{bmatrix} v^{\Sigma}_{cla} \\ v^{\Sigma}_{clb} \\ v^{\Sigma}_{clc} \end{bmatrix},\ \mathbf{v}_{uabc}=\begin{bmatrix} v_{ua} \\ v_{ub} \\ v_{uc} \end{bmatrix},$$

$$\mathbf{i}_{uabc}=\begin{bmatrix} i_{ua} \\ i_{ub} \\ i_{uc} \end{bmatrix},\ \mathbf{v}_{labc}=\begin{bmatrix} v_{la} \\ v_{lb} \\ v_{lc} \end{bmatrix},\quad \mathbf{i}_{labc}=\begin{bmatrix} i_{la} \\ i_{lb} \\ i_{lc} \end{bmatrix},\quad \mathbf{i}_{cabc}=\begin{bmatrix} i_{ca} \\ i_{cb} \\ i_{cc} \end{bmatrix},\ \mathbf{V}_{dc}=\begin{bmatrix} V_{dc} \\ V_{dc} \\ V_{dc} \end{bmatrix},\quad \mathbf{v}_{n}=\begin{bmatrix} v_{n} \\ v_{n} \\ v_{n} \end{bmatrix},$$

$$\mathbf{n}_{uabc}=\begin{bmatrix} n_{ua} & 0 & 0 \\ 0 & n_{ub} & 0 \\ 0 & 0 & n_{uc} \end{bmatrix},\quad \mathbf{n}_{labc}=\begin{bmatrix} n_{la} & 0 & 0 \\ 0 & n_{lb} & 0 \\ 0 & 0 & n_{lc} \end{bmatrix},\quad \mathbf{R}_{m}=\begin{bmatrix} R_{m} & 0 & 0 \\ 0 & R_{m} & 0 \\ 0 & 0 & R_{m} \end{bmatrix},$$

$$\mathbf{L}_{m}=\begin{bmatrix} L_{m} & 0 & 0 \\ 0 & L_{m} & 0 \\ 0 & 0 & L_{m} \end{bmatrix},\mathbf{C}_{m}=\begin{bmatrix} C_{m} & 0 & 0 \\ 0 & C_{m} & 0 \\ 0 & 0 & C_{m} \end{bmatrix},\triangle\mathbf{v}_{pabc}=\begin{bmatrix} \triangle v_{pa} \\ \triangle v_{pb} \\ \triangle v_{pc} \end{bmatrix},\triangle\mathbf{i}_{cabc}=\begin{bmatrix} \triangle i_{ca} \\ \triangle i_{cb} \\ \triangle i_{cc} \end{bmatrix},$$

$$\triangle\mathbf{i}_{gabc}=\begin{bmatrix} \triangle i_{ga} \\ \triangle i_{gb} \\ \triangle i_{gc} \end{bmatrix},\ \triangle\mathbf{v}^{\Sigma}_{cuabc}=\begin{bmatrix} \Delta v^{\Sigma}_{cua} \\ \triangle v^{\Sigma}_{cub} \\ \triangle v^{\Sigma}_{cuc} \end{bmatrix},\ \triangle\mathbf{v}^{\Sigma}_{clabc}=\begin{bmatrix} \triangle v^{\Sigma}_{cla} \\ \triangle v^{\Sigma}_{clb} \\ \triangle v^{\Sigma}_{clc} \end{bmatrix},\ \mathbf{N}_{uabc}=\begin{bmatrix} N_{ua} & 0 & 0 \\ 0 & N_{ub} & 0 \\ 0 & 0 & N_{uc} \end{bmatrix},$$

$$\mathbf{N}_{labc}=\begin{bmatrix} N_{la} & 0 & 0 \\ 0 & N_{lb} & 0 \\ 0 & 0 & N_{lc} \end{bmatrix},\ \triangle\mathbf{n}_{uabc}=\begin{bmatrix} \triangle n_{ua} \\ \triangle n_{ub} \\ \triangle n_{uc} \end{bmatrix},\ \triangle\mathbf{n}_{labc}=\begin{bmatrix} \triangle n_{la} \\ \triangle n_{lb} \\ \triangle n_{lc} \end{bmatrix},\quad \mathbf{I}_{cabc}=\begin{bmatrix} I_{ca} & 0 & 0 \\ 0 & I_{cb} & 0 \\ 0 & 0 & I_{cc} \end{bmatrix},$$

$$\mathbf{I}_{gabc}=\begin{bmatrix} I_{ga} & 0 & 0 \\ 0 & I_{gb} & 0 \\ 0 & 0 & I_{gc} \end{bmatrix},\ \mathbf{V}^{\Sigma}_{cuabc}=\begin{bmatrix} V^{\Sigma}_{cua} & 0 & 0 \\ 0 & V^{\Sigma}_{cub} & 0 \\ 0 & 0 & V^{\Sigma}_{cuc} \end{bmatrix},\text{ and }\ \mathbf{V}^{\Sigma}_{clabc}=\begin{bmatrix} V^{\Sigma}_{cla} & 0 & 0 \\ 0 & V^{\Sigma}_{clb} & 0 \\ 0 & 0 & V^{\Sigma}_{clc} \end{bmatrix}.$$

where these matrices are defined for the equation (4.6).

$$\Gamma\left[\mathbf{A}_s\right]=\begin{bmatrix}
\mathbf{A}_s^0 & \mathbf{A}_s^{-1} & \dots & \mathbf{A}_s^{-h} & & & \\
\mathbf{A}_s^1 & \ddots & \ddots & \ddots & \ddots & & \\
\vdots & \ddots & \mathbf{A}_s^0 & \mathbf{A}_s^{-1} & \ddots & \ddots & \\
\mathbf{A}_s^h & \dots & \mathbf{A}_s^1 & \mathbf{A}_s^0 & \mathbf{A}_s^{-1} & \dots & \mathbf{A}_s^{-h} \\
 & \ddots & \ddots & \mathbf{A}_s^1 & \mathbf{A}_s^0 & \ddots & \vdots \\
 & & \ddots & \ddots & \ddots & \ddots & \mathbf{A}_s^{-1} \\
 & & & \mathbf{A}_s^h & \dots & \mathbf{A}_s^1 & \mathbf{A}_s^0
\end{bmatrix}$$

$$\Gamma\left[\mathbf{B}\right]=\begin{bmatrix}
\mathbf{B}^0 & \mathbf{B}^{-1} & \dots & \mathbf{B}^{-h} & & & \\
\mathbf{B}^1 & \ddots & \ddots & \ddots & \ddots & & \\
\vdots & \ddots & \mathbf{B}^0 & \mathbf{B}^{-1} & \ddots & \ddots & \\
\mathbf{B}^h & \dots & \mathbf{B}^1 & \mathbf{B}^0 & \mathbf{B}^{-1} & \dots & \mathbf{B}^{-h} \\
 & \ddots & \ddots & \mathbf{B}^1 & \mathbf{B}^0 & \ddots & \vdots \\
 & & \ddots & \ddots & \ddots & \ddots & \mathbf{B}^{-1} \\
 & & & \mathbf{B}^h & \dots & \mathbf{B}^1 & \mathbf{B}^0
\end{bmatrix}$$

$$\Gamma\left[\mathbf{M}\right]=\begin{bmatrix}
\mathbf{M}^0 & \mathbf{M}^{-1} & \dots & \mathbf{M}^{-h} & & & \\
\mathbf{M}^1 & \ddots & \ddots & \ddots & \ddots & & \\
\vdots & \ddots & \mathbf{M}^0 & \mathbf{M}^{-1} & \ddots & \ddots & \\
\mathbf{M}^h & \dots & \mathbf{M}^1 & \mathbf{M}^0 & \mathbf{M}^{-1} & \dots & \mathbf{M}^{-h} \\
 & \ddots & \ddots & \mathbf{M}^1 & \mathbf{M}^0 & \ddots & \vdots \\
 & & \ddots & \ddots & \ddots & \ddots & \mathbf{M}^{-1} \\
 & & & \mathbf{M}^h & \dots & \mathbf{M}^1 & \mathbf{M}^0
\end{bmatrix}$$

$$\mathbf{HG_A}=\begin{bmatrix}
\mathbf{G_A}(s-jh\omega_0) & & & & & & \\
 & \ddots & & & & & \\
 & & \mathbf{G_A}(s-j\omega_0) & & & & \\
 & & & \mathbf{G_A}(s) & & & \\
 & & & & \mathbf{G_A}(s+j\omega_0) & & \\
 & & & & & \ddots & \\
 & & & & & & \mathbf{G_A}(s+jh\omega_0)
\end{bmatrix}$$

$$\mathbf{HG_B} = \begin{bmatrix} \mathbf{G_B}(s - jh\omega_0) & & & & & & \\ & \ddots & & & & & \\ & & \mathbf{G_B}(s - j\omega_0) & & & & \\ & & & \mathbf{G_B}(s) & & & \\ & & & & \mathbf{G_B}(s + j\omega_0) & & \\ & & & & & \ddots & \\ & & & & & & \mathbf{G_B}(s + jh\omega_0) \end{bmatrix}$$

$$\mathbf{Q} = \begin{bmatrix} -jh\omega_0\mathbf{I} & & & & & & \\ & \ddots & & & & & \\ & & -j\omega_0\mathbf{I} & & & & \\ & & & 0\cdot\mathbf{I} & & & \\ & & & & j\omega_0\mathbf{I} & & \\ & & & & & \ddots & \\ & & & & & & jh\omega_0\mathbf{I} \end{bmatrix}$$

$$\mathbf{\Delta X}_{PN0} = \begin{bmatrix} \mathbf{\Delta x}_{PN0}(s - jh\omega_0) \\ \vdots \\ \mathbf{\Delta x}_{PN0}(s - j\omega_0) \\ \mathbf{\Delta x}_{PN0}(s) \\ \mathbf{\Delta x}_{PN0}(s + j\omega_0) \\ \vdots \\ \mathbf{\Delta x}_{PN0}(s - jh\omega_0) \end{bmatrix}$$

$$\mathbf{\Delta U}_{PN0} = \begin{bmatrix} \mathbf{\Delta v}_{PN0}(s - jh\omega_0) \\ \vdots \\ \mathbf{\Delta v}_{PN0}(s - j\omega_0) \\ \mathbf{\Delta v}_{PN0}(s) \\ \mathbf{\Delta v}_{PN0}(s + j\omega_0) \\ \vdots \\ \mathbf{\Delta v}_{PN0}(s - jh\omega_0) \end{bmatrix}$$

where the above matrices are defined for equation (4.17).

In the case of h=0, that is, the dc component is considered, the dc related matrix $\mathbf{A}_s^0$ in the matrix $\Gamma[\mathbf{A}_s]$ can be expressed as

$$\mathbf{A}_s^0=\begin{bmatrix} -\dfrac{\mathbf{R}_m}{\mathbf{L}_m} & \mathbf{0} & -\dfrac{\mathbf{PN}_{uabc}^0\mathbf{P}^{-1}}{2\mathbf{L}_m} & -\dfrac{\mathbf{PN}_{labc}^0\mathbf{P}^{-1}}{2\mathbf{L}_m} \\ \mathbf{0} & -\dfrac{\mathbf{R}_m}{\mathbf{L}_m}\cdot\mathbf{C}_z & -\dfrac{\mathbf{PN}_{uabc}^0\mathbf{P}^{-1}}{\mathbf{L}_m} & \dfrac{\mathbf{PN}_{labc}^0\mathbf{P}^{-1}}{\mathbf{L}_m} \\ \dfrac{\mathbf{PN}_{uabc}^0\mathbf{P}^{-1}}{\mathbf{C}_m} & \dfrac{\mathbf{PN}_{uabc}^0\mathbf{P}^{-1}}{2\mathbf{C}_m}\cdot\mathbf{C}_z & \mathbf{0} & \mathbf{0} \\ \dfrac{\mathbf{PN}_{labc}^0\mathbf{P}^{-1}}{\mathbf{C}_m} & -\dfrac{\mathbf{PN}_{labc}^0\mathbf{P}^{-1}}{2\mathbf{C}_m}\cdot\mathbf{C}_z & \mathbf{0} & \mathbf{0} \end{bmatrix}$$

where $\mathbf{N}_{uabc}^0$ and $\mathbf{N}_{labc}^0$ are the dc component matrices of the steady-state modulation ratio of the upper and lower arms .

For each phase, both the dc components for the upper and lower arms are 0.5 and there exits

$$\mathbf{N}_{uabc}^0=\begin{bmatrix} \frac{1}{2} & 0 & 0 \\ 0 & \frac{1}{2} & 0 \\ 0 & 0 & \frac{1}{2} \end{bmatrix};\quad \mathbf{N}_{labc}^0=\begin{bmatrix} \frac{1}{2} & 0 & 0 \\ 0 & \frac{1}{2} & 0 \\ 0 & 0 & \frac{1}{2} \end{bmatrix}$$

In the matrix $\Gamma[\mathbf{M}]$, the dc component related elements can be written in the matrix form as

$$\mathbf{M}^0=\begin{bmatrix} -\dfrac{\mathbf{PV}_{cuabc}^{\Sigma 0}\mathbf{P}^{-1}}{2\mathbf{L}_m} & -\dfrac{\mathbf{PV}_{clabc}^{\Sigma 0}\mathbf{P}^{-1}}{2\mathbf{L}_m} \\ -\dfrac{\mathbf{PV}_{cuabc}^{\Sigma 0}\mathbf{P}^{-1}}{\mathbf{L}_m} & \dfrac{\mathbf{PV}_{clabc}^{\Sigma 0}\mathbf{P}^{-1}}{\mathbf{L}_m} \\ \dfrac{(2\mathbf{PI}_{cabc}^{0}\mathbf{P}^{-1}+\mathbf{PI}_{gabc}^{0}\mathbf{P}^{-1})}{2\mathbf{C}_m} & \mathbf{0} \\ \mathbf{0} & \dfrac{(2\mathbf{PI}_{cabc}^{0}\mathbf{P}^{-1}-\mathbf{PI}_{gabc}^{0}\mathbf{P}^{-1})}{2\mathbf{C}_m} \end{bmatrix}$$

where $\mathbf{V}_{cuabc}^{\Sigma 0}$ and $\mathbf{V}_{clabc}^{\Sigma 0}$ denote the dc component matrices of the equivalent capacitor of the upper and lower arms and are expressed as $\mathbf{V}_{cuabc}^{\Sigma 0}=\begin{bmatrix} V_{cua}^{\Sigma 0} & 0 & 0 \\ 0 & V_{cub}^{\Sigma 0} & 0 \\ 0 & 0 & V_{cuc}^{\Sigma 0} \end{bmatrix}$ and $\mathbf{V}_{clabc}^{\Sigma}=\begin{bmatrix} V_{cla}^{\Sigma 0} & 0 & 0 \\ 0 & V_{clb}^{\Sigma 0} & 0 \\ 0 & 0 & V_{clc}^{\Sigma 0} \end{bmatrix}$; $\mathbf{I}_{cabc}^{0}$ is the matrix composed by dc component of the three-phase circulating current. $\mathbf{I}_{gabc}^{0}=\begin{bmatrix} I_{ga}^{0} & 0 & 0 \\ 0 & I_{gb}^{0} & 0 \\ 0 & 0 & I_{gc}^{0} \end{bmatrix}$ denotes the dc component of the steady-state ac current of the MMC. Due to the ac current without the dc component, $\mathbf{I}_{gabc}^{0}$ is a 3 by 3 matrix with zero element.

In the matrix $\Gamma[\mathbf{B}]$, the matrix $\mathbf{B}^0$ associated with the dc component can be written as

$$\mathbf{B}^0=\begin{bmatrix} \mathbf{0} \\ -\dfrac{2}{\mathbf{L_m}} \\ \mathbf{0} \\ \mathbf{0} \end{bmatrix}$$

The perturbation components for the state variables and the input are expressed

as $\Delta\mathbf{x}_{PN0}(s)$ and $\Delta\mathbf{v}_{PN0}(s)$. The transfer function matrices for the corresponding controller are denoted as $\mathbf{G}_{\mathbf{A}}(s)$ and $\mathbf{G}_{\mathbf{B}}(s)$.

In the case of $h\neq 0$, in the matrix $\Gamma[\mathbf{A}_s]$, the matrix $\mathbf{A}_s^{\pm h}$ composed by $\pm h\omega_0$ order harmonic associated elements are expressed as

$$\mathbf{A}_s^{\pm h}=\begin{bmatrix} \mathbf{0} & \mathbf{0} & -\dfrac{\mathbf{PN}_{uabc}^{\pm h}\mathbf{P}^{-1}}{2\mathbf{L}_m} & -\dfrac{\mathbf{PN}_{labc}^{\pm h}\mathbf{P}^{-1}}{2\mathbf{L}_m} \\ \mathbf{0} & \mathbf{0} & -\dfrac{\mathbf{PN}_{uabc}^{\pm h}\mathbf{P}^{-1}}{\mathbf{L}_m} & \dfrac{\mathbf{PN}_{labc}^{\pm h}\mathbf{P}^{-1}}{\mathbf{L}_m} \\ \dfrac{\mathbf{PN}_{uabc}^{\pm h}\mathbf{P}^{-1}}{\mathbf{C}_m} & \dfrac{\mathbf{PN}_{uabc}^{\pm h}\mathbf{P}^{-1}}{2\mathbf{C}_m}\cdot\mathbf{C}_z & \mathbf{0} & \mathbf{0} \\ \dfrac{\mathbf{PN}_{labc}^{\pm h}\mathbf{P}^{-1}}{\mathbf{C}_m} & -\dfrac{\mathbf{PN}_{labc}^{\pm h}\mathbf{P}^{-1}}{2\mathbf{C}_m}\cdot\mathbf{C}_z & \mathbf{0} & \mathbf{0} \end{bmatrix}$$

where $\mathbf{N}_{uabc}^{\pm h}$ and $\mathbf{N}_{labc}^{\pm h}$ are the matrices composed by h order harmonic of the steady-state modulation ratio in abc frame and can be expressed as

$$\mathbf{N}_{uabc}^{\pm h}=\begin{bmatrix} \dfrac{M_{nua}^{\pm h}e^{\pm j\theta_{nua}^{\pm h}}}{2} & 0 & 0 \\ 0 & \dfrac{M_{nub}^{\pm h}e^{\pm j\theta_{nub}^{\pm h}}}{2} & 0 \\ 0 & 0 & \dfrac{M_{nub}^{\pm h}e^{\pm j\theta_{nub}^{\pm h}}}{2} \end{bmatrix},$$

$$\mathbf{N}_{labc}^{\pm h}=\begin{bmatrix} \dfrac{M_{nla}^{\pm h}e^{\pm j\theta_{nla}^{\pm h}}}{2} & 0 & 0 \\ 0 & \dfrac{M_{nlb}^{\pm h}e^{\pm j\theta_{nlb}^{\pm h}}}{2} & 0 \\ 0 & 0 & \dfrac{M_{nub}^{\pm h}e^{\pm j\theta_{nuc}^{\pm h}}}{2} \end{bmatrix}$$

$$\mathbf{A}_s^{\pm h}=\begin{bmatrix} \mathbf{0} & \mathbf{0} & -\dfrac{\mathbf{PN}_{uabc}^{\pm h}\mathbf{P}^{-1}}{2\mathbf{L}_m} & -\dfrac{\mathbf{PN}_{labc}^{\pm h}\mathbf{P}^{-1}}{2\mathbf{L}_m} \\ \mathbf{0} & \mathbf{0} & -\dfrac{\mathbf{PN}_{uabc}^{\pm h}\mathbf{P}^{-1}}{\mathbf{L}_m} & \dfrac{\mathbf{PN}_{labc}^{\pm h}\mathbf{P}^{-1}}{\mathbf{L}_m} \\ \dfrac{\mathbf{PN}_{uabc}^{\pm h}\mathbf{P}^{-1}}{\mathbf{C}_m} & \dfrac{\mathbf{PN}_{uabc}^{\pm h}\mathbf{P}^{-1}}{2\mathbf{C}_m}\cdot\mathbf{C}_z & \mathbf{0} & \mathbf{0} \\ \dfrac{\mathbf{PN}_{labc}^{\pm h}\mathbf{P}^{-1}}{\mathbf{C}_m} & -\dfrac{\mathbf{PN}_{labc}^{\pm h}\mathbf{P}^{-1}}{2\mathbf{C}_m}\cdot\mathbf{C}_z & \mathbf{0} & \mathbf{0} \end{bmatrix}$$

$$\mathbf{N}_{uabc}^{\pm h}=\begin{bmatrix} \dfrac{M_{nua}^{\pm h}e^{\pm jQ_{nua}^{\pm h}}}{2} & 0 & 0 \\ 0 & \dfrac{M_{nub}^{\pm h}e^{\pm jQ_{nub}^{\pm h}}}{2} & 0 \\ 0 & 0 & \dfrac{M_{nub}^{\pm h}e^{\pm jQ_{nub}^{\pm h}}}{2} \end{bmatrix} \mathbf{N}_{labc}^{\pm h}=\begin{bmatrix} \dfrac{M_{nla}^{\pm h}e^{\pm jQ_{nla}^{\pm h}}}{2} & 0 & 0 \\ 0 & \dfrac{M_{nlb}^{\pm h}e^{\pm jQ_{nlb}^{\pm h}}}{2} & 0 \\ 0 & 0 & \dfrac{M_{nub}^{\pm h}e^{\pm jQ_{nuc}^{\pm h}}}{2} \end{bmatrix}$$

$$\mathbf{M}^0=\begin{bmatrix} -\dfrac{\mathbf{PV}_{cuabc}^{\Sigma 0}\mathbf{P}^{-1}}{2\mathbf{L}_m} & -\dfrac{\mathbf{PV}_{clabc}^{\Sigma 0}\mathbf{P}^{-1}}{2\mathbf{L}_m} \\ -\dfrac{\mathbf{PV}_{cuabc}^{\Sigma 0}\mathbf{P}^{-1}}{\mathbf{L}_m} & \dfrac{\mathbf{PV}_{cuabc}^{\Sigma 0}\mathbf{P}^{-1}}{\mathbf{L}_m} \\ \dfrac{(2\mathbf{PI}_{cabc}^{0}\mathbf{P}^{-1}+\mathbf{PI}_{gabc}^{0}\mathbf{P}^{-1})}{2\mathbf{C}_m} & \mathbf{0} \\ \mathbf{0} & \dfrac{(2\mathbf{PI}_{cabc}^{0}\mathbf{P}^{-1}-\mathbf{PI}_{gabc}^{0}\mathbf{P}^{-1})}{2\mathbf{C}_m} \end{bmatrix} \mathbf{M}^h=\begin{bmatrix} -\dfrac{\mathbf{PV}_{cuabc}^{\Sigma h}\mathbf{P}^{-1}}{2\mathbf{L}_m} & -\dfrac{\mathbf{PV}_{clabc}^{\Sigma h}\mathbf{P}^{-1}}{2\mathbf{L}_m} \\ -\dfrac{\mathbf{PV}_{cuabc}^{\Sigma h}\mathbf{P}^{-1}}{\mathbf{L}_m} & \dfrac{\mathbf{PV}_{cuabc}^{\Sigma h}\mathbf{P}^{-1}}{\mathbf{L}_m} \\ \dfrac{(2\mathbf{PI}_{cabc}^{h}\mathbf{P}^{-1}+\mathbf{PI}_{gabc}^{h}\mathbf{P}^{-1})}{2\mathbf{C}_m} & \mathbf{0} \\ \mathbf{0} & \dfrac{(2\mathbf{PI}_{cabc}^{h}\mathbf{P}^{-1}-\mathbf{PI}_{gabc}^{h}\mathbf{P}^{-1})}{2\mathbf{C}_m} \end{bmatrix}$$

$$\mathbf{V}_{cuabc}^{\Sigma 0}=\begin{bmatrix} M_{vcua}^{0}e^{\pm jQ_{vcua}^{0}} & 0 & 0 \\ 0 & M_{vcub}^{0}e^{\pm jQ_{vcub}^{0}} & 0 \\ 0 & 0 & M_{vcuc}^{0}e^{\pm jQ_{vcuc}^{0}} \end{bmatrix} \mathbf{V}_{cuabc}^{\Sigma\pm h}=\begin{bmatrix} \dfrac{M_{vcua}^{\pm h}e^{\pm jQ_{vcua}^{\pm h}}}{2} & 0 & 0 \\ 0 & \dfrac{M_{vcub}^{\pm h}e^{\pm jQ_{vcub}^{\pm h}}}{2} & 0 \\ 0 & 0 & \dfrac{M_{vcuc}^{\pm h}e^{\pm jQ_{vcuc}^{\pm h}}}{2} \end{bmatrix}$$

Taking $h=1$ for example, $\mathbf{V}_{cuabc}^{\Sigma 1}$ denotes the operational three-phase voltage at fundamental frequency.

$$\mathbf{V}_{cua}^{\Sigma 1}=M_{vcua}^{1}\cdot\cos(\omega_0 t+Q_{vcua}^{1})=\frac{M_{vcua}^{1}e^{j(\omega_0 t+Q_{vcua}^{1})}+M_{vcua}^{1}e^{-j(\omega_0 t+Q_{vcua}^{1})}}{2}$$
$$=\frac{M_{vcua}^{1}e^{jQ_{vcua}^{1}}}{2}e^{j\omega_0 t}+\frac{M_{vcua}^{1}e^{-jQ_{vcua}^{1}}}{2}e^{-j\omega_0 t}$$

Author's Publication and Report

[1] **Y. Chen**, L. Xu, "Coupling Admittance Analysis of VSC Connected to Weak Grid System in Sequence-Frame" presented at the 10th International Conference on Power Electronics, Machines and Drives, 2020, United Kingdom. (Accepted. The conference is postponed until December due to COVID-19.)

Abstract: The small-signal admittance of voltage source converter (VSC) with different controls in the synchronous reference (*dq*) frame has been derived in previous studies. However, the admittance terms in *dq* frames are coupled, which increases difficulties of analyzing the system. To simplify the stability analysis, the admittance is mapped into the positive-negative (*pn*) sequence-frame. Based on the converter admittance in *pn* frame, the stability problems associated with the coupling admittance created by the phase-locked loop (PLL) and outer loop controller are studied separately. To overcome the disadvantage of the traditional outer loop controller, an improved outer loop controller that can reduce the coupling admittance is proposed to improve the system stability. A weak grid connected VSC system is modelled in MATLAB-SIMULINK® environment to validate the theoretical study.

[2] **Y. Chen**, L. Xu, A. Egea, B. Marshall, M. Rahman, O. Adeuyi, "MMC Impedance Modelling and Interaction of Converters in Close Proximity", in print IEEE Journal of Emerging and Selected Topics in Power Electronic.

Abstract: This paper develops a small-signal impedance model of modular multilevel converters (MMCs) using harmonic state-space (HSS) method and studies the stability in a multiple converter scenario. In order to simplify analysis on the coupling characteristics between different frequencies in MMCs, the proposed model is

developed in the positive-negative-zero (PN0) sequence-frame, where the zero-sequence current in three-phase three-wire system is directly set to zero without introducing complicated method. A simple 2 by 2 admittance matrix in PN0-frame is extracted from the MMC small-signal model for ease of system stability analysis. Using the developed impedance model, the multi-infeed interaction factor (MIIF) measure is adopted to analyze the most significant interactions for multi-infeed converter systems to be prioritized. Different outer-loop controllers are adopted and compared in the analysis to illustrate the effect of different control modes on converter impedance and system stability. Analytical studies and time-domain simulation results are provided to validate the proposed model and stability analysis.

[3] D. Guo, **Y. Chen**, A. Egea and G. Amico, "Stability Assessment and Mitigation HVDC Converter Interactions Report I: Development and Validation of MMC Converter Impedance Models," Report for the UK National HVDC Centre, Oct. 2019.

[4] D. Guo, **Y. Chen** and L. Xu, "Stability Assessment and Mitigation HVDC Converter Interactions Report II: Development of Typical AC Network Configuration for Converter Interaction Study," Report for the UK National HVDC Centre, Feb. 2020.

[5] **Y. Chen**, L. Xu, and D. Guo, "Stability Assessment and Mitigation HVDC Converter Interactions Report III: Development of MMC Impedance Models and Interaction of Converters in Close Proximity", Report for the UK National HVDC Centre, June 2020 .

.